Developing a Reasoned Argument That No Large-Scale Fracturing or Faulting Will Be Induced in the Host Rock by a Deep Geological Repository

NWMO TR-2008-14 December 2008

Rodney S. Read

RSRead Consulting Inc.

nwmo

NUCLEAR WASTE MANAGEMENT ORGANIZATION

SOCIÉTÉ DE GESTION DES DÉCHETS NUCLÉAIRES

Nuclear Waste Management Organization
22 St. Clair Avenue East, 6th Floor
Toronto, Ontario
M4T 2S3
Canada

Tel: 416-934-9814
Web: www.nwmo.ca

Developing a Reasoned Argument that No Large-Scale Fracturing or Faulting Will Be Induced in the Host Rock by a Deep Geological Repository

NWMO TR-2008-14

December 2008

Rodney S. Read
RSRead Consulting Inc.

ABSTRACT

Title: **Developing a Reasoned Argument that No Large-Scale Fracturing or Faulting Will Be Induced in the Host Rock by a Deep Geological Repository**
Report No.: **NWMO TR-2008-14**
Author(s): Rodney S. Read
Company: RSRead Consulting Inc.
Date: December 2008

Abstract
This report provides a Reasoned Argument that no large-scale fracturing or faulting will be induced in the host rock by a deep geological repository (DGR). The report considers four DGR designs in three possible host rocks, including crystalline and sedimentary rock types. The Reasoned Argument draws information from results of previously conducted thermal-mechanical analyses and simple scoping calculations using closed-form solutions, along with evidence from experiments conducted in Canada and elsewhere. The report concludes that large-scale fracturing in the far-field is implausible given the expected in situ stress conditions in relation to rock strength. Near-field damage development and fracturing are expected in many of the DGR scenarios in the different rock types, but these near-field effects are not expected to lead to large-scale fracturing that would compromise the integrity of the DGR and surrounding rock mass. The report identifies thermo-poroelastic effects as one possible driving mechanism that should be studied further, and provides other recommended analysis and characterization activities to further validate the conclusions drawn from the Reasoned Argument.

TABLE OF CONTENTS

Page

ABSTRACT ..... **v**

1. INTRODUCTION **1**

2. TERMS OF REFERENCE **1**

2.1 DEFINITION OF THE REASONED ARGUMENT **2**
2.2 DEEP GEOLOGICAL REPOSITORY **3**
2.2.1 General 3
2.2.2 AECL-type In-Room Placement Design 6
2.2.3 KBS-3V-type In-floor Borehole Placement Design 8
2.2.4 KBS-3H-type Horizontal Borehole Placement Design 10
2.2.5 NAGRA-type In-Room Placement Design 12
2.3 CRYSTALLINE HOST ROCK **13**
2.3.1 General Geology 14
2.3.2 Fracture Characteristics 14
2.3.3 Rock Mass Properties 18
2.3.4 Initial In Situ Conditions 21
2.4 SEDIMENTARY HOST ROCK **24**
2.4.1 General Geology 24
2.4.2 Fracture Characteristics 26
2.4.3 Rock Mass Properties 26
2.4.4 Initial In Situ Conditions 26

3. INDUCED FRACTURING OF ROCK **30**

3.1 EVOLUTION OF IN SITU CONDITIONS **30**
3.1.1 Effective Stress Changes 30
3.1.2 Rock Mass Property Changes 33
3.2 FAILURE MECHANISMS **35**
3.2.1 Extensile Fracturing 35
3.2.2 Shear Fracturing 44
3.2.3 Other Failure Mechanisms 46
3.3 CRITICAL FEATURES, EVENTS AND PROCESSES **46**
3.3.1 Excavation Design 46
3.3.2 Excavation Method 48
3.3.3 Heat Generation 48
3.3.4 Groundwater Table 50
3.3.5 Chemical Alteration of Rock 50
3.3.6 Glaciation and Permafrost 50
3.3.7 Discontinuities 51
3.3.8 Material Properties Contrast 51
3.3.9 Seismicity 52
3.3.10 Heave 53
3.3.11 Backfill/Rock Interaction 53

4. ANALYSIS SUPPORTING THE REASONED ARGUMENT 54

4.1 METHODOLOGY AND CRITERIA 54
4.2 FAR-FIELD ANALYSIS OF A DEEP GEOLOGICAL REPOSITORY 56
4.2.1 Repository in Crystalline Rock at 500 and 1000 m Depth 56
4.2.2 Repository in Sedimentary Rock at 500 and 750 m Depth 60
4.3 NEAR-FIELD ANALYSIS OF DEEP GEOLOGICAL REPOSITORY DESIGNS 68
4.3.1 Overview of Analyses 68
4.3.2 AECL-type In-Room Placement Design 71
4.3.2.1 DGR in Crystalline Rock at 500 and 1000 m Depth 71
4.3.2.2 DGR in Shale at 500 m Depth 75
4.3.2.3 DGR in Limestone at 750 m Depth 75
4.3.3 KBS-3V-type In-floor Borehole Placement Design 78
4.3.3.1 DGR in Crystalline Rock at 500 and 1000 m Depth 78
4.3.3.2 DGR in Shale at 500 m Depth 81
4.3.3.3 DGR in Limestone at 750 m Depth 83
4.3.4 KBS-3H-type Horizontal Borehole Placement Design 85
4.3.4.1 DGR in Crystalline Rock at 500 and 1000 m Depth 85
4.3.4.2 DGR in Shale at 500 m Depth 87
4.3.4.3 DGR in Limestone at 750 m Depth 89
4.3.5 NAGRA-type In-Room Placement Design 91
4.3.5.1 DGR in Crystalline Rock at 500 and 1000 m Depth 91
4.3.5.2 DGR in Shale at 500 m Depth 93
4.3.5.3 DGR in Limestone at 750 m Depth 94

5. DISCUSSION 98

6. CONCLUSIONS AND RECOMMENDATIONS 103

6.1 CONCLUSIONS 103
6.2 RECOMMENDATIONS 105

ACKNOWLEDGEMENTS 105

REFERENCES 106

APPENDIX A: BACKGROUND ON THE ORIGINAL AECL REPOSITORY DESIGNS 115

APPENDIX B: RESULTS FROM NEAR-FIELD ANALYSES OF DGR DESIGNS 119

LIST OF TABLES

Page

Table 1: Thermal-Mechanical Material Properties for Granite 18
Table 2: Glacial-Ice Surload....23
Table 3: Thermal-Mechanical Properties for Rock Types of the Michigan Basin....27
Table 4: Stresses used in Far-field Analyses of a Repository in Crystalline Rock....56
Table 5: Stresses used in Far-field Analyses of a Repository in Sedimentary Rock....62

LIST OF FIGURES

Page

Figure 1: Conceptual Arrangement of a DGR in Canada (AECL 1994)....3
Figure 2: Radiogenic Heat Generation for a Kilogram of Original Uranium in the CANDU Fuel and 324 Bundles (6237 kg U) in a UFC (unpublished report)....5
Figure 3: In-Room Placement Design of the DGR (CTECH 2002)....7
Figure 4: Typical Placement Room in the In-Room Placement Design (CTECH 2002)....8
Figure 5: In-Floor Placement Concept (RWE-NUKEM 2003)....9
Figure 6: KBS-3H Concept for Placement of UFCs in Long Horizontal Boreholes (unpublished report)....11
Figure 7: KBS-3H Concept for an Encapsulated UFC (unpublished report)....11
Figure 8: NAGRA Placement Concept in Horizontal Circular Tunnels (NAGRA Website)....13
Figure 9: Geology Observed at the URL in (a) Upper Rectangular and (b) Lower Circular Shafts. Numerals on the Left Side of Each Perimeter Map Represent Litho-Structural Domains. (Everitt et al. 1998)....15
Figure 10: Major Thrust Faults and Fracture Domains at the URL....16
Figure 11: Fracture Domains Observed in the URL Shafts (Everitt and Lajtai 2004)....17
Figure 12: Hoek-Brown Strength Envelopes for Lac du Bonnet Granite (Baumgartner et al. 1996)....21
Figure 13: In Situ Stress Distributions Specified for Canadian Shield Granite. Stress Conditions at the 240 and 420 Levels of the URL are Shown for Comparison (unpublished report). ..23
Figure 14: Stratigraphic Section Through the Michigan Basin (Mazurek 2004)....24
Figure 15: Simplified Lithostratigraphic Section for DGR Studies (after Golder 2003)....25
Figure 16: Comparison of Stress Measurement Results and Lithostatic Stress Profile for the St. Lawrence Platform (after Adams and Bell 1991)....29
Figure 17: Illustration of Situations Leading to Rock Failure: (Top) Increase in Pore Pressure or Change in Deviatoric Stress with Constant Rock Strength, and (Bottom) Constant Stress with Degrading Rock Strength....31
Figure 18: Stress-Strain Response of a Typical Unconfined Compressive Test on Lac du Bonnet Granite (Read and Martin 1996)....33
Figure 19: Three Modes of Extensile Fracturing in a Compressive Stress Field (Kemeny and Cook 1991): a Soft Inclusion Where E1<<E2 (Left), an Inclined Crack with Developing Wing Cracks (Middle), and Elastic Mismatch Between Materials in Intimate Contact with E1<E2 (Right). 37
Figure 20: Estimated Frequency Distributions for Crack Initiation in Three Main Constituent Minerals of Lac du Bonnet Granite Weighted to the Percent Occurrence of Each Mineral..39
Figure 21: Estimated Cumulative Frequency Distribution for Crack Initiation in Constituent Minerals of Lac du Bonnet Granite Weighted to the Percent Occurrence of Each Mineral..39

Figure 22: Mohr Envelopes for Slip on an Existing Fracture (Red), Initiation of Mode I Extensile Cracks (Olive), and Initiation of Mode II Shear Cracks (Blue). The Initial Fracture is Oriented at (a) 45° to the Maximum Applied Stress, and (b) 30° to the Maximum Applied Stress. 41
Figure 23: Thresholds Associated with (a) Slip on an Existing Fracture, Initiation of Extensile Cracks, and Initiation of Mode II Shear Cracks; and (b) Extensile Wing Crack Length at Initiation of Extensile and Shear Cracks (Based on Kemeny and Cook 1991). The Conceptual Fracture Model Associated with this Work is Shown in the Lower Right Hand Corner of the Figure. Rock Properties are the Same as Shown in Figure 22(a). 42
Figure 24: Comparison of Ambient Far-Field In Situ Stress States at 500 and 1000 m Depth in Crystalline Rock to Relevant Strength Envelopes. 57
Figure 25: Comparison of Thermally-Induced In Situ Stress States Near the Centre of a DGR at 500 and 1000 m Depth in Crystalline Rock to Relevant Strength Envelopes, Assuming No Thermally-Induced Increase in Vertical Stress. 58
Figure 26: Comparison of Thermally-Induced In Situ Stress States Near the Centre of a DGR at 500 and 1000 m Depth in Crystalline Rock to Relevant Strength Envelopes, Assuming a Thermally-Induced Increase in Vertical Stress. 59
Figure 27: Comparison of Glacier-Induced In Situ Stress States at 500 and 1000 m Depth in Crystalline Rock to Relevant Strength Envelopes. 59
Figure 28: Comparison of Thermal + Glacier-Induced In Situ Stress States Near the Centre of a DGR at 500 and 1000 m Depth in Crystalline Rock to Relevant Strength Envelopes (a) Assuming No Thermally-Induced Increase in Vertical Stress, and (b) Assuming a Thermally-Induced Increase in Vertical Stress. 61
Figure 29: Comparison of Ambient Far-Field In Situ Stress State at 500 m Depth in Queenston Formation Shale to Relevant Strength Envelopes. 63
Figure 30: Comparison of Ambient Far-Field In Situ Stress State at 750 m Depth in Lindsay Formation Limestone to Relevant Strength Envelopes. 63
Figure 31: Comparison of Thermally-Induced Far-Field In Situ Stress States at 500 m Depth in Queenston Formation Shale to Relevant Strength Envelopes. 64
Figure 32: Comparison of Thermally-Induced Far-Field In Situ Stress State at 750 m Depth in Lindsay Formation Limestone to Relevant Strength Envelopes. 65
Figure 33: Comparison of Glacier-Induced Far-Field In Situ Stress State at 500 m Depth in Queenston Formation Shale to Relevant Strength Envelopes. 65
Figure 34: Comparison of Glacier-Induced Far-Field In Situ Stress State at 750 m Depth in Lindsay Formation Limestone to Relevant Strength Envelopes. 66
Figure 35: Comparison of Thermal + Glacier-Induced Far-Field In Situ Stress State at 500 m Depth in Queenston Formation Shale to Relevant Strength Envelopes. 67
Figure 36: Comparison of Thermal + Glacier-Induced Far-Field In Situ Stress State at 750 m Depth in Lindsay Formation Limestone to Relevant Strength Envelopes. 67
Figure 37: Model Grid Used in Near-Field Simulations of the AECL-Type DGR Design. 69
Figure 38: Hoek-Brown Strength Ratio Around an AECL-Type DGR at 500 m in Crystalline Rock Under Ambient Conditions (Room Parallel to Maximum Horizontal Stress). 70
Figure 39: Ratio of Minimum to Maximum Principal Stress Relative to Mohr-Coulomb Threshold for Fracture Slip Around an AECL-Type DGR at 500 m in Crystalline Rock Under Ambient Conditions (Room Parallel to Maximum Horizontal Stress). 70
Figure 40: Stresses and Stress Ratio Along the Vertical Axis Above the Crown of a Placement Room Parallel to the Intermediate Principal Stress Based on Results from CTECH (2002). This Figure Includes the Effects of Thermal Loading. 73

Figure 41: Stresses and Stress Ratio Along the Vertical Axis Above the Crown of a Placement Room Parallel to the Maximum Principal Stress Based on Results from CTECH (2002). This Figure Includes the Effects of Thermal Loading. 73
Figure 42: Hoek-Brown Strength Ratio Around an AECL-Type DGR at 500 m in Shale Under Ambient Conditions (Room Parallel to Maximum Horizontal Stress).....76
Figure 43: Ratio of Minimum to Maximum Principal Stress Relative to Mohr-Coulomb Threshold for Fracture Slip Around an AECL-Type DGR at 500 m in Shale Under Ambient Conditions (Room Parallel to Maximum Horizontal Stress). 76
Figure 44: Hoek-Brown Strength Ratio Around an AECL-Type DGR at 750 m in Limestone Under Ambient Conditions (Room Parallel to Maximum Horizontal Stress). 77
Figure 45: Ratio of Minimum to Maximum Principal Stress Relative to Mohr-Coulomb Threshold for Fracture Slip Around an AECL-Type DGR at 750 m in Limestone Under Ambient Conditions (Room Parallel to Maximum Horizontal Stress). 77
Figure 46: Hoek-Brown Strength Ratio Around a Placement Borehole in a KBS-3V-Type DGR at 500 m in Crystalline Rock Under Ambient Conditions (Room Parallel to Maximum Horizontal Stress; Data Shown are for Conditions Near the Bottom of the Borehole).....80
Figure 47: Ratio of Minimum to Maximum Principal Stress Relative to Mohr-Coulomb Threshold for Fracture Slip Around a Placement Borehole in a KBS-3V-Type DGR at 500 m in Crystalline Rock Under Ambient Conditions (Room Parallel to Maximum Horizontal Stress; Data Shown are for Conditions Near the Bottom of the Borehole).....80
Figure 48: Hoek-Brown Strength Ratio Around a Placement Borehole in a KBS-3V-Type DGR at 500 m in Shale under Ambient Conditions (Room Parallel to Maximum Horizontal Stress; Data Shown are for Conditions Near the Bottom of the Borehole).....82
Figure 49: Ratio of Minimum to Maximum Principal Stress Relative to Mohr-Coulomb Threshold for Fracture Slip Around a Placement Borehole in a KBS-3V-Type DGR at 500 m in Shale Under Ambient Conditions (Room Parallel to Maximum Horizontal Stress; Data Shown are for Conditions Near the Bottom of the Borehole).....82
Figure 50: Hoek-Brown Strength Ratio Around a Placement Borehole in a KBS-3V-Type DGR at 750 m in Limestone Under Ambient Conditions (Room Parallel to Maximum Horizontal Stress; Data Shown are for Conditions Near the Bottom of the Borehole).....84
Figure 51: Ratio of Minimum to Maximum Principal Stress Relative to Mohr-Coulomb Threshold for Fracture Slip Around a Placement Borehole in a KBS-3V-Type DGR at 750 m in Limestone Under Ambient Conditions (Room Parallel to Maximum Horizontal Stress; Data Shown are for Conditions Near the Bottom of the Borehole).....84
Figure 52: Hoek-Brown Strength Ratio Around a KBS-3H-Type DGR at 500 m in Crystalline Rock Under Ambient Conditions (Room Parallel to Maximum Horizontal Stress). 86
Figure 53: Ratio of Minimum to Maximum Principal Stress Relative to Mohr-Coulomb Threshold for Fracture Slip Around a KBS-3H-Type DGR at 500 m in Crystalline Rock Under Ambient Conditions (Room Parallel to Maximum Horizontal Stress) 86
Figure 54: Hoek-Brown Strength Ratio Around a KBS-3H-Type DGR at 500 m in Shale Under Ambient Conditions (Room Parallel to Maximum Horizontal Stress).....88
Figure 55: Ratio of Minimum to Maximum Principal Stress Relative to Mohr-Coulomb Threshold for Fracture Slip around a KBS-3H-Type DGR at 500 m in Shale Under Ambient Conditions (Room Parallel to Maximum Horizontal Stress) 88
Figure 56: Hoek-Brown Strength Ratio Around a KBS-3H-Type DGR at 750 m in Limestone Under Ambient Conditions (Room Parallel to Maximum Horizontal Stress). 90
Figure 57: Ratio of Minimum to Maximum Principal Stress Relative to Mohr-Coulomb Threshold for Fracture Slip Around a KBS-3H-Type DGR at 750 m in Limestone Under Ambient Conditions (Room Parallel to Maximum Horizontal Stress) 90

Figure 58: Hoek-Brown Strength Ratio Around a NAGRA DGR at 500 m in Crystalline Rock Under Ambient Conditions (Room Parallel to Maximum Horizontal Stress). 92
Figure 59: Ratio of Minimum to Maximum Principal Stress Relative to Mohr-Coulomb Threshold for Fracture Slip Around a NAGRA-Type DGR at 500 m in Crystalline Rock Under Ambient Conditions (Room Parallel to Maximum Horizontal Stress) 92
Figure 60: Hoek-Brown Strength Ratio Around a NAGRA-Type DGR at 500 m in Shale Under Ambient Conditions (Room Parallel to Maximum Horizontal Stress)....95
Figure 61: Ratio of Minimum to Maximum Principal Stress Relative to Mohr-Coulomb Threshold for Fracture Slip Around a NAGRA-Type DGR at 500 m in Shale Under Ambient Conditions (Room Parallel to Maximum Horizontal Stress) 95
Figure 62: Hoek-Brown Strength Ratio Around a NAGRA-Type DGR at 750 m in Limestone Under Ambient Conditions (Room Parallel to Maximum Horizontal Stress). 97
Figure 63: Ratio of Minimum to Maximum Principal Stress Relative to Mohr-Coulomb Threshold for Fracture Slip Around a NAGRA-Type DGR at 750 m in Limestone Under Ambient Conditions (Room Parallel to Maximum Horizontal Stress) 97

1. INTRODUCTION

The Canadian approach for placement of spent nuclear fuel (used fuel) in a deep geological repository (DGR) relies on multiple barriers to prevent or retard the release of radionuclides to the biosphere. The system includes the host rock (or geosphere) as a natural barrier, and a series of engineered barriers placed in underground excavations in the host rock. Both crystalline rock and sedimentary rock are considered potentially suitable host rocks formations (NWMO 2005). These formations exhibit desirable mechanical and hydrological properties. They also cover large areas at sufficient depth below surface, and are not considered rich in mineral resources, thus limiting the potential for disturbance by erosion or accidental interception during drilling.

For the purposes of safety assessment of a DGR, the integrity of the natural barrier is assumed to remain substantially unchanged over the 100,000 year period following waste placement (i.e., the period in which release of radionuclides to the biosphere would constitute a possible safety risk). Over this time period, the host rock will experience mechanical effects from excavation and development of underground openings, thermal-mechanical effects from heat generated by the placed waste, and possible long-term mechanical effects associated with glaciation and seismicity. None of these effects is expected to lead to the development of large-scale fracturing or faulting near the DGR over the time period of interest.

The purpose of this report is to present a Reasoned Argument (RA) with respect to the likelihood of fracturing and/or faulting of the host rock in response to the development of a DGR and subsequent underground disposal of used fuel. The RA is developed based on the assessment of a number of possible scenarios for induced fracturing of the rock mass in response to repository development. The RA incorporates observational and experimental evidence from the Canadian and other national radioactive waste management programs, and information from literature related to rock mechanics, geology and seismology.

This report is not intended as a definitive demonstration of the validity of conclusions drawn from the RA, but is meant to establish a framework and supporting evidence for the RA, and to identify further work required to validate conclusions. The report is organized into six sections (including this introductory section) covering terms of reference related to the DGR and host rock, a summary of factors affecting induced fracturing of rock, analysis of far-field and near-field responses for the different DGR scenarios, a discussion of results and associated uncertainty, and a concluding summary and recommendations.

2. TERMS OF REFERENCE

The terms of reference for the RA include the following:

- The DGR is constructed in either crystalline rock, typified for example by sparsely fractured Lac du Bonnet granite of the Canadian Shield, or by sedimentary rock, typified, for example, by the Ordovician sedimentary rock of the Michigan basin in Ontario (including both shale and limestone).
- Waste placement options considered include the Canadian in-room (AECL-type) option, the in-floor borehole (KBS-3V-type) option, the horizontal borehole (KBS-3H-type)

option, and a NAGRA-type option involving placement in long horizontal cylindrical tunnels.

- Repository depths considered for the analysis are 500 and 1000 m for crystalline rock, 500 m for shale, and 750 m for limestone.
- Relevant near-term processes or events include the construction, operation and backfilling of underground openings in the host rock.
- Relevant intermediate-term processes or events include temperature changes due to the heat-generating used fuel and prolonged monitoring for up to 300 years, during which time the shaft and access tunnels would remain open for possible waste retrieval.
- Relevant long-term processes or events include temperature changes associated with the repository (with placed containers reaching a maximum temperature of 100°C), and geological processes or events such as glaciation and seismicity.

The potential for both vertical and horizontal fracturing/faulting of the host rock, including fracture propagation between sedimentary rock layers, is considered in this context. Large-scale fracturing and faulting are differentiated from small-scale near-field fracturing on the basis of the surface area of induced fractures. Large-scale refers to fracture surface area on the order of 10 m^2 or greater (Martin et al., 1994). Owing to the two-dimensional nature of the analyses in this report, large-scale fracturing is defined as the development of new fractures or remobilization of existing fractures longer than 10 m. It should be noted that an explicit analysis of the effects of thermally-induced pore pressure was outside the scope of this report.

2.1 DEFINITION OF THE REASONED ARGUMENT

Based on a review of proposed disposal concepts and expected in situ conditions, the Reasoned Argument presented in this report can be summarized as follows:

> *The development and propagation of large-scale fractures either between repository rooms, or between the repository level and other remote natural hydraulic pathways, is improbable in the various DGR designs in each of the rock types considered. The rock properties in each case are sufficiently competent and stress conditions sufficiently benign to effectively impede the possible fracturing mechanisms discussed in this report. Specifically, the fact that the repository lies in a compressive stress field with relatively low deviatoric stresses in a thrust fault regime suggests that insufficient driving force would exist to initiate and propagate the two types of possible fractures of concern (large-scale horizontal extensile fractures, or thrust faults oriented at a shallow angle to horizontal) within the 100,000 year period following placement. A dramatic erosional event that might reduce the depth of cover by hundreds of metres could alter this conclusion, but the likelihood of such an event over the 100,000 years following placement is considered extremely remote and is therefore not covered in this report.*

Information supporting each of the DGR scenarios is presented in the following sections. Analysis results supporting the RA are contained in Section 4 of the report.

2.2 DEEP GEOLOGICAL REPOSITORY

2.2.1 General

The DGR concept for disposal of Canada's used fuel was developed by Atomic Energy of Canada Limited (AECL) between 1978 and 1996. The original concept described in an Environmental Impact Statement (AECL 1994) involves a DGR at 500 to 1000 m depth in the crystalline rock of the Canadian Shield. The DGR includes up to 512 placement rooms connected by access tunnels and shafts to surface, covering an area approximately 2 km by 2 km. The design is based on vertical placement of used-fuel containers (UFCs) in augured cavities in clay-based buffer compacted in large-diameter boreholes in the invert of placement rooms (Simmons and Baumgartner 1994). As part of the placement process, each placement room in this design is backfilled with a mixture of clay and crushed rock materials and sealed with a concrete bulkhead at the room entrance. This design is based on an inventory of 10.1 million used fuel bundles placed in approximately 140,000 titanium containers. The main components of this design are described in Table A.1 (Appendix A). A conceptual arrangement for such a repository is shown in Figure 1.

Following delivery of the Environmental Impact Statement to the Seaborn Panel under the 1984 Federal Environmental Assessment and Review Process Guidelines Order, an alternative placement design was developed by AECL to demonstrate robustness of the disposal concept under three scenarios of representative in situ conditions (Baumgartner et al. 1995). The alternative design (Baumgartner et al. 1996) incorporates in-room placement of used fuel in shorter, larger-diameter copper containers. The UFCs in this design are placed horizontally within cylindrical cavities in pre-compacted clay-based buffer blocks surrounded by backfill materials filling the placement room. This arrangement eliminates the need for large vertical placement boreholes. Each placement room has a low-heat high-performance concrete invert and is sealed with a concrete bulkhead. Based on a series of 512 placement rooms covering a 2 km by 2 km area, the capacity of this alternative design is 5.8 million used fuel bundles placed in 80,707 containers. The main components of this modified design are presented in Table A.2 (Appendix A).

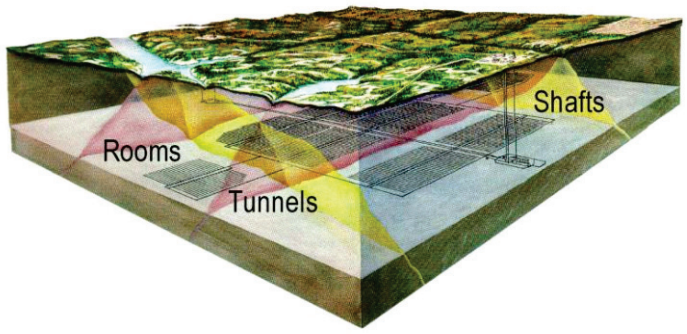

Figure 1: Conceptual Arrangement of a DGR in Canada (AECL 1994)

Since 1996, Ontario Hydro, and subsequently Ontario Power Generation (OPG) and the other members of the Joint Waste Owners[1], have further developed the original AECL DGR concept to refine in-room placement of UFCs, adding provisions for extended monitoring and retrieval of used fuel after placement in the repository (NWMO 2005). Several changes to the reference concept have been made as a result. Some of the generic aspects of the refined design specifications are as follows:

- Thermal calculations are based on a reference 37-element used-fuel bundle with a mass of 19.25 kg U in the fuel initially inserted into the reactor (CTECH 2002) and a burnup of 220 MWh/kg U (Tait and Hanna 2001, Tait et al. 2000). This burnup is higher than values used in the original AECL placement designs.
- The average post-reactor discharge time for the used fuel at the time of waste placement is 30 years (CTECH 2002, Baumgartner and Ates 2002) instead of the 10 years assumed in the original AECL placement designs.
- The quantity of used fuel is assumed to be 3.6 million used-fuel bundles, based on a minimum of 3,518,575 bundles (Simmons 2000). The derived uranium inventory of the repository is 69,300 Mg U. This quantity is significantly lower than the quantities assumed in the original AECL placement designs.
- The UFC is the IV-324-hex container (CTECH 2002, Maak and Simmons 2001), comprising a copper outer shell and a steel inner shell. The UFC has a nominal outside diameter of 1168 mm and overall length of 3867 mm, and accommodates 324 fuel bundles (i.e., 6237 kg U) (Russell and Simmons 2003). A total of 11,111 UFCs are required to handle the used fuel inventory. This UFC is substantially larger than those considered in either of the original AECL placement designs, and the number of required UFCs is significantly reduced as a result of the larger UFC capacity and smaller used fuel inventory.
- The initial heat output per container is assumed to be 1139 W (unpublished report). The heat generation from the IV-324-hex UFC as a function of its post-reactor discharge time is illustrated in Figure 2. This heat output is significantly larger than the value associated with the smaller UFCs in the original AECL placement designs.
- The specified maximum design temperature on the outside surface of the placed container is 100°C (Simmons 2000). This is the same as the original in-floor placement design, but higher than the original AECL in-room design.
- The spacing between containers along the length of the placement room and the spacing between rooms is to be uniform in order to meet the maximum container temperature specification. This design approach is consistent with that used for the original AECL placement designs.
- The repository footprint is assumed to be square with a maximum extraction ratio[2] of 0.25. This is consistent with the original AECL designs, although the original in-floor placement design had an extraction ratio slightly above this target value (Simmons and Baumgartner 1994).

[1] The Joint Waste Owners include Ontario Power Generation (OPG), Hydro-Québec (HQ), New Brunswick Power (NBP) and Atomic Energy of Canada Limited (AECL).

[2] Extraction ratio is defined as the ratio of the width of the placement room to the combined width of the placement room and the pillar between rooms (Simmons 2000).

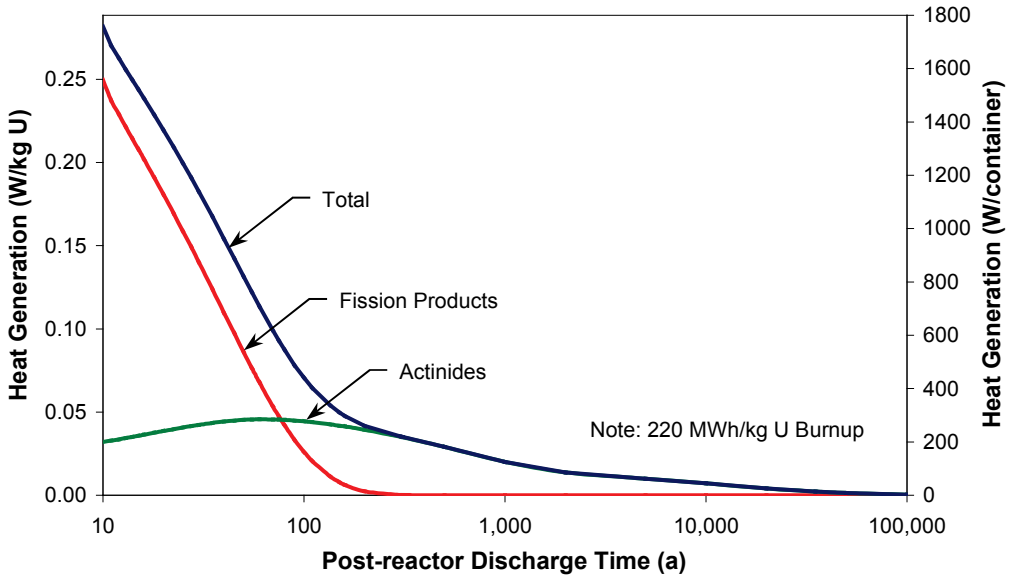

Figure 2: Radiogenic Heat Generation for a Kilogram of Original Uranium in the CANDU Fuel and 324 Bundles (6237 kg U) in a UFC (unpublished report)

In terms of the general placement sequence (NWMO 2005), used fuel cooled for 30 years would be gradually transported from existing interim storage facilities at nuclear reactor sites to the repository where it would be packaged in corrosion resistant containers. Over an operational period of about 30 years, these containers would be placed underground in the placement rooms, and individual rooms would be backfilled and sealed. Performance of the repository would be monitored during placement of the used fuel, and for a specified period following placement, after which the remaining underground excavations would be backfilled and sealed. After closure, requirements for maintenance, inspection and security related operations would be minimal. Such a facility would be designed to be passively safe over the long term, and would not rely on institutional controls to ensure safety.

In keeping with the refinements to the original AECL conceptual designs, various DGR designs have been advanced in Canada and other countries. Four of the designs that have been investigated for possible application in Canada are as follows:

- an AECL-type in-room placement design (CTECH 2002, Baumgartner and Ates 2002, Baumgartner et al. 1996),
- a KBS-3V-type in-floor borehole placement design (RWE-NUKEM 2004, Birgersson et al. 2001, Simmons and Baumgartner 1994),
- a KBS-3H-type in-room placement design (Lindgren et al. 2003), and
- a NAGRA-type in-room placement design (NAGRA 2002).

These four designs are discussed briefly in the following subsections as background for the RA. References to more detailed documentation related to each of these designs are provided.

2.2.2 AECL-type In-Room Placement Design

The refined conceptual in-room placement design (CTECH 2002) involves a DGR located at a nominal depth of 1000 m in the crystalline rock of the Canadian Shield. The design includes the following features:

- Four vertical shafts ranging from 3.66 to 7.30 m internal diameter connect the repository level to ground surface. This design has only one upcast exhaust ventilation shaft compared to the original AECL design with two exhaust shafts.
- The repository level (Figure 3) comprises room-and-pillar excavations, including twinned central and section access tunnels connected to a perimeter access tunnel. These access tunnels are rectangular (4.2 m high by 7.0 m wide) with an arched back. The twinned central and section access tunnels divide the repository into four sections, each section containing two panels of placement rooms. The twinned access tunnels are spaced 50 m centreline-to-centreline.
- Each placement panel comprises 13 elliptical placement rooms (4.2 m high by 7.14 m wide) with single-ended access. Placement rooms are oriented parallel to the maximum principal stress direction to minimize stress concentrations around the underground openings. Individual placement rooms are 315 m long, including a 37 m segment to accommodate a sealing bulkhead and turning radius of 25 m. Placement rooms are spaced a minimum of 45 m centreline-to-centreline from one another and about 60 m from the perimeter access tunnels. There is a minimum distance of 22.7 m between ends of placement rooms in adjacent panels in a given section.
- Within each room, the UFC spacing is 5.13 m centre-to-centre longitudinally along the room, with two parallel rows of UFCs spaced 2.52 m laterally across the room (Figure 4). The UFCs are located in a mass of pre-compacted buffer and dense backfill blocks, and associated sealing materials and structures. A minimum thickness of 0.5 m of bentonite/buffer and another 0.5 m of dense backfill is required around each container. Each placement room can accommodate 108 containers (two abreast by 54 along the room) for a total repository capacity of 11,232 UFCs (or 3,639,168 used-fuel bundles). The maximum surface temperature of the UFCs in this arrangement is 97°C, reached 16 years after placement.
- The placement area in this conceptual design is 1358 m by 1343 m based on ideal site conditions (i.e., assuming no adaptation required to accommodate unfavourable geological structures or conditions in the rock mass). The actual layout and size of the repository will depend on in situ conditions encountered at a selected repository site. At a target placement rate of 120,000 fuel bundles/year, the repository is assumed to have an operational life of 30 years.
- Once filled, each placement room is sealed with a 12 m long concrete bulkhead. Monitoring of seals and conditions in the repository is planned to continue for an extended period of time during which access tunnels and shafts will remain open. Following this monitoring period, decommissioning of the DGR involves removing all underground support works, and backfilling and sealing the balance of the underground facilities.

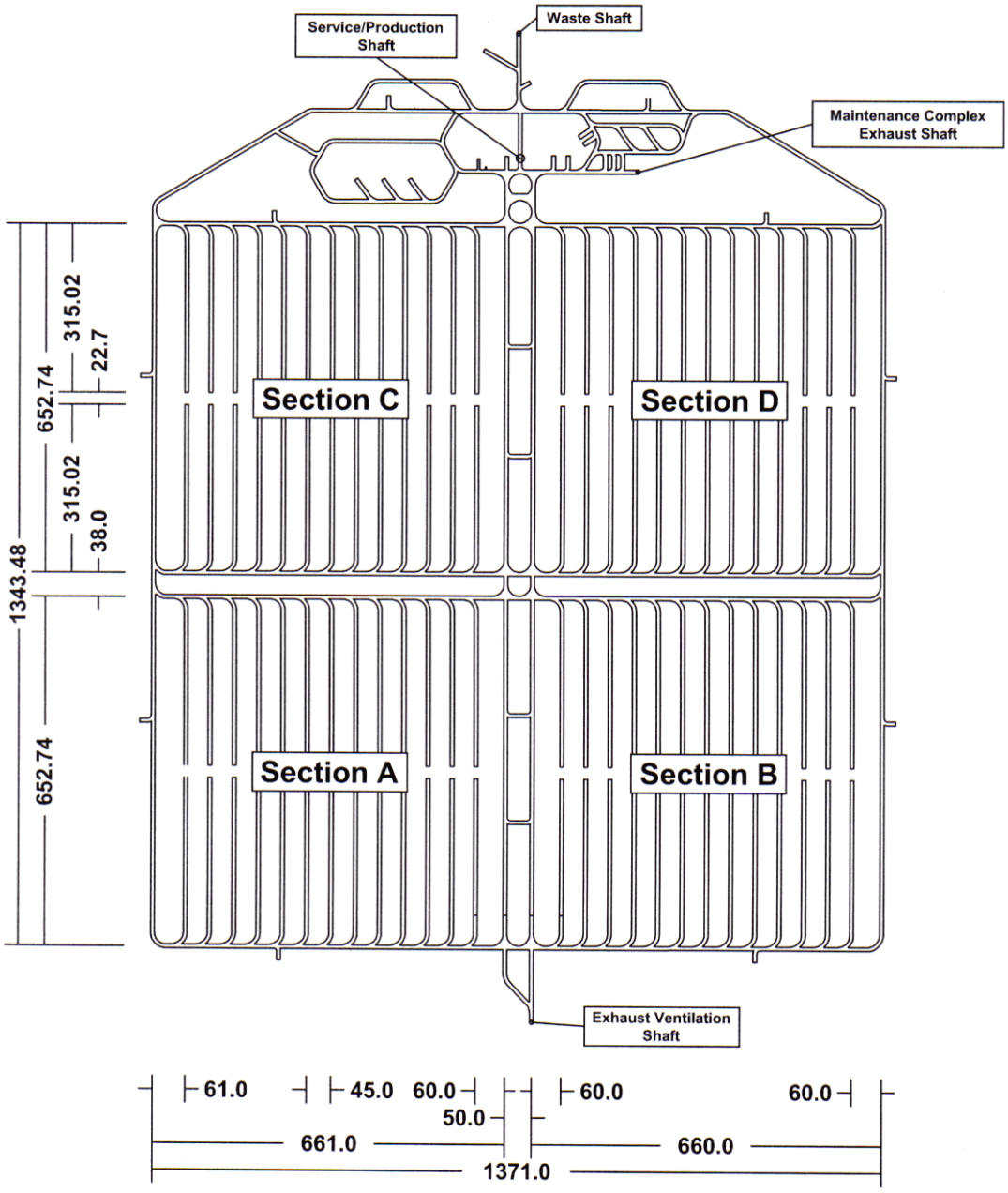

Figure 3: In-Room Placement Design of the DGR (CTECH 2002)

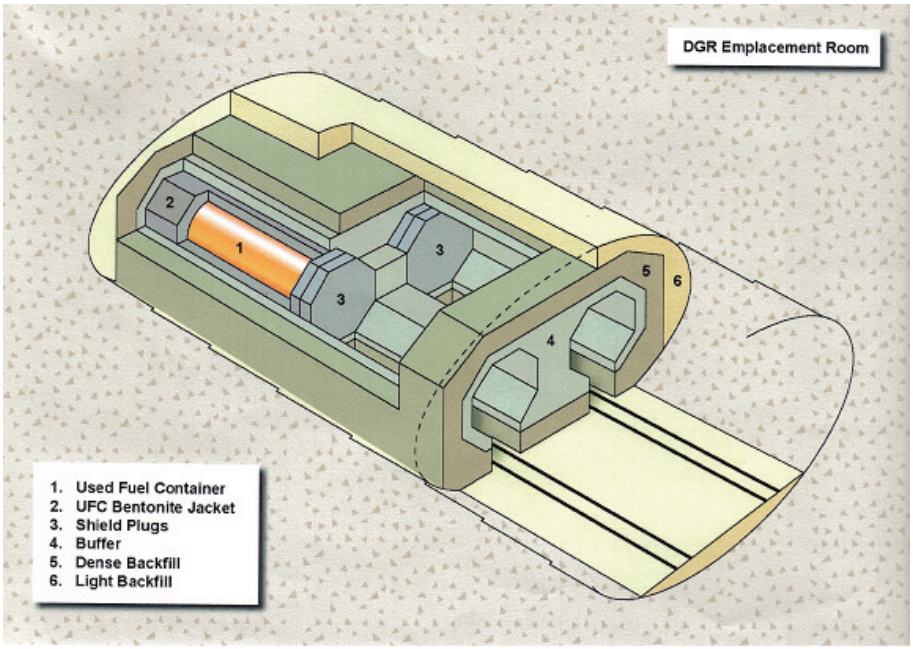

Figure 4: Typical Placement Room in the In-Room Placement Design (CTECH 2002)

2.2.3 KBS-3V-type In-floor Borehole Placement Design

Following completion of the revised conceptual in-room placement design, a DGR design that incorporates placement of UFCs within boreholes constructed in the invert of placement rooms was further examined (RWE-NUKEM 2003; 2004). This revised conceptual design (Figure 5) incorporates features required for in-floor placement based on the Swedish KBS-3V design (Birgersson et al. 2001). It utilizes some of the key features of the conceptual in-room placement design (CTECH 2002). The main points of comparison between this design and the in-room design are as follows:

- The shafts and repository level are similar to those in the in-room design. The twinned central and section access tunnels divide the repository into four sections, each section containing two panels of placement rooms. The twinned access tunnels are spaced 50 m centreline-to-centreline.
- Each placement panel comprises 20 elliptical placement rooms (4.3 m high by 7.31 m wide) with single-ended access. Placement rooms are oriented parallel to the maximum principal stress direction to minimize stress concentrations around the underground openings. These room dimensions are dictated by the size of equipment required to drill the boreholes and to place a UFC in a borehole. Individual placement rooms are 325 m long, including a 37 m segment to accommodate a sealing bulkhead and turning radius of 25 m. Placement rooms are spaced a minimum of 30 m centreline-to-centreline from one another, and a minimum of 50 m from the perimeter access tunnel. There is a minimum distance of 50 m between ends of placement rooms in adjacent panels in a given section.

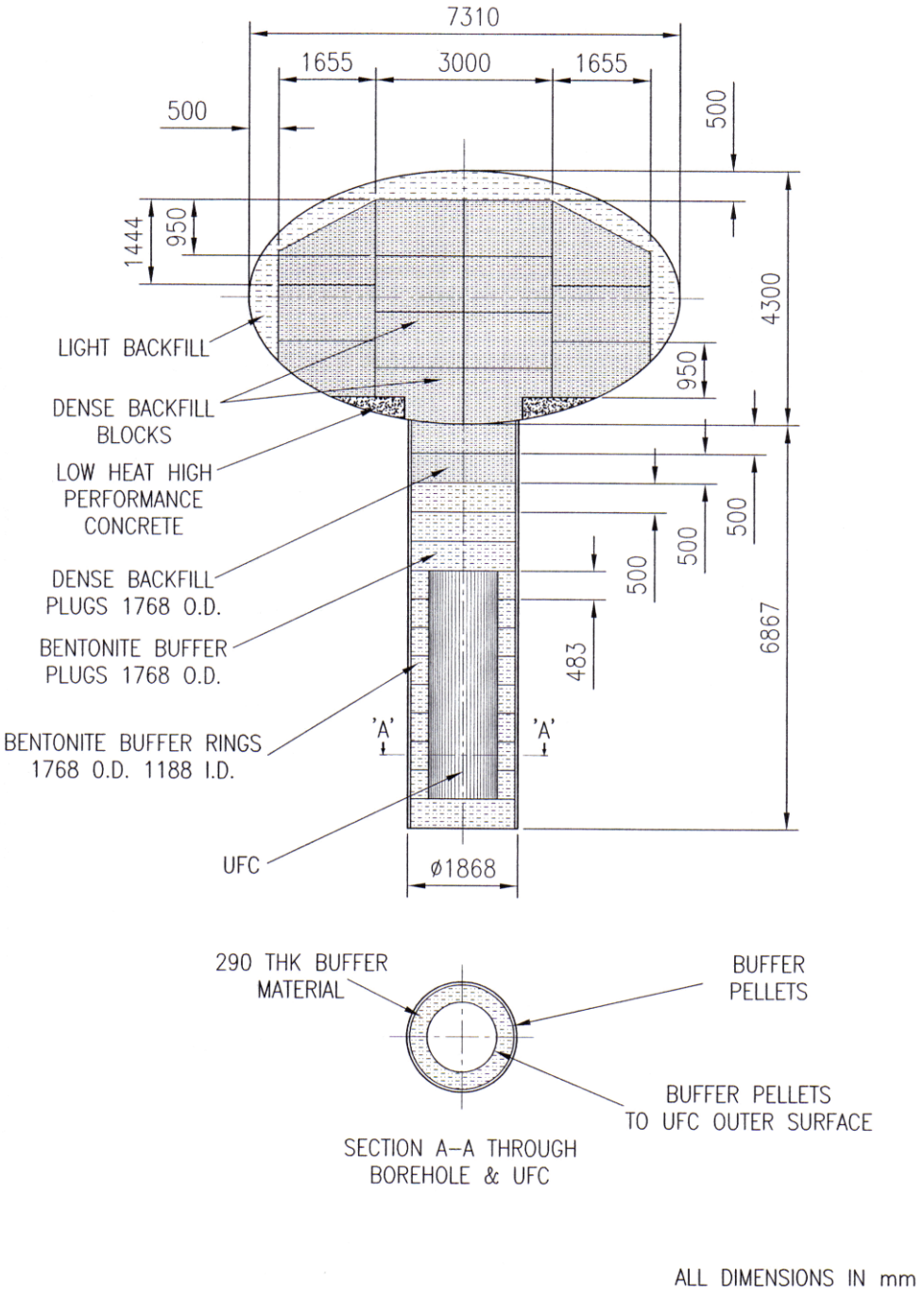

Figure 5: In-Floor Placement Concept (RWE-NUKEM 2003)

- Within each room, boreholes are drilled along the centreline of the room, spaced 4.0 m centre-to-centre. Each borehole is 1.868 m diameter drilled to a depth of 6.867 m below the lowest point in the excavated room (or 7.323 m below the top of the concrete invert in the room). The borehole is filled with one pre-compacted bentonite buffer plug and eight pre-compacted bentonite buffer rings prior to UFC placement. Three more buffer plugs and two dense backfill plugs are placed above the UFC to seal the borehole, then a series of pre-compacted dense backfill blocks and light backfill are placed to seal the room.
- Each placement room can accommodate 70 containers for a total repository capacity of 11,200 UFCs (or 3,628,800 used-fuel bundles). The maximum surface temperature of the UFCs in this arrangement is 79°C after 29 years, and 90°C after 6500 years (assuming an initial ambient temperature of 17°C).
- The placement area in this conceptual design is 1390 m by 1450 m based on ideal site conditions. The repository is assumed to have an operational life of 30 years based on a target placement rate of 120,000 fuel bundles/year.
- Once filled, each placement room is sealed with a 12 m long concrete bulkhead keyed into the rock mass and grouted to seal the excavation damaged zone (EDZ). Monitoring of seals and conditions in the repository is planned to continue for an extended period of time during which access tunnels and shafts will remain open. Following the monitoring period, DGR decommissioning involves removing all underground support works, backfilling and sealing remaining underground facilities.

2.2.4 KBS-3H-type Horizontal Borehole Placement Design

In addition to the revised conceptual design for in-floor placement of UFCs, a DGR design that incorporates placement of UFCs within long horizontal boreholes constructed from niches off of the DGR access tunnels was investigated (RWE-NUKEM 2004a). With reference to Figures 6 and 7, this revised conceptual design incorporates features based on the Swedish KBS-3H design (Thorsager and Lindgren 2004). It utilizes some of the features of the conceptual in-room placement design (CTECH 2002). The main points of comparison between this design and the in-room design are as follows:

- The shafts and repository level are similar to those in the in-room design. The twinned central and section access tunnels divide the repository into six sections, each section containing two panels of placement boreholes. The twinned access tunnels are spaced 50 m centreline-to-centreline.
- Each placement panel comprises 18 circular placement boreholes (1.918 m diameter) with single-ended access, inclined 5° upward to promote drainage. Borehole diameter is dictated by the minimum thickness of bentonite buffer around the container and equipment/operational consideration for placement of UFCs. Placement boreholes are oriented parallel to the maximum principal stress direction to minimize stress concentrations around the underground openings. Individual placement boreholes are 297.2 m long drilled from a 33 m long niche off of the section access tunnels (comprising an 8 m long straight section and a 25 m long section with a 25 m turning radius). Placement rooms are spaced a minimum of 55 m centreline-to-centreline, and a minimum of 50 m from the perimeter and central access tunnels. There is a minimum distance of 25.6 m between ends of placement boreholes in adjacent panels in a given section.

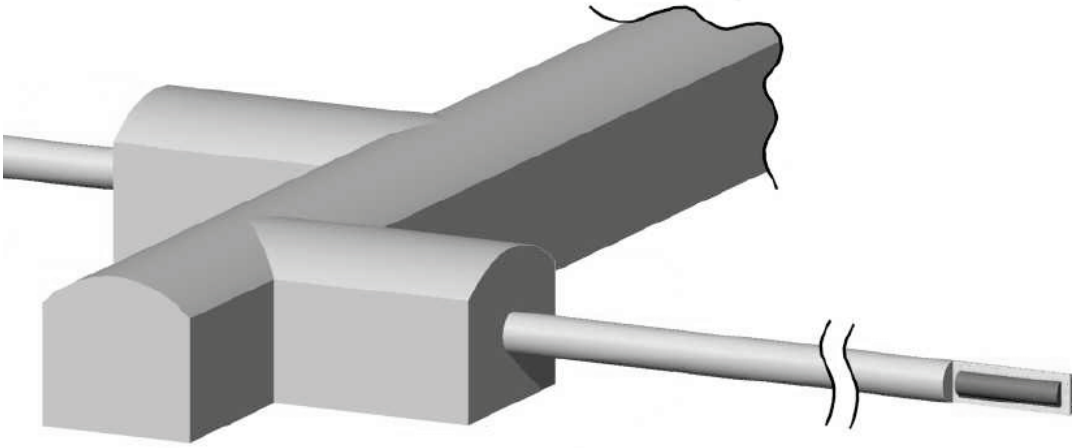

Figure 6: KBS-3H Concept for Placement of UFCs in Long Horizontal Boreholes (unpublished report)

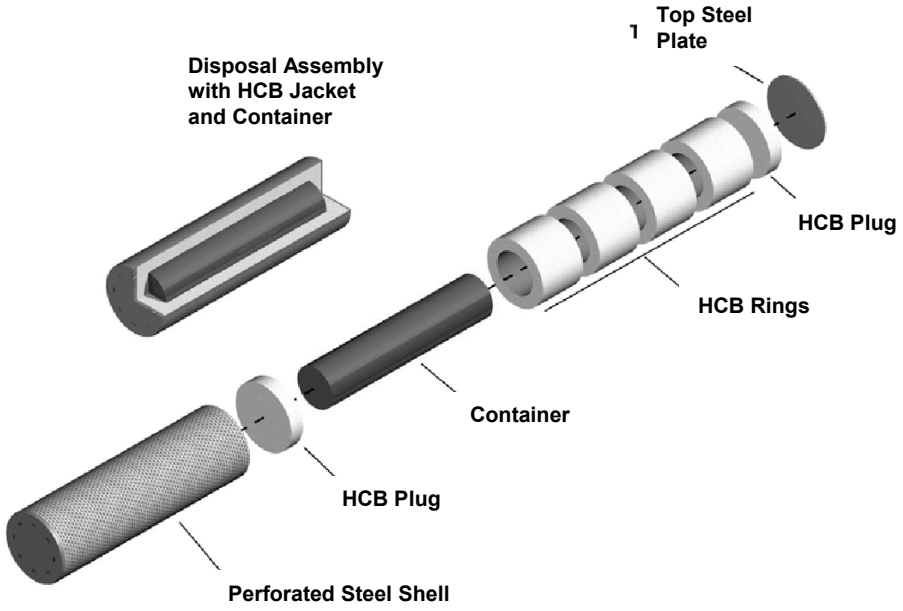

Figure 7: KBS-3H Concept for an Encapsulated UFC (unpublished report)

- Each UFC is encased within a bentonite jacket with a nominal thickness of 300 mm, which is in turn surrounded by a perforated carbon steel cage to prevent damage during handling and placement. There is an initial 50 mm thick annular air gap left around the placed UFC package, although the package may sit eccentrically on the bottom of the borehole (unpublished report). Within each borehole, UFCs are spaced 5.6 m centre-to-centre with a bentonite plug separating individual UFC packages. This design accommodates 52 UFCs per hole, providing a total repository capacity of 11,232 UFCs (or 3,639,168 used-fuel bundles). The maximum surface temperature of the UFCs in this arrangement is 94°C, reached 3 years after placement.
- The placement area in this conceptual design is 2120 m by 2158 m based on ideal site conditions, assuming no adaptation required to accommodate unfavourable geological structures or conditions in the rock mass. The actual layout and size of the repository will depend on in situ conditions encountered at an actual repository site. At a target placement rate of 120,000 fuel bundles/year, the repository is assumed to have an operational life of 30 years.
- Once filled, each placement borehole is sealed with a 6 m long concrete bulkhead. Monitoring of seals and conditions in the repository is planned to continue for an extended period of time during which access tunnels and shafts will remain open. Following this monitoring period, decommissioning of the DGR would involve removal of all underground support works, backfilling and sealing remaining underground facilities.

2.2.5 NAGRA-type In-Room Placement Design

In addition to the other revised conceptual designs for placement of UFCs, a DGR design that incorporates placement of UFCs within long horizontal cylindrical tunnels was investigated (RWE-NUKEM 2004b). This revised conceptual design incorporates features based on the NAGRA disposal concept (NAGRA 2002). It utilizes some of the features of the conceptual in-room placement design (CTECH 2002). The main features of this design are as follows:

- The shafts and repository level are similar to those in the in-room design. The twinned central and section access tunnels divide the repository into four sections, each section containing one panel of placement rooms. The twinned access tunnels are spaced 50 m centreline-to-centreline.
- Each placement panel comprises 25 placement tunnels (2.5 m diameter) with double-ended access. Placement tunnels are oriented parallel to the maximum principal stress direction to minimize stress concentrations around the underground openings. Individual placement tunnels are 820 m long excluding the 45 m long curved access drift extension at each end of the tunnel. Placement tunnels are spaced a minimum of 40 m centreline-to-centreline from one another, and a minimum of 50 m from the perimeter and central access tunnels.
- Each UFC is placed on a compacted bentonite block pedestal within the placement tunnel and the remainder of the tunnel is filled with compacted bentonite pellets. This arrangement creates a 666-mm-thick bentonite buffer ring around the placed UFC. Within each tunnel, UFCs are spaced 6.9 m centre-to-centre. This design accommodates 112 UFCs per tunnel, providing a total repository capacity of 11,200 UFCs (or 3,628,800 used-fuel bundles). The maximum surface temperature of the UFCs in this arrangement may reach 125°C.

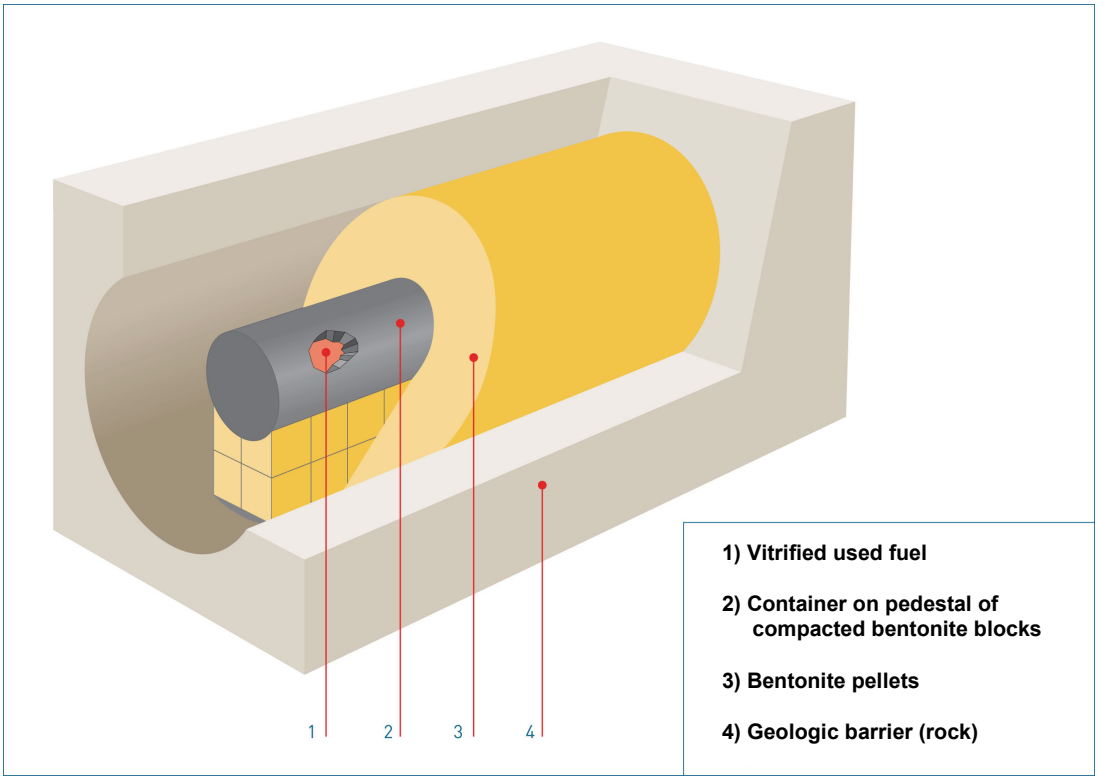

Figure 8: NAGRA Placement Concept in Horizontal Circular Tunnels (NAGRA Website)

- The placement area in this conceptual design is 1870 m by 2170 m based on ideal site conditions. The repository is assumed to have an operational life of 30 years assuming a target placement rate of 120,000 fuel bundles/year.
- Once filled, each placement borehole is sealed with a 20 m long bentonite seal (consistent with the NAGRA approach). Monitoring of seals and conditions in the repository is planned to continue for an extended period of time during which access tunnels and shafts will remain open. Following this monitoring period, decommissioning of the DGR would involve removing all underground support works, backfilling and sealing remaining underground facilities.

2.3 CRYSTALLINE HOST ROCK

For the purposes of assessing the feasibility of the various DGR concepts, the host rock in the base case scenarios is assumed to be sparsely fractured crystalline rock of the Canadian Shield. The properties and in situ conditions of the rock mass are based largely on studies conducted by AECL in the Lac du Bonnet batholith at the Underground Research Laboratory (URL) near Lac du Bonnet, Manitoba. This particular site was selected for the report because the rock mass at the site has been studied more thoroughly than any other crystalline rock mass in Canada, and large-scale fracturing scenarios are more conceivable at this site due to high stress conditions, isolated fracture zones, and otherwise intact rock.

2.3.1 General Geology

The Lac du Bonnet batholith is located on the western edge of the Superior Province of the Canadian Shield. The batholith is of Late Kenoran age (2680 ± 81 Ma), and is approximately 85 km long, 25 km wide, and at least 5 km deep. It is a relatively undifferentiated massive porphyritic granite-granodiorite, although subsurface mapping has demonstrated that the rock mass is coarsely layered with vertical gradations in alteration, lithology and structure. Textural and compositional layering is evident in the URL shaft (Everitt et al. 1998), where it has been shown to influence localization of low-dip thrust faulting, and the frequency and properties of subvertical fractures. Geological maps of the upper rectangular and lower circular shafts at the URL are presented in Figure 9 to illustrate the observed geological variability.

In addition to the main phase of the granite, three systems of auto-intrusive dykes, sills, and recrystallized zones are recognized at the URL. Late magmatic granodioritic dykes are the predominant rock type below 300 m depth at the URL, but the dyke swarm narrows rapidly with increasing elevation, and at surface is represented only by narrow zones of alteration and ductile deformation. Late pegmatite-aplite dykes are pervasive across all rock types at surface, but are limited to the larger fine-grained granite dykes at 420 m depth at the URL. Low-dipping fractures, including thrust faults, parallel the large-scale compositional layering, and are generally confined to the contacts between massive leucocratic and foliated xenolithic litho-structural domains (Everitt et al. 1998). These variations in lithology and rock fabric have also been shown to influence the nature and character of excavation-induced damage around underground excavations (Read and Martin 1996; Read 2004; Everitt and Lajtai 2004).

2.3.2 Fracture Characteristics

The Lac du Bonnet batholith hosts a variety of fracture types including large-scale thrust faults, discrete joint sets, and microfracturing at the grain scale. As shown in Figure 10, within the first few hundred metres of the surface at this site, the granite contains subvertical joint sets and several major low-dipping thrust faults (referred to as Fracture Zones). The most prominent of these thrust faults, Fracture Zone 2, intersects the URL shaft at a depth of about 270 m below surface. These thrust faults formed about 2300 Ma during the cooling period following magma intrusion (Brown et al. 1995). Reverse dip-slip displacements of 7.3 m on Fracture Zone 2, and 1 m on Fracture Zone 3, have been measured in the URL shaft. Below Fracture Zone 2 and its splays, other thrust faults are possible (e.g., Fracture Zone 1 was intersected in deep boreholes drilled from surface near the URL), but in general the rock mass at depth is sparsely fractured and relatively unaltered.

The thrust faults are low-dipping (i.e., 20 to 30°) horizons containing both low-dipping and steeply dipping fractures (Everitt and Brown 1996). These faults have chloritic slip surfaces that grade into complex cataclasite zones where fault movement on the order of metres has occurred. The cataclasite zones comprise recrystallized fault rubble cemented by a fine grained chlorite-carbonate matrix; these zones are crosscut by chloritic slip surfaces, minor fractures, and seams of soft clay - goethite gouge. These complex assemblages are in varying stages of groundwater-induced decomposition, and exhibit variable permeability.

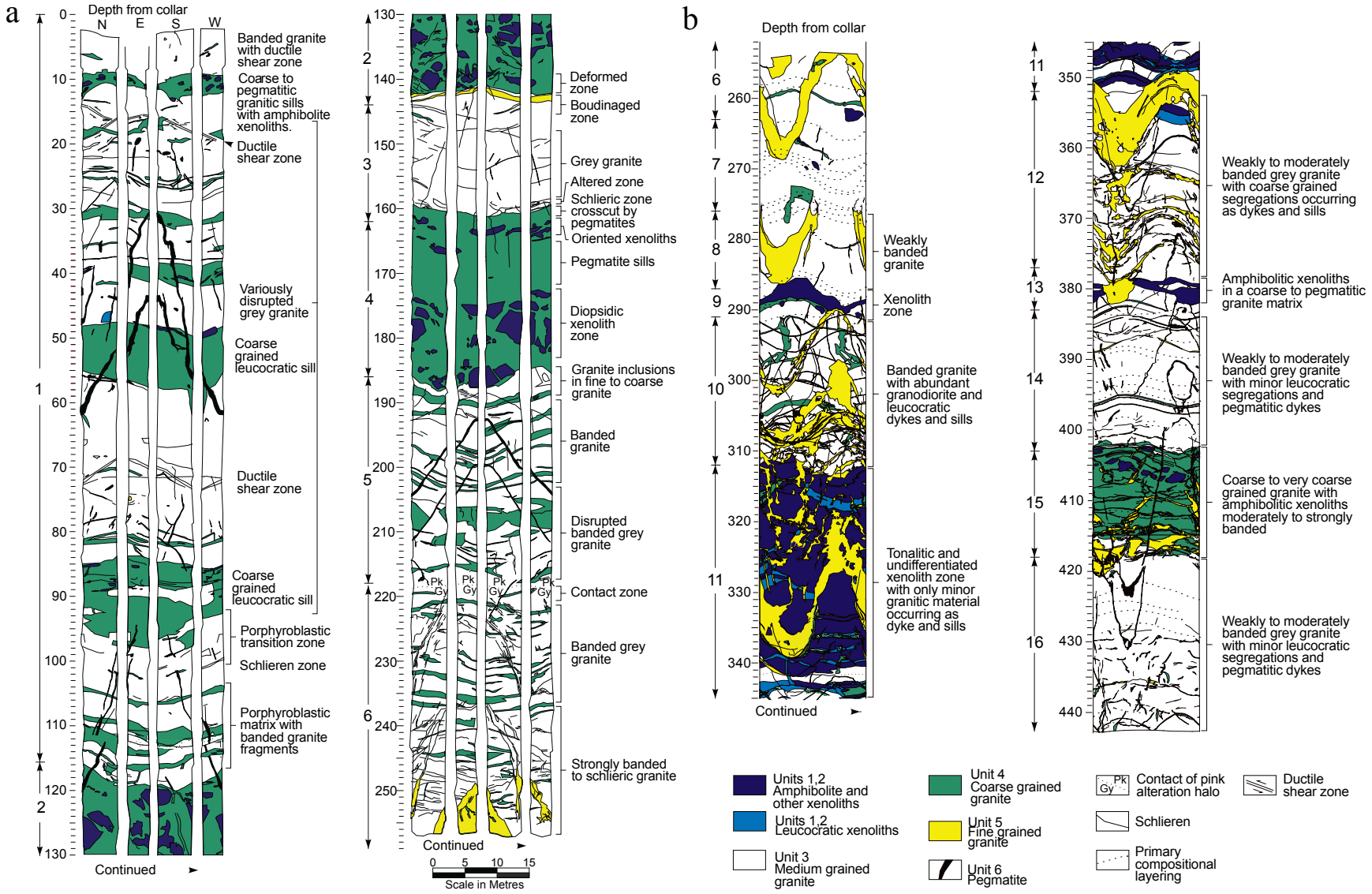

Figure 9: Geology Observed at the URL in (a) Upper Rectangular and (b) Lower Circular Shafts. Numerals on the Left Side of Each Perimeter Map Represent Litho-Structural Domains. (Everitt et al. 1998)

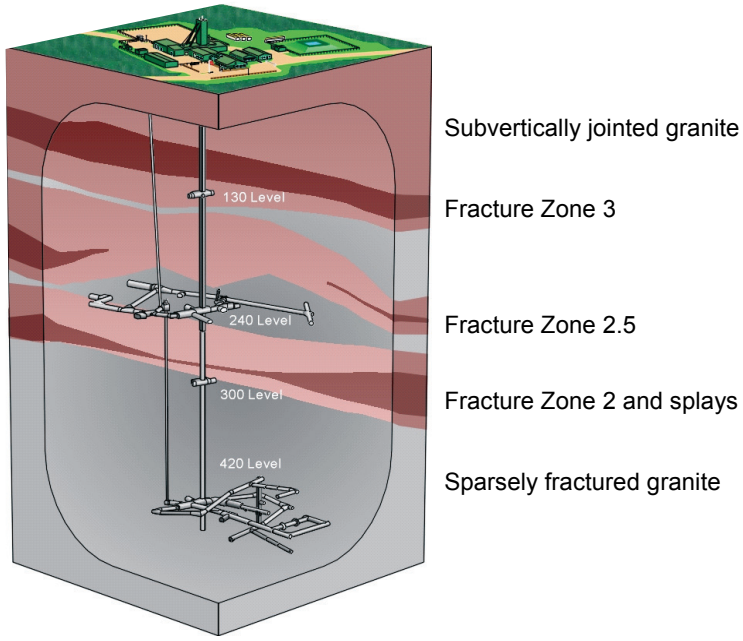

Figure 10: Major Thrust Faults and Fracture Domains at the URL

The thrust faults and splays follow the large scale compositional layering, and divide the rock mass into a number of tabular to wedge-shaped blocks. These blocks are cross-cut by one or more sets of subvertical joints, the pattern and frequency of which varies from one block to the next (Figure 11). The factors influencing the pattern of intrablock joints include the overall distance from the surface, the proximity to the bounding faults, and the local rock type.

With increasing depth, the subvertical joints become less frequent, less continuous, and exhibit fewer preferred orientations. They also become increasingly confined to the immediate margins of the fault zones or to lithologic heterogeneities such as dykes. The subvertical joints have been interpreted as extensional intrablock fracturing generated during and after faulting (Everitt and Brown 1986). Flexing of the fault blocks during thrusting is considered the most likely mechanism for their initiation, with possible reactivation and new fracture development resulting from regional extension associated with subsequent cycles of uplift and erosion. The current erosional surface has been at essentially its present position for the last 400 Ma (Fairhurst et al. 1996).

In the sparsely fractured rock mass below Fracture Zone 2 and its splays, only six dry quartz-chlorite filled fractures were observed in excavations at the URL. These fractures appear to be smaller-scale and lower temperature equivalents of the pegmatite-aplite dykes, formed by parting along the flow banding during cooling and contraction of the dykes. They are estimated to be approximately 1 m in diameter. The rock mass below a depth of about 300 m can therefore be considered massive and unfractured for the purposes of thermal-mechanical analyses.

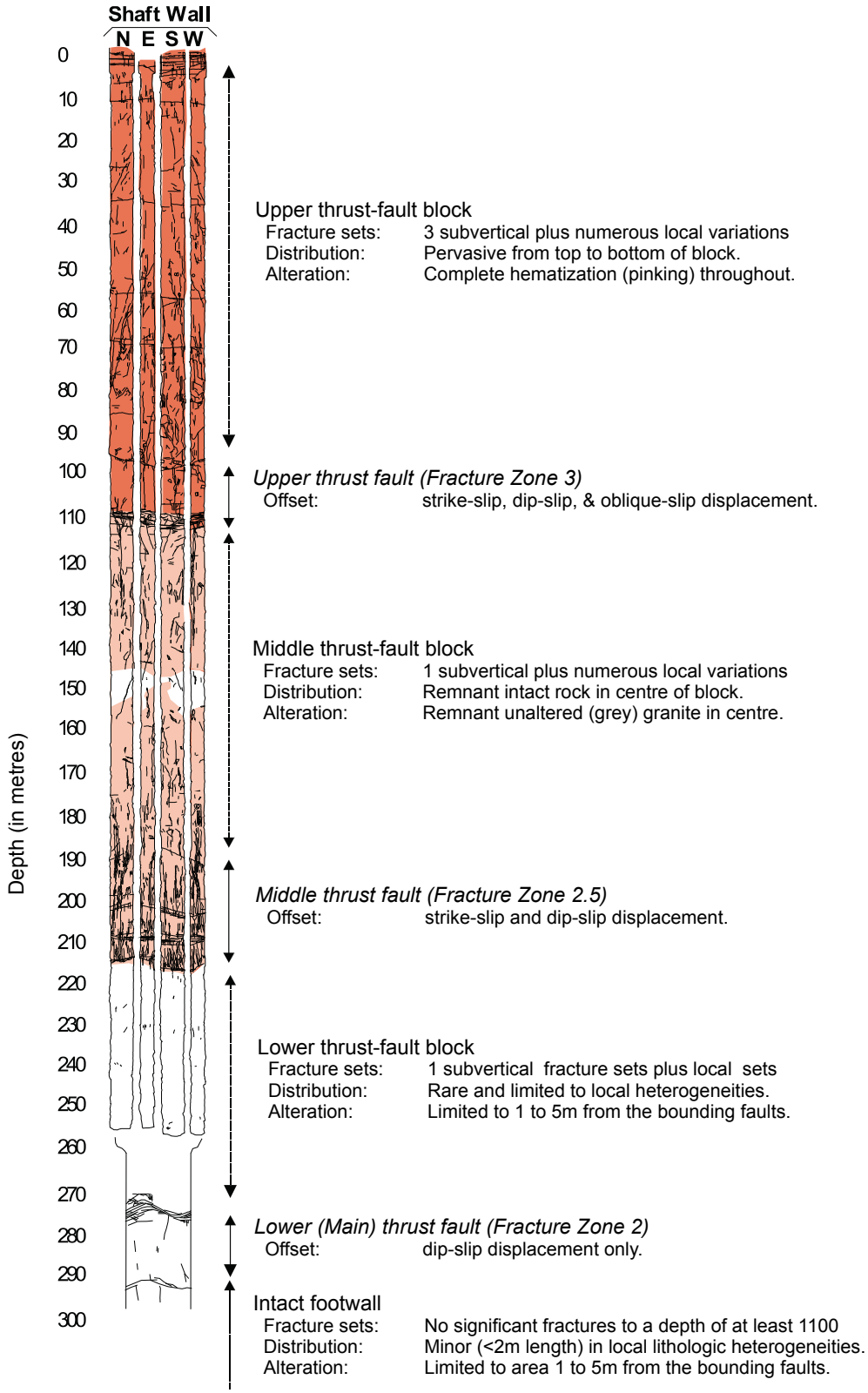

Figure 11: Fracture Domains Observed in the URL Shafts (Everitt and Lajtai 2004)

2.3.3 Rock Mass Properties

The sparsely fractured rock mass is typically considered a continuous, homogeneous, isotropic, linear elastic material. This assumption is made to simplify numerical analyses of rock response. Everitt and Lajtai (2004) argue that the rock mass at the URL is neither homogenous nor continuous. There is considerable evidence of non-linear rock response, particularly above Fracture Zone 2. Everitt and Lajtai (2004) also provide considerable evidence of highly anisotropic strength properties controlled by rock fabric. Nonetheless, the assumptions of a homogenous and linear elastic rock mass are considered sufficient for mechanical analyses. This is particularly applicable below Fracture Zone 2 (about 300 m depth) where there is a nearly linear rock mass response to stress change and where the elastic properties of the three major rock units are very similar and nearly isotropic. The mechanical properties that are typically used to describe the stress-strain behaviour of an isotropic linear elastic medium are Young's modulus and Poisson's ratio, although any two elastic parameters (such as bulk and shear modulus) will suffice. Thermal properties include thermal conductivity, specific heat, and thermal diffusivity (which is defined as thermal conductivity divided by volumetric specific heat). The thermal-mechanical coupling parameter is the coefficient of thermal expansion. Density is an additional physical parameter of the rock mass used in numerical analysis.

Typical parameter values specified for thermal-mechanical analysis are shown in Table 1. It should be noted that the most reliable laboratory measurement of the thermal expansion coefficient is 7×10^{6} °C^{-1} (Lau and Chandler 2004), which results in calculated thermal stresses that are about 50% lower than those calculated using the coefficient value in Table 1. The coefficient in Table 1 is therefore conservative when used in thermal-mechanical analyses.

Table 1: Thermal-Mechanical Material Properties for Granite

Properties	Granite
Dry Density (Mg/m^3)	2.65
Young's Modulus (GPa)	60
Poisson's Ratio	0.25
Thermal Conductivity (W/(m·°C))	3
Specific Heat (J/(kg·°C))	845
Thermal Diffusivity (m^2/a)	42.3
Coefficient of Thermal Expansion (strain/°C)	1×10^{-5}

(unpublished report)

Extensive laboratory testing has been conducted on rock core samples from the URL to determine representative virgin properties of the main granite and granodiorite dyke materials (Read and Martin 1992). Results from these tests suggest that the density of granite and granodiorite are 2.63 ± 0.01 and 2.66 ± 0.02 Mg/m^3, respectively. Both rock types have a Poisson's ratio (ν) of 0.25 ± 0.1. Tangent Young's modulus (E) values are 65 ± 10 and 66 ± 10 GPa for granite and granodiorite, respectively.

Recent thermal-mechanical analyses of the various DGR configurations in granite have reported using a Young's modulus value of 50 GPa and a Poisson's ratio value of 0.1 for

granite (CTECH 2002; RWE-NUKEM 2003, 2004a). These property values contradict those in Annex 2 of the CTECH 2002 report, where Young's modulus and Poisson's ratio for granite are listed as 60 GPa and 0.25, respectively. This contradiction suggests that there may be a transcription error from one part of the report to the next. If not a transcription error, then these two numbers are both low for typical values of Lac du Bonnet granite. The value for the thermal expansion coefficient in the CTECH (2002) report is the same as that in Table 1. Since thermal stress is approximately proportional to the bulk modulus (K), where K = E/(3(1-2 ν)), using the lower values of Young's modulus and Poisson's ratio will decrease the thermal stress by about 40% for the same thermal expansion coefficient. Young's modulus and Poisson's ratio values of 65 GPa and 0.25, respectively, were used for the analyses supporting the RA.

For the purposes of thermal mechanical analyses of sparsely fractured granite, rock strength is defined by the Hoek-Brown strength criterion (Hoek and Brown 1980) given by:

$$\sigma_{1f} = \sigma_3 + \sqrt{m\sigma_c\sigma_3 + s\sigma_c{}^2} \tag{1}$$

where

σ_{1f} is the maximum principal stress at failure,
σ_3 is the minimum principal stress,
σ_c is the unconfined compressive strength of intact rock material,
m is a parameter controlling the shape of the strength envelope, and
s is a scaling factor to account for the presence of in situ joints or discontinuities.

The uniaxial tensile strength can be calculated from the Hoek-Brown parameters as follows:

$$\sigma_t = 0.5\sigma_c\left(m - \sqrt{m^2 + 4s}\right) \tag{2}$$

The strength factor (SF) is calculated as the ratio of the maximum principal stress difference at failure calculated from Equation 1 to the actual in situ value of the maximum principal stress difference at a given point in the rock mass as follows:

$$SF = \frac{\sigma_{1f} - \sigma_3}{\sigma_1 - \sigma_3} = \frac{\sqrt{m\sigma_c\sigma_3 + s\sigma_c{}^2}}{\sigma_1 - \sigma_3} \tag{3}$$

Rock failure is assumed to occur if $SF < 1$. This same definition is termed the Hoek-Brown strength ratio in the analyses conducted in Section 4 of this report. For isotropic stress conditions, SF can be redefined as σ_{1f}/σ_1 to avoid numerical instability.

The selection of representative Hoek-Brown parameters to define rock mass strength is complicated by several factors:

- Loading rate – Rock strength measured in standard laboratory compression tests using a rapid loading rate generally exceeds that measured in tests using a slow loading rate. Short-term laboratory compression tests tend to over-estimate the long-term strength of the rock mass.

- Scale effects – Rock strength measured in laboratory compression tests on core samples may over-estimate in situ rock mass strength in situations where the rock mass contains discontinuities that are not adequately represented at laboratory scale.
- Damage – Rock strength measured in laboratory compression tests on core containing damage in the form of microcracks tends to be lower than that measured on relatively undamaged core. Likewise, in situ rock strength may be degraded in areas where damage may develop (e.g., near the periphery of unsupported underground openings).
- Stress path - Rock strength is influenced by the stress path to which a rock mass is subjected during and following excavation of an underground opening. Complex three-dimensional stress paths generated by the excavation process and gradual warming of the rock may locally reduce rock strength near the periphery of underground openings. This effect is not readily reproducible in laboratory tests on rock core.

Read et al. (1998) recognized these effects and specified two compressive strength design limits for use in preliminary structural analyses of repository openings. A conservative lower bound design limit was used for mechanical analyses of excavation-induced stresses at the tunnel periphery. Application of the lower design limit to excavation design was intended to ensure an undamaged rock mass near the tunnel boundary. For thermal-mechanical analyses following waste placement, an intermediate strength envelope was used as a design criterion to represent long-term strength of intact granite in the near-and far-field around an underground opening. The intermediate strength envelope used by Read et al. (1998) for thermal-mechanical analyses is appropriate for analysis of large-scale fracturing in the intact rock mass away from excavations, whereas the lower design limit would be unduly conservative and is not used in any far-field analysis. Hoek-Brown parameters associated with these two bounding envelopes are shown in Figure 12 as limits on the possible range of in situ strength (shaded area). The corresponding tensile strength for these envelopes is about 6 MPa according to Equation 2. The other two envelopes (laboratory peak strength and crack initiation threshold) are not used in the analysis of large-scale fracturing in this report, but are shown for completeness.

Based on extensive laboratory testing on Lac du Bonnet granite, the measured tensile strength of rock core samples is 6±2 MPa; the corresponding value for granodiorite is 10±2 MPa (Read and Martin 1996). Recent results from point load tests investigating anisotropic strength properties have shown tensile strength values as low as 3.5 MPa for granite and 4.6 MPa for granodiorite depending on loading direction relative to rock fabric (Everitt and Lajtai 2004). Read (1994) has shown that progressive microcracking occurs in the region where the tensile strength of the rock mass is exceeded during excavation, locally reducing the shear modulus of the rock mass. Tensile strength limits of 6 and 11 MPa, and shear moduli reductions of 81 and 62% in the tensile region around a circular tunnel at the 420 Level of the URL, were back analyzed for granite and granodiorite, respectively (Read 1994). Changes in properties of the rock mass near excavations are not considered in the analyses conducted to support the RA, but should be considered in more detailed analyses. On the basis of in situ rock mass conditions and properties, rock mass classification indicates Norwegian Geotechnical Institute (NGI) Tunnelling Quality Index (Q) values of 84 and 250 for the 420 and 240 Levels, respectively (Read 1997). These values are equivalent to rock mass rating (RMR) values of 84 and 94, respectively. These values correspond to Very Good Rock (Rock Mass Class 1) for tunnelling (Bieniawski 1976).

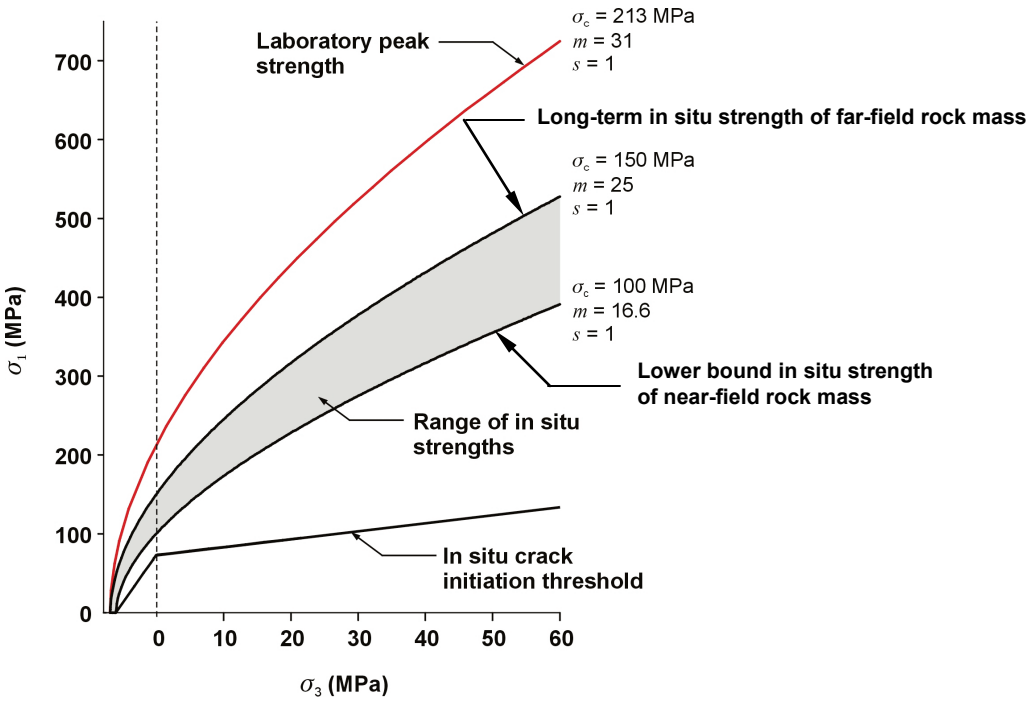

Figure 12: Hoek-Brown Strength Envelopes for Lac du Bonnet Granite (Baumgartner et al. 1996)

2.3.4 Initial In Situ Conditions

The initial in situ conditions relevant to thermal-mechanical analysis of the rock mass are the temperature, stress, and pore pressure distributions with depth. Initial pore pressures are required to calculate effective stresses, and are included explicitly in more complex analyses involving hydro-thermal-mechanical coupling. Only thermal-mechanical coupling is considered in this report.

A geothermal gradient of 0.012°C/m depth, with an assumed mean annual surface temperature of 5°C, is considered representative of conditions in the Lac du Bonnet batholith (Drury and Lewis 1983, Jessop and Lewis 1978). Under these conditions, the ambient rock temperature of the repository level at 1000 m depth is 17°C. To account for possible continental glaciation, the mean annual surface temperature was reduced to 0°C beyond 10,000 years in recent analyses (CTECH 2002).

In situ stresses in the Canadian Shield vary considerably depending on the amount of surface erosion that has occurred over time, and the degree of fracturing and faulting in the rock mass resulting from the associated stress changes. At the URL, the low-dipping thrust faults in the upper 300 m of the batholith act as stress domain boundaries, with stresses in the displaced fault blocks perturbed relative to the general stress distributions for the Canadian Shield (Martin 1990). The stress distributions specified for thermal-mechanical analyses (unpublished report) are shown in Figure 13. Stress conditions at the two main development levels of the URL are shown for comparison, and are described as follows:

- At the 240 Level, the in situ stresses are typical of other sites at similar depths in the Canadian Shield. Stress magnitudes and orientations (given as trend/plunge) are σ_1 = 26 MPa (228°/08°), σ_2 = 17 MPa (132°/23°) and σ_3 = 13 MPa (335°/65°).
- At the 420 Level, the maximum and intermediate principal stresses are significantly higher than those above Fracture Zone 2, and the minor principal stress approaches the lithostatic stress. Stress magnitudes and orientations are σ_1 = 60 MPa (145°/11°), σ_2 = 45 MPa (054°/08°) and σ_3 = 11 MPa (290°/77°).

The almost 90° change in maximum principal stress direction between the two levels is associated with stress relief of the overlying fault block in the reverse dip direction of the major thrust faults at this site (Chandler and Martin 1994). Perturbations in the stress tensor are evident near Fracture Zone 2, and near a subvertical fracture at the 240 Level of the URL. It is important from the viewpoint of excavation design to note that the maximum and intermediate principal stresses are inclined up to 11° from horizontal at the 420 Level and up to 23° from horizontal at the 240 Level of the URL (i.e., the declination of σ_3 is strongly influenced by the dip and proximity of Fracture Zone 2). Design analyses conducted for a DGR at 1000 m depth in crystalline rock have assumed that σ_1 = 65 MPa, σ_2 = 49 MPa and σ_3 = 26 MPa, and that the minimum principal stress is vertical. This implies far-field stress ratios of σ_1/σ_3 = 2.5 and σ_2/σ_3 = 1.9.

The pore pressure profile with depth is assumed to follow a standard hydrostatic distribution, and is based on fresh water with a density of 1000 kg/m^3 and a water table at ground surface. At 1000 m depth, the equivalent pore pressure is 9.8 MPa. However, because of the very low porosity of the rock mass (approximately 0.2%), and estimates of the Biot coefficient α as low as 0.2 under high stress conditions, the effective stresses have typically been assumed to be almost equal to the total stresses at depth in relatively intact rock. Chandler (2001) suggests using a Biot coefficient of 0.8 for moderate to low confinement conditions, increasing the relevance of pore pressures in thermal-mechanical analysis. For the purposes of thermal-mechanical analysis, the rock mass has been assumed in some prior analyses to be fully-drained and thermo-poroelastic effects have been ignored. These assumptions are at odds with observations of measured pore pressure increases around excavations at the URL that persisted for more than 10 years after excavation, suggesting that poroelastic effects are an important consideration in detailed analyses of rock mass response to excavation.

As the rock mass is heated after waste placement, the rock mass above the repository level will expand and heave, creating a decrease in the near-surface lateral stresses. If sufficient heave occurs, the near-surface lateral stresses will become tensile, creating a zone of lateral extension. The tensile strength limit of this zone is conservatively set to zero to account for the influence of near-surface fracture systems. Based on numerical analysis of a homogeneous rock mass with a thermal expansivity of 10^{-5} °C^{-1}, the maximum depth of the near-surface extension zone, measured from ground surface, has been specified to be less than 100 m (Baumgartner et al. 1995). It should be noted that near surface stresses and vertical surface heave are very sensitive to material properties and assumptions made regarding the quality of near surface rock. Values quoted for surface heave and depth of the extension zone are from analyses performed by others using simplified representations of the rock mass.

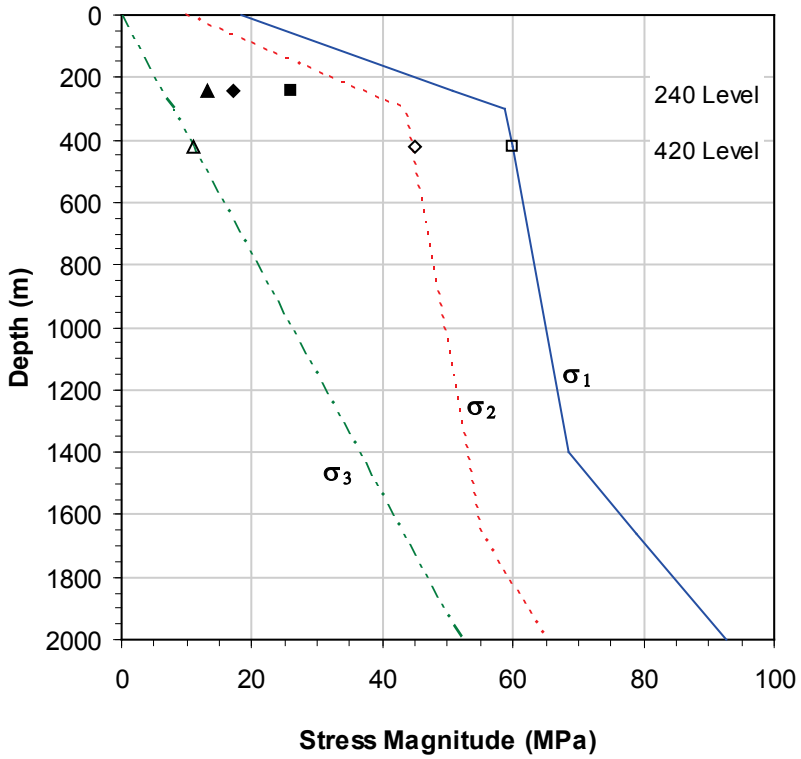

Figure 13: In Situ Stress Distributions Specified for Canadian Shield Granite. Stress Conditions at the 240 and 420 Levels of the URL are Shown for Comparison (unpublished report).

To account for continental glacial loading effects, numerical analyses (unpublished report) have included the application of a surload to the ground surface after 60,000 years as defined in Table 2 (after Peltier 2002). Numerical analyses performed by others have assumed a 3000 m thick ice sheet placed instantaneously at 10,000 years after UFC placement (CTECH 2002). At a density of 920 kg/m^3, this translates into a surcharge of about 27 MPa applied at ground surface. Assuming an average Poisson's ratio of 0.25, the associated increase in horizontal stress is expected to be $\Delta\sigma_v\ (\nu/(1-\nu))$ = 9 MPa.

Table 2: Glacial-Ice Surload

Time after Waste Placement (years)	Glacial Ice Thickness (m)	Glacial Normal Stress* (MPa)
60,000	0	0.0
66,000	1,500	13.5
86,000	3,000	27.1
96,000	3,200	28.9
104,000	2,100	18.9
105,000	0	0.0

*Based on an ice density of 920 kg/m^3 (Paterson 1994)

2.4 SEDIMENTARY HOST ROCK

The sedimentary rock of southern Ontario is considered a potential host rock for a DGR. Specifically, the Ordovician Lindsay Formation limestone and the Queenston Formation clay shale represent potential repository horizons. The general geology and geotechnical characteristics of the rock of the Michigan Basin have been investigated by Mazurek (2004). Specific investigations near the Bruce Site at Tiverton, Ontario (Golder 2003) provide information used in feasibility studies of DGR development (RWE-NUKEM 2004b).

2.4.1 General Geology

Southern Ontario is located along the southeastern rim of the North American Craton (Mazurek 2004). The crystalline basement rocks in this area are overlain by the Paleozoic sedimentary rocks of the Western St. Lawrence Platform (Johnson et al. 1992). Within the central part of this area, the SW-NE trending Algonquin Arch occurs in the crystalline basement, separating the Michigan Basin to the northwest and the Appalachian Basin (or Allegheny Trough) to the southeast. The Michigan Basin is a circular-shaped intracratonic basin with a diameter of 500 to 600 km, centred in Michigan, with a maximum depth of over 4 km.

The general stratigraphy of southern Ontario (Figure 14) comprises Paleozoic formations of Cambrian to Devonian (543 - 354 Ma) age. These stratigraphic units are near-horizontally bedded and are only weakly deformed. These units include shales, limestones, dolomites, sandstones and evaporites (salt, gypsum/anhydrite) of the Michigan and Appalachian sedimentary basins, and reach a maximum thickness of about 1500 m along the section line shown in Figure 14 (Mazurek 2004).

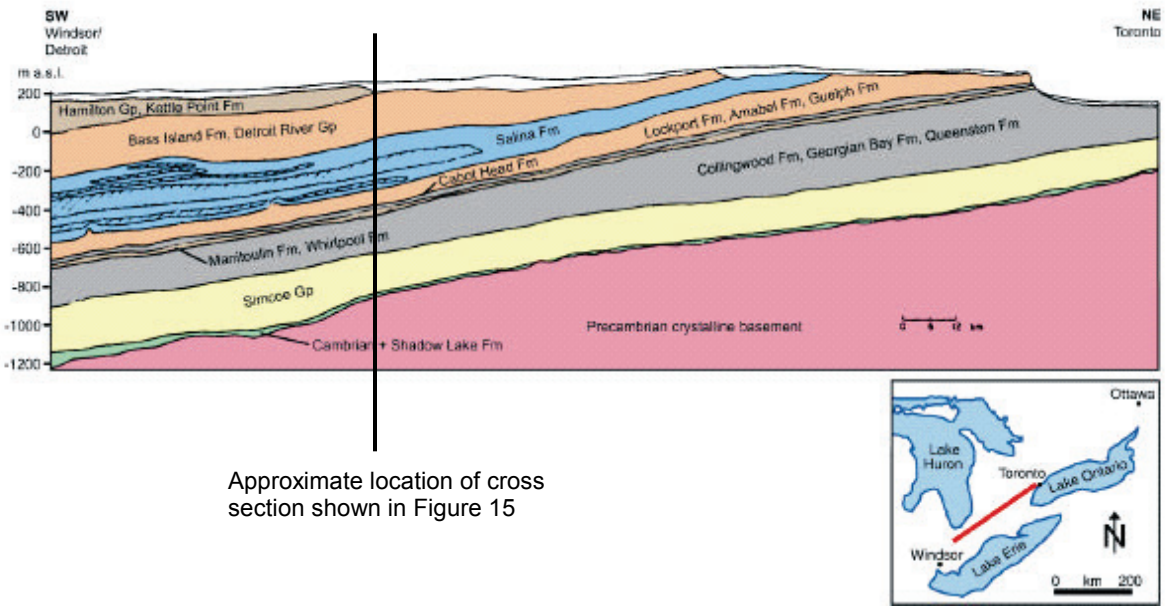

Figure 14: Stratigraphic Section Through the Michigan Basin (Mazurek 2004)

Based on four selection criteria (Mazurek 2004), the Middle/Upper Ordovician age (ca. 470 – 443 Ma) shales (Blue Mountain, Georgian Bay and Queenston Formations) and underlying limestones (Simcoe Group including the Gull River, Bobcaygeon, Verulam and Lindsay Formations[3]) were identified as potentially suitable bedrock formations for a DGR. These formations are laterally continuous throughout large regions of southern Ontario. The stratigraphic sequence dips gently to the SW with salt of the Salina Formation above the deeper Queenston Formation shale and Lindsay Formation limestone over much of the section (Figure 14).

For the purposes of conducting feasibility studies related to a DGR in either the Queenston Formation shale or the Lindsay Formation limestone, a simplified lithostratigraphic profile was developed based on conditions near the Bruce site (Figure 15). The Queenston Formation shale (typical of the shales at about 450 to 650 m depth) is described as a reddish-brown shale (mudstone) with occasional interbeds and nodules of green siltstone (less than 30% of green siltstone in the upper beds). The red colour reflects a marine deltaic deposit (iron oxide). The Lindsay Formation limestone (about 650 to 840 m depth) is described as a very fine grained to lithographic, non-porous, argillaceous to shaly limestone of very consistent lateral continuity. This unit has been mapped as horizontally bedded with horizontal fractures spaced 0.5 to 1 m, and vertical fractures spaced 10 m (Golder 2003). The depths of these units vary along the section line in Figure 14 due to variations in surface topography and thickness of surficial deposits. Conceptual repository depths are 500 m in shale, and 750 m in limestone.

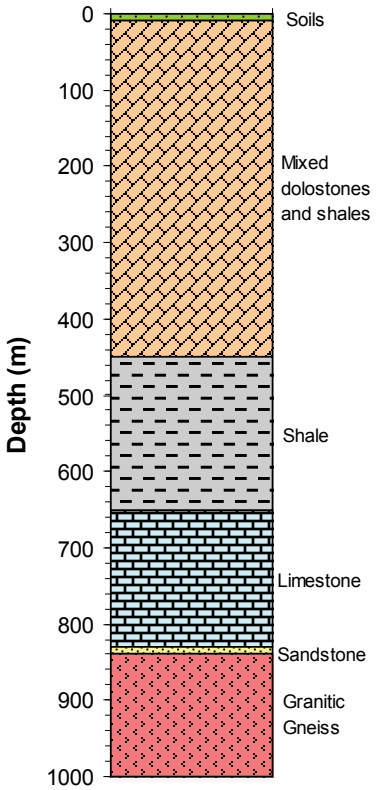

Figure 15: Simplified Lithostratigraphic Section for DGR Studies (after Golder 2003)

[3] The Bobcaygeon, Verulam and Lindsay Formations are referred to as Kirkfield, Sherman Fall, and Cobourg Formations, respectively, in the Ontario Geological Survey classification of the Michigan Basin stratigraphy

2.4.2 Fracture Characteristics

Sanford et al. (1985) identified major lineaments separating crustal blocks in southern Ontario. One major lineament runs from the Georgian Bay coast line southeast toward the Toronto area. A second lineament runs SW-NE beneath southern Ontario, roughly coinciding with the Algonquin Arch, and terminates against the first lineament. These lineaments bound the Bruce Megablock in the northwestern part of southern Ontario and the Niagara Megablock in the southeastern part. These blocks are considered as units with a partly independent tectonic evolution dominated by periodic basement reactivation (Mazurek 2004).

The fracture pattern in the Bruce Megablock inferred by Sanford et al. (1985) is relatively simple compared to that in the Niagara Megablock. The length of the fractures lies in the range of tens to hundreds of kilometres, and their spacing is 10 to 30 km. Historic earthquakes are rare in the Bruce Megablock. Synsedimentary faulting in southwestern Ontario is attributed mainly to relative movements along basement faults between the Algonquin Arch and the basins on either side. Salt dissolution in the Upper Silurian Salina Formation has produced salt collapse structures in the overlying Silurian and Devonian strata in some areas (Mazurek 2004). According to Golder (2003), the sub-erosion of the Salina salts from beneath the Bruce Site has structurally influenced the entire overlying rock sequence through collapse and differential subsidence. This has resulted in warping of overlying strata, development of vertical fracturing and enhancement of formational permeability extending through the Devonian sequence.

2.4.3 Rock Mass Properties

The rock mass properties for the various lithologic units in the stratigraphic profile shown in Figure 15 are summarized in Table 3. These values are derived primarily from Golder (2003) based on limited information and testing of representative samples from outcrop. The data are extrapolated from sites primarily along the shore of Lake Ontario to the area around the Bruce site. It is noted that properties of many of the stratigraphic units are unknown (N/A in Table 3).[4]

For the Queenston Formation shale and the Lindsay Formation limestone, rock mass classification yields values of 11 and 32 for Tunnel Quality Index (Q), and values of rock mass rating (RMR) of 65 and 75, respectively (Golder 2003). These values correspond to Good Rock (Rock Mass Class 2). The corresponding Geological Strength Index (GSI) values (Hoek et al. 1995) are 66 and 74 for the two units, respectively. The low values of the Hoek-Brown parameter s suggest that both rock types are jointed near outcrops. These units may be less fractured, and may have higher rock mass ratings, at great depth.

2.4.4 Initial In Situ Conditions

The initial conditions assumed for thermal-mechanical analysis of the Michigan Basin are summarized by Baumgartner (2005). A geothermal gradient of 0.019°C/m depth, with an

[4] Since the time of writing, more detailed information on rock mechanical properties and in situ stress conditions has been collected by NWMO. This new information was not used in the analyses described in later sections of this report. However, the input data and results of the analyses are considered sufficiently accurate to support the development of the RA.

Table 3: Thermal-Mechanical Properties for Rock Types of the Michigan Basin

Properties	Soils	Mixed Dolostones and Shales	Shale	Limestone	Sandstone	Granitic Gneiss
Dry Density (Mg/m^3)	1.8	2.6	2.6	2.6	2.6	2.8
Porosity (%)	30	7	11	2	0.5	<0.4
Young's Modulus (GPa)	N/A	N/A	12 (6-23)	40 (16-66)	N/A	60 (est.)
Poisson's Ratio	N/A	N/A	0.3 (0.1–0.44)	0.3	N/A	N/A
Uniaxial Compressive Strength (MPa)	N/A	N/A	40 (33-46)	60 (25-140)	N/A	N/A
Tensile Strength (MPa)	N/A	N/A	3 (2-4.6)	N/A	N/A	N/A
Hoek-Brown *m* Parameter	N/A	N/A	4.26	3.89	N/A	N/A
Hoek-Brown *s* Parameter	N/A	N/A	0.0221	0.0529	N/A	N/A
Thermal Conductivity (W/(m·°C))	1.5	2.3	2.1	2.3	2.5	3.0
Specific Heat (J/(kg·°C))	1500	920	975	830	810	810
Thermal Diffusivity (m^2/a)	N/A	N/A	N/A	N/A	N/A	N/A
Coefficient of Thermal Expansion $(°C)^{-1}$	N/A	N/A	$2x10^{-6}$	$6.7x10^{-6}$	N/A	$10x10^{-6}$

(Source: Baumgartner 2005 and other unpublished sources)

assumed mean annual surface temperature of 7°C, is considered representative of this region. The ambient rock temperature of the repository level at 500 and 750 m depth is 16.5 and 21.3°C, respectively. To account for possible continental glaciation, the mean annual surface temperature is reduced to 0°C beyond 10,000 years in previous analyses (CTECH 2002). This condition is assumed to persist from 60,000 to over 105,000 years based on Table 2. For the sake of the analyses conducted in this report to support the RA, the timing of glaciation is not critical to the results

Specific in situ stress conditions in the various stratigraphic units in the Michigan Basin are not known. However, regional stress data (Adams and Bell 1991; Reinecker et al. 2004) suggest that within the area east of the Canadian Cordillera (part of the Mid-Plate Stress Province), the maximum horizontal stress σ_H is larger than the vertical stress σ_v. In this area, σ_H strikes ENE to NE. Overcoring tests in the uppermost 2 km of the Precambrian basement show that the minimum horizontal stress σ_h often exceeds σ_v, although not consistently (Mazurek 2004). Consequently, stress conditions most frequently correspond to those of a thrust fault regime in the Precambrian basement, particularly north of the lower Great Lakes.

Overcoring and hydraulic fracturing tests have been conducted in the sedimentary rocks of the St. Lawrence Platform to a depth of about 300 m (Adams and Bell 1991). Shallow overcore tests within 70 m of ground surface show considerable scatter, with the maximum and minimum horizontal stresses typically larger than the vertical stress. Hydraulic fracturing tests conducted below 70 m depth (Figure 16) show a similar pattern. Scatter in the data for the maximum horizontal stress is possibly due to stress variations across stratigraphic units, with stiffer rock types carrying more stress than softer rock types. This pattern suggests a tectonic contribution to the in situ stress state at some locations. Extrapolating the trends in the hydraulic fracturing data, the horizontal stress components are approximated by the following empirical equations:

$$\sigma_H = 0.0208 \cdot z + 12.3 \text{ MPa} \quad (4)$$

$$\sigma_h = 0.0246 \cdot z + 4.7 \text{ MPa} \quad (5)$$

where *z* is the depth in metres.

Assuming that the vertical stress is lithostatic, the estimated initial stress conditions at the conceptual repository depths based on the stratigraphic section in Figure 15 are as follows:

- For a repository level at 500 m depth in the Queenston Formation shale, the estimated stress conditions are σ_H = 23, σ_h = 17, and σ_v = 13 MPa. This implies far-field stress ratios of σ_1/σ_3 = 1.7 and σ_2/σ_3 = 1.3.
- For a repository level at 750 m depth in the Lindsay Formation limestone, the estimated stress conditions are σ_H = 28, σ_h = 23, and σ_v = 20 MPa. This implies far-field stress ratios of σ_1/σ_3 = 1.4 and σ_2/σ_3 = 1.2.

Measured horizontal stress values of 9 to 13 MPa in the Lindsay Formation limestone, and 5 to 9 MPa in the Queenston Formation shale at depths less than 200 m (Golder 2003) confirm that the stiffer limestone carries higher stresses than the softer shale. Consequently, the horizontal stresses calculated from Equations 4 and 5 may be over-estimated, but provide a conservative basis for the analysis of large-scale fracturing. It should be noted that these stress measurements were conducted at locations where these units are relatively close to surface and extrapolation of these data to greater depths may be tenuous. Likewise, the interpretation methods used to derive these data were not reviewed as part of this report, but merit review if these data are to be relied upon for design. Although the relations represented by Equations 4 and 5 are used for the purposes of this report, reliable stress measurements from potential repository sites are considered essential to support these and more detailed future analyses.

Hydraulic head in boreholes penetrating Upper Ordovician to Middle Silurian strata (Queenston to Guelph Formations) of the Niagara region have been investigated (Novakowski and Lapcevic 1988) to derive a pore pressure profile with depth. Hydrostatic pressures were found in the Guelph Formation within 60 m of ground surface. All underlying units to a maximum depth of 150 m show over- or under-pressures of 20 to 50 m. Under-pressures are likely due to hydraulic connection of dolomite aquifers to exfiltration areas at lower elevation in the Niagara Gorge. Over-pressures are at least partially related to low permeability units such as the Rochester Shale. The largest vertical hydraulic gradients often occur along lithologic contacts to shales such as the Queenston Formation, suggesting very low vertical hydraulic conductivity in these units. Gas migration below shale caprock also accounts for some over-pressures in southern Ontario. Although the actual pore pressure conditions for the Queenston and Lindsay

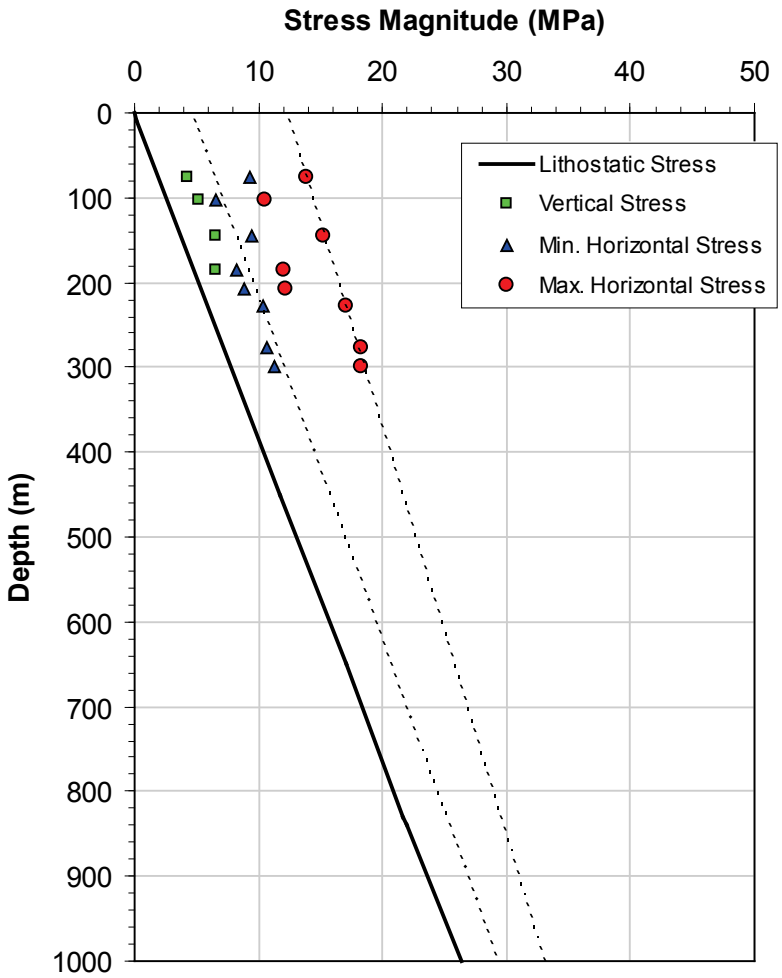

Figure 16: Comparison of Stress Measurement Results and Lithostatic Stress Profile for the St. Lawrence Platform (after Adams and Bell 1991)

Formations probably vary considerably with distance from the Niagara Gorge, it is likely that they range from hydrostatic to values up to about 1 MPa higher in the lower permeability shales. At 500 m depth in shale, the hydrostatic pore pressure is estimated to be 4.9 MPa. At 750 m depth in limestone, the hydrostatic pore pressure is estimated to be 7.4 MPa.

Like the crystalline rock scenario, the rock mass above the repository level will expand and heave as the repository level is heated, creating a decrease in the near-surface lateral stresses. The near-surface lateral stresses will become tensile given sufficient heave, creating a zone of lateral extension. The tensile strength limit of this zone is conservatively set to zero to account for the influence of near-surface fracture systems. As part of design criteria for a repository in crystalline or other rock types, the maximum depth below ground level of the near-surface extension zone has been specified to be less than 100 m (Baumgartner et al. 1995).

Glaciation effects have been considered in previous analyses in the same fashion as for the crystalline rock scenario, applying a surload equivalent to 3000 m of ice to the ground surface after 10,000 years (CTECH 2002). Based on an ice density of 920 kg/m^3, this adds about

27 MPa to the vertical stress below ground surface. Assuming an average Poisson's ratio of 0.3, the associated increase in horizontal stress is expected to be $\Delta\sigma_v\ (\nu/(1-\nu))$ = 12 MPa.

3. INDUCED FRACTURING OF ROCK

This section of the report considers the mechanics of rock fracturing and possible scenarios under which fractures may develop and propagate. The key features, events and processes associated with the construction and operation of a DGR are identified as the basis for the RA.

3.1 EVOLUTION OF IN SITU CONDITIONS

Rock fracture is possible only under evolving in situ conditions. These conditions include the state of effective stress in the rock mass, and/or the rock mass properties. Changes in either of these conditions can increase or decrease the likelihood of rock fracturing. These two mechanisms are illustrated conceptually in Figure 17 using Mohr circles to represent the state of stress at a point in the rock mass relative to a Mohr strength envelope (Hoek and Brown 1980). The envelopes shown are equivalent to the Hoek-Brown in situ strength envelopes in Figure 12, but plotted in terms of effective normal stress and shear stress rather than effective principal stresses. As discussed in Section 2, because of the localized nature of excavation damage and strength degradation around underground openings, the scenario where effective stress changes occur under conditions of constant rock strength is more relevant to the RA. However, the linkage between changes in near- and far-field conditions is discussed as part of the RA. The following sections describe the relation between the stress state and the strength envelopes.

3.1.1 Effective Stress Changes

In poroelastic theory of rock and other stiff materials, applied compressive stresses are borne partly by the rock matrix, and partly by the fluid that fills the rock pores. The component of the stresses carried by the rock matrix is related to the rock stiffness through the Biot parameter α, given as:

$$\alpha = 1 - \frac{K}{K_s} \tag{6}$$

where K is the bulk modulus of the bulk rock skeleton and K_s is the bulk modulus of single rock grains or crystals. For compressible soils, the parameter α is usually taken as unity given the large disparity between bulk modulus of the soil skeleton and the stiffness of individual soil grains. For stiff low porosity rocks, the parameter α can differ significantly from unity. For Lac du Bonnet granite, α = 0.8 for unconfined samples and is 0.2 for rock under high confining stress (Chandler 2001).

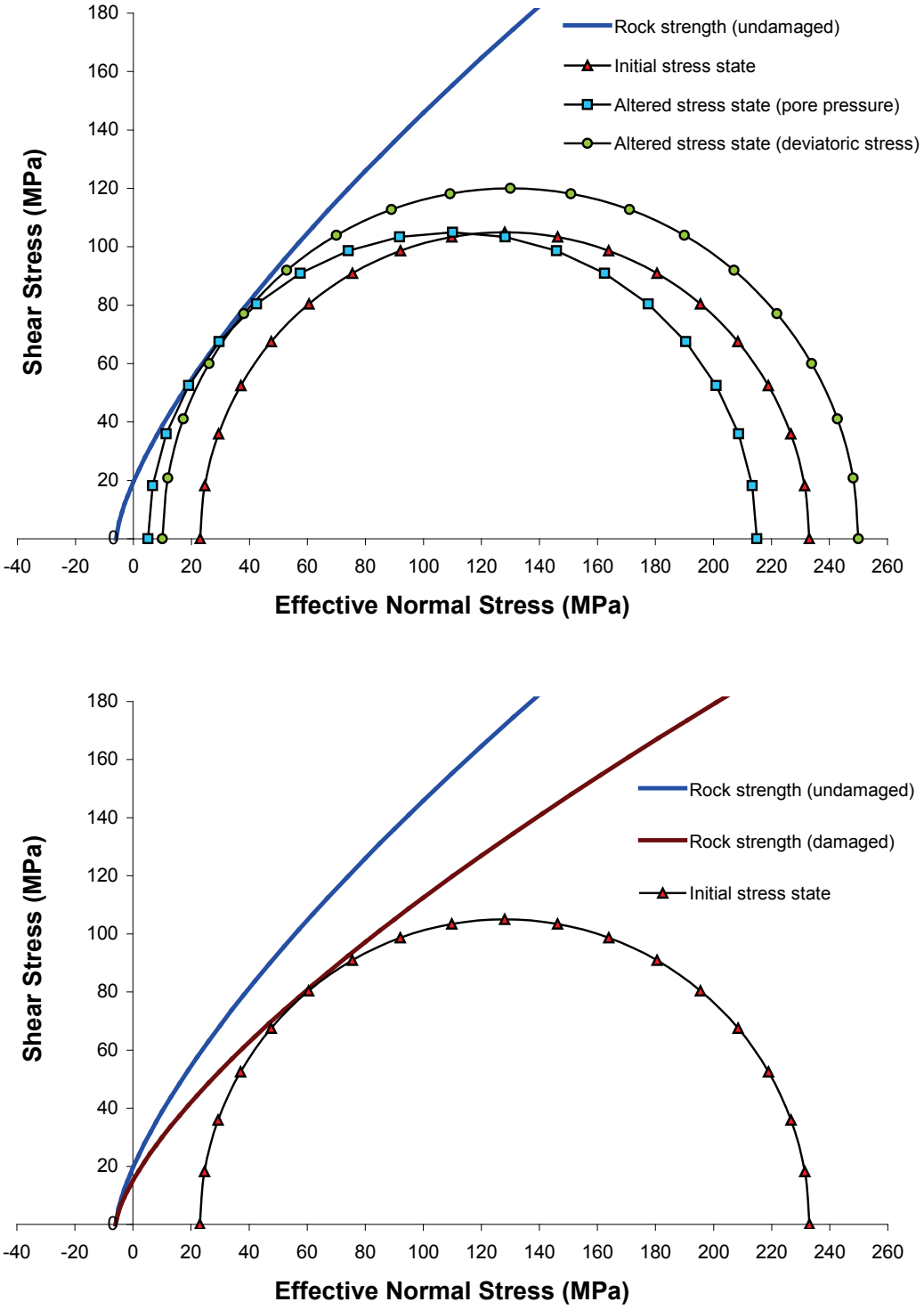

Figure 17: Illustration of Situations Leading to Rock Failure: (Top) Increase in Pore Pressure or Change in Deviatoric Stress with Constant Rock Strength, and (Bottom) Constant Stress with Degrading Rock Strength

The effective compressive stress carried by the rock matrix in a porous medium is given by:

$$\sigma' = \sigma - \alpha u \tag{7}$$

where σ is the total stress, σ' is the effective stress, u is pore pressure and α is the Biot coefficient. For low values of α, the total and the effective stresses are similar in magnitude at typical repository depths.

In addition to the Biot coefficient, the Skempton coefficient B is the ratio of the change in pore pressure to the change in mean stress in an undrained material. For compressible soils, this parameter is equal to unity. For low porosity granite, the value of this parameter is about 0.98. Consequently there is a strong coupling between changes in mean stress and changes in pore pressure in rock (Chandler 2001).

Changes in the effective stresses in the rock mass may result from changes in applied boundary loads, thermal expansion of the rock mass, or pore pressure changes and thermal expansion associated with heating. Thermo-poroelastic theory can be used to assess the effects of heating on pore pressure and volumetric strain according to the following equation:

$$p - p_o = M(\zeta - \alpha\varepsilon) + \beta_m M\theta \tag{8}$$

where p-p_o is the change in pore pressure, ζ is the change in fluid content, α is the Biot coefficient, ε is volumetric strain, θ is temperature variation, B_m is a hydro-thermal coupling coefficient and M is the Biot modulus (Chandler 2001). The thermo-poroelastic response of granite has been studied extensively at the URL in the Thermal-Hydraulic Experiment (Martino and Chandler 1999) and through laboratory testing (Lau and Chandler 2004). Application of thermo-poroelasticity to an idealized repository scenario has been documented (Chandler 2001). Results indicate that, depending on the thermo-poroelastic properties of the rock mass and the assumed thermal power, significant pore pressures can be generated around the repository by heating (Read and Chandler 2002). A decrease in vertical stress of about 20 MPa was predicted at specific locations outside the repository after 4000 years of heating at a thermal power of 20 kW. This stress change is insufficient to create tensile stress conditions, but it would shift the Mohr circle significantly to the left on the Mohr diagram.

With reference to the top of Figure 17, the initial effective stress state is assumed to be well below the strength envelope (i.e., the Mohr circle is to the right of, and does not intersect, the strength envelope). In this scenario, the effective stress evolves either due to an increase in pore pressure (i.e., lateral translation of the Mohr circle to the left), or increase in deviatoric stress (i.e., increase in the diameter of the Mohr circle), such that the strength envelope is intersected. The deviatoric stress could increase as a result of glacial erosion, for example. Another situation that would produce failure is a decrease in the minimum principal stress to the point where the tensile strength of the rock is reached. This scenario would involve the leftmost intersection point between the Mohr circle and the horizontal axis occurring to the left of the intersection of the strength envelope and the horizontal axis. This effect is associated most commonly with hydraulic fracturing caused by an increase in pore pressure.

3.1.2 Rock Mass Property Changes

The strength envelope for rock can be affected by changes in the tensile and compressive strengths of intact rock, which in turn are affected by the development of micro- and macro-fractures in, or chemical alteration of, the rock matrix. The initiation and propagation of microcracks is particularly important in understanding the process of progressive failure of a rock mass (Martin et al. 1994; Martin and Chandler 1994; Read and Martin 1996).

The compressive strength of rock is typically determined from unconfined compression tests on cylindrical specimens, with an axial stress applied monotonically at a loading rate of between 0.5 and 1 MPa/s. The peak axial stress at failure σ_f is taken as the unconfined compressive strength σ_c of the rock sample. Typical stress-strain curves for such a test are shown in Figure 18. Near the beginning of the test, the applied load tends to close preferentially-oriented microcracks in the unstressed sample, resulting in an increase in the tangent Young's modulus of the sample. Once the microcracks close, the rock behaves as a linear elastic material, with no new microcrack development up to a stress level of about 0.3 to 0.4σ_f (termed the crack initiation stress σ_{ci}). Up to a stress level of between 0.7 and 0.8σ_f (termed the crack damage stress σ_{cd}), any new microcracks that initiate are stable (i.e., they do not propagate in an unstable manner due to the compressive stress field). At stresses above σ_{cd}, unstable growth of microcracks occurs in the sample, reducing the cohesion component of rock strength, and eventually leading to rock failure under sustained load (Martin et al. 1994). Acoustic

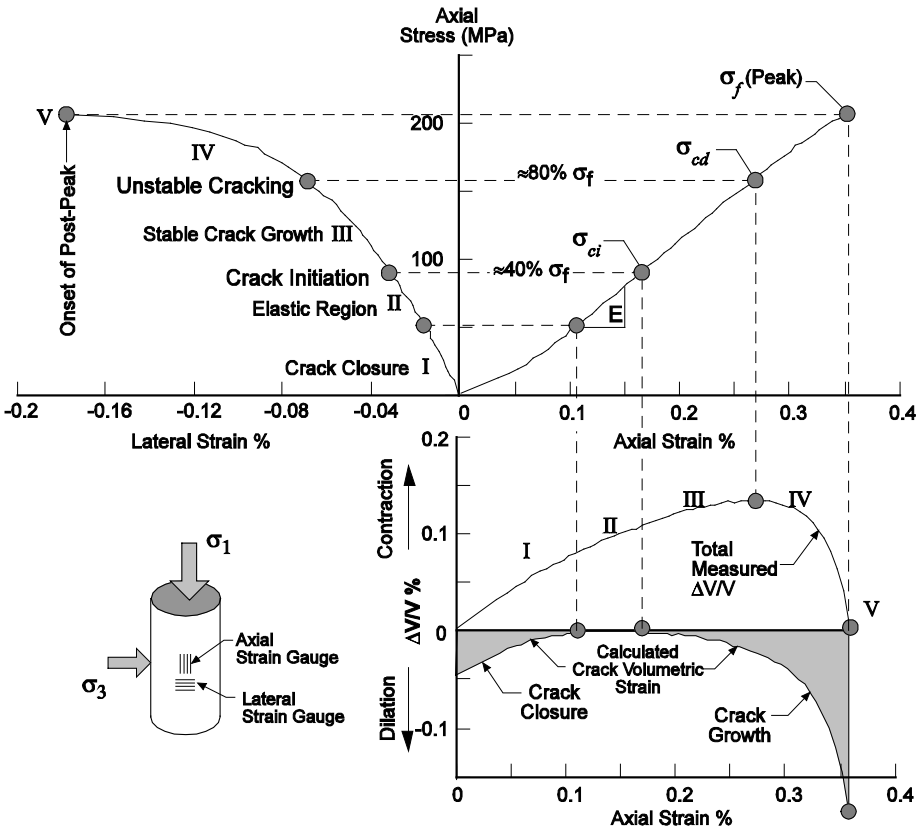

Figure 18: Stress-Strain Response of a Typical Unconfined Compressive Test on Lac du Bonnet Granite (Read and Martin 1996).

emission/microseismic (AE/MS) monitoring has been used to corroborate these findings in situ and in the laboratory (Read and Martin 1996; Eberhardt et al. 1997).

The amount of damage accumulated in a sample is characterized by the volumetric strain associated with the crack volume. As shown in Figure 18, in the early loading stage of the test, the applied stress closes those pre-existing microcracks that are at an oblique angle to the applied loading direction, but tends to open microcracks oriented subparallel to the applied loading direction. Although the microcrack crack volume increases at stresses above σ_{ci}, there is not a dramatic increase in crack volume (i.e., damage) until σ_{cd} is exceeded. The crack damage stress σ_{cd} corresponds to the point of volumetric strain reversal on the volumetric strain plot in Figure 18, and is taken as the long-term strength of the rock. For Lac du Bonnet granite, the peak unconfined compressive strength measured on relatively undisturbed rock core samples is 213 ± 20 MPa (Read and Martin 1996). The corresponding crack damage stress is about 150 MPa. This latter value is considered representative of the long-term in situ unconfined compressive strength of relatively undamaged Lac du Bonnet granite.

In addition, larger rock specimens tend to fail at lower peak stress values due to the greater likelihood of a critical low-strength material heterogeneity or flaw in the specimen (Hoek et al. 1995). Results from the Mine-by Experiment at the URL (Read 1994; Read and Martin 1996) further showed that the combination of stress rotation and development of shear stresses in zones of low or tensile confinement conditions ahead of an advancing tunnel face may induce damage that is eventually exposed at the tunnel periphery as the tunnel advances (Read et al. 1998).

Observations from laboratory tests indicate that cyclic loading (i.e., load-unload cycles) can also reduce rock strength through incremental damage development at low confinement (Read et al. 1998) depending on the stress increments from one cycle to the next. Similarly, AE/MS monitoring of the Mine-by Experiment, Heated Failure Tests and Tunnel Sealing Experiment at the URL demonstrated that a small confining stress of 50 kPa or less was required to effectively eliminate AE/MS activity (and by inference, damage development) close to excavations (Read and Chandler 2002; Read 2003). Therefore, it is reasoned that while crack initiation may be controlled by deviatoric stress associated with σ_{ci}, damage development significant enough to reduce rock strength upon increased loading is limited to regions above the crack initiation threshold where confining stress is low or tensile (Read et al. 1998). Microcrack growth is expected to be most significant where $\sigma_3 < 0$ (i.e., tensile), relatively high where $0 \leq \sigma_3/\sigma_1 \leq 0.05$, and relatively low elsewhere (Read et al. 1998, Shen and Stephansson 1996). Taken together, these strength criteria can be used to assess the expected near- and far-field rock strength in situ.

In situ studies of the rock mass response to excavation (Read and Martin 1996, Read et al. 1998) have shown that the in situ strength of the rock mass at the periphery of an underground opening may be significantly less than the long-term strength estimated from tests on relatively undamaged rock core samples. This strength degradation near the opening is attributed to complex 3D stress path effects associated with the excavation process (Read et al. 1998). These effects are controlled or influenced by the tunnel geometry and orientation, in situ stress conditions, excavation method, and other factors (Read et al. 1998, Read 2004). Read (1994) demonstrated that the in situ rock compressive strength around a 3.5 m diameter test tunnel driven sub-parallel to the maximum principal stress direction using a non-explosive excavation technique was as low as 120 MPa based on the tangential stress at which spalling initiated, while the minimum rock strength around a 1.24 m diameter vertically-bored hole in the invert of

an adjacent room was about 150 MPa. The difference in strengths is attributable primarily to the differences in stress history experienced ahead of the face of the advancing excavation, although differences in opening dimensions and excavation method may have contributed to the observed differences.

A series of thermal-mechanical tests using 600-mm-diameter vertical boreholes (Read and Martino 1996) demonstrated that the in situ compressive strength of the rock mass is affected by the thermal-mechanical stress history and the rock type. Damage was more prevalent in a hole drilled into a pre-heated rock mass than an adjacent hole drilled into an ambient temperature rock mass, then heated. The addition of a small confining pressure to the periphery of the hole prior to heating effectively arrested damage development (Read et al. 1997). Coarser, more heterogeneous rock types (granite and pegmatites) were more susceptible to damage development and strength degradation than finer, more homogeneous rock types (e.g., granodiorite). Granodiorite was shown to have a higher uniaxial crack damage strength, and a higher threshold for crack initiation, than granite (Read 1994). However, it was also noted that the strength of granodiorite is strongly anisotropic (Everitt and Lajtai 2004) with the material losing its high strength advantage over medium-grained granite when stresses are applied in certain directions.

Rock strength degradation, particularly in sedimentary rock, may also occur as a result of chemical alteration, desiccation of clay minerals, slaking, and freeze-thaw effects. Hoek and Brown (1980) report a two-fold decrease in rock strength simply by the addition of water to certain sedimentary rock types, unrelated to pore pressure effects. These types of effects along with those described above reduce the strength envelope for the rock mass, effectively decreasing the distance between the Mohr circle and the strength envelope. The bottom part of Figure 17 illustrates the concept of degrading rock strength in a compressive stress field whereby the rock weakens under constant load and eventually fails.

3.2 FAILURE MECHANISMS

The mechanisms associated with rock failure include extensile fracturing under applied compressive or tensile loading, shear fracturing under high deviatoric stress conditions, and crushing under high isotropic compressive stresses. This latter case applies only to specific rock types with large porosity in the form of collapsible voids. Reactivation of existing fractures and faults is included in the first two categories.

3.2.1 Extensile Fracturing

Extensile (or Mode I) fracturing involves tensile loading perpendicular to the plane of an existing crack such that the opposing surfaces of the crack separate without any relative shear displacement. The loading scenarios under which this type of fracturing may occur includes direct tensile loading of the rock mass, pore pressure development within an existing crack, or axial compressive loading parallel to the crack (Martin et al. 1994). In the absence of high induced pore pressures, the initiation of Mode I cracks in a compressive stress field is attributed to induced tensile stress concentrations around flaws or discontinuities in the rock. Kemeny and Cook (1991) identified three possible scenarios under which local tensile stresses could develop (Figure 19). The existence of a soft inclusion or void in the rock mass, where the elastic modulus of the inclusion is much less than that of the surrounding rock mass, can

induce tensile cracks. Similarly, a mismatch in the elastic modulus of two grains or mineral crystals in intimate contact can result in fracturing of the stiffer material under an increased load perpendicular to the interface. In addition to these modes, an increase in compressive loading at an oblique angle to an inclined crack may result in shearing along the crack interface, and the development of extensile fracturing at the tips of the inclined crack in the form of wing cracks.

In each of these cases, a fracture will initiate only if the tensile strength of the material is overcome at the boundary of the original discontinuity. According to Linear Elastic Fracture Mechanics (LEFM) theory, once a crack forms, the continued growth or propagation of the crack is dependent on the stress intensity factor K_I at the new crack tip. For an idealized elliptical crack, the stress intensity factor at the crack tip is given by:

$$K_I = (u - \sigma_3)\sqrt{\pi c} \tag{9}$$

where c is the crack half-width, u is pore pressure, and σ_3 is the minimum principal stress normal to the long-axis of the crack (tensile stress being negative).

The resistance to fracture propagation is a material property called the fracture toughness (or critical stress intensity factor) K_{Ic}. Fracture propagation is expected under conditions where the stress intensity factor exceeds the fracture toughness. The measured fracture toughness for Lac du Bonnet granite is between 1.5 and 2.0 MPa $m^{0.5}$, with a mean value of 1.7 MPa $m^{0.5}$ (Martin et al 1994). Higher values up to 2.5 MPa $m^{0.5}$ have been measured by Svab and Lajtai (1981).

In a compressive stress field, the stress intensity factor at the tip of the propagating crack decreases as the crack lengthens in each of the scenarios in Figure 19. Although there are a number of theorists (e.g., Ashby and Hallam 1986, Horri and Nemat Nasser 1986) who show that wing crack length can exceed that of the initial discontinuity, it is generally accepted that the wing crack does not equilibrate until the crack length is at least equal to the length of the original discontinuity under low confinement. These findings suggest that, in the absence of pore pressure effects, large-scale extensile fracture propagation in a compressive stress field (were it to initiate) would be limited to the approximate size of existing flaws responsible for the local stress concentrations in the rock mass.

Slow crack growth parallel to the maximum principal stress has been shown to occur in some circumstances when the stress intensity factor is less than the fracture toughness of rock. This phenomenon is called subcritical crack growth, and accounts for creep behaviour in rock (Scholz 1990). Subcritical crack growth is often attributed to stress corrosion, which is caused by chemical reactions at the crack tip (Wilkins et al. 1984). Crack velocity is given by the following equation:

$$V = AK_{Ic}^{n} \tag{10}$$

where A and n are constants associated with stress corrosion. For Lac du Bonnet granite, the value of n is about 40 (Wilkins et al. 1984). The limiting stress intensity factor for stress corrosion is about 0.5 K_{IC} (Cook 1986). Below this value, crack velocity is zero. Stress corrosion cracking in Lac du Bonnet granite was also investigated by Lajtai and Bielus (1986), Lajtai and Schmidtke (1986), and Wilkins (1987).

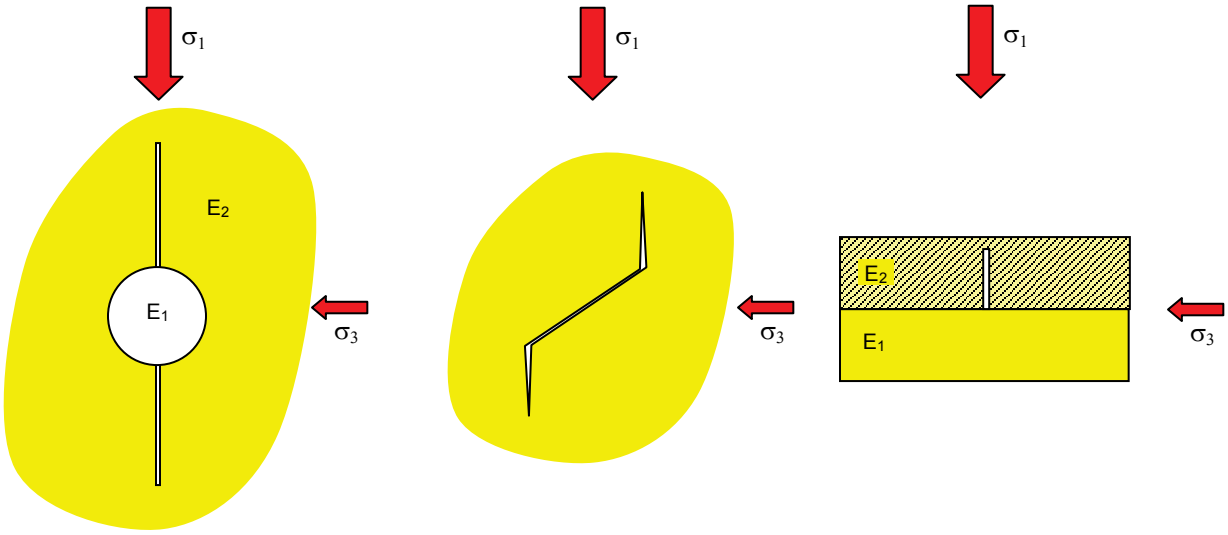

Figure 19: Three Modes of Extensile Fracturing in a Compressive Stress Field (Kemeny and Cook 1991): a Soft Inclusion Where E1<<E2 (Left), an Inclined Crack with Developing Wing Cracks (Middle), and Elastic Mismatch Between Materials in Intimate Contact with E1<E2 (Right).

Although Figure 19 provides a simplified framework to understand rock fracturing, crack initiation and propagation in polymineralic crystalline materials such as granite can be complex. Mineralogy data for Lac du Bonnet granite (Read 1994) indicate that a typical granite specimen comprises about 42% alkali feldspar, 23% plagioclase, 29% quartz, 5% biotite and other micaceous minerals, and less than 1% other minerals. In the samples examined, the grain sizes for these different minerals ranged from 0.5 to 8 mm for alkali feldspar, 0.5 to 6 mm for plagioclase, <0.25 to 4 mm for quartz, and <0.25 to 2.5 mm for biotite (Kelly et al.1993).

In a series of uniaxial compression tests on core specimens, Lajtai (1988) found that the load required to initiate cracks at the grain scale in the constituent minerals of granite varied considerably. Lajtai's results are shown as "Observed Data" in Figure 20. To further analyze these results, three normal distributions were fit to the data to account for crack initiation in feldspar, quartz and biotite. As shown in Figure 20, the sum of these three distributions reproduces the original data reasonably well. The associated cumulative frequency distribution for the sum of the three normal distributions also compares well with Lajtai's observed data (Figure 21).

These figures illustrate that crack initiation can occur in micaceous and some preferentially-oriented feldspar mineral grains at relatively low compressive stress levels under zero confinement, but higher loads are required to initiate cracks in quartz grains and less preferentially-oriented feldspars. Individual extensile cracks in these types of polymineralic crystalline materials are therefore isolated and stable, limited in size by the mineral grains in which they occur. The distribution and orientation of these isolated cracks is controlled by the grain or crystal distribution in a given rock type, and the applied load. For the various mineral grains in Lac du Bonnet granite, the crack length is on the order of the grain size, and cracks are expected to be sub-parallel to the maximum applied stress. These types of extensile cracks do not affect the macroscopic rock strength, and are therefore unlikely to contribute significantly

to the development of large-scale fracturing in the rock mass via a strength reduction mechanism (see Figure 17).

Fracture propagation in polymineralic crystalline materials can also be complex. Svab and Lajtai (1981) demonstrated that the microstructure of granite has a strong influence on the crack path that forms under applied tensile loading. For samples of Lac du Bonnet granite, about 15% of the crack advance was along grain boundaries, and 60% was along cleavage planes in feldspars and biotite. The remaining 25% involved multiple cracks through quartz mostly along internal quartz grain boundaries. As shown by Lajtai (1988), cracks that initiate at low stress levels in polymineralic crystalline rocks do not propagate beyond the associated mineral grain unless perhaps there are similar grains in contact. For a randomly distributed mineral fabric, mineral types requiring higher stress levels to initiate cracks will control the propagation and coalescence of cracks formed around weaker minerals. In other words, the stronger minerals increase the resistance to fracture growth, and strongly influence the stress level at which isolated cracks at the mineral scale may coalesce into larger connected fractures. The upper bound uniaxial compressive stress required to fracture the strongest minerals in Figure 21 is only slightly lower than the long-term strength value determined from uniaxial compressive tests on relatively undamaged core specimens. These findings suggest that, in polymineralic rocks, variation in properties of the different mineral grains increases resistance to fracturing. Consequently, higher loads are required to overcome this effect than would be necessary in a continuous homogeneous isotropic linear elastic material shown in Figure 19.

Shen and Stephansson (1996) investigated fracture initiation and coalescence in the immediate vicinity of a DGR tunnel and deposition hole based on the Swedish KBS-3V design in crystalline rock. The study used the boundary element method incorporating a fracture propagation criterion based on the Displacement Discontinuity Method (DDM) to assess a range of loading conditions associated with excavation, swelling pressure, thermal loading, and glaciation. For a more detailed discussion of the approach used in this modelling effort, the interested reader is referred to the original report.

Key results from Shen and Stephansson (1996) related to rock fracture are summarized in Figure 22. For a single 1 m long cohesionless fracture with a friction angle of 30°, the following observations were made:

- No new fracturing initiates until shear displacement occurs on the initial fracture
- For low stress ratios ($\sigma_3/\sigma_1 \leq 0.05$), extensile fracture propagation dominates, initiating from the original fracture tips towards the σ_1 direction. This is a stable process with the wing cracks extending to about the same length as the original crack.
- Once the extensile crack forms and stabilizes, a shear fracture initiates at the tip of the original fracture and grows unstably until it intersects a geological boundary or other feature that restricts its growth. These shear fractures are oriented at about 20° to the maximum principal stress.
- For stress ratios in the range of 0.1 to 0.15, the extensile fractures extend only a short distance before shear rupture occurs, arresting the extensile fracture. The shear fractures in this range of stress ratios are between 25 and 30° to the maximum principal stress direction.

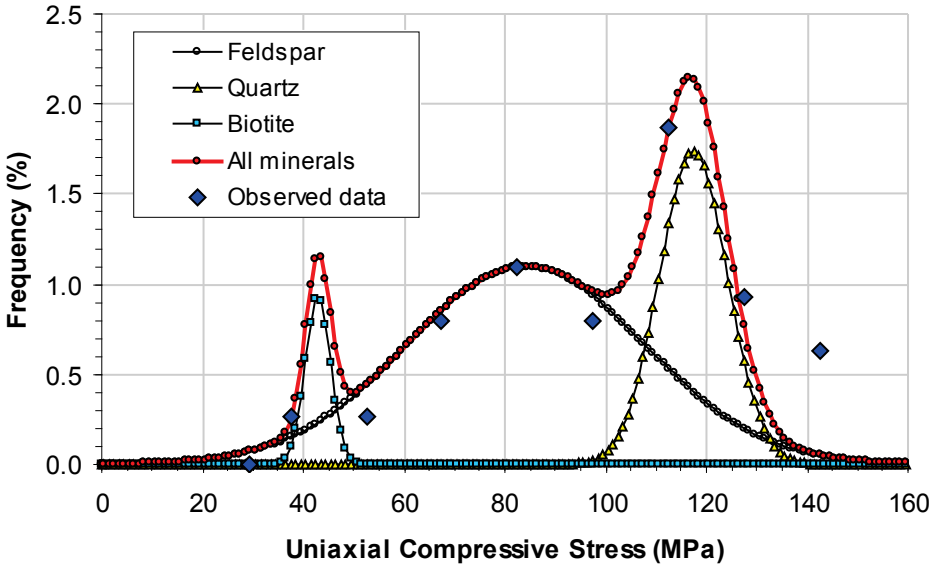

Figure 20: Estimated Frequency Distributions for Crack Initiation in Three Main Constituent Minerals of Lac du Bonnet Granite Weighted to the Percent Occurrence of Each Mineral.

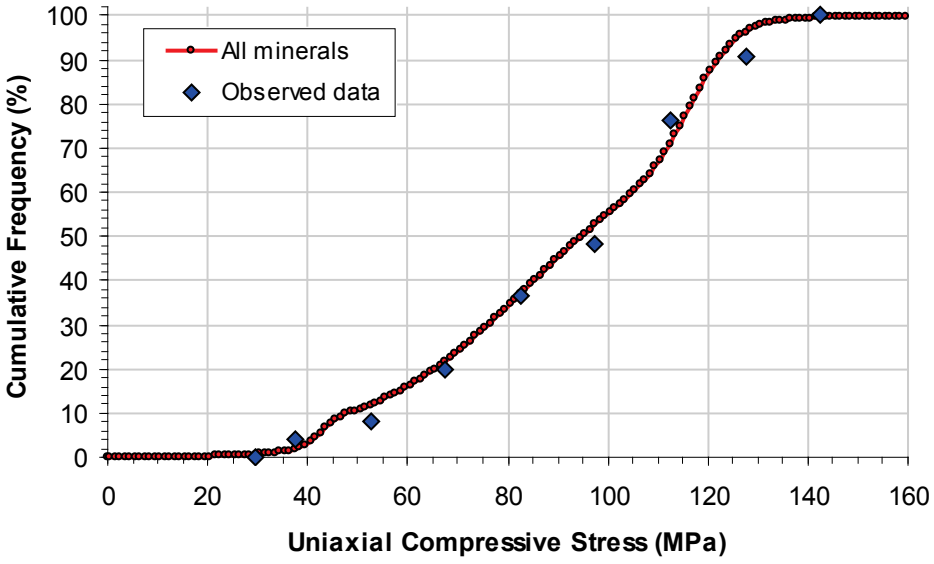

Figure 21: Estimated Cumulative Frequency Distribution for Crack Initiation in Constituent Minerals of Lac du Bonnet Granite Weighted to the Percent Occurrence of Each Mineral.

- At a stress ratio of 0.2, no extensile fractures develop. Shear fractures at this stress ratio initiate only under high applied load, and extend under increasing load in a stable manner until the load is increased beyond a critical threshold. The shear fracture propagates at 30° to the maximum principal stress.
- For stress ratios larger than 0.2, no fracture initiation or propagation of any type was observed up to a maximum principal stress value of 200 MPa.
- The angle of the initial fracture relative to the maximum applied stress strongly influenced the stress at which rupture occurred. An angle of about 30° between the initial fracture and the maximum principal stress produced the lowest fracture initiation stresses.

These results indicate that, in order for extensile or shear fractures to initiate and propagate from an existing fracture, the Mohr circle representing the stress state must exceed the envelope in Figure 22 associated with slip on the existing fracture, and intersect one of the other envelopes. Note that with the exception of the envelope for slip along the existing fracture, the other envelopes terminate at relatively low values of effective normal stress based on the work of Shen and Stephansson (1996). However, a broader range of testing scenarios may offer additional insight about termination of these envelopes. The envelope for fracture slip therefore provides a useful criterion to assess the likelihood of new fracturing or remobilization of existing fractures.

The boundary element modelling performed by Shen and Stephansson (1996) can be approximated from LEFM formulae provided by Kemeny and Cook (1991) based on the conceptual model shown in Figure 23b. In this model, there are three linear envelopes associated with (a) slip along an infinitely long fracture plane, (b) initiation of an extensile wing crack, and (c) initiation of a Mode II (shear) fracture (Figure 23a). The relevant formulae for each threshold are given in Figure 23a, with the following parameters: normal stress (N), shear stress (T), friction angle (ϕ), initial fracture length ($L=2l$), Mode I fracture toughness (K_{IC}), Mode II fracture toughness (K_{IIC}), and the angle between minimum principal stress and initial crack (β). Additional parameters required to assess the shear stress required to extend a wing crack once initiated (Figure 23b) include the extensile wing crack length (a) and minimum in-plane principal stress (σ_2).

Based on the relations in Figure 23a, the shear stress required to cause fracture slip represents a lower bound condition for the initiation or extension of Mode I or Mode II cracks from the initial crack. Extensile wing crack initiation occurs at a slightly higher shear stress level than that required to cause slip on an existing fracture plane. As shown in Figure 23b, at zero or very low confining stress, the wing crack will develop to a certain length under the shear stress causing initiation, then increasing shear stress is required to extend the wing crack. For higher confining stress, the wing crack length at initiation is negligible without increasing shear stress. Once the shear stress reaches the threshold required for shear crack extension, the wing crack ceases to grow and shear crack extension begins. As shown in Figure 23b, the length of the extensile wing crack at the point where shear crack extension begins is controlled to a large extent by the value of the in-plane minimum principal stress. For the rock properties used in this example (same as in Figure 22a), wing crack growth is suppressed completely beyond a confining stress of about 6.3 MPa. This finding is consistent with the results from Shen and Stephansson (1996) shown in Figure 22a. Although the slope of the lines in Figures 22a and 23a differ slightly, the general fracturing behaviour is the same.

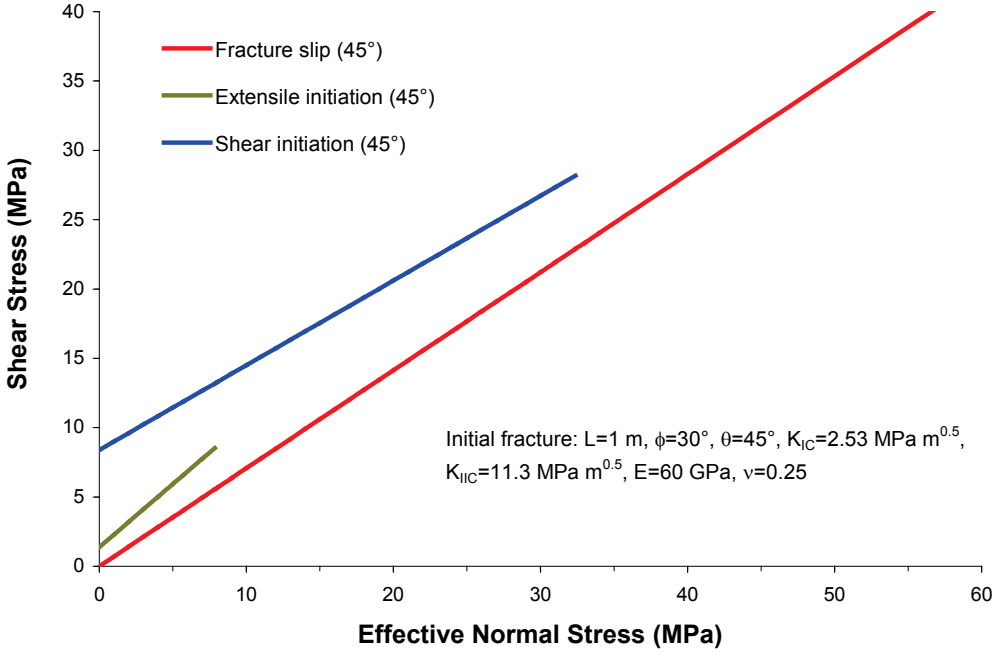

(a)

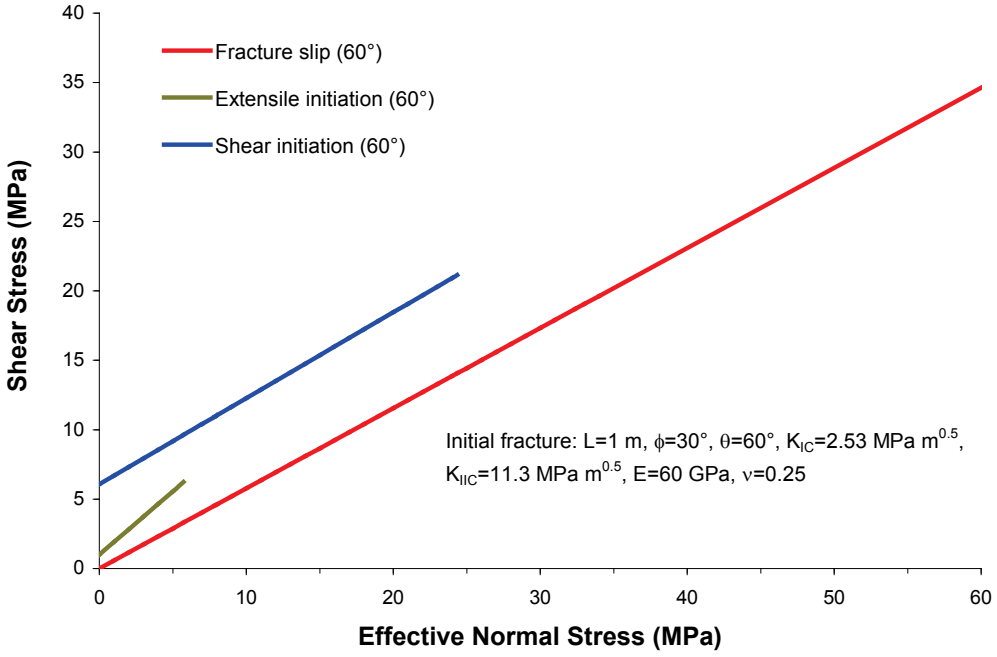

(b)

Figure 22: Mohr Envelopes for Slip on an Existing Fracture (Red), Initiation of Mode I Extensile Cracks (Olive), and Initiation of Mode II Shear Cracks (Blue). The Initial Fracture is Oriented at (a) 45° to the Maximum Applied Stress, and (b) 30° to the Maximum Applied Stress.

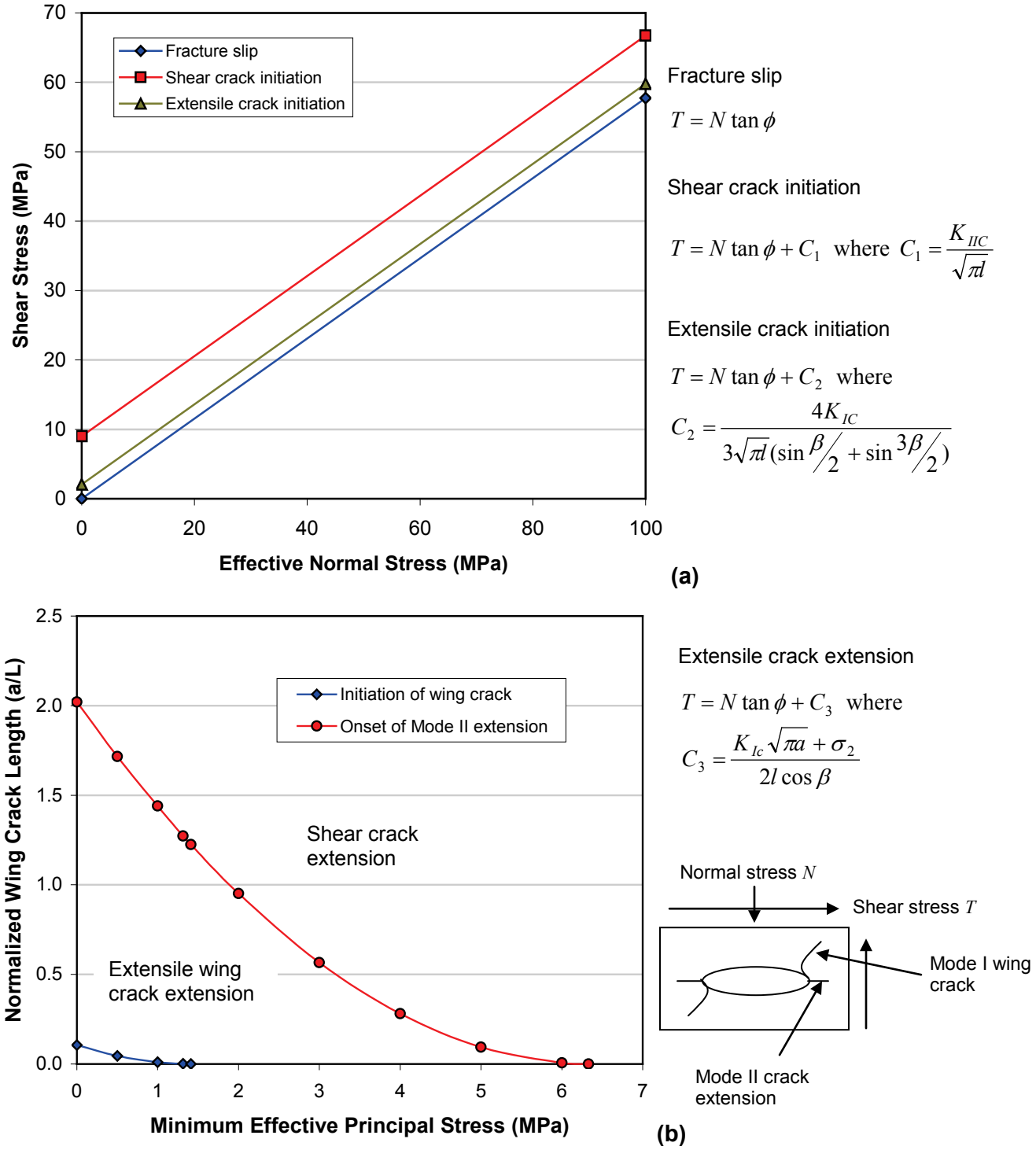

Figure 23: Thresholds Associated with (a) Slip on an Existing Fracture, Initiation of Extensile Cracks, and Initiation of Mode II Shear Cracks; and (b) Extensile Wing Crack Length at Initiation of Extensile and Shear Cracks (Based on Kemeny and Cook 1991). The Conceptual Fracture Model Associated with this Work is Shown in the Lower Right Hand Corner of the Figure. Rock Properties are the Same as Shown in Figure 22(a).

On the basis of the analysis details summarized above, it appears that significant extensile fracture propagation is improbable in a compressive stress field without an additional driving force to create tensile stresses at the fracture tip. As discussed in Section 3.1.1, pore pressure generated in fluid-filled pores or cracks will reduce the effective compressive stresses in the rock and the normal stress acting on a water-filled fracture. Increased pore pressure will also increase the stress intensity factor at the crack tip as per Equation 9. Therefore, situations in which high pore pressures may develop are of particular interest in terms of fracture propagation.

Rock fracturing induced by increasing pore pressure is referred to as hydraulic fracturing. There are two common criteria for hydraulic fracturing under ambient temperature conditions (Chandler 2001). The first involves the pore pressure exceeding the sum of the minimum principal stress and the tensile strength of the rock mass, given as follows:

$$u \geq \frac{(\sigma_3 + \sigma_t)}{\alpha} \tag{11}$$

The second criterion has the stress intensity factor in an existing fracture exceeding the fracture toughness, rewritten in terms of pore pressure as follows:

$$u \geq \sigma_3 + \frac{K_{Ic}}{\sqrt{\pi c}} \tag{12}$$

In both cases, it is assumed that a fracture will propagate in the plane orthogonal to the minimum principal stress.

Based on thermo-hydro-mechanical analysis, Selvaduri and Nguyen (1995) postulated that it is possible for horizontal fractures to propagate near a repository as a result of thermally-induced pore pressures, assuming zero tensile strength for the rock mass. Detournay and Berchenko (2001) conducted similar analyses and concluded that it is unlikely that the minimum effective stress would become tensile as a result of increased pore pressure, based on the URL scenario for in situ stresses and rock properties. Assuming that a situation with pore pressure greater than the minimum compressive stress (i.e., natural hydraulic fracturing) were to exist, it was shown that a fracture would propagate unstably at a velocity governed by the rate of water inflow from the rock to the fracture as long as the thermal, hydraulic and mechanical boundary conditions remained constant over the region through which the fracture propagates (Chandler 2001). This finding suggests that prevention of natural hydraulic fracturing through site selection and engineering design of a repository should be priorities.

For hydraulic fracture initiation at the periphery of a cylindrical opening oriented parallel to the intermediate principal stress, several solutions exist for the fracture breakdown pressure P_c depending on whether or not the fluid penetrates the rock during injection (Thompson et al. 2002). For a fluid that does not penetrate the pores of the rock during cavity pressurization, the fracture breakdown pressure is given by:

$$P_c \geq 3\sigma_3 - \sigma_1 - u + \sigma_t \tag{13}$$

where σ_1 and σ_3 are the maximum and minimum principal stresses, respectively, u is the pore pressure in the rock, and σ_t is the tensile strength of the rock. For a fully-penetrating fluid, the fracture breakdown pressure is given by:

$$P_c \geq \frac{3\sigma_3 - \sigma_1 - u + \sigma_t}{2 - \alpha\left(\frac{1-2\nu}{1+2\nu}\right)} \tag{14}$$

where α is the Biot coefficient. Other solutions for fracture breakdown pressure include a linear elastic fracture mechanics treatment of the problem, and a point stress model. Details of these techniques are provided by Thompson et al. (2002). Other equations can be derived for non-circular holes subjected to internal pressure based on linear elasticity theory.

Chandler (2001) points out that some key rock properties such as drained bulk modulus are stress-dependent and are therefore nonlinear. This translates into nonlinearity in other properties such as the Biot coefficient. These effects are generally ignored in assessing hydraulic fracturing potential, but may affect the results of such analysis. Nonlinearity in rock properties is not considered in this report.

3.2.2 Shear Fracturing

Shear fracturing occurs as a result of shear stresses that exceed the shear strength of the rock mass. On the macro-scale, different types of faults are possible depending on the relative orientations and magnitudes of the three principal stresses (Engelder 1993). For a situation with the maximum principal stress vertical, normal faulting is possible, with the strike of the fault plane coincident with the intermediate principal stress direction. For situations with the maximum principal stress horizontal, a strike-slip regime is possible where the intermediate principal stress is vertical, and a thrust fault regime is possible where the minimum principal stress is vertical.

As shown in Sections 2.2.4 and 2.3.4, it is likely that the ambient stress conditions in both the crystalline rock of the Canadian Shield and the sedimentary rock of the Michigan Basin are characteristic of a thrust fault regime, with the minimum principal stress vertical and close to lithostatic. The likelihood of large-scale shear failure leading to thrusting depends on the effective stress state relative to the strength envelope for the rock mass as described in Section 3.1. With the exception of tensile failure, contact between the Mohr circle and the Mohr strength envelope indicates the onset of shear failure. A requirement for shear failure is therefore a non-isotropic stress state (i.e., a difference between the effective maximum and minimum principal stresses) sufficient to intersect the Mohr envelope.

In a homogeneous isotropic material, shear failure will occur along a preferentially oriented plane. The angle of this plane can be derived from the Hoek and Brown (1980) failure envelope parameters. The effective normal and shear stresses (σ and τ, respectively) along this plane are defined in terms of the effective principal stresses σ_1 and σ_3, and Hoek-Brown parameters m and σ_c, (s is taken to be 1) by the following equations:

$$\tau = (\sigma - \sigma_3)\sqrt{1 + \frac{m\sigma_c}{4\tau_m}} \tag{15}$$

and

$$\sigma = \sigma_3 + \frac{\tau_m^2}{\tau_m + \frac{m\sigma_c}{8}} \tag{16}$$

where $\tau_m = 0.5(\sigma_1 - \sigma_3)$.

The angle β between the failure plane and the maximum principal stress direction is determined from the Mohr circle construction, and is given by:

$$\sin(2\beta) = \frac{\tau}{\tau_m} \tag{17}$$

In materials containing a defined weak plane or discontinuity, shearing will occur along the weak plane under certain loading conditions defined by:

$$\sigma_1 - \sigma_3 \geq \frac{2(c + \sigma_3 \tan\phi)}{(1 - \tan\phi \tan\theta)\sin(2\theta)} \tag{18}$$

where c and ϕ are the cohesive strength and friction angle of the rock surfaces, respectively, and θ is the angle between the optimally oriented weak plane and the minimum principal stress. Martin and Chandler (1994) used the Mohr Coulomb definition of rock strength to define the in situ long-term strength of a material.

The orientation of the plane (relative to the maximum principal stress) requiring the minimum shear stress to slip is given by:

$$\theta = 45° + \frac{\phi}{2} \tag{19}$$

Although the theoretical angle of minimum shear resistance for both the Hoek-Brown and Mohr-Coulomb failure conditions are similar, the Mohr-Coulomb angle depends only on friction angle whereas the Hoek-Brown angle is dependent upon both stress and failure parameters. Fracture Zone 2 and associated splays at the URL are excellent examples of thrust faults developed along weaker biotite-rich layers in the crystalline rock mass. Pre-existing faults of this type will in general act as preferred weak planes for future displacement in the event of increasing deviatoric stresses (Fairhurst et al. 1996). Shear displacement along Fracture Zone 2 at the URL relieved shear stresses and perturbed the in situ stress state, resulting in a rotation of the maximum principal stress from 0° to about 11° from horizontal at the 420 Level some 150 m below. Such perturbations to the in situ stress field should be expected in the vicinity of faults and major fractures/joints, and may present complications for tunnel design (Read et al. 1997a).

Other approaches are required to account for naturally occurring anisotropy in rocks such as slate. Hoek and Brown (1980) present one method for characterizing the variation in rock strength with orientation of the applied stress. Such methods are likely applicable to bedded shales and other sedimentary rocks that exhibit strong strength anisotropy. Hoek and Brown (1980) also demonstrate the influence of multiple discontinuities on rock shear strength. As the

number of joint sets increases, the overall rock strength decreases, but becomes more uniform. For two sets of discontinuities, the variability in rock shear strength with loading direction can be large depending on the strength properties of the discontinuities. Rock mass anisotropy and the effects of multiple joint sets on rock mass response are not considered in the analyses in this report.

In each of the above cases, the effect of increasing pore pressure is to reduce the mean stress, effectively shifting the Mohr circle to the left, closer to the strength envelope. Therefore, significant changes in pore pressure due to mechanical loading or heating are important considerations in terms of the expected behaviour of existing discontinuities, and the likelihood of generating new shear fractures or faults.

3.2.3 Other Failure Mechanisms

In addition to extensile and shear fracturing, other failure mechanisms are possible. Ductile cataclastic failure is possible at very high compressive stresses. The brittle-ductile transition is expressed as a line through the origin with a slope of 3.4 in principal stress space, or 0.89 in shear – normal stress space (Hoek and Brown 1980). Where this line intersects the strength envelope, failure is assumed to switch from brittle to ductile. In addition, for very porous rocks, crushing via collapse of the pore structure is possible at high mean stress values. These modes of failure are generally not applicable to the rock types and stress conditions in question, but should be kept in mind during specific analyses.

3.3 CRITICAL FEATURES, EVENTS AND PROCESSES

Based on the proposed repository designs and construction details provided various design specifications, the critical features, events and processes related to large-scale fracturing and faulting are summarized in this section.

3.3.1 Excavation Design

The geometry, spacing and orientation of underground openings affect the nature of stress concentrations around the openings. For elliptical openings aligned with a principal stress component in a linear elastic medium with horizontal and vertical principal in-plane stresses σ_h and σ_v, the maximum and minimum tangential stress concentrations σ_θ are related to the principal in-plane stresses as follows:

$$\sigma_\theta = \left(1 + \frac{2b}{a}\right)\sigma_h - \sigma_v \text{ at the centre of the crown and invert,} \quad (20)$$

and

$$\sigma_\theta = \left(1 + \frac{2a}{b}\right)\sigma_v - \sigma_h \text{ at mid-height of the sidewalls} \quad (21)$$

where a is half the length of the horizontal major axis and b is half the length of the vertical major axis of the ellipse (Jaeger and Cook 1979). Depending on the aspect ratio of the ellipse

and the in situ stress ratio, stresses exceeding the tensile and compressive strengths of the rock mass may develop at the tunnel periphery (Read 1997). The near-field stress concentrations around one opening may affect the stress field around adjacent openings if the spacing between openings is small enough.

Where the option exists, tunnels are commonly oriented parallel to the maximum principal stress to reduce the stress concentrations around the completed rooms. However, this approach presumes that the principal stresses are vertical and horizontal. At the URL, none of the principal stresses is vertical or horizontal. In this circumstance, it was possible to construct stable openings using elliptical or oval-like tunnel cross-sections (Read and Chandler 1997), but the major axis of the ellipse or oval was inclined to align with the major principal stress. This may not be a practical solution in an actual repository setting. Although excavation of these inclined elliptical openings was shown to be feasible, it may be an impractical shape for the equipment types that travel along the tunnels. The implications of ignoring this misalignment between the ellipse axes and the principal stress is that tangential stress concentrations higher than those predicted by Equation 20 are possible depending on the shape of the opening, and on the degree of misalignment between the cross-sectional axes and the principal stresses. For circular openings in an anisotropic stress field, the stress concentrations around the opening are more severe than for an ellipse or oval. However, owing to the axisymmetric geometry, circular openings are insensitive to inclination of the stress field in the plane orthogonal to the tunnel axis.

A consequence of orienting tunnels parallel to the maximum principal stress direction is the increased likelihood of strength degradation around the tunnel periphery due to three-dimensional stress path effects ahead of the advancing tunnel face (Read et al. 1998). Possible considerations to mitigate these effects include pilot-and-slash excavation sequencing, and altering the shape of the tunnel face (Read 1994). Pilot-and-slash trials at the URL did not provide clear evidence of a reduction in near-field effects, but stress conditions at other sites may be more conducive to this approach. In general, stress perturbations around single openings resulting from excavation tend to be near-field effects unless tunnels are closely spaced. For elliptical tunnels with a 3.65 m semi-major axis, spacing of 30 m between adjacent tunnel centrelines is expected to reduce the influence of one excavation on the other to a minimal level.

Close to the tunnel periphery, the principal stresses are oriented tangential and orthogonal to the boundary. Therefore, Mode I microcracks and small-scale fractures are expected to be oriented tangentially in a compressive stress field (possibly leading to spalling), or radially in areas of tensile stress. Small-scale near-field Mode II fracturing is expected in areas of high compressive tangential stress close to the periphery where confining stress is close to zero. These near-field microcracks and small-scale fractures cannot progress far from an underground opening in a compressive stress field because the minimum principal stress increases to far-field conditions within a short distance from the opening. Therefore they are not expected to contribute to large-scale fracturing of the rock mass without high sustained pore pressure within the fracture. Analyses in Section 4 of the report support this assumption.

The length of time that an unsupported opening is expected to remain stable, and the type of tunnel support required to maintain stability, are related to the maximum unsupported span and the rock mass classification using either the CSIR Geomechanics Classification (Bieniawski 1976) or the Norwegian Geotechnical Institute (NGI) Tunnel Quality Rating (Q) (Barton et al. 1974). The unsupported span is either the maximum distance between the face and start of

ground support, or the tunnel width, whichever is greater. Based on the rock mass rating (RMR) values for the potential host rocks and an assumed 10 m unsupported span, stand-up times are expected to range from about 1 to 6 months for Good Rock (shale and limestone) up to about 2 years for granite. Experience at the URL in sparsely fractured granite suggests that stand-up time may be indefinite without the influence of existing joint sets. Based on the Q values for the potential host rocks, the maximum spans for which no support is required in Queenston Formation shale, Lindsay Formation limestone, and Lac du Bonnet granite are about 6, 9, and 11 m, respectively. These estimates suggest that, depending on the DGR design, tunnel support may be required to keep the unsupported span to within tolerable levels for the length of time required to place UFCs in placement rooms.

3.3.2 Excavation Method

The excavation methods proposed for the various placement room options include drill-and-blast for the elliptical openings and tunnel boring for the circular openings (both horizontal openings and vertical boreholes). Experience with both the drill-and-blast method and mechanical excavation in Canada during the Mine-by Experiment (Read and Martin 1996) and the Excavation Stability Study (Read et al. 1997a) at the URL, and in Sweden during the ZEDEX experiment (Olsson et al. 1996) suggests that the excavation-damaged zone (EDZ) around underground excavations in low stress environments is less for a non-explosive excavation technique given identical tunnel shapes. For higher stress environments, the difference in the EDZ is less distinct owing to the influence of stress-induced damage.

In addition to the elimination of dynamic stress and gas pressure effects that can destroy rock cohesion, the smoother geometry of bored openings compared to blasted openings[5] also reduces the likelihood of localized stress concentrations associated with irregular geometry. Hence bored openings are expected to sustain higher compressive stresses at the tunnel periphery compared to blasted tunnels. Likewise, for tunnels expected to experience localized tensile stress concentrations at the tunnel periphery, mechanical excavation is less likely to induce discrete macro-scale tensile fracturing compared to blasting (Read et al. 1997a). The use of pilot-and-slash excavation sequencing may eliminate some of the three-dimensional stress path effects associated with excavation in a high horizontal stress field, but results from the URL have been inconclusive in this regard.

3.3.3 Heat Generation

Heat generation due to UFC placement in underground openings will cause the overall temperature of the repository horizon to increase with time. This increase in temperature ΔT will cause thermal expansion of the rock mass and increase the isotropic component of stress σ_i in the horizontal plane in accordance with the following relation:

$$\sigma_i = \alpha_t \Delta T \left(\frac{E}{1-\nu} \right) \tag{22}$$

[5] Drill-and-blast excavations require each subsequent round to be drilled at a slight look-out angle to create a telescope-like profile in order to maintain the average tunnel dimensions.

where α_t is the coefficient of linear thermal expansion, E is Young's modulus and ν is Poisson's ratio. This relation assumes that there is no increase in vertical stress, which may underestimate the actual thermally-induced stress. Equation 22 illustrates that the stress change is directly proportional to Young's modulus, which can vary with mean or confining stress (Chandler 2001). In situations where the stress distribution around an underground opening is not uniform, the Young's modulus may vary considerably between regions of increased compression versus regions of unloading. Therefore the superposition of thermally-induced stresses may exaggerate the difference in these stress concentrations.

The Heated Failure Tests at the URL (Read et al. 1997) illustrated the influence of heating on the development of compressive failure by way of 'breakouts' in a series of 600-mm-diameter vertical boreholes. The results of this experiment effectively demonstrated the effects of thermal-mechanical stress path on the excavation-induced damage around vertical cylindrical openings in granite.

As discussed in Section 3.1.1, heating may also induce significant pore pressure increases in the rock mass as a result of thermo-poroelastic effects. If these pore pressures are high enough to overcome the minimum principal stress and the tensile strength of the rock mass, then extensile fracturing is expected. Thermally-generated pore pressures measured in the rock around the Heated Failure Tests were on the order of 1.5 MPa for a temperature increase of 100°C. In the Thermal-Hydraulic Experiment (Martino and Chandler 1999), a temperature increase of about 12°C produced local pore pressures of about 3 MPa in a small-diameter borehole. The difference in these responses is likely related to abundance of drainage locations (other open boreholes) in the Heated Failure Tests and the lack of nearby open boreholes in the Thermal-Hydraulic Experiment. In situ at the URL, the undrained pore pressure increases at a rate of about 400 kPa/°C.

Heating may also reduce the shear modulus of the rock mass by increasing the crack volume through differential expansion of mineral grains. This is more apparent in unstressed rock that has already experienced some degree of damage. Laboratory studies have shown that intact rock under zero stress conditions is unaffected by heating up to temperatures in excess of 100ºC. Thermal expansion may lead to localized spalling or may weaken the rock mass in the vicinity of underground openings and increase connected permeability on the micro-scale. In a tensile regime, it may reduce tensile strength of the rock mass through micro-crack development (Read 1994). These effects alone are not expected to result in large-scale fracturing.

Heating was also shown to cause desiccation of clay-based buffer material in the Buffer-Container Experiment (Chandler et al. 1992). These same types of effects could be expected in clay shale. The author's personal experience from the Oldman River Dam test tunnel in Alberta excavated in Cretaceous claystone and siltstones demonstrated the deleterious effects of desiccation resulting from ventilation of the tunnel. This condition required shotcrete application and pattern bolting of the tunnel to prevent slabbing-type failures from the tunnel crown. Exposure of the rock mass to freezing temperatures also has the potential to cause deterioration of the rock mass near the tunnel periphery.

Stress corrosion cracking at subcritical stress levels has also been shown to be affected by temperature (Wilkins et al. 1984). Immersion of a sample of Lac du Bonnet granite in water at 20°C reduced the fracture toughness by 13% relative to a dry sample at the same temperature. Increasing the sample temperature to 80°C resulted in an additional 10% drop in fracture

toughness in samples immersed in either freshwater or brine. These results suggest that the thresholds for fracture initiation and propagation may decline to some extent due to changes in the in situ thermal or hydraulic conditions (Martin et al. 1994). The limiting stress intensity factor for subcritical crack growth has been shown to be about 50% of the fracture toughness for Lac du Bonnet granite (Cook 1986; Cruden 1983).

3.3.4 Groundwater Table

The location of the groundwater table and the pore pressure profile with depth are important site characteristics in determining the potential for large-scale fracturing. Perched water tables or over-pressured horizons may create locally unique conditions in layered systems such as the sedimentary stratigraphy of the Michigan Basin. The pore pressure gradient is also affected by the fluid density, which for saline conditions may significantly exceed that of fresh water.

If there is interconnection between horizons of different salinity, or if fresh water is introduced into smectite-rich marine shales, there is a possibility of swelling of the shale and associated deterioration of the shale strength. This phenomenon may create near-field fracturing and rock failure if not prevented or controlled. Likewise, swelling of clay materials in faults and fractures can generate high swelling pressures and result in significant strength loss (Brady and Brown 1985). Cycles of wetting and drying of the rock mass may lead to slaking in some materials, resulting in deterioration of the rock mass.

3.3.5 Chemical Alteration of Rock

Chemical alteration of the rock mass may occur as a result of circulating fluids in permeable zones such as faults and cataclastic zones. This alteration may degrade the rock to clay-like material with relatively low strength. Although this is typically a very slow process measured in geological time, it may result in decreasing shear strength on existing faults and fracture systems over long periods of time. Depending on stress conditions over the same time period, it may be possible to reactivate existing fault and fracture systems. The change in permeability that accompanies severe alteration may also contribute to changes in pore pressure distribution and potential hydraulic pathways within the rock mass (e.g., channelized groundwater flow within fracture Zone 2 at the URL). These effects are not anticipated to lead to new large-scale fracturing remote from existing faults or fractures, and may be remediated through the use of grouting of major fractures and faults to reduce hydraulic conductivity and water flow.

3.3.6 Glaciation and Permafrost

Glaciation may impose several changes to the in situ conditions. It applies a surcharge to the ground surface, effectively increasing the vertical stress, and to a lesser extent, the horizontal stresses at depth. Depending on the thickness of the ice, the change in stresses may alter the environment enough to promote reactivation of preferentially oriented fractures. In a thrust fault regime, where the vertical stress is the minimum principal stress, the induced stress changes are likely to reduce the deviatoric stress, and create more isotropic conditions.

Depending on the shape of the glacial front, the leading edge of the advancing glacial ice may generate high shear stresses, and possibly promote near-surface fracturing (similar to bearing-type failure near the edge of a footing). This effect is attenuated with depth as the σ_v/σ_H stress

ratio decreases below the applied load. Near-surface freezing and eventual thawing may help to disaggregate the rock mass. Depending on the rate of advance of the glacial ice, excess pore pressures may also be generated. These effects are considered near-surface effects and are not analyzed in this report. However, confirmatory analysis would help quantify the depth to which this effect may extend.

Glacial ice also imposes a sub-zero temperature boundary at surface, and will cool the rock mass with time, the rate depending on the thermal conductivity of the rock mass. This effect will reduce the thermally-induced stresses caused by heating of the repository, and will help to reduce thermally-generated pore pressure. Cooling of the rock mass has not been accounted for in the analyses in this report.

3.3.7 Discontinuities

Discontinuities in the rock mass may act to concentrate stresses or to perturb the in situ stress field (Martin et al. 1994; Martin and Chandler 1993). Movement along these features may re-orient the stresses for a considerable distance from the feature. Existing faults are more likely to be reactivated than new fractures forming if the fault regime does not change (Fairhurst et al 1996). Glaciation or erosion of the ground surface are the main factors in significantly altering the vertical in situ stress, possibly changing or exacerbating the thrust fault regime. Pore pressures generated by heating may also affect the effective stress state and stability of existing fractures and faults. Although the Biot coefficient in connected discontinuities is generally higher than in low porosity rock typical of a repository horizon, drainage within the discontinuities reduces the likelihood of excess pore pressure development. Only the intact low-permeability granite between discontinuities is expected to be potentially affected by thermally-induced pore pressures.

Large-scale shear movements along faults may create unique stress domains at a site (Martin 1990). This movement may promote other types of fracturing such as extensile jointing due to flexure of the overlying displaced rock volume (Martin et al. 1994). Shear faults of this type are expected to act as boundaries across which extensile cracks will not penetrate due to the lack of stress relief below such faults (Fairhurst et al. 1996).

3.3.8 Material Properties Contrast

In layered systems, such as the sedimentary sequence in the Michigan Basin, stress changes within the system caused by heating or glaciation may create or contribute to a non-uniform stress distribution with depth if the layers have contrasting properties, specifically Young's modulus and Poisson's ratio. Differential straining of adjacent rock layers may result in relative shear displacement along the interface between layers, or extensile cracking in the stiffer layer. This type of phenomenon is a concern in the petroleum industry where steam-assisted processes are used to extract heavy oil or bitumen from formations underlying shale caprocks. Depending on the strain localization that occurs along the interface, it is possible to generate shear fractures along the interface and/or along inclined heterolithic strata (IHS) within the shale.

In crystalline rock, the presence of biotite-rich layers in the rock mass may represent a contrast in strength properties. Xenolithic layers in the Lac du Bonnet batholith at the URL have acted as preferred weak planes along which shearing has occurred (Everitt and Lajtai 2004).

Likewise, anisotropic strength and deformation properties are common to both crystalline and sedimentary rocks, particularly shales. These property contrasts affect the initiation and propagation of fractures within the rock mass. These effects should be considered in detailed analyses of DGR options. They are not taken into account in this report.

3.3.9 Seismicity

Seismicity is a concern primarily from the point of view of creating new fractures or reactivating faults that may alter the hydraulic pathways to surface. Provided that seismically active faults are not in the immediate vicinity of underground openings, the risk to safety from earthquake damage underground during the construction and operation of a DGR is not considered significant (Ates et al. 1994). Seismicity may occur naturally due to tectonic activity, or as a result of effective stress changes within the rock mass. Dynamic stresses generated by seismic events may alter the stress state around critical features enough to generate fracturing or localized rock failure near openings, or to reactivate existing faults and fracture systems.

The seismic potential in much of the Canadian Shield is very low compared to other parts of North America (AECL 1994). Seismic zoning for much of the Canadian Shield, based on seismic ground motion values with 10% probability of exceedence over a 50 year period, shows much of the Canadian Shield as negligible risk in relation to surface structures. A probabilistic seismic hazard evaluation of the Canadian Shield in northwest Ontario (Atkinson and McGuire, 1993) indicated that, as long as no seismically active fault was within 50 m of a disposal vault, the annual probability of an earthquake capable of causing fracturing that would reach the disposal rooms of the vault was less than $5x10^{-7}$. This probability was reduced to effectively zero for offset distances of 1000 m for a 2 km long active fault, and 200 m for a 5 km long active fault, respectively.

In southern Ontario, seismicity is weak and largely limited to the Niagara Megablock; the Bruce Megablock is virtually aseismic (Mazurek 2004). On the basis of historic earthquake records and ground motion relations, Adams and Halchuk (2003) provide probabilistic maps of spectral seismic acceleration in Canada. In their analysis, southern Ontario lies in a region where seismic acceleration is less than 0.4 g for an earthquake having a 2% probability of occurrence in the next 50 years. In the Bruce Megablock, the expected acceleration is <0.2 g, which is considered very low (Mazurek 2004). The return period used for this analysis may not be applicable to a DGR, but the general results indicate low seismic risk.

In terms of induced seismicity, Ortlepp (1992) assessed the risk of rockbursting at the URL, and at a hypothetical repository constructed in similar conditions. A rock burst is defined as “the signficant damage caused by a seismic event (i.e., transient energy released by a sudden fracture or failure in the rock mass).” Of the five types of rockbursts (strain-bursting, buckling, pillar or face crushing, shear rupture, and fault-slip), only strain-bursting and fault-slip were considered as possible mechanisms in the Lac du Bonnet granite at the URL; the other three types were considered to have no possibility whatsoever of occurrence. Strain-bursting similar to the spalling observed in the Mine-by test tunnel (Read and Martin 1996) is expected at or very close to the tunnel periphery in some circumstances, particularly if blasting is not used to destress the near-field rock by creating some damage. Fault-slip is not anticipated because of the absence of major faults at depth and the small extraction ratio associated with a typical DGR design. Martin and Chandler (1996) compared the extraction ratio of 0.25 for a DGR to an extraction ratio of 0.6 required to produce rock burst conditions in mines. Ortlepp (1992)

concluded that there is no significant rock burst risk associated with further development of the URL or with the creation and operation of a functional repository in the same environment.

3.3.10 Heave

Heave of the rock mass overlying the repository horizon is expected as a result of heating the rock mass. This displacement tends to be upward near the centre of the repository, with a lateral component towards the edges of the repository. The maximum shear stresses generated by heave are located above the edges of the repository. If there are preferentially oriented weaknesses in the rock mass, areas of shear stress may generate near-surface shear fractures under certain conditions. Heave of the rock mass will also decrease the lateral stresses in the near-surface rock mass to the point where sub-vertical extensile fracturing may occur to some depth. It is inconceivable that these tension cracks would penetrate to the repository level as confining stress increases with depth and with increased temperature near the repository, but in some cases they may provide near-surface connection between isolated groundwater systems where layered stratigraphy exists. Although unlikely for vertical deformation on the order of tens of centimetres, heave at surface may disrupt the natural surface drainage patterns and alter the groundwater system accordingly.

3.3.11 Backfill/Rock Interaction

Clay-based buffer and backfill is expected to swell once saturated, and provide an internal swelling pressure of between 100 kPa and 4 MPa on the periphery of boreholes and placement rooms. The rate of swelling is dependent on water availability which is in turn a function of the rock mass connected permeability and pore pressure distribution. Studies such as the Buffer/Container Experiment (Chandler et al. 1992) and the Isothermal Test (Dixon et al. 2001) have shown that buffer saturation is a slow process, and that reliance on swelling pressure in placement room design is not a conservative assumption. Results from the Mine-by Experiment, the Tunnel Sealing Experiment and the Heated Failure Tests demonstrate clearly that a small confining pressure of 50 kPa is sufficient to prevent ongoing strength degradation through microcracking at or near the tunnel periphery (Read 2003). The weight of buffer and backfill materials alone should be sufficient to prevent further degradation of rock strength below excavations. However, intentional gaps between the rock and buffer/backfill materials in certain borehole placement designs or at the crown of excavations in an in-room design may lead to some degradation of the rock mass before the gaps close. In cases where there is initially no contact pressure by the swelling clay, the beneficial aspects of small confinement for the prevention of rock damage will not be present until the gaps close. Support pressure from backfill was not taken into account in the analyses in this report.

4. ANALYSIS SUPPORTING THE REASONED ARGUMENT

4.1 METHODOLOGY AND CRITERIA

The various DGR options are evaluated in this section with respect to several criteria for fracturing of the rock mass. These criteria have been described in previous sections of this report, but are summarized here for clarity.

The analysis first considers the possible development of large-scale fractures in the far-field rock mass. In this scenario, the likelihood of large-scale fractures initiating remote from the DGR and possibly propagating to intersect the DGR placement rooms or the near-field excavation damaged zone around these rooms is investigated. In the extreme case, the effect of this type of occurrence could be a new hydraulic pathway for contaminant transport away from placed UFCs. This set of analyses is independent of the design of individual DGR placement rooms and therefore considers only far-field rock mass strength criteria and stress conditions.

The selected criteria to assess the direct initiation and propagation of large-scale fracturing in the far-field, including re-mobilization of existing fractures and faults, are as follows:

- Hoek-Brown envelope for long-term in situ strength of the far-field rock mass (see Figure 12). This envelope represents the far-field stress conditions at which the long-term in situ strength of the far-field rock mass is exceeded in the absence of pre-existing large-scale fractures or faults.
- Mohr-Coulomb envelope for slip along pre-existing faults or large-scale fractures in the far-field (see Figures 22 and 23). This envelope represents the far-field stress conditions at which slip along an existing fracture or fault may occur, a pre-cursor to the initiation and propagation of new extensile wing cracks and Mode II shear fractures.

Both these criteria are plotted in shear-normal stress space to compare to Mohr circles depicting various in situ stress states expected following placement of UFCs. Where the Mohr circle intersects one or more of these envelopes, fracturing (or re-mobilization of an existing fracture or fault) is expected. If slip is expected on an existing fracture or fault, further analysis could be undertaken to assess the likelihood of initiation and propagation of new extensile wing cracks or Mode II shear fractures, as per Figure 23 for example. Given the large influence of confining stress on the development and length of extensile fractures, a general criterion based on a ratio of $\sigma_3'/\sigma_1' \leq 0.05$ is used to identify the possible development of long extensile wing cracks from existing fractures or faults.

Following analysis of far-field stress conditions, near-field analysis of the various DGR options is undertaken. This set of analyses considers the possibility of small-scale near-field fracturing around underground openings leading to large-scale fracturing of the far-field rock mass. It should be emphasized that the development of small-scale fractures within the excavation damaged zone is generally anticipated due to in situ stress conditions and/or excavation method. The presence of these small-scale fractures does not in and of itself constitute large-scale fracturing of the rock mass. Although the excavation damaged zone may be relatively continuous along the axis of an underground excavation, it is only a concern as a hydraulic pathway if it connects to a relatively permeable natural fracture system within the rock mass some distance from the excavation. The effects of mechanical and thermal-mechanical loading

on the near-field rock mass are examined for the various DGR options to assess the possible extent and severity of near-field fracturing, and its implications in terms of large-scale fracturing.

The selected criteria to assess the development of small-scale fracturing in the near-field rock mass are as follows:

- Lower bound Hoek-Brown envelope for in situ strength of the near-field rock mass (see Figure 12). This envelope represents the near-field stress conditions at which the in situ strength of the near-field rock mass is exceeded at or very near the tunnel periphery in the absence of existing large-scale fractures or faults. The use of this envelope assumes significant excavation-induced damage has occurred close to the tunnel periphery, resulting in some strength degradation relative to the long-term strength of the far-field rock mass. This criterion identifies the locations around an opening where small-scale fracturing may be expected.
- Mohr-Coulomb envelope for slip along an existing fracture (see Figures 22 and 23). This envelope represents the near-field stress conditions at which slip along a small-scale fracture may occur as a result of changing effective stress conditions around the DGR. This criterion is intended to assess the likelihood of small-scale fractures slipping and acting as drivers for large-scale fracture development.

To simplify the analysis, small-scale near-field fracturing is assumed to occur if the tangential stress at the tunnel periphery is either greater than the compressive strength, or less than the tensile strength, associated with the Hoek-Brown envelope for in situ strength of the near-field rock mass (compression positive). The extent of this small-scale fracturing is assessed using the Hoek-Brown strength ratio (see Equation 3). The extent of possible fracture growth from these small-scale fractures is then assessed using the Mohr-Coulomb envelope for slip along an existing fracture. Assuming that the existing fracture plane is cohesionless and oriented at a critical angle to the minimum principal stress such that the shear stress along the plane is maximized, the critical effective principal stress ratio associated with the Mohr-Coulomb envelope for fracture slip is given by:

$$\frac{\sigma_3'}{\sigma_1'} = \frac{1-\sin(\phi)}{1+\sin(\phi)} \tag{23}$$

where ϕ is the friction angle of the fracture plane.

By comparing this ratio with stress conditions around an underground opening, the extent to which fractures within the excavation damaged zone can propagate under different loading scenarios can be approximated. This analysis does not account for changes in near-field material properties or changes in excavation shape as a result of tunnel instability. However, it provides a preliminary estimate of the maximum distance to which a small-scale fracture in the excavation damaged zone may extend under specific thermal-mechanical loading conditions. This analysis does not account for thermo-poroelastic effects that may generate excess pore pressure at or near the fracture tip; these effects should be examined in more detailed analysis.

4.2 FAR-FIELD ANALYSIS OF A DEEP GEOLOGICAL REPOSITORY

4.2.1 Repository in Crystalline Rock at 500 and 1000 m Depth

The ambient in situ stress conditions at repository levels of 500 and 1000 m in the sparsely-fractured crystalline rock (based on studies at the URL in Canada) are summarized in Table 4 along with estimated stress conditions associated with thermal and glacial loading of the rock mass. For the thermal analysis, two bounding cases were considered: one assuming no increase in vertical stress as a result of heating, and the second assuming a vertical stress change equal to 30% of the thermally-induced horizontal stress change. The rock mass properties used for these analyses included a thermal expansion coefficient α_t=1x10^{-5} (a conservative value), Young's modulus E=65 GPa, and Poisson's ratio ν=0.25. In each case, pore pressure was assumed to follow a hydrostatic trend from surface, with a Biot coefficient α=0.2 used to calculate effective stress.

Table 4: Stresses used in Far-field Analyses of a Repository in Crystalline Rock

Scenario	**Effective Stress Component (MPa)**				
Repository depth =500 m	**$\Delta\sigma_h$'**	**$\Delta\sigma_v$'**	**σ_H'**	**σ_h'**	**σ_v'**
Ambient Stress	-	-	60	44	12
Thermal Stress ($\Delta\sigma_v$=0)	49	0	108	93	12
Thermal Stress ($\Delta\sigma_v$=0.3 $\Delta\sigma_h$)	54	16	114	99	45
Glacial Stress	9	27	69	53	39
Thermal ($\Delta\sigma_v$=0) + Glacial Stress	58	27	117	102	39
Thermal ($\Delta\sigma_v$=0.3 $\Delta\sigma_h$) + Glacial Stress	63	43	123	107	55
Repository depth =1000 m	**$\Delta\sigma_h$'**	**$\Delta\sigma_v$'**	**σ_H'**	**σ_h'**	**σ_v'**
Ambient Stress	-	-	63	47	24
Thermal Stress ($\Delta\sigma_v$=0)	49	0	112	96	24
Thermal Stress ($\Delta\sigma_v$=0.3 $\Delta\sigma_h$)	54	16	117	101	40
Glacial Stress	9	27	72	56	51
Thermal ($\Delta\sigma_v$=0) + Glacial Stress	58	27	121	105	51
Thermal ($\Delta\sigma_v$=0.3 $\Delta\sigma_h$) + Glacial Stress	63	43	126	110	67

Under ambient conditions, the far-field stress ratio σ_3'/σ_1' = 0.20 at 500 m depth and 0.38 at 1000 m depth based on effective stresses. Slip along existing fractures, and hence propagation of new extensile or shear fractures from existing discontinuities in the rock mass, is not possible if the Mohr circle for the ambient in situ effective stress state does not intersect the Mohr-Coulomb envelope for fracture slip. A representative residual friction angle for Lac du Bonnet granite is about ϕ=45° (Read and Martin 1996). The corresponding condition for slip on existing fractures is $\sigma_3'/\sigma_1' \leq 0.17$ for this rock type. As shown in Figure 24, it is improbable that the rock mass at 500 or 1000 m in its ambient state is prone to new extensile or shear fracturing without significant changes in the in situ stress or pore pressure conditions. This is reflected in the fact that the Mohr circles for the in situ effective stress states do not intersect the critical strength envelopes for crystalline rock. The Mohr circle for 1000 m depth is further from the strength envelopes than that for 500 m depth, and is therefore a more stable condition.

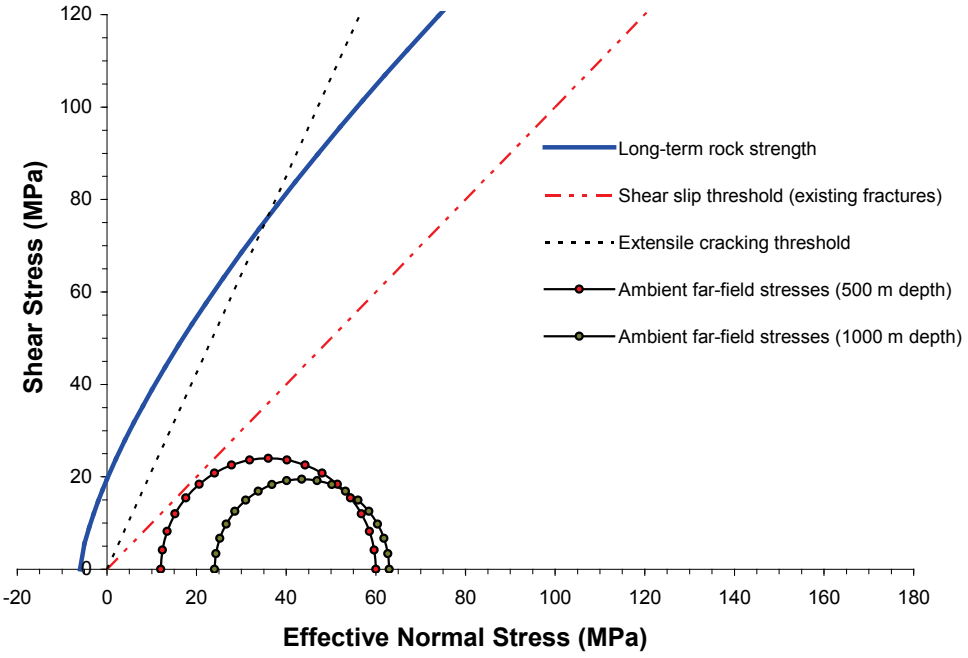

Figure 24: Comparison of Ambient Far-Field In Situ Stress States at 500 and 1000 m Depth in Crystalline Rock to Relevant Strength Envelopes.

To account for the effects of thermally-induced stresses on the in situ stress states at 500 and 1000 m depth, the central part of the plane of the repository can be considered as a heated plate with constraints on lateral displacement. Thermal modelling of a repository in crystalline rock (CTECH 2002) predicts a maximum temperature rise of about 56°C in the rock mass near the placement rooms. Based on Equation 22, the incremental horizontal stress associated with a temperature rise of 56°C is about 49 MPa, assuming no increase in vertical stress. Adding this value to the pre-existing horizontal stresses, the far-field effective stress ratio σ_3'/σ_1' = 0.11 at 500 m depth and 0.22 at 1000 m depth. These stress ratios are insufficient to initiate new fracturing in the absence of existing fractures or faults. The stress ratio at 500 m indicates that existing fractures at this depth may be re-mobilized, assuming a residual friction angle of ϕ=45° (Figure 25). The Mohr circle associated with the stress state at 500 m intersects the Mohr-Coulomb envelope for slip on existing fractures, and depending on the assumed values for fracture toughness, may lead to shear extension of critically-oriented fractures or faults. Owing to the high confining stress, no significant extensile fracturing from these remobilized fractures is expected. It should be emphasized that the assumption of no increase in vertical stress due to heating is not a realistic scenario. Nonetheless, this result suggests that there is a significant benefit in selecting a DGR site at 1000 m depth rather than 500 m depth in terms of reducing the likelihood of fracture slip.

It should be noted that prior thermal-mechanical analyses of a DGR at 1000 m depth in granite (Yuen 1993) demonstrated that an increase in temperature at the repository level resulted in increases in both the horizontal and vertical stresses. Assuming that the increase in vertical stress is 30% of the increase in horizontal stress, the thermally-generated increment in horizontal stress is given by the relation:

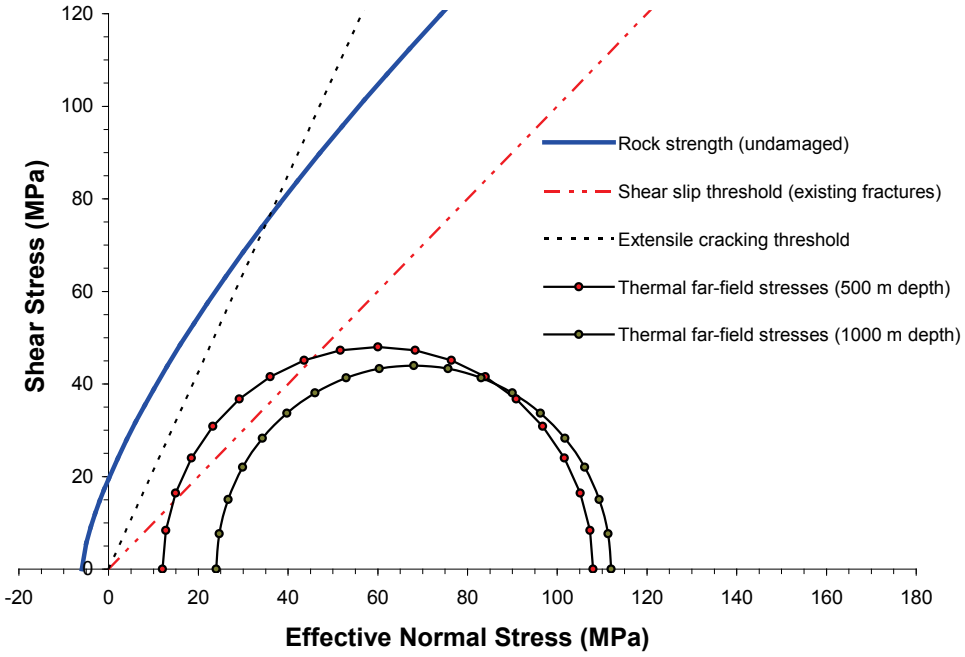

Figure 25: Comparison of Thermally-Induced In Situ Stress States Near the Centre of a DGR at 500 and 1000 m Depth in Crystalline Rock to Relevant Strength Envelopes, Assuming No Thermally-Induced Increase in Vertical Stress.

$$\sigma_i = \alpha_t \Delta T \left(\frac{E}{1-1.3\nu} \right) \tag{24}$$

The increment in horizontal stress associated with a temperature rise of 56°C is about 54 MPa based on Equation 24, and the vertical stress increment is 16 MPa. Adding these values to the pre-existing stresses, the far-field effective stress ratio σ_3'/σ_1' = 0.40 at 500 m depth and 0.34 at 1000 m depth. These stress ratios are higher than those calculated assuming no vertical stress increase. The associated Mohr circles are shown in Figure 26. Neither of the circles intersects the strength envelopes. Under this assumption, thermal loading reduces the likelihood of large-scale fracturing relative to ambient conditions. Compared to the stress states represented in Figure 25, the stress states in Figure 26 are much less likely to promote fracturing or fracture remobilization. This comparison illustrates the importance of selecting the correct equations for calculating thermally-induced stresses. Further work is required to determine the expected percentage increase in thermally-induced vertical stress relative to horizontal stress increment, but it is anticipated to be closer to 30% than to 0%.

In thrust fault stress regimes, glacial loading acts to reduce the deviatoric stress in the rock mass below a glacier. Since the glacier is considered to be large with respect to the rock mass around the repository, the stress change is assumed to be the same at all depths. The additional vertical stress imposed by a 3000-m thick glacier is 27 MPa. Assuming a Poisson's effect, the horizontal stresses are increased by 9 MPa. Adding these values to the pre-existing ambient stresses, the far-field effective stress ratio σ_3'/σ_1' = 0.57 at 500 m depth and 0.71 at 1000 m depth in the absence of thermally-induced stresses. As shown in Figure 27, the in situ

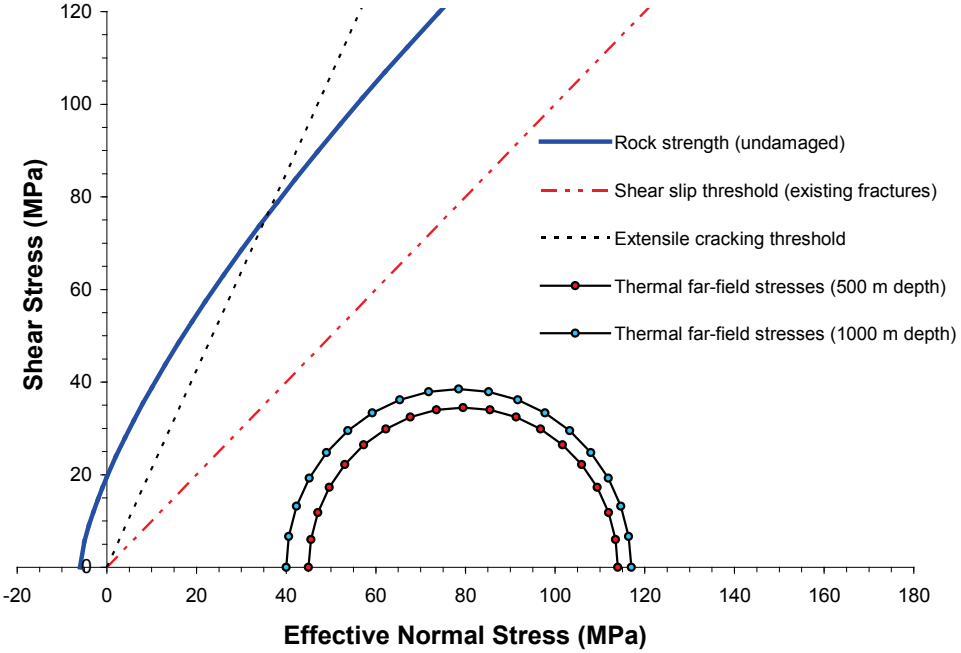

Figure 26: Comparison of Thermally-Induced In Situ Stress States Near the Centre of a DGR at 500 and 1000 m Depth in Crystalline Rock to Relevant Strength Envelopes, Assuming a Thermally-Induced Increase in Vertical Stress.

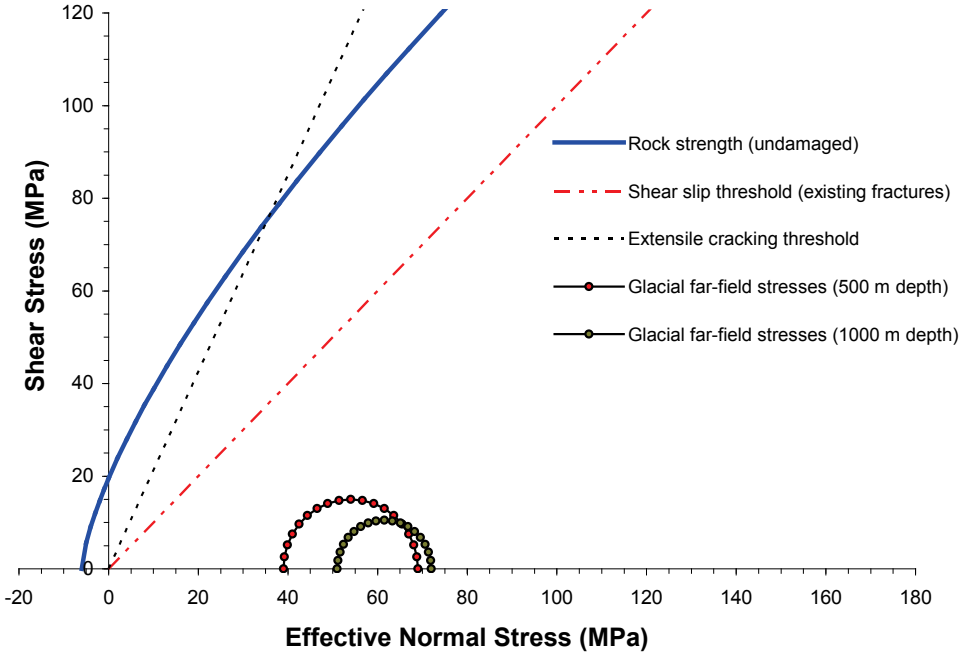

Figure 27: Comparison of Glacier-Induced In Situ Stress States at 500 and 1000 m Depth in Crystalline Rock to Relevant Strength Envelopes.

stress states at 500 and 1000 m are well below the strength envelopes, and are more stable than the ambient condition.

Superimposing the thermally-induced stresses shown in Figure 25 and those associated with glacial loading in Figure 27, the far-field effective stress ratio σ_3'/σ_1' = 0.33 at 500 m depth and 0.42 at 1000 m depth (Figure 28a). In this scenario, the Mohr circles are shifted to the right relative to the thermal loading scenario, and the diameter of the Mohr circles (i.e., the deviatoric stress) is reduced. The Mohr circles lie below the strength envelopes. Substituting the thermally-induced stress shown in Figure 26, the Mohr circles for the combined thermal and glacial loading are reduced in diameter and further shifted to the right (Figure 28b), indicating a more stable stress state than the ambient condition.

These far-field analyses generally support the conclusion of the RA that the stress states associated with the various loading scenarios for a DGR at 500 and 1000 m depth in sparsely fractured crystalline rock are insufficient to initiate large-scale fracturing or remobilize existing fractures in the rock mass. The one exception is the case of a DGR at 500 m depth subjected to thermal loading, assuming no thermally-induced increase in vertical stress. However, this is an unrealistic scenario, as the vertical stress is expected to increase upon thermal loading thereby decreasing the deviatoric stress, and increasing the mean stress (represented by the position of the centre of the Mohr circle on the horizontal axis). This scenario with no increase in vertical stress upon heating is included as a bounding case, and should be further evaluated.

4.2.2 Repository in Sedimentary Rock at 500 and 750 m Depth

Analyses based on the in situ conditions at the repository level in both the Queenston Formation shale at 500 m depth, and in the Lindsay Formation limestone at 750 m depth, support the RA. Although there have been no formal thermal-mechanical analyses of a DGR in either of these formations, a preliminary review of the feasibility of constructing a DGR in either of these formations was favourable (RWE-NUKEM 2004b; 2004c).

The ambient effective in situ stress conditions at repository levels of 500 and 750 m in the sedimentary rock of the Michigan Basin are summarized in Table 5. Effective stresses are calculated assuming a hydrostatic pore pressure trend from surface, and a Biot coefficient α=0.2. The Biot coefficients for the Queenston Formation shale and the Lindsay Formation limestone have not been measured, but are assumed to be similar to that of granite for the purposes of this analysis. Higher values of the Biot coefficient will produce lower effective stress values. However, even for a Biot coefficient value of 1.0, the general findings of these analyses hold true. Also included in Table 5 are the estimated stress conditions associated with thermal and glacial loading of the rock mass. As in the previous section, two bounding cases were considered for the thermal analysis: one assuming no increase in vertical stress as a result of heating, and the second assuming a vertical stress change equal to 30% of the thermally-induced horizontal stress change. The latter case is more realistic than the former.

In the Queenston Formation shale at 500 m depth, the minimum principal stress is vertical and the ambient effective stress ratio σ_3'/σ_1' = 0.5. Assuming a friction angle of 34° for fractured shale, the limiting stress ratio for slip on existing fractures is σ_3'/σ_1' = 0.28. No fracture slip and hence no fracture initiation or propagation from existing fractures is expected for stress ratios above this limiting value. The high σ_3'/σ_1' stress ratio at this level precludes the development of

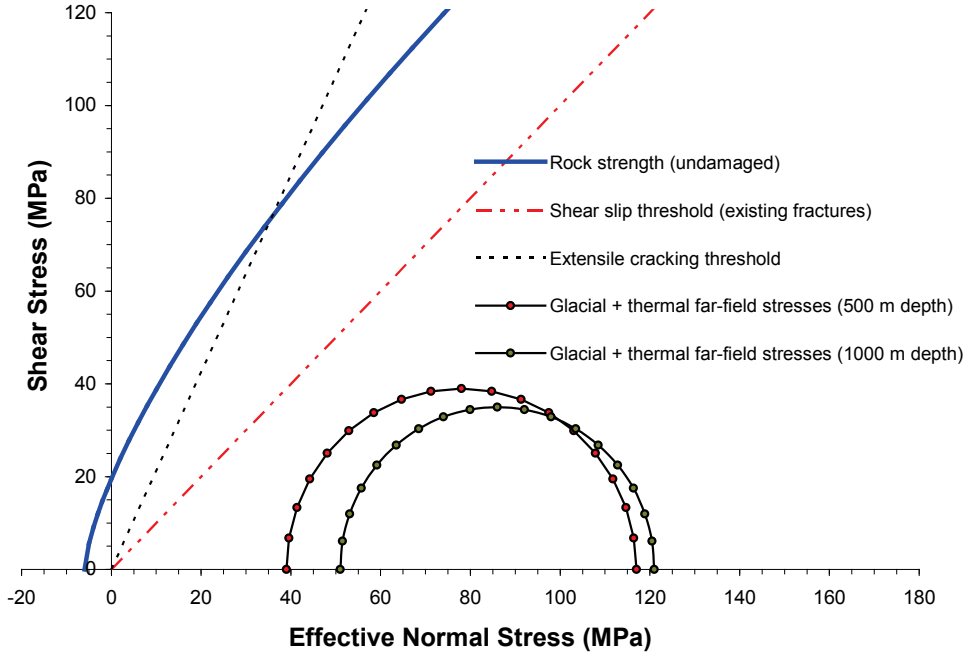

(a)

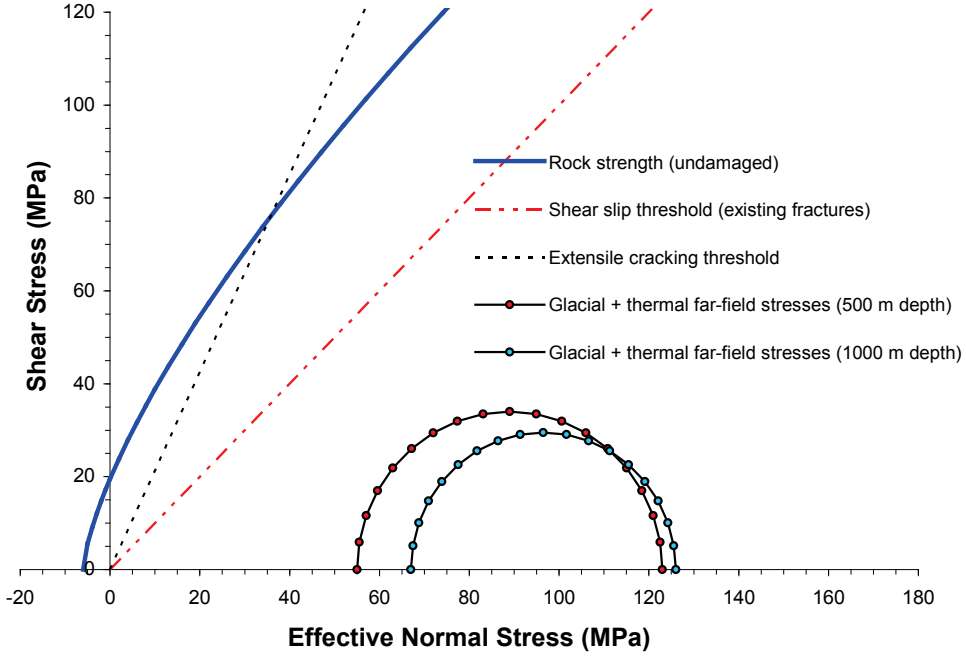

(b)

Figure 28: Comparison of Thermal + Glacier-Induced In Situ Stress States Near the Centre of a DGR at 500 and 1000 m Depth in Crystalline Rock to Relevant Strength Envelopes (a) Assuming No Thermally-Induced Increase in Vertical Stress, and (b) Assuming a Thermally-Induced Increase in Vertical Stress.

Table 5: Stresses used in Far-field Analyses of a Repository in Sedimentary Rock

Scenario	Effective Stress Component (MPa)				
Repository depth =500 m	**$\Delta\sigma_h$'**	**$\Delta\sigma_v$'**	**σ_H'**	**σ_h'**	**σ_v'**
Ambient Stress	-	-	20	14	9
Thermal Stress ($\Delta\sigma_v$=0)	2	0	22	15	9
Thermal Stress ($\Delta\sigma_v$=0.3 $\Delta\sigma_h$)	2	1	22	16	10
Glacial Stress	9	27	29	23	37
Thermal ($\Delta\sigma_v$=0) + Glacial Stress	11	27	31	24	37
Thermal ($\Delta\sigma_v$=0.3 $\Delta\sigma_h$) + Glacial Stress	11	28	31	25	37
Repository depth =750 m	**$\Delta\sigma_h$'**	**$\Delta\sigma_v$'**	**σ_H'**	**σ_h'**	**σ_v'**
Ambient Stress	-	-	26	22	18
Thermal Stress ($\Delta\sigma_v$=0)	21	0	48	43	18
Thermal Stress ($\Delta\sigma_v$=0.3 $\Delta\sigma_h$)	25	7	51	46	26
Glacial Stress	9	27	35	31	45
Thermal ($\Delta\sigma_v$=0) + Glacial Stress	30	27	57	52	45
Thermal ($\Delta\sigma_v$=0.3 $\Delta\sigma_h$) + Glacial Stress	34	34	60	55	53

large-scale fracturing, as illustrated by the Mohr circle for the ambient stress state at this level (Figure 29).

In the Lindsay Formation limestone at 750 m depth, the minimum principal stress is vertical and the ambient effective stress ratio σ_3'/σ_1' = 0.7. Assuming a friction angle of 35° for fractured limestone, the limiting stress ratio for slip on existing fractures is σ_3'/σ_1' =0.27. As for the conditions at 500 m depth, development of large-scale fracturing in the far-field at 750 m depth is not possible due to the high σ_3'/σ_1' stress ratio. The Mohr circle for the ambient stress state at this level is shown in Figure 30.

Thermally-induced stresses were calculated using Equations 22 and 24. In the first case, the vertical stress increment due to heating is assumed to be zero. In the second case, the thermally-induced increase in vertical stress is assumed to be 30% of the calculated horizontal stress increment. For an estimated maximum temperature rise of about 56°C in the rock mass near the placement rooms, and using values of α_t=2.0e^{-6}, E=12 GPa, and ν=0.3 for Queenston shale, the effective stress ratio σ_3'/σ_1' = 0.44 and 0.46 for the two thermal cases, respectively. These stress ratios are insufficient to initiate new fracturing or to remobilize existing fractures, assuming a residual friction angle of ϕ=34°. The associated Mohr circles are shown in Figure 31. The incremental stress associated with a temperature rise of 56°C is only about 2 MPa for this rock type owing to the relatively low thermal expansion coefficient and Young's modulus value. It should be noted that the predicted temperature increase used in this analysis is larger than the 29°C predicted by Baumgartner (2005) for some DGR options, and is therefore considered conservative.

Using the same methodology, thermally-induced stresses associated with an estimated maximum temperature rise of 56°C in the rock mass near the DGR were calculated using values of α_t=6.7e^{-6}, E=40 GPa, and ν=0.3 for Lindsay limestone at 750 m depth. The predicted temperature increase is larger than the 31°C predicted by Baumgartner (2005), and is therefore conservative. This results in effective stress ratios of σ_3'/σ_1' = 0.38 and 0.50 for the two thermal cases, respectively. These stress ratios are insufficient to initiate new fracturing or to

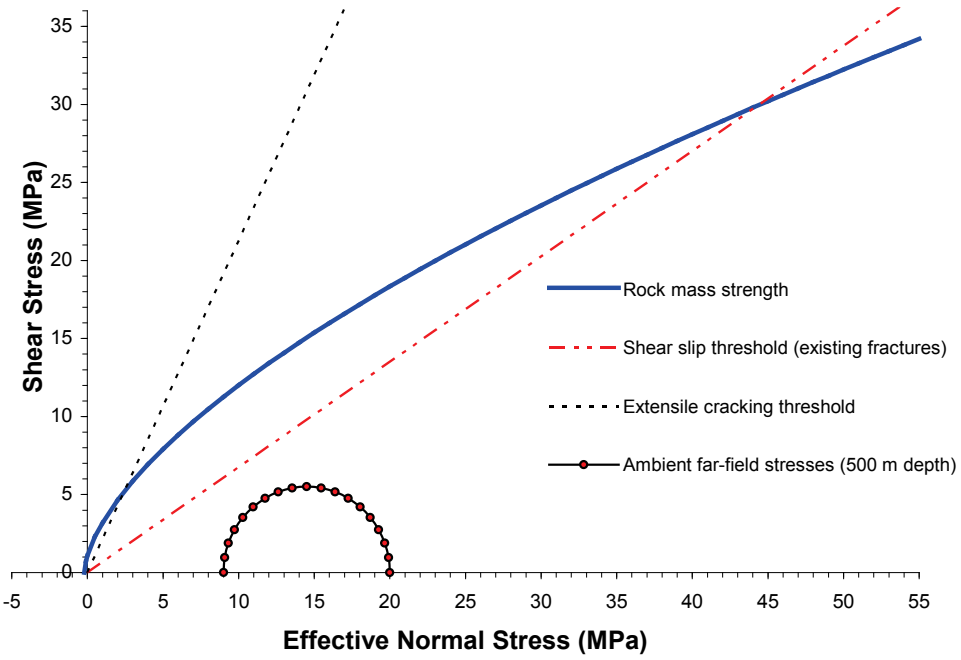

Figure 29: Comparison of Ambient Far-Field In Situ Stress State at 500 m Depth in Queenston Formation Shale to Relevant Strength Envelopes.

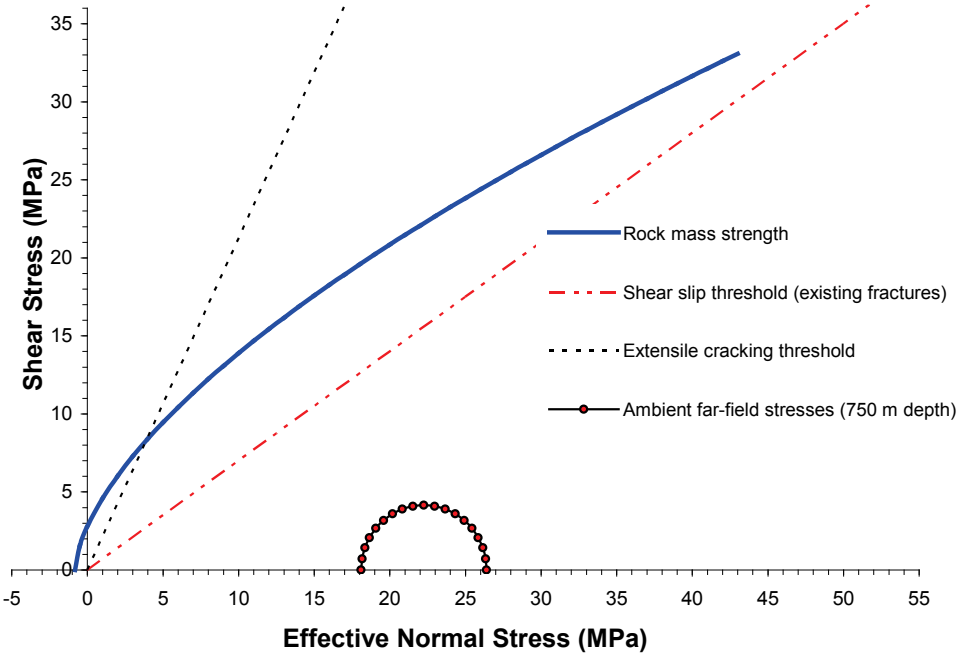

Figure 30: Comparison of Ambient Far-Field In Situ Stress State at 750 m Depth in Lindsay Formation Limestone to Relevant Strength Envelopes.

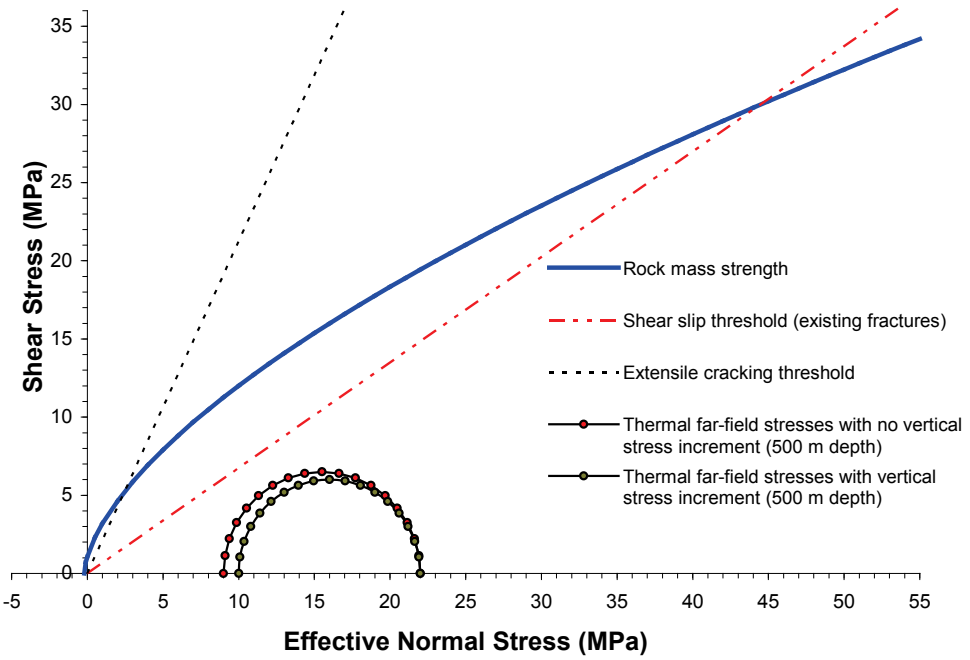

Figure 31: Comparison of Thermally-Induced Far-Field In Situ Stress States at 500 m Depth in Queenston Formation Shale to Relevant Strength Envelopes.

remobilize existing fractures, assuming a residual friction angle of ϕ=35°. This is reflected by the fact that the Mohr circles do not intersect the relevant strength envelopes (Figure 32).

Glacial loading is simulated by assuming a surcharge at ground surface. The additional vertical stress imposed by a 3000-m thick glacier is about 27 MPa. Assuming a Poisson's effect (for ν = 0.3), the horizontal stresses are increased by almost 12 MPa. The effective stress ratios at 500 m depth in the Queenston Formation shale and at 750 m depth in the Lindsay Formation limestone are therefore σ_3'/σ_1' = 0.69 and 0.73, respectively, in the absence of thermally-induced stresses. As shown in Figure 33 and 34, the Mohr circles associated with these stress states are well-below the relevant strength envelopes. In both these cases, the maximum principal stress is rotated from horizontal to vertical indicating a switch from a thrust faulting regime to a normal faulting regime. Therefore, were new fractures to form under this loading scenario, they would be steeply dipping. However, the stress ratios are high relative to the critical values associated with fracture slip, thereby precluding large-scale fracturing.

Superimposing the two cases of thermally-induced stresses shown in Figure 31 and that associated with glacial loading in Figure 33, the combined stresses result in effective stress ratios in σ_3'/σ_1' = 0.74 (for no thermally-induced vertical stress increment) and 0.73 (for a

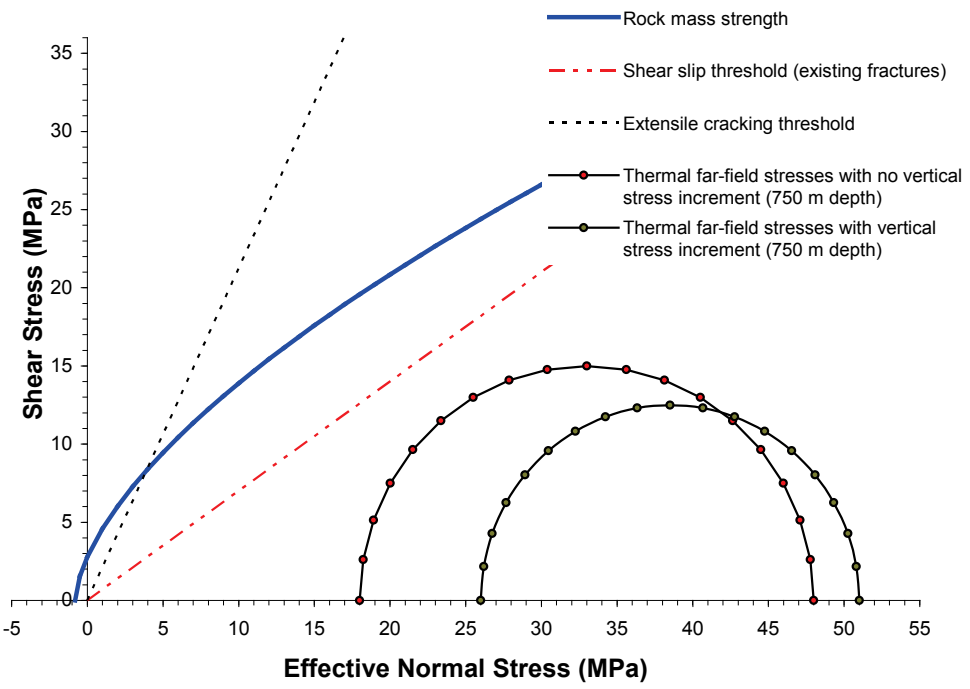

Figure 32: Comparison of Thermally-Induced Far-Field In Situ Stress State at 750 m Depth in Lindsay Formation Limestone to Relevant Strength Envelopes.

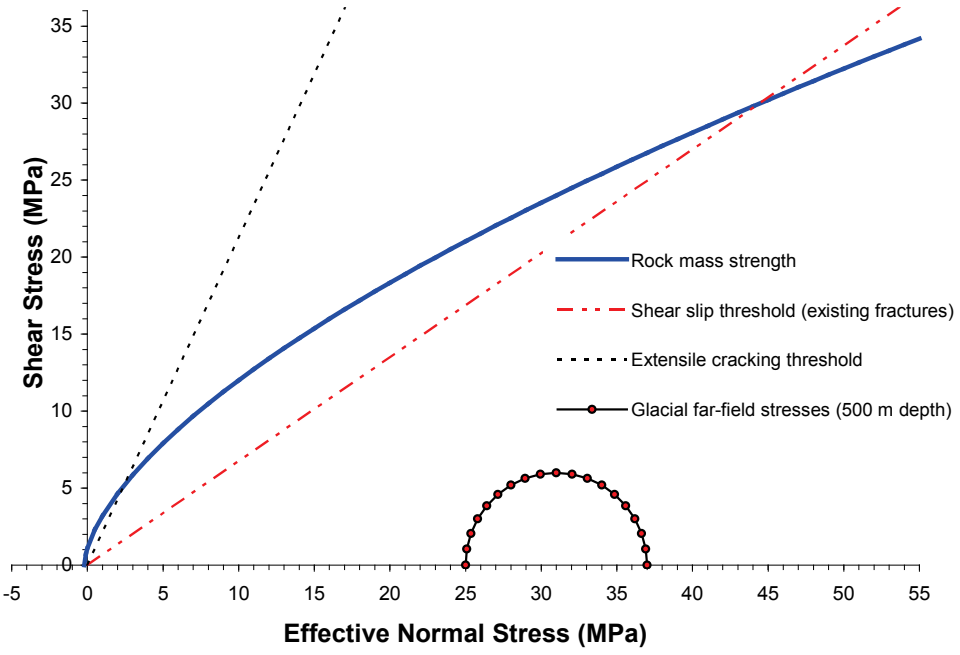

Figure 33: Comparison of Glacier-Induced Far-Field In Situ Stress State at 500 m Depth in Queenston Formation Shale to Relevant Strength Envelopes.

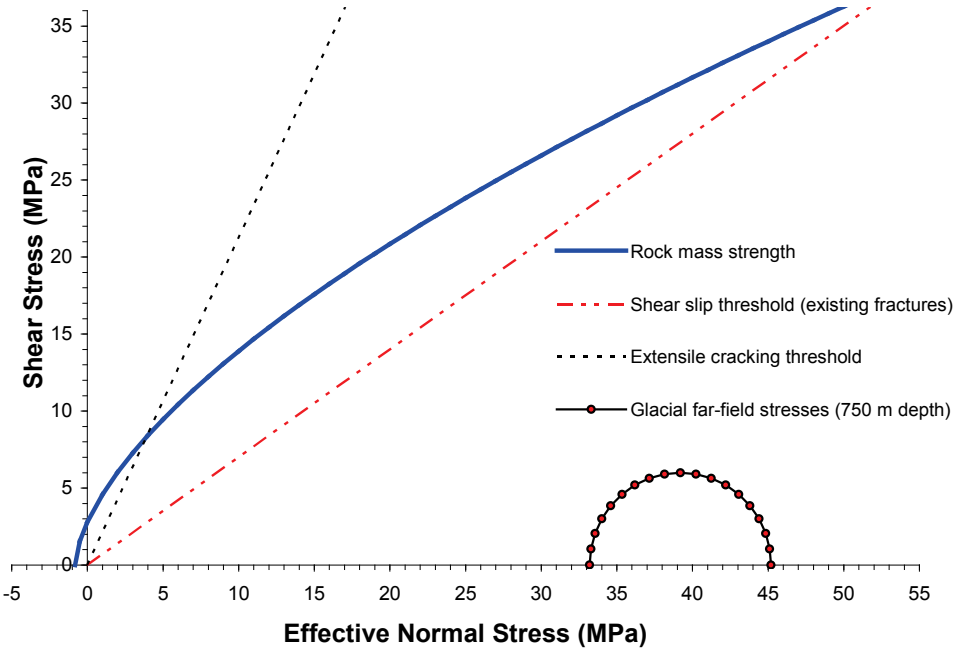

Figure 34: Comparison of Glacier-Induced Far-Field In Situ Stress State at 750 m Depth in Lindsay Formation Limestone to Relevant Strength Envelopes.

thermally-induced vertical stress increment) in the Queenston Formation shale at 500 m depth. The Mohr circles for these stress states are shown in Figure 35. Neither circle intersects the strength envelopes. The maximum principal stress is vertical, indicating a switch to a normal fault regime relative to the original ambient condition.

Likewise, for Lindsay Formation limestone at 750 m depth, the combined thermal and glacial stresses from Figure 32 and 34 produce relatively stable stress states well removed from the relevant strength envelopes (Figure 36). The effective stress ratio σ_3'/σ_1' = 0.76 (for no thermally-induced vertical stress increment) and 0.84 (for a thermally-induced vertical stress increment). In each of these cases, the minimum principal stress is vertical, indicating a switch back to a thrust fault regime relative to the glacial loading scenario without thermal loading.

Like the crystalline rock analyses, these far-field analyses support the RA that the stress states associated with the various loading scenarios for a DGR in sedimentary rock at 500 or 750 m depth are insufficient to initiate large-scale fracturing or to remobilize existing fractures in the rock mass. In addition, the Queenston Formation shale was shown to be relatively insensitive to thermal loading due to low Young's modulus and thermal expansion coefficient compared to the other rock types. A consequence of the lower stress conditions in these sedimentary units relative to the crystalline rock scenarios is the alteration in maximum principal stress direction from horizontal to vertical in some cases. This change in fault regime is more conducive to developing or reactivating subvertical fracture systems and faults. However, the anticipated vertical stresses in the various scenarios are well below those required for fracture slip or development of new fractures. This effect has the added benefit of decreasing the likelihood of development or reactivation of shallow-dipping fractures and faults.

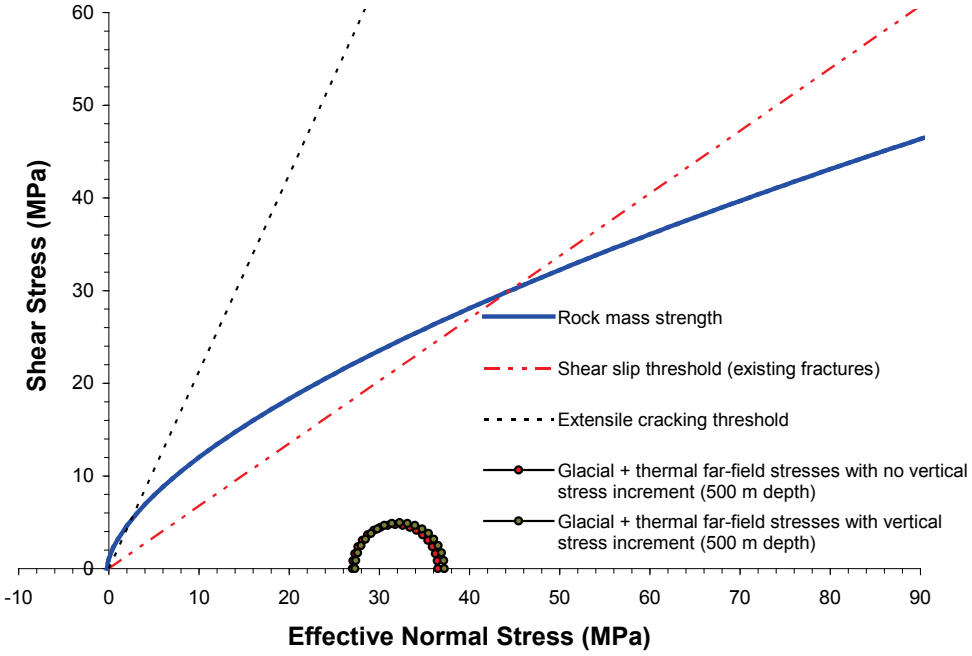

Figure 35: Comparison of Thermal + Glacier-Induced Far-Field In Situ Stress State at 500 m Depth in Queenston Formation Shale to Relevant Strength Envelopes.

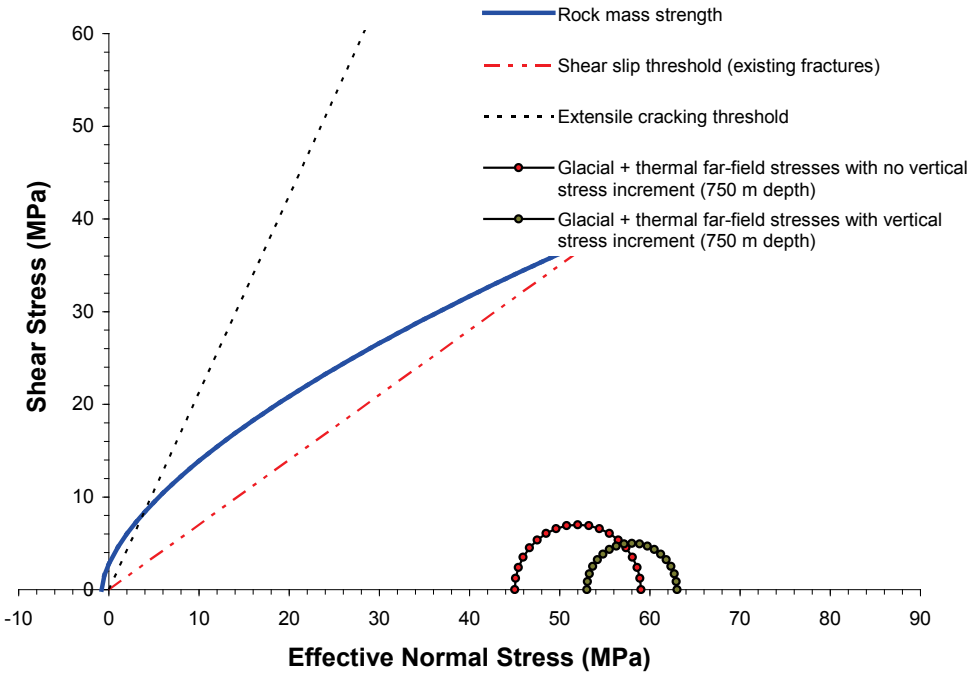

Figure 36: Comparison of Thermal + Glacier-Induced Far-Field In Situ Stress State at 750 m Depth in Lindsay Formation Limestone to Relevant Strength Envelopes.

4.3 NEAR-FIELD ANALYSIS OF DEEP GEOLOGICAL REPOSITORY DESIGNS

4.3.1 Overview of Analyses

To investigate the likelihood of large-scale fracturing resulting from near-field conditions associated with the various DGR designs, 240 individual analyses of excavations in crystalline and sedimentary rock were conducted. The results of these analyses are summarized in Appendix B of this report. Table B.1 contains the results for six loading scenarios for four DGR designs at two different depths in both crystalline and sedimentary rock. In each of these cases, the placement room (or access tunnel in the KBS-3V design) is parallel to the maximum horizontal stress direction. Table B.2 contains the results for the same cases, but with the placement rooms oriented parallel to the minimum horizontal stress direction. Also included in these tables are the input values used in the calculations.

The analyses associated with the KBS-3H, KBS-3V, and NAGRA designs were undertaken using an EXCEL spreadsheet based on the closed-form solution for stresses around a single circular opening (Kirsch 1898). These analyses did not account for the effect of adjacent parallel openings as their influence on near-field conditions was considered to be relatively minor. Further analyses of multiple openings could be undertaken to quantify this effect.

For the KBS-3V design, two sets of analyses were completed using the closed-form solution. One set simulated conditions near the bottom of a vertical placement hole assuming no influence of the horizontal elliptical access tunnel. A second set simulated conditions near the top of the vertical placement hole accounting for the proximity of the access tunnel. In this latter case, the tangential boundary stress at the base of the elliptical access tunnel calculated from Equations 20 and 21 was used as the horizontal far-field stress component acting on the vertical borehole perpendicular to the access tunnel axis. The far-field stress component acting parallel to the access tunnel axis was used as the other horizontal stress component in the calculations. This approach is approximate and does not address the elevated tangential compressive stresses in the invert of the access tunnel near the vertical placement hole collar. These effects could be assessed in more detailed analyses using a three-dimensional numerical model, but such analysis is beyond the scope of this report.

For the AECL elliptical room design, a two-dimensional finite difference model[6] was used to calculate the near-field stresses under various loading scenarios. The model comprised a 100x100 zone quarter-symmetry grid, with the distance to the outer rectangular boundary set to about 10 times the opening dimension in the vertical and horizontal directions. The model grid is shown in Figure 37. An elastic constitutive relation was used for the analyses. Results from each model simulation were exported to an EXCEL file for further analysis. The simulations did not account for adjacent openings, but provided scoping results to support the RA.

To illustrate the method for generating the results in Appendix B, typical plots summarizing the key points of the analysis are shown in Figures 38 and 39. The strength ratio (i.e., the ratio of strength calculated from the Hoek-Brown strength envelope to deviatoric stress) is compared to a threshold value of 1.0 in Figure 38. Below this threshold, localized small-scale fracturing is

[6] The model was constructed using the code FLAC (Ver. 5.0) from Itasca Consulting Group, Inc., Mill Place, 111 Third Avenue South, Suite 450, Minneapolis, Minnesota 55401 USA.

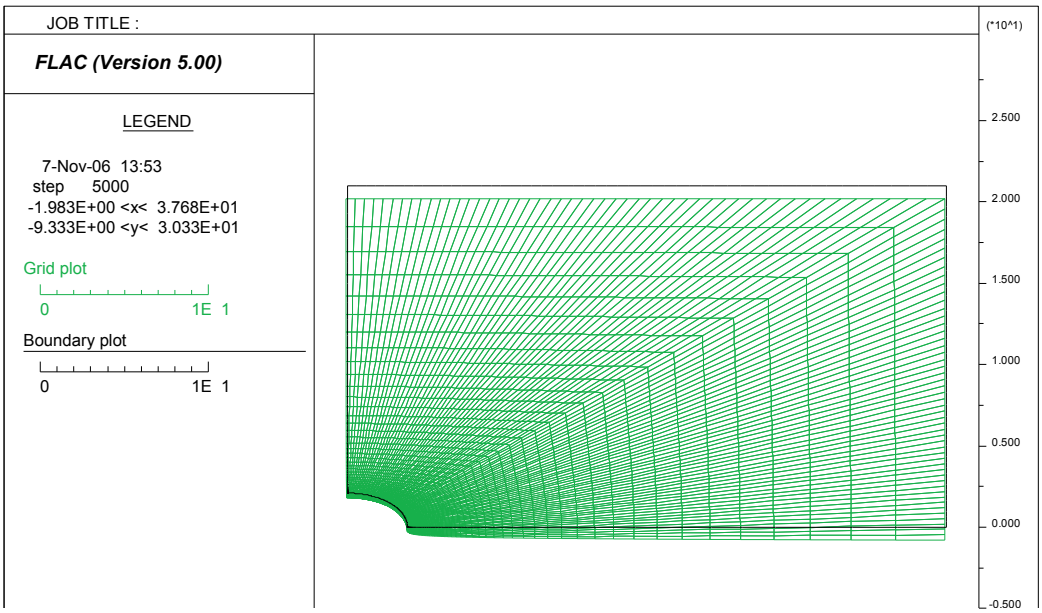

Figure 37: Model Grid Used in Near-Field Simulations of the AECL-Type DGR Design

possible. For the analyses of crystalline rock, the lower bound Hoek-Brown strength envelope in Figure 12 was used, although it is recognized that this strength envelope may over-predict small-scale fracturing other than in localized areas very close to the opening periphery (i.e., it is conservative). For the analyses of shale and limestone, the Hoek-Brown envelope reflects the anticipated conditions of the far-field rock mass. In these cases, the envelope does not account for possible localized excavation-induced damage owing to the lack of quantitative data for these rock types. The data in this figure represent conditions along vertical and horizontal sampling lines extending outward from the excavation periphery in the crown and sidewall regions, respectively. The curve for the minimum strength ratio around the opening represents the minimum value of this ratio in the region between these two bounding sampling lines (termed the intermediate region). Where this curve deviates from one of the other curves, it indicates a localized region of lower strength relative to conditions along the horizontal or vertical sampling lines. These three curves are used to asses the location and extent of possible small-scale fracturing in the near-field.

The effective principal stress ratio σ_3'/σ_1' is compared in Figure 39 to the limiting value associated with slip on a preferentially-oriented cohesionless fracture (calculated from Equation 23). Below this threshold, fracture slip is possible in zones where preferentially-oriented fractures exist. Data in this figure represent conditions along vertical and horizontal sampling lines in the crown and sidewall as described above. The third curve represents the minimum value of the effective principal stress ratio in the intermediate region. Where this third curve coincides with one of the other curves, it reflects that the stress concentration in the roof or sidewall extends some distance either side of the vertical or horizontal sampling line. Departure of this curve from one of the other curves indicates a zone of lower effective principal stress ratio in the intermediate region. These three curves are used to assess the possible distance to which existing near-field fractures may extend away from the opening. This approach is conservative because it assumes the existence of preferentially-oriented fractures within the zone where the Hoek-Brown strength ratio falls below unity, and the potential for these fractures to grow into the zone of low effective stress ratio.

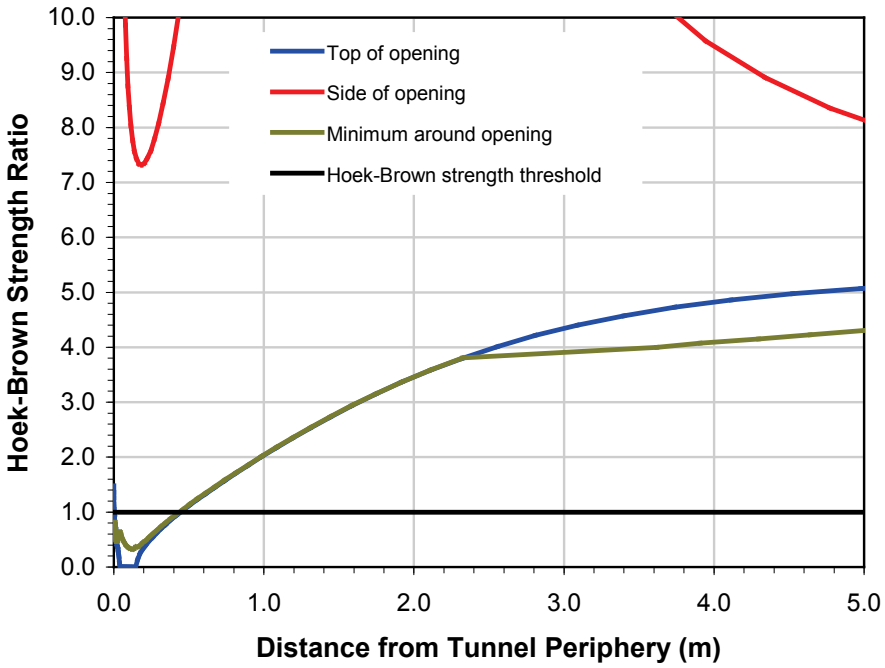

Figure 38: Hoek-Brown Strength Ratio Around an AECL-Type DGR at 500 m in Crystalline Rock Under Ambient Conditions (Room Parallel to Maximum Horizontal Stress).

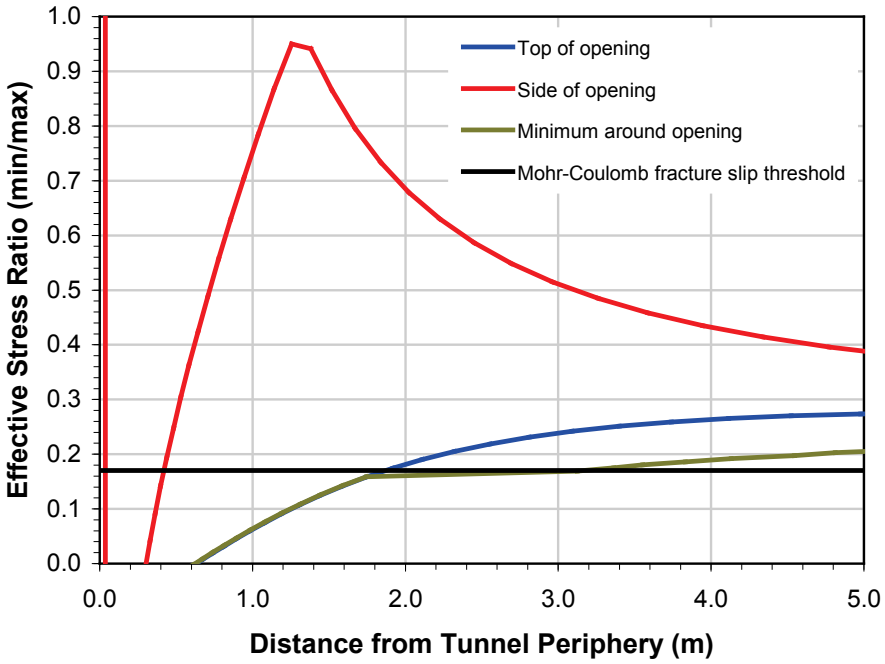

Figure 39: Ratio of Minimum to Maximum Principal Stress Relative to Mohr-Coulomb Threshold for Fracture Slip Around an AECL-Type DGR at 500 m in Crystalline Rock Under Ambient Conditions (Room Parallel to Maximum Horizontal Stress).

With reference to the results in Appendix B, the following sections provide a summary of findings from the analyses for each of the DGR designs under the various loading scenarios and host rock conditions. Findings from analyses performed by others are also presented. In each of the DGR designs, placement rooms are planned to be oriented parallel to the maximum horizontal stress. Consequently, the analyses related to this room orientation are most relevant to the RA, and are the focus of this section of the report. For the sake of brevity, loading cases are summarized in terms of their potential for large-scale fracturing without repeating many numerical values from the analyses. Quantitative results from analyses of the most and least favourable placement room orientations are included in Appendix B for completeness, and are referenced by specific cases.

4.3.2 AECL-type In-Room Placement Design

4.3.2.1 DGR in Crystalline Rock at 500 and 1000 m Depth

Several analyses of the AECL-type elliptical in-room placement concept (Baumgartner et al. 1995; Baumgartner et al. 1996) have been conducted since its introduction. The most current thermal-mechanical analyses of expected conditions around a DGR based on this placement concept in sparsely fractured crystalline rock at 1000 m depth (CTECH 2002) support the conclusions of the RA. In that report, separate near- and far-field analyses were conducted to capture the long-term temperature distribution and associated rock mass response. Backfill stiffness was assumed to be 0.1 GPa for the analysis, but backfill swelling interaction with the rock mass was not taken into account.

The CTECH near-field analysis suggests that the rock mass temperature at the crown of each placement room rises from 17°C to 73°C after 57 years, while at the springline the rock mass reaches 70°C after 60 years. The near-field model did not account for lateral heat loss at the edge of model, so a late rise in temperature was over-estimated. The far-field model results show a peak temperature at centre of repository of 70°C at 4000 years. At the edge of the repository, the maximum temperature is 46°C at 5000 years. At the corner of the repository, the temperature peaks at 33°C at 6000 years. Blending the near and far-field results, the temperature of the repository is expected to rise from an ambient temperature of about 17°C to about 70°C over 60 years, stay relatively constant for 4000 years, then decline.

A three-dimensional finite element model was used in the CTECH analysis to calculate stresses around placement rooms oriented parallel and perpendicular to the maximum horizontal stress direction. The extent of the zone of fracture propagation was estimated using a criterion of $\sigma_1 - \sigma_3$ = 75 MPa. However, as shown in previous sections of this report, crack initiation and propagation are controlled by the stress ratio and the confining stress in addition to the deviatoric stress. Therefore, the use of a deviatoric stress criterion alone to assess the extent of fracturing is questionable. The main findings from the CTECH analysis, considering multiple parallel placement rooms, are as follows:

- Under ambient temperature conditions, placement rooms oriented parallel and perpendicular to the maximum principal stress are predicted to be stable with no small- or large-scale fracturing of the rock mass.
- Under thermal loading conditions, localized spalling is predicted in the crown of the placement room. The lower bound Hoek-Brown strength envelope for crystalline rock (see Figure 12) is exceeded up to a distance of 0.1 m from the periphery of a placement room parallel to the minimum horizontal stress direction, and up to 0.05 m

for a room parallel to the maximum horizontal stress direction. In the sidewall, stresses are compressive and there is no indication of fracturing.

- Under these same conditions, a limiting stress ratio of, σ_3'/σ_1'=0.17 is reached at about 1.5 m above the crown of a placement room oriented parallel to the minimum horizontal stress direction. For a room parallel to the maximum horizontal stress direction, this value is reduced to 1.4 m. These values are taken as the maximum extent of the zone of possible fracture slip, a necessary precursor for fracture extension. Figures 40 and 41 show the stresses and stress ratio above the placement room crown for different room orientations.
- Effects of additional loads attributable to changes in the in situ stress state, including glaciation, were assumed to be adequately buffered by clay-based sealing materials, and were not considered in the analyses.
- Heating of the rock mass is expected to result in about 0.25 m of heave at the ground surface directly above the centre of the DGR after 10,000 years. The maximum tensile stress developed at ground surface is about 1 MPa over this time frame. The depth to which some limited opening or extension of subvertical fractures could occur is less than 9 m centred above the DGR. This is significantly less than the specified limit of 100 m depth, and indicates that new subvertical fracture zones will not be initiated as a result of the DGR. Given the relatively small amount of ground heave and limited extent of possible opening of existing fractures near surface, negligible impact on groundwater and surface water flow is anticipated.
- CTECH (2002) recommends using a drill-and-blast excavation method, possibly with a pilot-and-slash sequence, to excavate the placement rooms and other underground openings. As shown by Read and Chandler (1997) and others, an optimized room geometry could reduce the maximum compressive stress in the placement room crown, possibly eliminating the zone exceeding the long-term strength of the rock mass.

Aside from the placement rooms, the arched rectangular access tunnels in this DGR design require careful design to accommodate the high thermal-mechanical stresses at the repository level, particularly those tunnels oriented parallel to the intermediate principal stress. Intersections of rooms and access tunnels are potential stress concentration areas and may require ground support or modifications to tunnel geometry. The circular shafts and perimeter tunnels are located far enough from the placement rooms that the temperature increase experienced by these openings will be significantly reduced compared to the placement rooms. Therefore, these openings are not expected to contribute to large-scale fracturing of the rock mass.

The results of the thermal-mechanical analyses conducted by CTECH (2002) support the RA that no large-scale fracturing will be generated by near-field stress conditions around excavations. Although localized spalling may occur in compressive regions at or slightly beyond the periphery of placement rooms, these small-scale fractures cannot extend very far from the opening. Specifically, the CTECH analysis indicates that no new fractures will be generated to interconnect adjacent rooms (i.e., the pillars between rooms are not prone to fracturing), and no fractures will connect a placement room with undetected fractures further than about 1.5 m from the excavation.

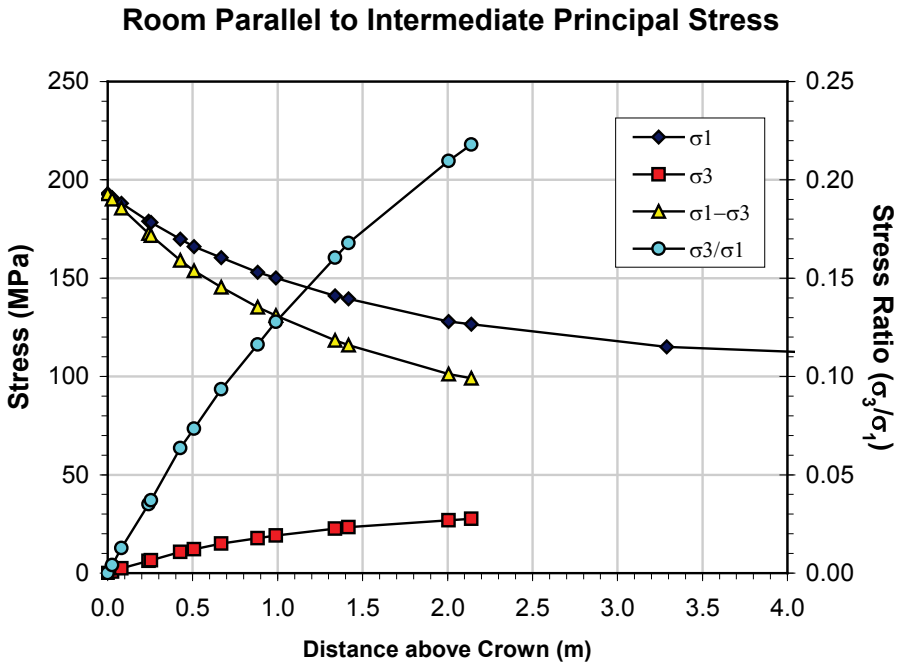

Figure 40: Stresses and Stress Ratio Along the Vertical Axis Above the Crown of a Placement Room Parallel to the Intermediate Principal Stress Based on Results from CTECH (2002). This Figure Includes the Effects of Thermal Loading.

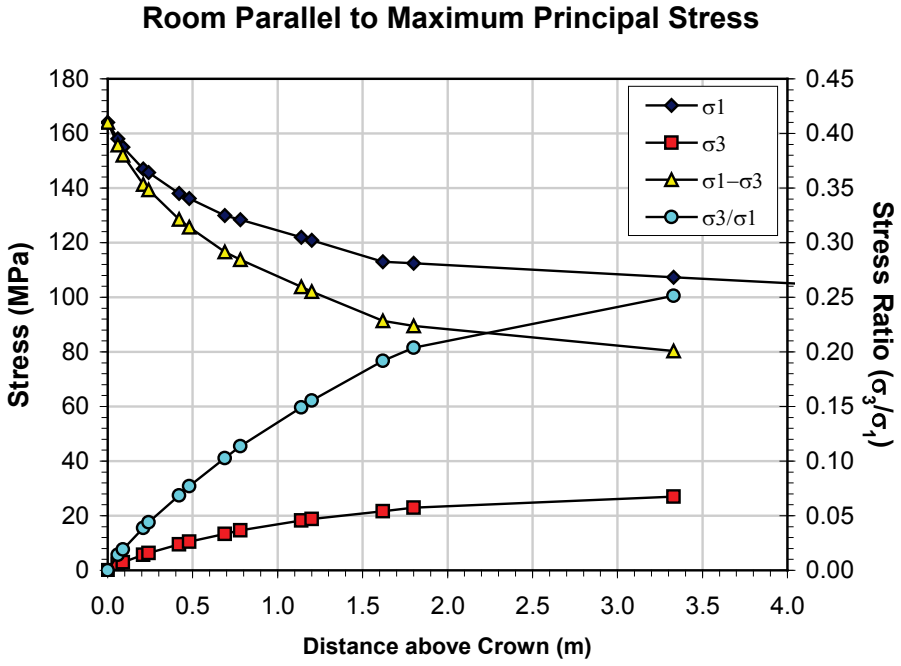

Figure 41: Stresses and Stress Ratio Along the Vertical Axis Above the Crown of a Placement Room Parallel to the Maximum Principal Stress Based on Results from CTECH (2002). This Figure Includes the Effects of Thermal Loading.

Additional finite difference analyses of single placement rooms oriented parallel and perpendicular to the maximum principal stress in crystalline rock at 500 and 1000 m depth conducted to support the RA are summarized in Appendix B (Cases 97 through 108 in Tables B.1 and B.2). With reference to analysis results for a placement room oriented parallel to the maximum horizontal stress in Table B.1, the main findings are described below.

- Under ambient temperature conditions (Figures 38 and 39), placement rooms are predicted to experience localized small-scale compressive fracturing (spalling) in the crown and invert, but no fracturing in the sidewalls. Without significant changes in near-field stress conditions, possible slip on, and extension of, preferentially-oriented small-scale fractures in the crown and invert is limited to a small zone within a maximum distance of 1.7 m of the excavation periphery. In the intermediate region around the opening at 500 m depth, a zone where the effective principal stress ratio falls below the threshold for fracture slip extends up to 3.3 m from the opening. However, because small-scale fracturing is localized near the crown and invert of the opening, fracture extension into this zone is improbable.
- Under thermal loading conditions (assuming a 56°C temperature increase), the localized small-scale fracturing in the crown and invert of the placement room is slightly exacerbated. The extent of small-scale fracturing is likely over-estimated using the lower bound Hoek-Brown strength envelope (see Figure 12), particularly considering that a placement room at this stage of its history contains backfill and may experience some swelling pressure on the rock/backfill interface. Small-scale fracturing is predicted to extend further from the opening in the crown and invert for thermal cases that assume no increase in vertical stress due to heating compared to those that assume an increase in vertical stress with heating. In these former cases, small-scale fracturing is also possible in the intermediate region and sidewall. The latter cases are considered more representative of the expected rock mass response. The zone of possible fracture slip in the crown and invert, the intermediate region, and the sidewall is limited to within a maximum distance of 1.6 m of the opening (a slight decrease relative to ambient conditions).
- Under glacial loading conditions, small-scale fracturing is predicted in the crown and invert, and in a very localized zone in the sidewall of the placement room. The zones of possible fracture slip are also localized in these areas, and do not extend further than 1.4 m from the opening.
- Under combined thermal and glacial loading conditions, small-scale fracturing is predicted in the crown and invert, and in a very localized zone in the sidewall of the placement room at 1000 m depth but not at 500 m depth. The zones of possible fracture slip are also localized in these areas, and do not extend further than 1.6 m from the opening.

Based on these analysis results, possible fracturing and fracture extension in the absence of excess pore pressure is limited to within less than 2 m of the placement room periphery. For placement rooms oriented parallel to the maximum horizontal stress (Table B.2), the findings are similar. Consequently, large-scale fracturing around an AECL-type DGR is not considered possible at either 500 or 1000 m depth in crystalline rock.

4.3.2.2 DGR in Shale at 500 m Depth

There have been no formal thermal-mechanical analyses conducted for an AECL-type in-room placement design in sedimentary rock of the Michigan Basin. However, for the purposes of a simple scoping analysis, it was assumed that the temperature history in sedimentary rock is similar to that in crystalline rock. A temperature rise of 56°C is assumed for thermal analyses. The methodology used for near-field analysis of this DGR design in crystalline rock was applied to a conceptual depth of 500 m in the Queenston Formation shale. Analysis results are summarized in Appendix B (Cases 109 through 114 in Tables B.1 and B.2). The main findings associated with a placement room oriented parallel to the maximum horizontal stress are as follows:

- Under ambient temperature conditions (Figure 42 and 43), small-scale compressive fracturing (spalling) is expected up to a maximum distance of 1.1 m from the crown and invert, and up to 0.2 m from the sidewall. Within 0.7 m of the crown and invert, small-scale tensile fracturing is also predicted. Possible fracture slip and extension is limited to within a maximum distance of 2.2 m of the excavation periphery. This zone is more extensive in the crown and invert than in the sidewall.
- Under thermal loading conditions (assuming a 56°C temperature increase), the zones of possible small-scale fracturing and fracture slip are almost identical to those under ambient conditions owing to the relatively low Young's modulus and thermal expansion coefficient for this rock type.
- Under glacial loading conditions, small-scale fracturing is suppressed in the crown and invert, but the zone of possible fracturing in the sidewall increases to 0.5 m from the opening. The zone of possible fracture slip in the crown and invert is significantly smaller than that under ambient conditions. Possible fracture slip is limited to within 1.7 m of the opening.
- Under combined thermal and glacial loading conditions, the zones of possible small-scale fracturing and fracture slip are almost identical to those under glacial loading conditions owing to the relatively minor influence of thermal loading in this rock type.

Based on these analysis results, possible fracturing and fracture extension in the absence of excess pore pressure is limited to within about 2.2 m of the placement room. For rooms in the perpendicular direction, this value is 2.6 m. Therefore, large-scale fracturing around an AECL-type DGR design in shale at 500 m depth is not considered possible.

4.3.2.3 DGR in Limestone at 750 m Depth

The methodology and assumptions about temperature history used for near-field analysis of this DGR design in shale were applied to a conceptual depth of 750 m in the Lindsay Formation limestone. Analysis results are summarized in Appendix B (Cases 115 through 120 in Tables B.1 and B.2). The main findings associated with a placement room oriented parallel to the maximum horizontal stress are as follows:

- Under ambient temperature conditions (Figure 44 and 45), small-scale compressive fracturing (spalling) is expected up to a maximum distance of 0.9 m from the crown and invert, and up to 0.3 m from the sidewall. Within 0.6 m of the crown and invert, small-scale tensile fracturing is also predicted. Possible fracture slip and extension is limited

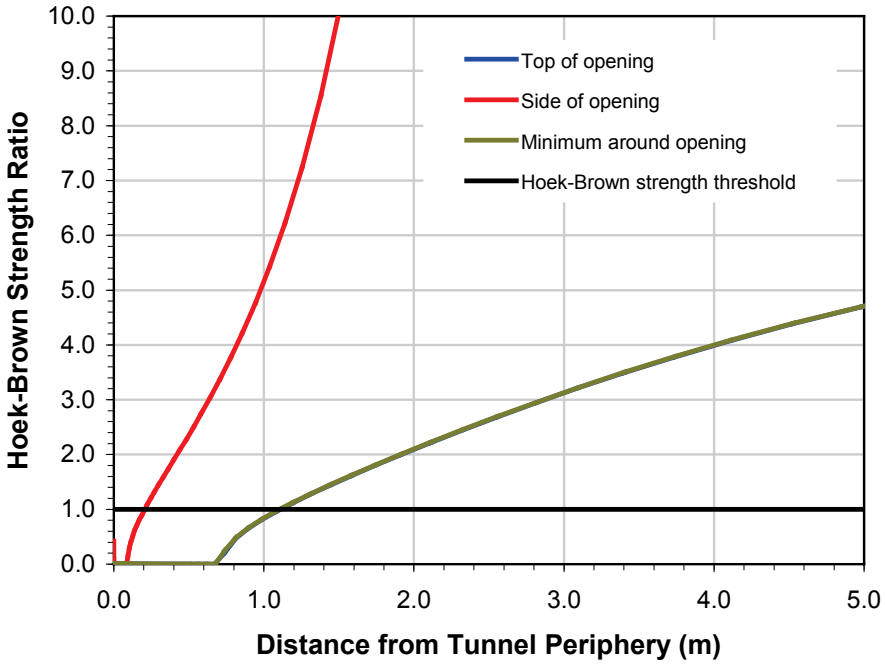

Figure 42: Hoek-Brown Strength Ratio Around an AECL-Type DGR at 500 m in Shale Under Ambient Conditions (Room Parallel to Maximum Horizontal Stress).

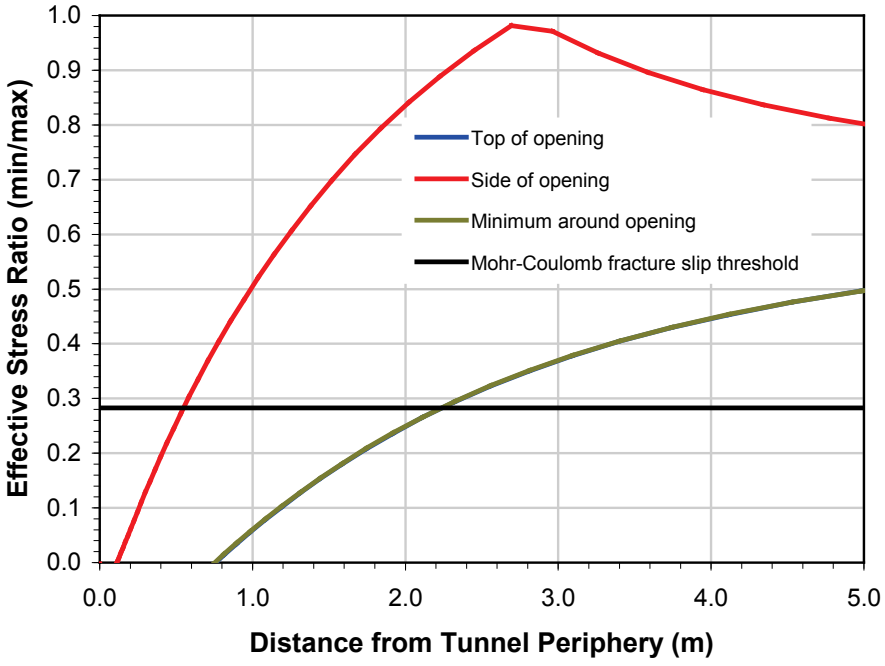

Figure 43: Ratio of Minimum to Maximum Principal Stress Relative to Mohr-Coulomb Threshold for Fracture Slip Around an AECL-Type DGR at 500 m in Shale Under Ambient Conditions (Room Parallel to Maximum Horizontal Stress).

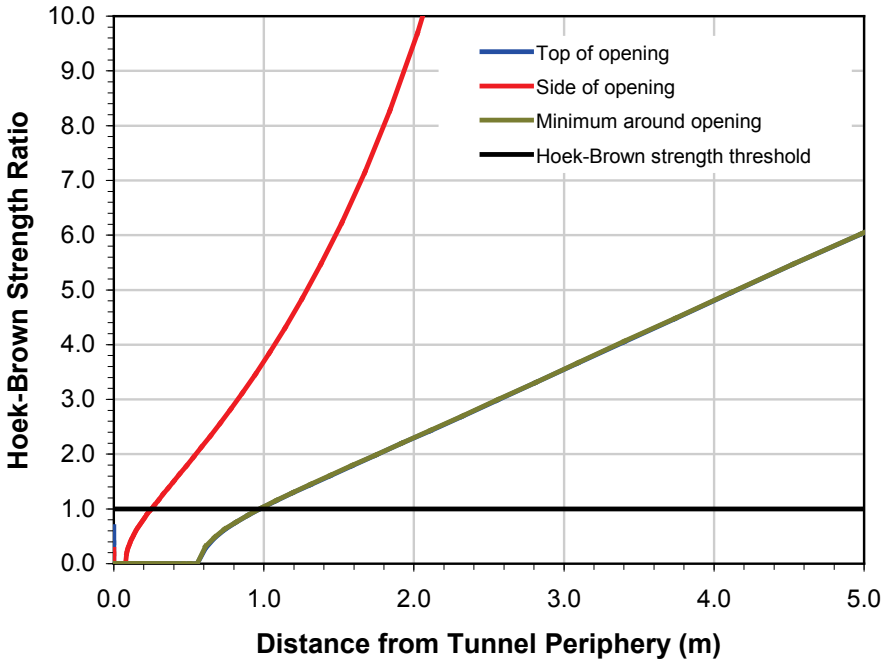

Figure 44: Hoek-Brown Strength Ratio Around an AECL-Type DGR at 750 m in Limestone Under Ambient Conditions (Room Parallel to Maximum Horizontal Stress).

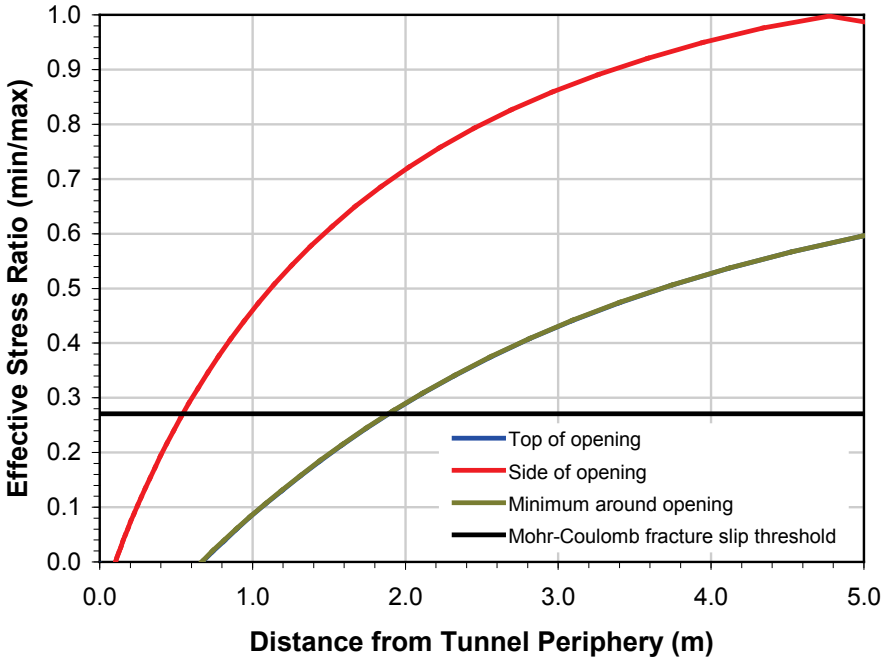

Figure 45: Ratio of Minimum to Maximum Principal Stress Relative to Mohr-Coulomb Threshold for Fracture Slip Around an AECL-Type DGR at 750 m in Limestone Under Ambient Conditions (Room Parallel to Maximum Horizontal Stress).

to within a maximum distance of 1.8 m of the excavation periphery. This zone is more extensive in the crown and invert than in the sidewall.

- Under thermal loading conditions (assuming a 56°C temperature increase), the zones of possible small-scale fracturing and fracture slip are increased in size relative to those under ambient conditions. The maximum extent of small-scale fracturing is about 1.5 m, while possible fracture slip is limited to within 2.1 m of the opening (assuming an increase in both vertical and horizontal stress with heating as per Equation 24).
- Under glacial loading conditions, small-scale fracturing is suppressed in the crown and invert, but the zone of possible fracturing in the sidewall increases to 0.5 m from the opening. The zone of possible fracture slip in the crown and invert is smaller than that under ambient conditions. Possible fracture slip is limited to within 1.5 m of the opening.
- Under combined thermal and glacial loading conditions, the zones of possible small-scale fracturing are larger, and the zones of possible fracture slip are almost identical, compared to those under ambient conditions.

Based on these analysis results, possible fracturing and fracture extension in the absence of excess pore pressure is limited to within about 2.1 m of the placement room. For rooms in the perpendicular direction, this value is 2.3 m. Therefore, large-scale fracturing around an AECL-type DGR design in limestone at 750 m depth is not considered possible.

4.3.3 KBS-3V-type In-floor Borehole Placement Design

4.3.3.1 DGR in Crystalline Rock at 500 and 1000 m Depth

Thermal-mechanical analysis of a KBS-3V-type in-floor borehole placement design was conducted by RWE-NUKEM (2003). The stated mechanical properties for the reference granite in that report included a Young's modulus of 50 GPa, and a Poisson's ratio of 0.10. These values are both low when compared to the laboratory test results for samples recovered from the Lac du Bonnet granite batholith.

The thermal analysis for this DGR design produced a similar temperature versus time response as the in-room design analysis. The rock temperature at the crown of the placement room is expected to rise from about 17°C to about 60°C after 100 years, and reach a peak of about 70°C after about 4000 years. Other parts of the rock mass closer to the UFC are expected to experience more severe temperatures.

The main findings of the RWE-NUKEM thermal-mechanical analyses are as follows:

- For placement rooms oriented parallel to the intermediate principal stress, the analyses predict that the stresses associated with excavation of the placement room and boreholes will produce some small-scale fracturing at the intersection of the borehole and placement room invert immediately after excavation.
- At the peak temperature after 6500 years, both the compressive and tensile strengths of the rock mass are exceeded in this location, and small-scale fracturing of the rock mass in the vicinity of the borehole/room intersection is expected to be more severe as a result. This prediction is consistent with observations from the Heated Failure Tests conducted at the URL (Read et al. 1997). In that experiment, breakouts in vertical

boreholes and extensile fracturing and dilation parallel to the invert of the tunnel developed as a result of the initial excavation-induced stresses and the thermal loading applied in the experiment. However, despite the near-field fracturing, the effects did not extend beyond the immediate near-field regime around the tunnel and borehole.

- For placement rooms oriented parallel to the maximum principal stress, the near-field stress conditions are less severe than in the previous case. However some small-scale fracturing is still expected under both ambient and thermal loading conditions.
- Far-field analyses produced almost identical results to the in-room case for heave at ground surface and maximum tensile stresses generated as a result of heave (see Section 4.2.2).

It appears from these preliminary analyses that although this DGR design is unlikely to produce large-scale fracturing, it is likely that there will be more severe small-scale fracturing near the intersection of the placement boreholes and the room. Based on an earlier version of the in-floor borehole placement concept, Fairhurst et al. (1996) recommended against the use of this design in high horizontal stress conditions typical of the URL to reduce near-field damage.

Results from additional analyses of a KBS-3V-type DGR design in crystalline rock at 500 and 1000 m depth conducted to support the RA are summarized in Appendix B (Cases 49 through 72 in Tables B.1 and B.2). The main findings associated with a placement room oriented parallel to the maximum horizontal stress are as follows:

- Under ambient temperature conditions, placement boreholes are expected to experience some minor small-scale compressive fracturing (spalling) at the borehole periphery. Near the bottom of the placement borehole (Figures 46 and 47), this zone is located at positions on the borehole wall that are perpendicular to the placement room axis (i.e., parallel to the minimum horizontal far-field stress). Near the top of the borehole, the positions rotate to become parallel to the placement room axis (i.e., parallel to the maximum horizontal far-field stress). Possible fracture slip and extension is limited to a small zone within a maximum distance of 0.2 m of the excavation periphery.
- Under thermal loading conditions (assuming a 56°C temperature increase), the localized zones of small-scale fracturing in the placement borehole are slightly exacerbated, and smaller zones at positions 90° to the initial zones are possible. The zone of possible fracture slip is limited to within 0.2 m of the borehole periphery (similar to ambient conditions).
- Under glacial loading conditions, small-scale fracturing and the zones of possible fracture slip are similar to ambient conditions owing to the vertical orientation of the borehole.
- Under combined thermal and glacial loading conditions, the zones of small-scale fracturing extend further from the borehole periphery than under ambient conditions. However, the zones of possible fracture slip are similar to those under ambient conditions and do not extend further than 0.2 m from the borehole periphery.

Based on these analysis results, possible fracturing and fracture extension in the absence of excess pore pressure is limited to within about 0.2 m of the placement borehole periphery, with possible localized small-scale fracturing parallel to the placement room periphery near the intersection of the placement borehole and room. For rooms in the perpendicular

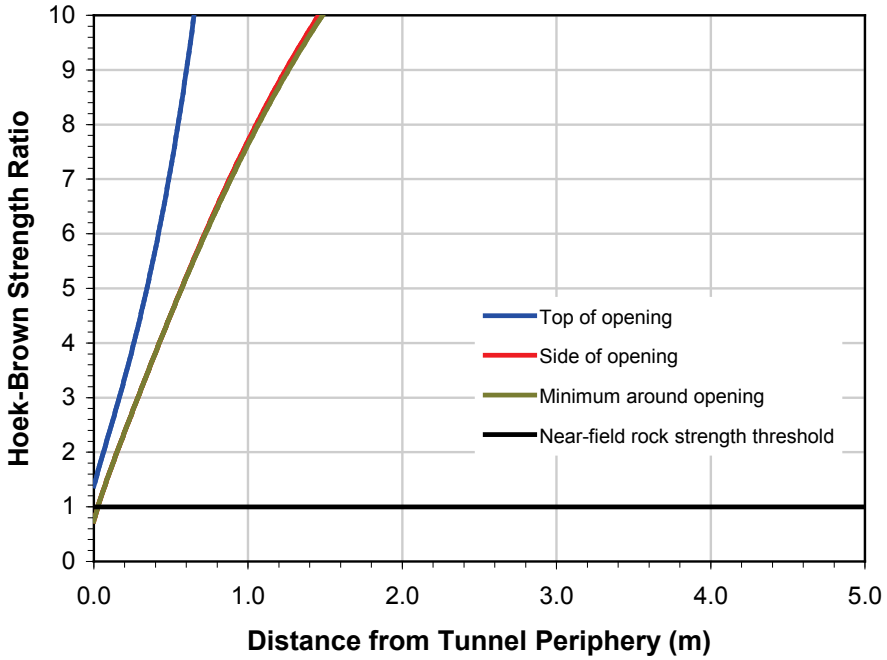

Figure 46: Hoek-Brown Strength Ratio Around a Placement Borehole in a KBS-3V-Type DGR at 500 m in Crystalline Rock Under Ambient Conditions (Room Parallel to Maximum Horizontal Stress; Data Shown are for Conditions Near the Bottom of the Borehole).

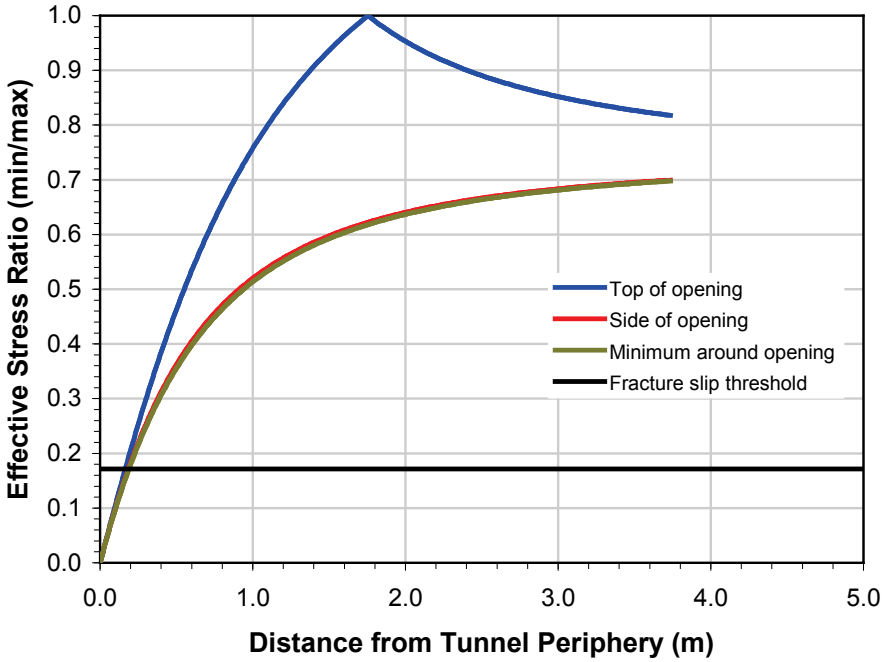

Figure 47: Ratio of Minimum to Maximum Principal Stress Relative to Mohr-Coulomb Threshold for Fracture Slip Around a Placement Borehole in a KBS-3V-Type DGR at 500 m in Crystalline Rock Under Ambient Conditions (Room Parallel to Maximum Horizontal Stress; Data Shown are for Conditions Near the Bottom of the Borehole)

direction, this value is 0.6 m. Therefore, large-scale fracturing around a KBS-3V-type DGR design in crystalline rock at 500 and 1000 m depth is not considered possible.

4.3.3.2 DGR in Shale at 500 m Depth

Formal thermal-mechanical analyses have not been conducted for a KBS-3V-type borehole placement design in sedimentary rock of the Michigan Basin. It is therefore assumed that the temperature history is similar to that in crystalline rock for the purposes of scoping analyses. Results from analyses of a KBS-3V-type DGR design in shale at 500 m depth conducted to support the RA are summarized in Appendix B (Cases 73 through 78 for conditions near the bottom of the placement borehole, and Cases 85 through 90 for conditions near the top of the placement borehole, in Tables B.1 and B.2). The main findings associated with a placement room oriented parallel to the maximum horizontal stress are as follows:

- Under ambient temperature conditions, placement boreholes are expected to experience small-scale compressive fracturing (spalling) at the borehole periphery. Near the bottom of the placement borehole (Figures 48 and 49), this zone is continuous around the opening but slightly more pronounced at positions on the borehole wall that are perpendicular to the placement room axis (i.e., parallel to the minimum horizontal far-field stress). Near the top of the borehole, the zone of small-scale fracturing is more uniform around the borehole periphery, extending to less than 0.2 m from the opening. Possible fracture slip and extension is limited to a continuous zone within a maximum distance of 0.4 m of the borehole periphery.
- Under thermal loading conditions (assuming a 56°C temperature increase), the localized zones of small-scale fracturing in the placement borehole are only slightly exacerbated. The zone of possible fracture slip is limited to within 0.4 m of the borehole periphery (similar to ambient conditions).
- Under glacial loading conditions, small-scale fracturing and the zones of possible fracture slip near the bottom of the placement borehole are similar to ambient conditions owing to the vertical orientation of the borehole. Near the top of the borehole, glacial loading induces a larger difference between the two horizontal stress components. Hence, small-scale fracturing on the borehole periphery is partly suppressed in positions parallel to the room axis, and slightly exacerbated in positions perpendicular to the room axis. The zone of possible fracture slip is limited to within 0.4 m of the borehole periphery (slightly larger than at ambient conditions).
- Under combined thermal and glacial loading conditions, the zones of small-scale fracturing extend slightly further from the borehole periphery than under ambient conditions. However, the zones of possible fracture slip are similar to those under ambient conditions and do not extend further than 0.4 m from the borehole periphery.

As discussed earlier in Section 4.3, the most severe stress concentrations in this DGR design occur at the intersection of the vertical borehole and the placement room. The stress concentrations around the borehole vary with depth. The simplified analysis approach used for this report underestimates the out-of-plane stress near the placement room. Likewise, the analysis assumes a plane strain condition for the borehole when in fact it is free to displace upward into the elliptical opening. Nevertheless, the results provide insight into the expected near-field rock mass response. Based on these analysis results, possible fracturing and fracture extension in the absence of excess pore pressure is limited to within about 0.4 m of the placement borehole periphery, with possible localized small-scale fracturing parallel to the

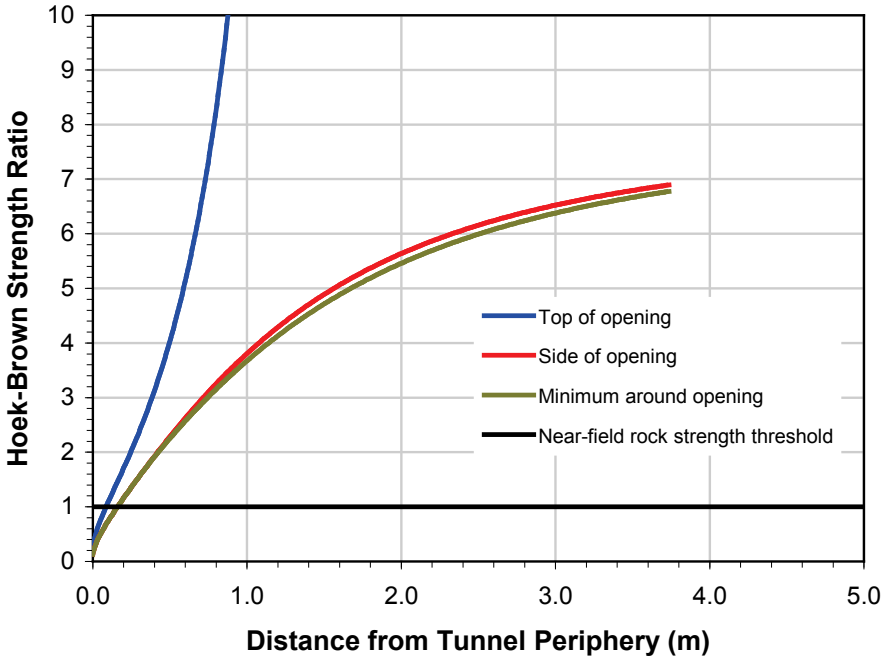

Figure 48: Hoek-Brown Strength Ratio Around a Placement Borehole in a KBS-3V-Type DGR at 500 m in Shale under Ambient Conditions (Room Parallel to Maximum Horizontal Stress; Data Shown are for Conditions Near the Bottom of the Borehole).

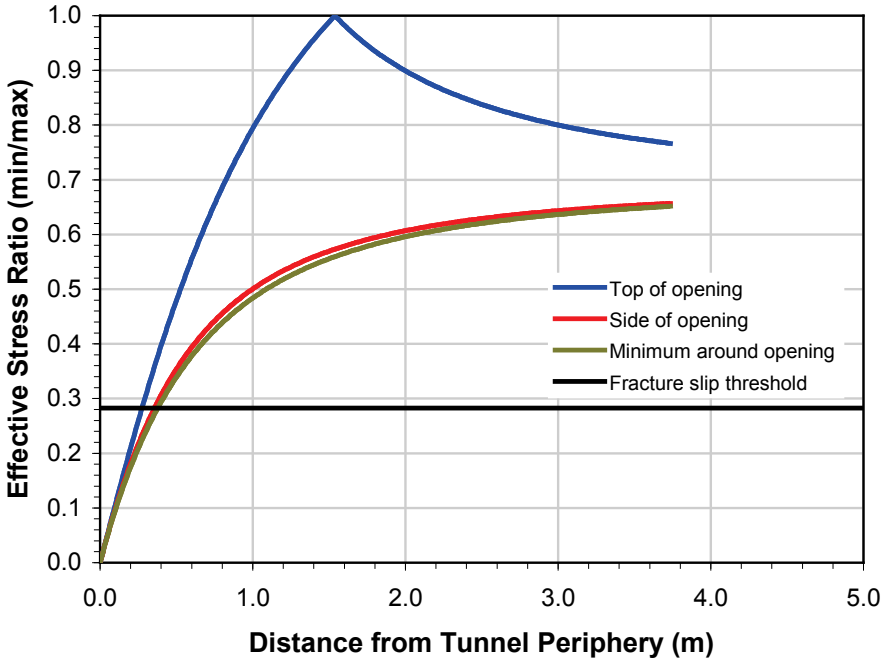

Figure 49: Ratio of Minimum to Maximum Principal Stress Relative to Mohr-Coulomb Threshold for Fracture Slip Around a Placement Borehole in a KBS-3V-Type DGR at 500 m in Shale Under Ambient Conditions (Room Parallel to Maximum Horizontal Stress; Data Shown are for Conditions Near the Bottom of the Borehole)

placement room periphery near the intersection of the placement borehole and room. For rooms in the perpendicular direction, this value is 1.3 m. Consequently, large-scale fracturing around a KBS-3V-type DGR design in shale at 500 m depth is not considered possible.

4.3.3.3 DGR in Limestone at 750 m Depth

Based on the same approach outlined in the previous section, results from analyses of a KBS-3V-type DGR design in limestone at 750 m depth conducted to support the RA are summarized in Appendix B (Cases 79 through 84 for conditions near the bottom of the placement borehole, and Cases 91 through 96 for conditions near the top of the placement borehole, in Tables B.1 and B.2). The main findings associated with a placement room oriented parallel to the maximum horizontal stress are as follows:

- Under ambient temperature conditions, placement boreholes are expected to experience small-scale compressive fracturing (spalling) at the borehole periphery. Near the bottom of the placement borehole (Figures 50 and 51), this zone is continuous around the opening but slightly more pronounced at positions on the borehole wall that are perpendicular to the placement room axis (i.e., parallel to the minimum horizontal far-field stress). Near the top of the borehole, the zone of small-scale fracturing is more uniform around the borehole periphery, extending to less than 0.2 m from the opening. Possible fracture slip and extension is limited to a continuous zone within a maximum distance of 0.3 m of the borehole periphery.
- Under thermal loading conditions (assuming a 56°C temperature increase), the localized zones of small-scale fracturing in the placement borehole are more severe, particularly in positions on the borehole periphery parallel to the room. The zone of possible fracture slip is limited to within 0.4 m of the borehole periphery (slightly larger than at ambient conditions).
- Under glacial loading conditions, small-scale fracturing and the zones of possible fracture slip near the bottom of the placement borehole are somewhat larger than those at ambient conditions. Near the top of the borehole, small-scale fracturing on the borehole periphery is partly suppressed in positions parallel to the room axis, and slightly exacerbated in positions perpendicular to the room axis. The zone of possible fracture slip is limited to within 0.4 m of the borehole periphery (slightly larger than at ambient conditions).
- Under combined thermal and glacial loading conditions, the zones of small-scale fracturing extend about twice as far from the borehole periphery than under ambient conditions. However, the zones of possible fracture slip are similar to those under ambient conditions and do not extend further than about 0.3 m from the borehole periphery.

Based on these analysis results, possible fracturing and fracture extension in the absence of excess pore pressure is limited to within about 0.3 m of the placement borehole periphery, with possible localized small-scale fracturing parallel to the placement room periphery near the intersection of the placement borehole and room. For rooms in the perpendicular direction, this value is 0.5 m. As a result, large-scale fracturing around a KBS-3V-type DGR design in limestone at 750 m depth is not considered possible.

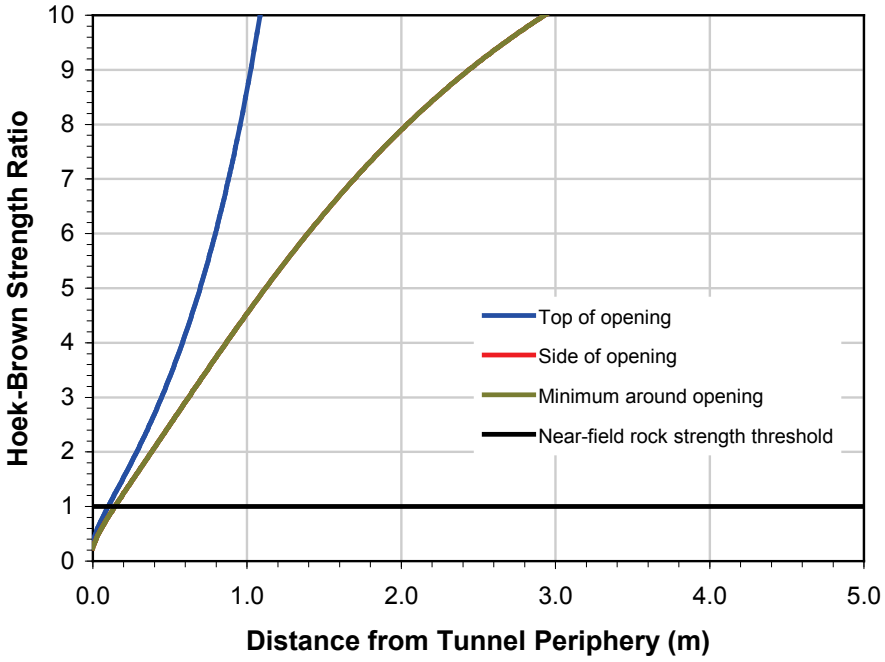

Figure 50: Hoek-Brown Strength Ratio Around a Placement Borehole in a KBS-3V-Type DGR at 750 m in Limestone Under Ambient Conditions (Room Parallel to Maximum Horizontal Stress; Data Shown are for Conditions Near the Bottom of the Borehole).

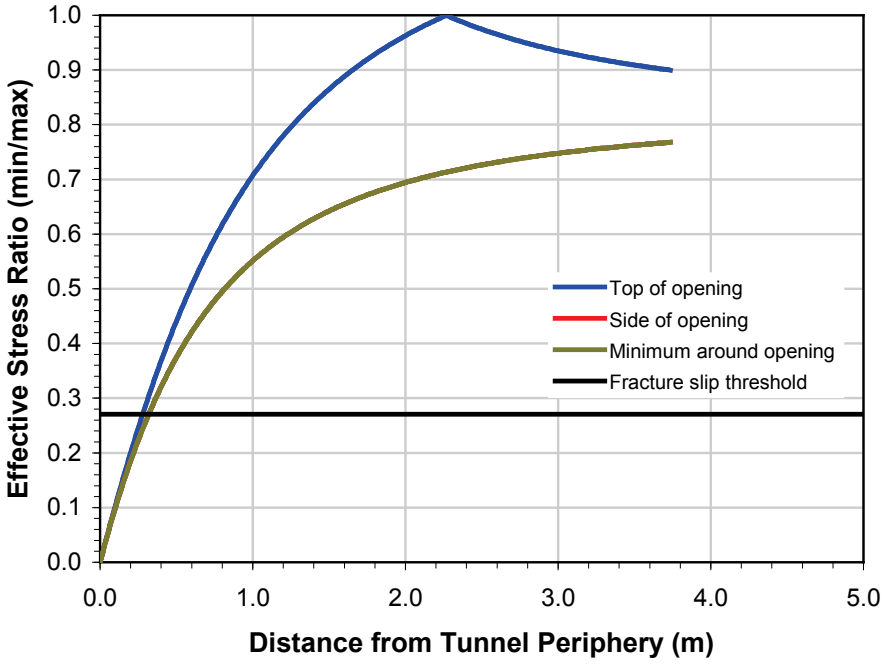

Figure 51: Ratio of Minimum to Maximum Principal Stress Relative to Mohr-Coulomb Threshold for Fracture Slip Around a Placement Borehole in a KBS-3V-Type DGR at 750 m in Limestone Under Ambient Conditions (Room Parallel to Maximum Horizontal Stress; Data Shown are for Conditions Near the Bottom of the Borehole)

4.3.4 KBS-3H-type Horizontal Borehole Placement Design

4.3.4.1 DGR in Crystalline Rock at 500 and 1000 m Depth

Thermal-mechanical analysis of a KBS-3H-type horizontal borehole placement design with borehole spacing of 55 and 70 m was conducted by RWE-NUKEM (2004a). The stated mechanical properties for Lac du Bonnet granite in that report included a Young's modulus of 60 GPa, and a Poisson's ratio of 0.10. These values differ from previous reports and should be confirmed. Alternate borehole spacing has also been considered (unpublished report).

The thermal analysis for this DGR design (RWE-NUKEM 2004a) considered the rock temperature at the bottom of the horizontal borehole. The rock temperature rises from 17°C to about 50°C after 12 years, declines to about 40°C between 100 and 1000 years, then rises again to about 45°C at 8300 years (based on a borehole spacing of 70 m). For a borehole spacing of 55 m, the initial peak at 12 years is unchanged, but the temperature between 100 and 1000 years is about 45°C, and rises to 51°C at 8300 years. These temperatures are significantly lower than those for the DGR design discussed in sections 4.2.2 and 4.2.3. Based on Equation 22, a temperature rise of 34°C will result in an increase in horizontal stress of about 29 MPa near the repository horizon, approximately 19 MPa less than that assumed in the far-field analysis.

The main findings based on results of the thermal-mechanical analyses of multiple parallel placement boreholes (RWE-NUKEM 2004a) are as follows:

- Small-scale compressive fracturing (spalling) is predicted in the crown and invert for boreholes oriented both parallel and perpendicular to the minimum horizontal stress, independent of borehole spacing, under ambient conditions.
- Thermal loading increases the severity of fracturing in these zones and introduces a small zone of radial tensile fracturing in the sidewall of the placement borehole. It is noted that the thermally-induced changes in near-field stresses are dependent on the spacing of placement boreholes assumed in the analysis.
- Far-field analyses indicate thermally-induced heave of about 0.2 m at ground surface and an associated maximum tensile stress of about -3 MPa at 10,000 years. This tensile stress zone extends from surface to a depth of 28 m, centered over the DGR. This is less than the specified design limit of 100 m (Baumgartner 2005). Extensile fracturing or reopening of existing fractures, and associated hydrogeological changes, are therefore constrained to the near surface regime.

Results from additional analyses of a KBS-3H-type DGR design in crystalline rock at 500 and 1000 m depth conducted to support the RA are summarized in Appendix B (Cases 13 through 24 in Tables B.1 and B.2). The main findings associated with a placement borehole oriented parallel to the maximum horizontal stress are as follows:

- Under ambient temperature conditions, placement boreholes are expected to experience some minor small-scale compressive fracturing (spalling) in the crown and invert of the borehole. This zone is limited to a thin skin on the order of 1 cm thick. Minor tensile fracturing is predicted to a similar extent in the sidewall at 500 m depth, but not at 1000 m depth. Possible fracture slip and extension is limited to a small zone within a maximum distance of about 1.7 m of the excavation periphery at 500 m depth, and within 0.3 m of the periphery at 1000 m depth.

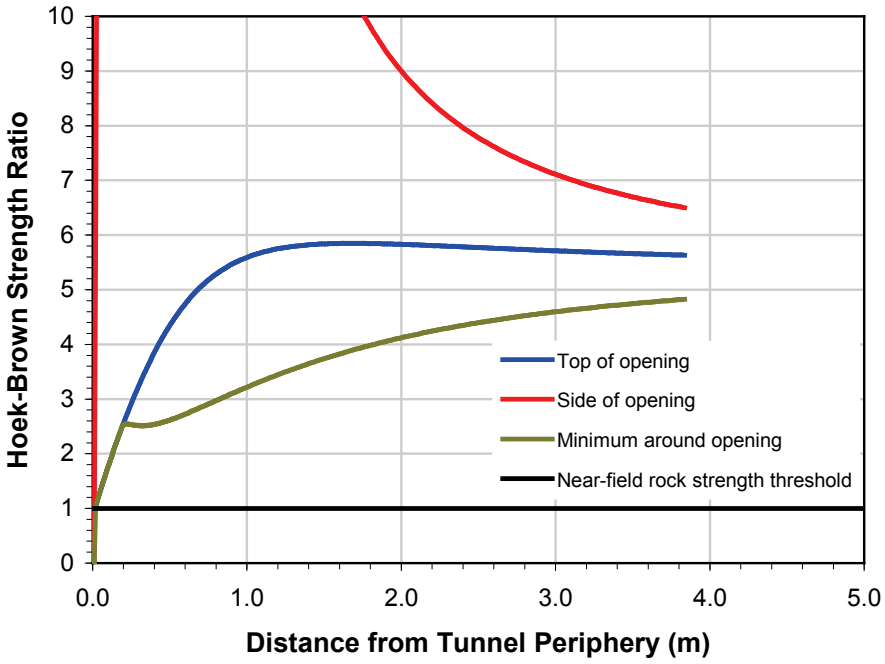

Figure 52: Hoek-Brown Strength Ratio Around a KBS-3H-Type DGR at 500 m in Crystalline Rock Under Ambient Conditions (Room Parallel to Maximum Horizontal Stress).

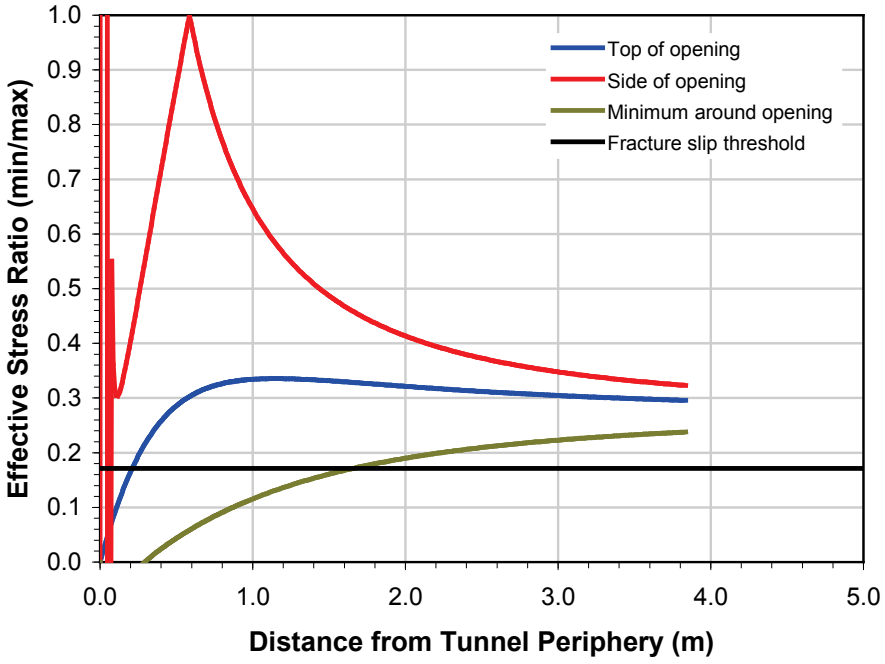

Figure 53: Ratio of Minimum to Maximum Principal Stress Relative to Mohr-Coulomb Threshold for Fracture Slip Around a KBS-3H-Type DGR at 500 m in Crystalline Rock Under Ambient Conditions (Room Parallel to Maximum Horizontal Stress)

- Under thermal loading conditions (assuming a conservative 56°C temperature increase), the localized zones of small-scale compressive fracturing in the placement borehole crown and invert are larger, but tensile fracturing in the sidewall is suppressed (assuming a thermally-induced increase in both horizontal and vertical stress as per Equation 24). The zone of possible fracture slip is limited to within 0.4 m of the borehole periphery at 500 m depth, and within 0.5 m at 1000 m depth.
- Under glacial loading conditions, small-scale compressive fracturing (spalling) in the crown and invert of the placement borehole is similar to that under ambient conditions. Tensile fracturing in the sidewall is suppressed under these conditions. The zone of possible fracture slip is limited to within 0.2 m of the borehole periphery.
- Under combined thermal and glacial loading conditions, the zones of small-scale fracturing in the crown and invert extend to about 0.1 m from the borehole periphery. Tensile fracturing in the sidewall is suppressed. The zone of possible fracture slip does not extend further than 0.3 m from the borehole periphery.

Based on these analysis results, possible fracturing and fracture extension in the absence of excess pore pressure is limited to within about 1.7 m of the placement borehole periphery in the extreme case. For rooms in the perpendicular direction, this value is 3.8 m. Therefore, large-scale fracturing around a KBS-3H-type DGR design in crystalline rock at 500 and 1000 m depth is not considered possible.

4.3.4.2 DGR in Shale at 500 m Depth

As in the previous scenarios, there have been no formal thermal-mechanical analyses conducted for a KBS-3H-type borehole placement design in sedimentary rock of the Michigan Basin. However, for the purposes of scoping analyses, it was assumed that the temperature history in sedimentary rock is similar to that in crystalline rock. A temperature rise of 56°C is assumed for thermal analyses.

The methodology used for near-field analysis of this DGR design in crystalline rock was applied to a conceptual depth of 500 m in the Queenston Formation shale. Analysis results are summarized in Appendix B (Cases 37 through 42 in Tables B.1 and B.2). The main findings associated with a placement borehole oriented parallel to the maximum horizontal stress are as follows:

- Under ambient temperature conditions (Figure 54 and 55), small-scale compressive fracturing (spalling) is expected up to a maximum distance of about 0.1 m from the crown and invert, and less than 0.1 m from the sidewall. Possible fracture slip and extension is limited to within a maximum distance of 0.4 m of the excavation periphery. This zone is slightly more extensive in the crown and invert than in the sidewall.
- Under thermal loading conditions (assuming a 56°C temperature increase), there is very little change in the extent of the possible small-scale fracturing and fracture slip owing to the relatively low Young's modulus and thermal expansion coefficient for this rock type.
- Under glacial loading conditions, the extent of possible small-scale fracturing is in the crown and invert is relatively unchanged, but the zone of possible fracturing in the sidewall increases to about 0.3 m from the opening. Compared to ambient conditions, the zone of possible fracture slip in the crown and invert is slightly smaller, but this zone

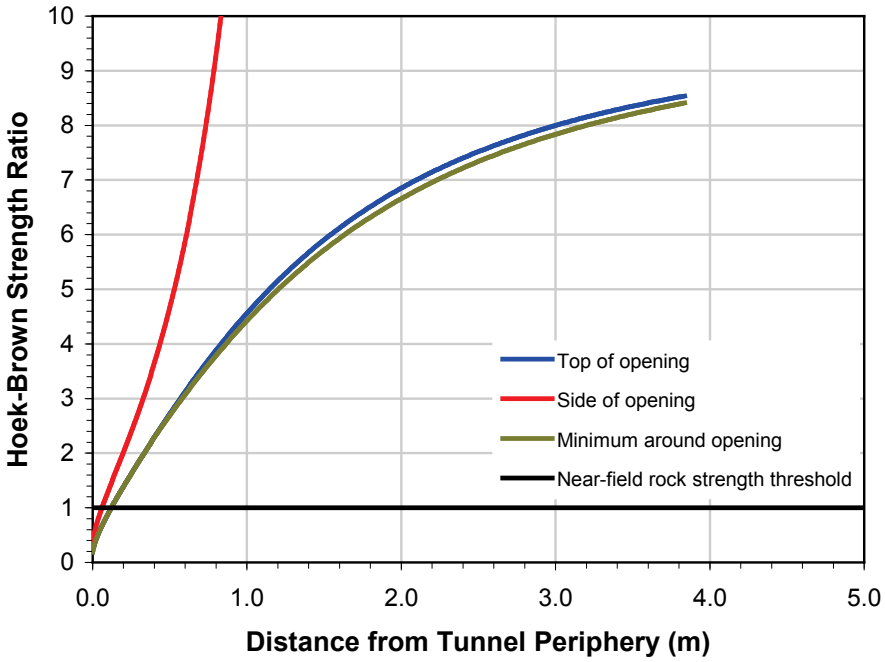

Figure 54: Hoek-Brown Strength Ratio Around a KBS-3H-Type DGR at 500 m in Shale Under Ambient Conditions (Room Parallel to Maximum Horizontal Stress).

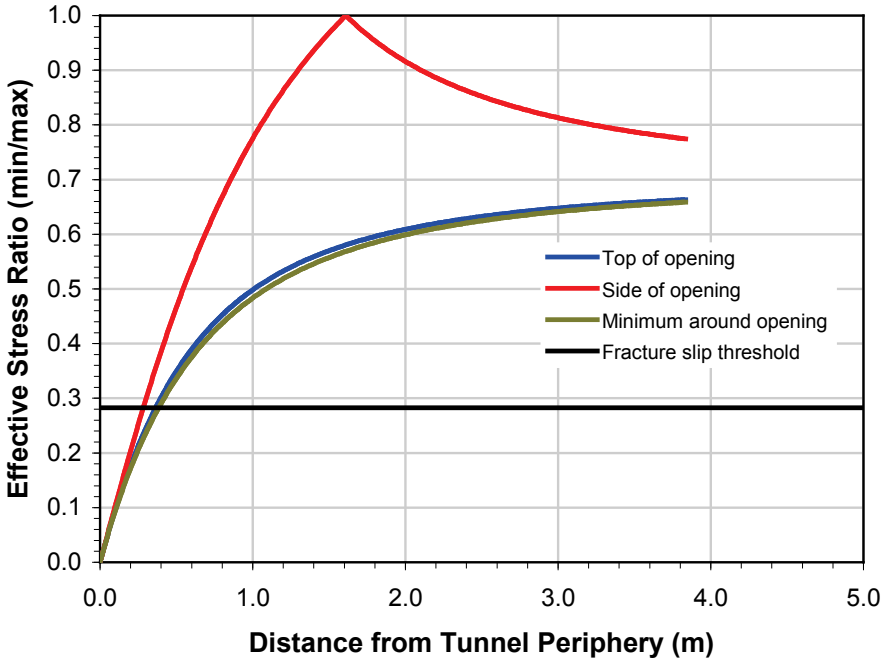

Figure 55: Ratio of Minimum to Maximum Principal Stress Relative to Mohr-Coulomb Threshold for Fracture Slip around a KBS-3H-Type DGR at 500 m in Shale Under Ambient Conditions (Room Parallel to Maximum Horizontal Stress)

is slightly larger in the sidewall. Possible fracture slip is limited to no further than 0.4 m from the opening.

- Under combined thermal and glacial loading conditions, the zones of possible small-scale fracturing and fracture slip are very similar to those under glacial loading conditions owing to the relatively minor influence of thermal loading in this rock type.

Based on these analysis results, possible fracturing and fracture extension in the absence of excess pore pressure is limited to within about 0.4 m of the placement borehole. For rooms in the perpendicular direction, this value is 0.9 m. Therefore, large-scale fracturing around a KBS-3H-type DGR design in shale at 500 m depth is not considered possible.

4.3.4.3 DGR in Limestone at 750 m Depth

The assumptions and methodology used for near-field analysis of this DGR design in shale were applied to a conceptual depth of 750 m in the Lindsay Formation limestone. Analysis results are summarized in Appendix B (Cases 43 through 48 in Tables B.1 and B.2). The main findings associated with a placement borehole oriented parallel to the maximum horizontal stress are as follows:

- Under ambient temperature conditions (Figure 56 and 57), small-scale compressive fracturing (spalling) is expected up to a maximum distance of about 0.1 m from the crown and invert, and less than 0.1 m from the sidewall. Possible fracture slip and extension is limited to within a maximum distance of 0.3 m of the excavation periphery. This zone is slightly more extensive in the crown and invert than in the sidewall.
- Under thermal loading conditions (assuming a 56°C temperature increase), there is very little change in the extent of possible small-scale fracturing in the sidewall, but the zone in the crown and invert doubles in size. The zone of possible fracture slip is relatively unchanged compared to ambient conditions, but develops up to 0.5 m in the intermediate zone between the vertical and horizontal sampling lines used in the analysis.
- Under glacial loading conditions, the extent of possible small-scale fracturing in the crown and invert is relatively unchanged, but the zone of possible fracturing in the sidewall increases to about 0.2 m from the opening. Compared to ambient conditions, the zone of possible fracture slip in the crown and invert is slightly smaller, but this zone is slightly larger in the sidewall. Possible fracture slip is limited to no further than 0.4 m from the opening.
- Under combined thermal and glacial loading conditions, the zones of possible small-scale fracturing in the crown and invert, and in the sidewall, are on the order of two times the extent of those under ambient conditions. In contrast, the zones of fracture slip are very similar to those under ambient conditions.

Based on these analysis results, possible fracturing and fracture extension in the absence of excess pore pressure is limited to within about 0.5 m of the placement borehole. For rooms in the perpendicular direction, this value is 0.6 m. Consequently, large-scale fracturing around a KBS-3H-type DGR design in limestone at 750 m depth is not considered possible.

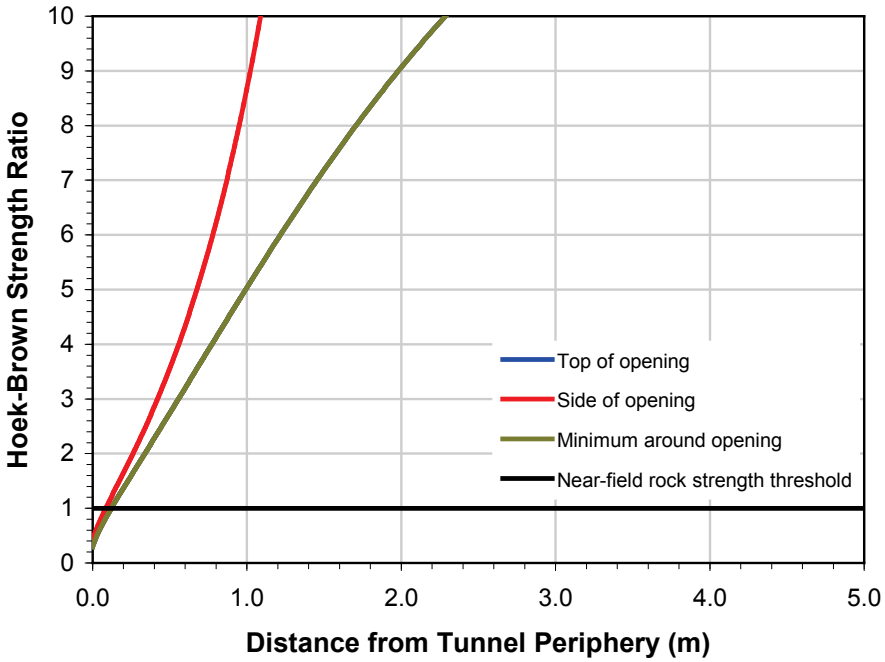

Figure 56: Hoek-Brown Strength Ratio Around a KBS-3H-Type DGR at 750 m in Limestone Under Ambient Conditions (Room Parallel to Maximum Horizontal Stress).

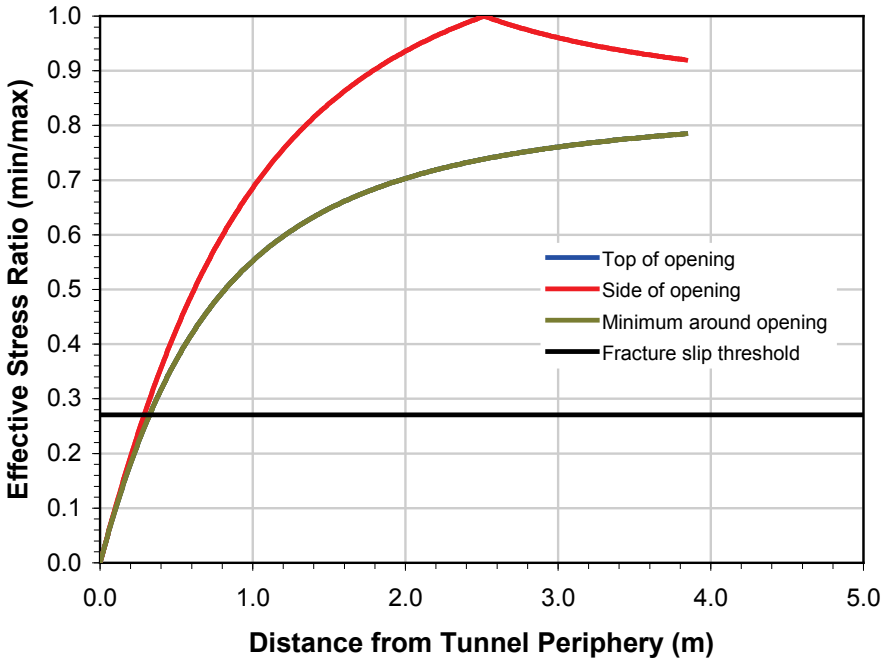

Figure 57: Ratio of Minimum to Maximum Principal Stress Relative to Mohr-Coulomb Threshold for Fracture Slip Around a KBS-3H-Type DGR at 750 m in Limestone Under Ambient Conditions (Room Parallel to Maximum Horizontal Stress)

4.3.5 NAGRA-type In-Room Placement Design

4.3.5.1 DGR in Crystalline Rock at 500 and 1000 m Depth

The NAGRA-type in-room placement concept was investigated using a range of room and UFC spacings (unpublished report). None of these cases matches the RWE-NUKEM (2004b) arrangement with rooms spaced 40 m and UFCs spaced 6.9 m within each room. The most comparable case is for a room spacing of 20 m and a UFC spacing of 6.5 m along the room axis. In this scenario, the used fuel is aged 50 years before placement, so the heat generated is less than for the 30 year old used fuel assumed by RWE-NUKEM (2004b).

For the case examined, the container temperature reaches 100°C at about 12 years after placement. The repository centre reaches a peak of 67°C at 1000 years. This value is less than that for the AECL-type in-room design, so the induced far-field thermal stresses are expected to be less severe. A full thermal-mechanical analysis of this concept has not been conducted, but would help to quantify expected effects on the rock mass.

Results from additional analyses of a NAGRA-type DGR design in crystalline rock at 500 and 1000 m depth conducted to support the RA are summarized in Appendix B (Cases 1 through 12 in Tables B.1 and B.2). The main findings associated with a placement room oriented parallel to the maximum horizontal stress are generally the same as those for the KBS-3H discussed in the previous section. However, given the different diameters of the openings in the two DGR designs, the findings are modified as follows:

- Under ambient temperature conditions (Figures 58 and 59), a thin skin of small-scale compressive fracturing (spalling) in the crown and invert of the placement room is expected. Minor tensile fracturing is predicted to a similar extent in the sidewall at 500 m depth, but not at 1000 m depth. Possible fracture slip and extension is limited to a small zone within a maximum distance of about 2.2 m of the excavation periphery at 500 m depth, and within 0.4 m of the periphery at 1000 m depth.
- Under thermal loading conditions (assuming a 56°C temperature increase), the localized zones of small-scale compressive fracturing in the placement borehole crown and invert are larger, but tensile fracturing in the sidewall is suppressed (assuming a thermally-induced increase in both horizontal and vertical stress as per Equation 24). The zone of possible fracture slip is limited to within 0.5 m of the borehole periphery at 500 m depth, and within 0.7 m of the periphery at 1000 m depth.
- Under glacial loading conditions, small-scale compressive fracturing (spalling) in the crown and invert of the placement borehole is similar to that under ambient conditions. Tensile fracturing in the sidewall is suppressed under these conditions. The zone of possible fracture slip is limited to within 0.3 m of the borehole periphery.
- Under combined thermal and glacial loading conditions, the zones of small-scale fracturing in the crown and invert extend to about 0.1 m from the borehole periphery. Tensile fracturing in the sidewall is suppressed. The zone of possible fracture slip does not extend further than about 0.4 m from the borehole periphery.

Based on these analysis results, possible fracturing and fracture extension in the absence of excess pore pressure is limited to within about 2.2 m of the placement borehole periphery in the extreme case. For rooms in the perpendicular direction, this value is 5.0 m. Therefore,

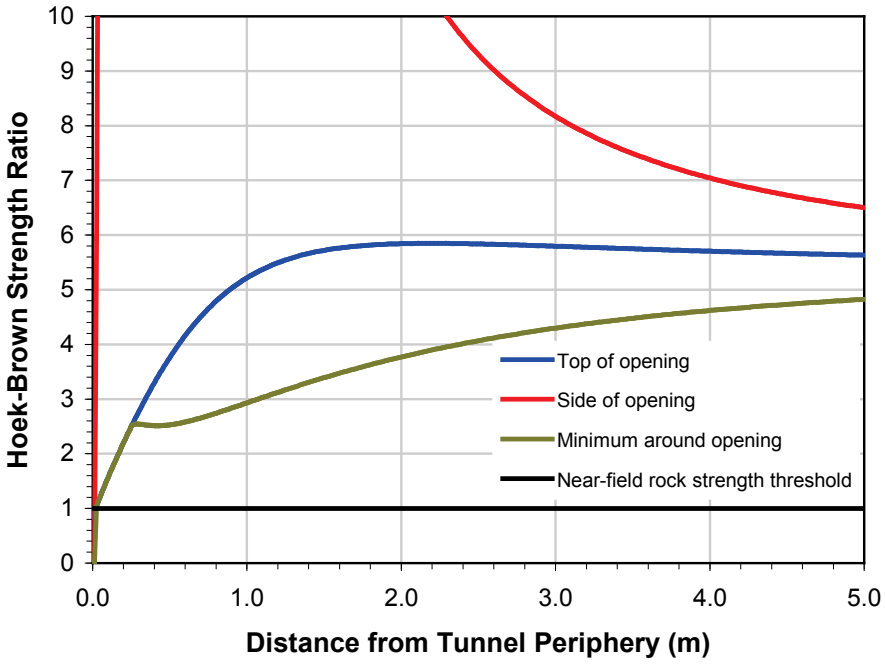

Figure 58: Hoek-Brown Strength Ratio Around a NAGRA DGR at 500 m in Crystalline Rock Under Ambient Conditions (Room Parallel to Maximum Horizontal Stress).

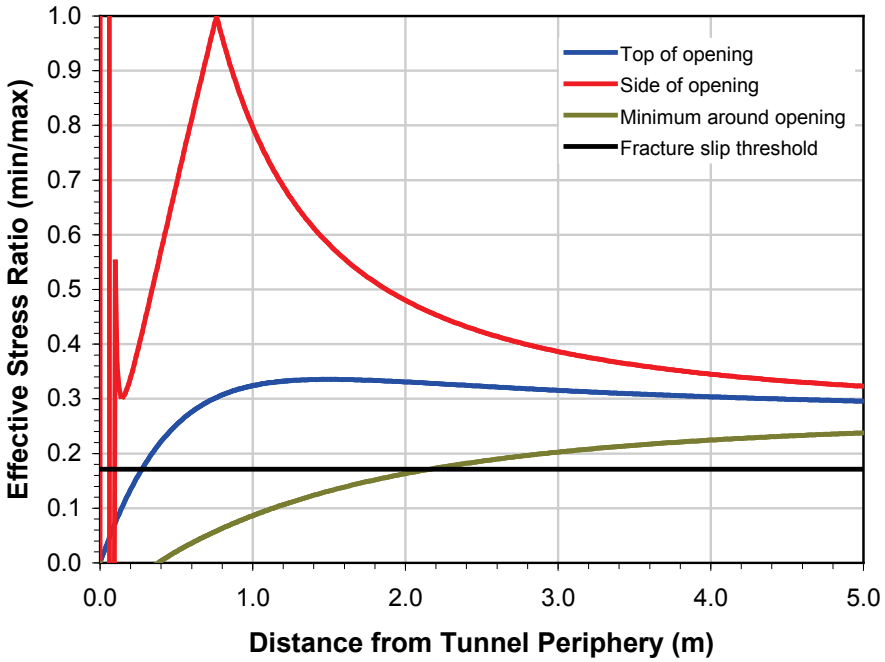

Figure 59: Ratio of Minimum to Maximum Principal Stress Relative to Mohr-Coulomb Threshold for Fracture Slip Around a NAGRA-Type DGR at 500 m in Crystalline Rock Under Ambient Conditions (Room Parallel to Maximum Horizontal Stress)

large-scale fracturing around a NAGRA-type DGR design in crystalline rock at 500 and 1000 m depth is not considered possible.

4.3.5.2 DGR in Shale at 500 m Depth

A high-level review of a NAGRA-type DGR in the sedimentary rock of the Michigan basin was completed by RWE-NUKEM (2004b). However, formal thermal-mechanical analyses have not been conducted based on the specific DGR layout in that review.

Baumgartner (2005) conducted a scoping analysis for a NAGRA-type DGR in the sedimentary rock of the Michigan Basin. He investigated a repository level at 500 m in the Queenston Formation shale. The study considered 2.5 m diameter placement rooms with a variety of room and UFC spacings. For the Queenston shale, the optimized design assumed a room spacing of 20 m and a container spacing of 12.3 m. In this scenario, the peak averaged rock temperature is 48°C at about 1500 years, representing a temperature rise of 31°C above ambient temperature. These spacings are different than those proposed by RWE-NUKEM (2004a), therefore the temperature distribution and expected thermal-mechanical response of the rock mass may differ.

Some of the more pertinent assumptions and findings from the analyses by Baumgartner (2005) are listed below:

- The analysis assumed instantaneous excavation of all openings, and accounted for the increase in vertical stress in the pillars between rooms by factoring the in situ vertical stress. For an extraction ratio of 0.125, the vertical stress used in near-field analyses was increased 12.5% relative to the far-field value. This is a reasonable approach for assessing overall performance of the repository following completion of all excavations. However, individual rooms may experience more severe near-field stresses during excavation when adjacent rooms do not yet exist.
- The ratio of the thermally-induced increase in vertical and horizontal stresses due to heating ($\Delta\sigma_{VT}/\Delta\sigma_{HT}$) was calculated as $\nu/(1-\nu)$, where ν is Poisson's ratio. This relation may over-estimate the thermally-induced increase in vertical stress depending on Poisson's ratio.
- The uniaxial compressive strength of Queenston shale was calculated to be 7.3 MPa using a Mohr-Coulomb approximation, slightly higher than the 5.9 MPa used in the current report.
- Even using this slightly higher compressive strength and more favourable near-field stress assumptions, it was concluded that self-supporting excavations cannot be developed in the Queenston Formation shale at 500 m depth. Yielding occurs in an annular zone extending up to about 0.5 m beyond the original room periphery.
- The use of rock bolts and shotcrete was recommended to provide ground support and to prevent deterioration of the shale through slaking.

Results from additional analyses of a NAGRA-type DGR design in shale at 500 depth conducted to support the RA are summarized in Appendix B (Cases 25 through 30 in Tables B.1 and B.2). The main findings associated with a placement room oriented parallel to the maximum horizontal stress are generally the same as those for the KBS-3H discussed in

the previous section. However, given the different diameters of the openings in the two DGR designs, the findings are updated as follows:

- Under ambient temperature conditions (Figure 60 and 61), small-scale compressive fracturing (spalling) is expected up to a maximum distance of about 0.2 m from the crown and invert, and less than 0.1 m from the sidewall. Possible fracture slip and extension is limited to within a maximum distance of 0.5 m of the excavation periphery. This zone is slightly more extensive in the crown and invert than in the sidewall.
- Under thermal loading conditions (assuming a 56°C temperature increase), there is very little change in the extent of the possible small-scale fracturing and fracture slip owing to the relatively low Young's modulus and thermal expansion coefficient for this rock type. This temperature increase is larger than the 31°C calculated by Baumgartner (2005), and is therefore conservative for the purposes of assessing the potential for large-scale fracturing.
- Under glacial loading conditions, the extent of possible small-scale fracturing in the crown and invert is relatively unchanged, but the zone of possible fracturing in the sidewall increases to about 0.3 m from the opening. Compared to ambient conditions, the zone of possible fracture slip in the crown and invert is slightly smaller, but this zone is slightly larger in the sidewall. Possible fracture slip is limited to no further than 0.5 m from the opening.
- Under combined thermal and glacial loading conditions, the zones of possible small-scale fracturing and fracture slip are very similar to those under glacial loading conditions owing to the relatively minor influence of thermal loading in this rock type.

These results suggest circular openings in the Queenston Formation shale will experience significant yielding around the room periphery. However, possible fracturing and fracture extension in the absence of excess pore pressure is limited to within about 0.5 m of the placement room. For rooms in the perpendicular direction, this value is 1.1 m. Therefore, large-scale fracturing around a NAGRA-type DGR design in shale at 500 m depth is not considered possible.

It should be noted that these analyses are based on assumptions of homogeneous isotropic linear elastic behaviour in shale. According to RWE-NUKEM (2004c), the Queenston shales exhibit anisotropic deformation behaviour, swell when unconfined, and weather rapidly when exposed to ventilation air. These unique characteristics are not accounted for in the analyses conducted to date, but should be assessed in more detailed analyses.

4.3.5.3 DGR in Limestone at 750 m Depth

Scoping analyses of a NAGRA-type DGR at 700 m depth in the Lindsay Formation limestone were conducted by Baumgartner (2005). The analyses used the same assumptions described in the previous section for the Queenston Formation shale, with some exceptions. These exceptions and general findings are listed below:

- The selected room spacing was 20 m and the container spacing was 14.3 m. In this latter case, the peak averaged rock temperature is 49.5°C at about 1350 years, representing a temperature rise of 29°C above ambient temperature.

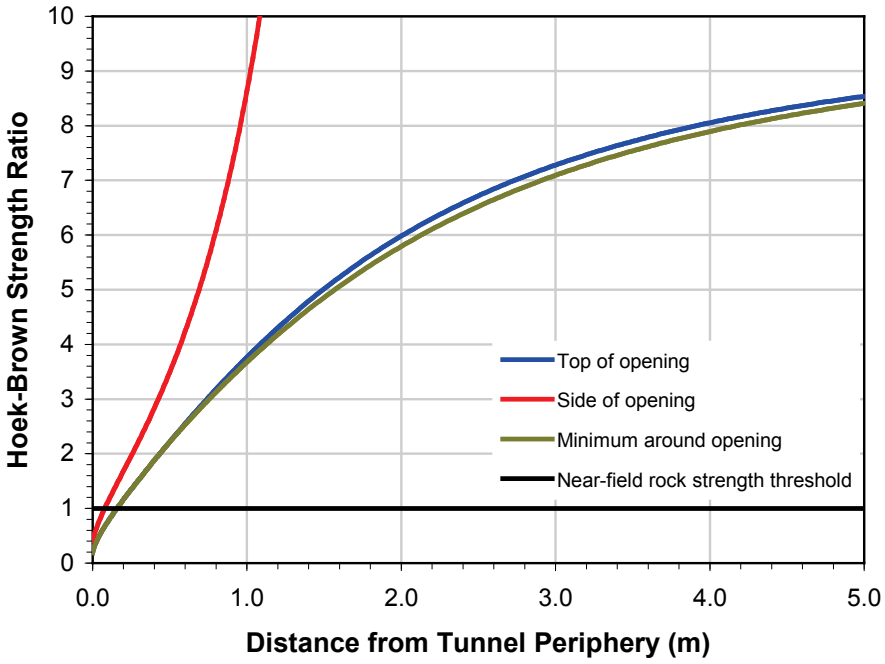

Figure 60: Hoek-Brown Strength Ratio Around a NAGRA-Type DGR at 500 m in Shale Under Ambient Conditions (Room Parallel to Maximum Horizontal Stress).

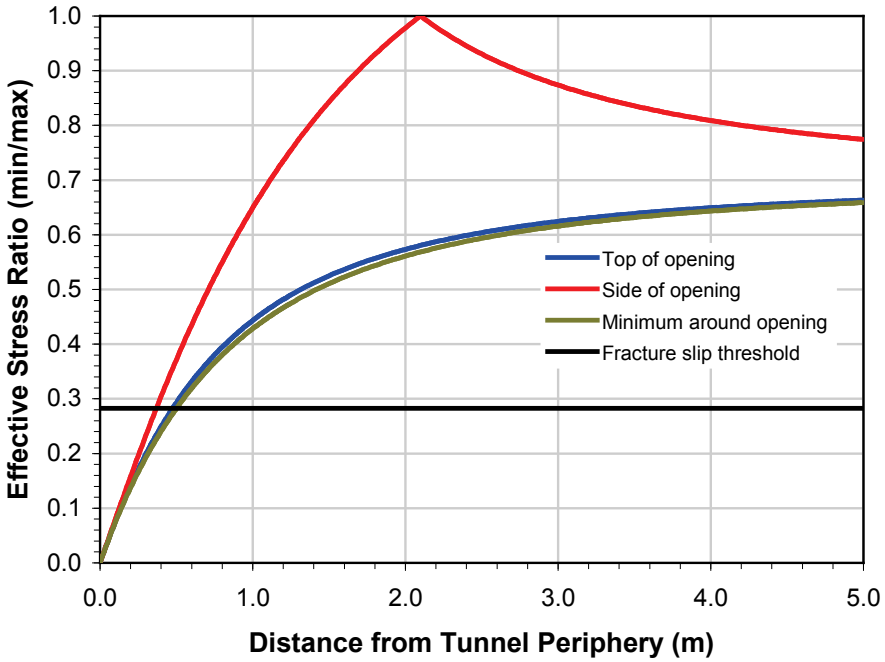

Figure 61: Ratio of Minimum to Maximum Principal Stress Relative to Mohr-Coulomb Threshold for Fracture Slip Around a NAGRA-Type DGR at 500 m in Shale Under Ambient Conditions (Room Parallel to Maximum Horizontal Stress)

- The in situ uniaxial compressive strength of Lindsay limestone was calculated as 14.9 MPa. This is slightly higher than the 13.8 MPa used in the analysis in the current report.
- Despite this slightly higher compressive strength and optimistic near-field stress assumptions, self-supporting excavations cannot be developed in the Lindsay limestone at a depth of 700 m. As in the case of Queenston Formation shale, yielding occurs in an annular zone extending up to about 0.5 m beyond the original room periphery.
- The use of spot bolting was recommended to stabilize the openings in limestone.

Results from additional analyses of a NAGRA-type DGR design in the Lindsay Formation limestone at 750 depth conducted to support the RA are summarized in Appendix B (Cases 31 through 36 in Tables B.1 and B.2). The main findings associated with a placement room oriented parallel to the maximum horizontal stress are generally the same as those for the KBS-3H discussed in the previous section. However, given the different diameters of the openings in the two DGR designs, the findings are revised as follows:

- Under ambient temperature conditions (Figure 62 and 63), small-scale compressive fracturing (spalling) is expected up to a maximum distance of less than 0.2 m from the crown and invert, and 0.1 m from the sidewall. Possible fracture slip and extension is limited to within a maximum distance of 0.4 m of the excavation periphery. This zone is slightly more extensive in the crown and invert than in the sidewall.
- Under thermal loading conditions (assuming a 56°C temperature increase), there is very little change in the extent of possible small-scale fracturing in the sidewall, but the zone in the crown and invert doubles in size. The zone of possible fracture slip is only slightly different compared to ambient conditions, but develops up to 0.7 m in the intermediate zone between the vertical and horizontal sampling lines used in the analysis.
- Under glacial loading conditions, the extent of possible small-scale fracturing in the crown and invert is relatively unchanged, but the zone of possible fracturing in the sidewall increases to about 0.3 m from the opening. Compared to ambient conditions, the zone of possible fracture slip in the crown and invert is slightly smaller, but this zone is slightly larger in the sidewall. Possible fracture slip is limited to no further than 0.5 m from the opening.
- Under combined thermal and glacial loading conditions, possible small-scale fracturing in the crown and invert, and in the sidewall, extends to about 0.3 m. This is up to three times the extent of these zones under ambient conditions. In contrast, the zones of fracture slip are very similar to those under ambient conditions.

Based on these analysis results, possible fracturing and fracture extension in the absence of excess pore pressure is limited to within about 0.7 m of the placement room. For rooms in the perpendicular direction, this value is 0.8 m. Therefore, large-scale fracturing around a NAGRA-type DGR design in limestone at 750 m depth is not considered possible.

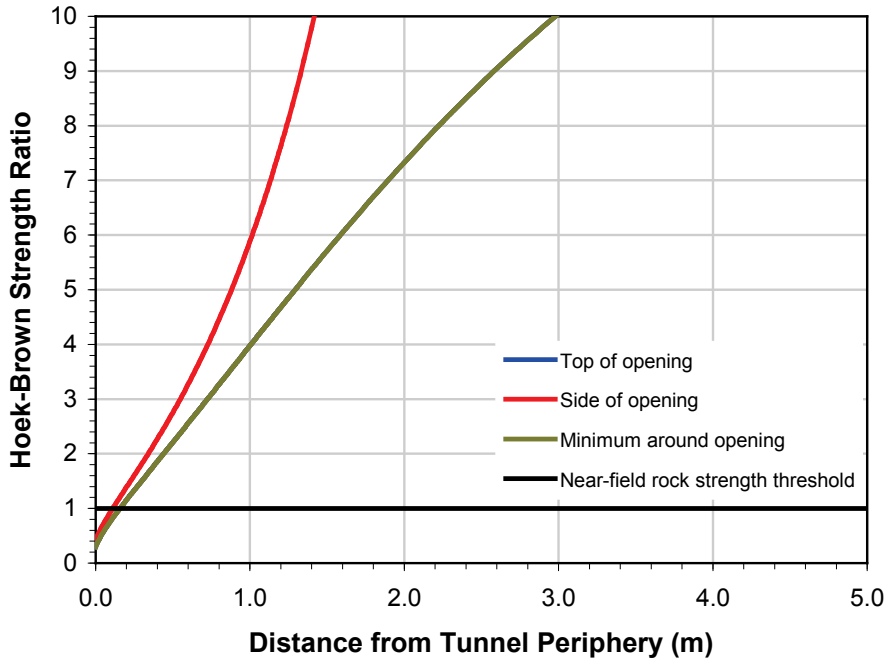

Figure 62: Hoek-Brown Strength Ratio Around a NAGRA-Type DGR at 750 m in Limestone Under Ambient Conditions (Room Parallel to Maximum Horizontal Stress).

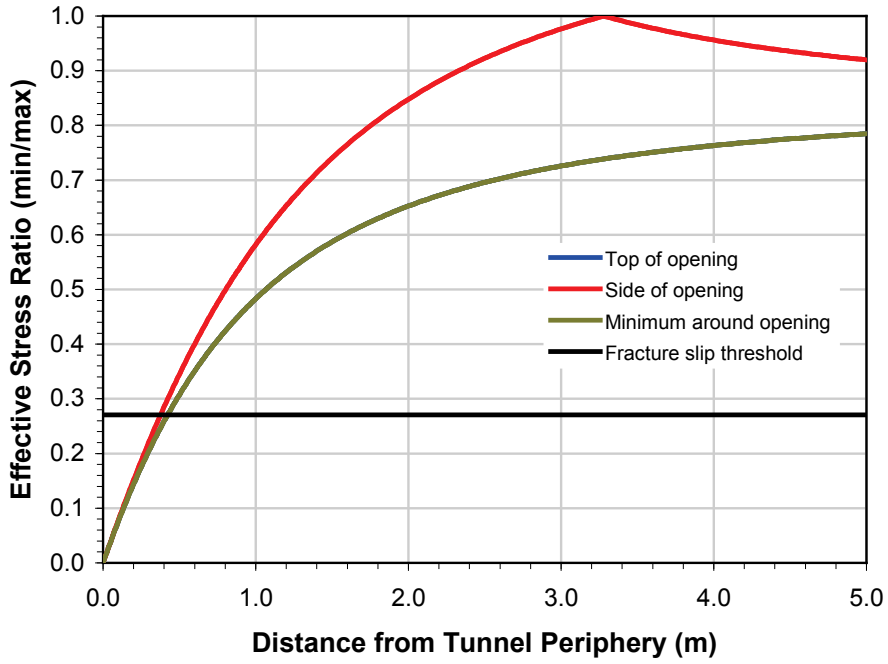

Figure 63: Ratio of Minimum to Maximum Principal Stress Relative to Mohr-Coulomb Threshold for Fracture Slip Around a NAGRA-Type DGR at 750 m in Limestone Under Ambient Conditions (Room Parallel to Maximum Horizontal Stress)

5. DISCUSSION

The analyses conducted as part of this report demonstrate that the key factors controlling large-scale fracturing and faulting are the effective in situ stress state and the rock mass strength and deformation properties. While the four specific DGR designs each created a unique near-field environment, the near-field effects were limited in all cases to less than about 2 m of the excavation periphery. Consequently, thorough characterization of in situ conditions and rock properties is critical in order to conduct a defensible assessment of rock mass response.

In general, the crystalline rock mass at the URL is well-characterized site, with in situ stress magnitudes and directions known to a high degree of certainty. However, even at this site, variability in the in situ stresses is possible near existing geological structures such as faults or fracture zones. It is not clear how representative the in situ stress state at the URL is of other potential repository sites in the Canadian Shield. While relevant rock properties have been measured for crystalline rock, the influence of lithologic variability and anisotropy on rock mass response have not been studied as thoroughly as other factors. Nonetheless, the uncertainty associated with geological variability at this site is considered to have a relatively minor effect on the assessment of the potential for large-scale fracturing and faulting.

The in situ conditions and properties of the sedimentary formations of the Michigan Basin are not well known. The effective stress state in particular has not been measured below about 300 m depth[7]. Many measurements were conducted by hydraulic fracturing, which has a number of limitations (Thompson et al. 2002). Confidence in the stress state would be improved by performing other types of stress determinations. In addition, the stress conditions in different areas of the Michigan Basin are expected to vary, so site specific data are required to conduct a defensible assessment of fracturing.

Likewise, the rock mass properties for the Queenston Formation shale and the Lindsay Formation limestone are compiled from various locations, including some outcrops and near-surface subcrops. It is likely that the fracture characteristics of these near-surface sites will differ significantly from those at depth, with fracture density likely decreasing with depth. If this is the case, then the Hoek-Brown parameters (particularly the s parameter) for the two rock types will be closer to unity, instead of less than 0.1. The resulting rock mass in situ compressive strength will then be much higher than the values used in the analyses in this report. While this refinement of estimated rock properties and in situ conditions will affect results from the near-field thermal-mechanical analyses, it is not expected to affect conclusions based on the far-field analyses. The analyses indicate that for the reference far-field stresses and any conceivable stress changes, no slip would occur along existing optimally oriented fractures. Intact rock strength was greater than the criterion for slippage along fractures, therefore propagation and creation of new large-scale fractures would not be possible in the absence of unexpected thermo-poroelastic properties associated with one of the potential host rocks.

One aspect of the Queenston Formation shale that has not been considered in the analyses is its anisotropic structure and associated deformation response. The fact that the Queenston Formation shale swells in the presence of fresh water in an unconfined state suggests that there may exist weak clayey seams within the shale that may act as preferred displacement

[7] Additional stress measurements compiled by NWMO after the time of writing were not included in these preliminary scoping analyses.

planes near openings. Since the shale will be initially saturated, shrinkage due to ventilation drying may result in some local cracking along these weak seams. Similarly, the interface between the shale and other sedimentary layers may represent a weak discontinuity upon which shear displacement will localize as the rock mass expands during heating. The analyses conducted as part of this report assumed a friction angle of 34° for discontinuities in the shale, but a weakened shale interface with softening could approach a very low friction angle (i.e., close to zero). These types of effects can be explored using a 2D numerical model that incorporates a ubiquitous joint model and interface simulation capabilities. These are general observations of shale, but strength and deformation properties may also differ from one location to another. The analyses would benefit from a comprehensive laboratory testing program to discern relevant material properties.

The initiation and propagation of new, or remobilization of existing, fractures/faults is controlled by the in situ stress conditions and the rock mass properties. Although some work has been done to characterize the crack initiation and propagation thresholds for granite (e.g., Shen and Stephansson 1996; Read et al. 1998; Martin et al. 2001), further analysis using site specific rock properties for fracture toughness, discontinuity strength, and deformation would help map out the stress regime where Mode I and Mode II fracture initiation and propagation are to be expected for different rock types.

The far-field analyses conducted as part of this report show that the computed current and future stress states due to excavation, heating and glaciation are insufficient to generate new fracturing or cause movement on existing fractures. The only mechanisms by which the stress state could be altered significantly is the generation of high pore pressures through a thermo-poroelastic response, or erosion to a great depth by glaciation, reducing the lithostatic stress. The former of these requires further analysis, especially in the shale and limestone formations. Severe glacial erosion of hundreds of metres of rock is considered unlikely over the 100,000 years following placement of used fuel, although further study in this area may be warranted.

This report corroborates the findings of Martin et al. (1994) whose analyses were based on the original AECL placement designs. Martin et al. concluded that given the compressive stress regime at the URL, large-scale Mode I fracturing is not likely. Without a significant erosional event, the fault regime in granite is not likely to change in the foreseeable future. Although thermal loading will increase the deviatoric stress, glaciation will reduce deviatoric stress and increase the mean stress, thus reducing the likelihood of future fracturing. Martin et al. (1994) emphasized that in situ stresses can vary considerably near existing faults and fracture zones, so careful site characterization is critical to assess the risk of large-scale fracturing.

Everitt and Brown (1994) examined the infillings in a subvertical fracture exposed at the 240 Level of the URL to determine a fracture propagation history. Based on their analysis, it was determined that the large subvertical fractures of this type developed relatively rapidly at the close of the batholith cooling history during a period of rapid uplift and erosion. Only very minor reactivation has occurred within the last 2000 Ma despite multiple cycles of regional deformation, rifting, uplift and erosion. This suggests that propagation of these fractures was associated primarily with the initial development of underlying thrust faults at the URL. It is anticipated that these types of subvertical fractures will remain dormant in the absence of the types of events required to radically change the stresses and topography, and that the existence of thrust faults at the base of these subvertical features will preclude vertical propagation (Fairhurst et al. 1996).

An expert panel was convened in 1994 to investigate the possibility of fracture propagation caused by a repository in the Canadian Shield (Fairhurst et al. 1996). The panel concluded that the existing thrust faults would prevent the development of new fractures or faults; any future dynamic or quasi-static faulting in the vicinity of the URL would occur by slip along the existing thrust faults. In the event of slip along the faults, any new secondary fracturing would be limited to the existing near-field fractured zone, and would be on the order of 1 m or less due to the existence of high normal compressive stresses parallel and normal to the thrust faults. Heating was considered unlikely to produce significant new fracturing but could produce small amounts of slip on existing thrust faults located within tens of metres of the repository. The panel considered it unlikely that future seismic activity on the existing faults would produce an earthquake of magnitude greater than 5.0 on the Richter scale, and that associated underground accelerations would not adversely affect the integrity of the rock mass. Any earthquake in the URL environment would have a thrust fault mechanism and would reduce pore pressure within a radius of several fault lengths for a period on the order of months before and after the earthquake. Given that the tectonic environment at the URL has been stable for at least 400 Ma, the panel concluded that no additional fracturing sufficient to compromise the integrity of a repository located several tens of metres from the thrust fault is likely to occur in the next 100,000 years (0.01 Ma).

Results from in situ experiments at the URL in Canada, including the Mine-by Experiment (Read and Martin 1996), the Heated Failure Tests (Read et al. 1997), the Excavation Stability Study (Read et al. 1997a), the Tunnel Sealing Experiment (Chandler et al. 2002), and the Thermal-Mechanical Stability Studies (Read and Chandler 2002) examined the stability of underground openings and the development of an excavation damaged zone (EDZ) under different conditions. These experiments confirm that, depending on tunnel geometry and orientation relative to the in situ stress state, excavation damage and in some cases progressive failure occur in the near-field around excavations, but are limited generally to within about 1 m of the opening. Results from the ZEDEX Experiment in Sweden (Olsson et al. 1996) confirm that excavation damage can be reduced by using tunnel boring equipment instead of drill-and-blast excavation methods in lower stress environments. Results from the Blast Damage Assessment Study (Martino and Chandler 2004) show that most of the blast damage is within 0.3 m of the excavation surface. Where stresses are high enough to yield the rock on the tunnel periphery, stress-induced damage extends beyond that produced by blasting. URL experience suggests that, although the extent and severity of stress-induced damage is relatively independent of excavation method, it is still constrained within about 1 m of the tunnel surface. These findings support the argument that near-field fracturing around underground openings will not propagate into the far-field under compressive stress conditions in the absence of very high pore pressures.

Near-term processes such as underground excavation and operation of the repository level are not expected to cause significant fracturing other than spalling that might occur in the near-field rock mass. Given the possibility of placement rooms being open for many months prior to backfilling, temporary support may be required to arrest the slow growth of extensile fractures parallel to the free surface of the opening. Backfilling the underground openings is expected to prevent deterioration of the rock mass with even a slight confining pressure of 50 kPa. Although the swelling pressure of backfill and buffer has not been explicitly accounted for in the thermal-mechanical analyses, it will inhibit the development of new fractures in the near-field once saturation is complete.

Intermediate term processes include monitoring of the DGR for up to 300 years following waste placement. During this time, the thermal effects of heating the rock mass will alter the in situ stress state, and may generate thermally-induced pore pressures. With some open access tunnels, there is the possibility of further deterioration of the rock mass in the near-field around these openings. Sealing of the remaining access tunnels will eliminate the near-field deterioration of the rock mass.

Long-term processes such as glaciation and seismicity will alter the in situ stresses, either quasi-statically in the former case or dynamically over short periods for the latter. Glaciation is not expected to promote large-scale fracturing, but rather to reduce the likelihood of new fracturing or remobilization of existing faults/fractures by decreasing the deviatoric stress and increasing the normal stress. Seismicity is not expected to cause any damage to underground facilities following backfilling, although some movement on existing faults is possible if there are highly variable stress conditions in the vicinity of these features. Any movement on existing faults is expected to be insignificant in terms of fracture initiation or propagation.

Based on the simple analyses of a preferentially inclined weak plane, shearing would occur first on a low-dipping discontinuity if the friction angle on this feature were low enough. Horizontal interfaces with very low friction angle could experience some shear displacement if shear stresses on the plane exceed shear strength. Given the post-excavation/heating thrust fault regime, fractures dipping more than about 60° would be clamped and would experience no shear displacement. In a thrust fault regime, the optimally oriented fractures to be exploited would be dipping at an angle of $(45 - \phi/2)°$. In cases where glacial loading creates a normal fault regime, the optimally oriented fractures would then be dipping at $(45 + \phi/2)°$, although mobilization of these more steeply-dipping fractures is unlikely. Each of these scenarios requires discontinuity friction angles that are significantly lower than the friction angle of freshly fractured rock. Therefore, characterization of discontinuity properties is also critical to building a defensible argument against large-scale fracturing. For the analyses in this report, friction angles are selected to represent typical fractures with no infilling, and may therefore be higher than actual discontinuity friction angle values.

The near-field analysis of the various DGR designs showed that the in-floor borehole design creates large stress concentrations at the intersection of the borehole and the invert of the placement room. Similar effects are expected at intersections of placement rooms and access tunnels. The in-floor borehole design results in predicted spalling in the borehole and uplift in the invert of the placement room, creating localized small-scale fracturing near the intersection of the borehole and room. Thermally-induced shear displacement along fractures in the invert EDZ was observed in the Heated Failure Tests (Read et al. 1997). Such fracturing does not reflect large-scale fracturing propagating away from the excavations, but is a design consideration for seals that may be constructed at a room or placement borehole scale. The cylindrical room designs were predicted to cause yielding either locally around the opening (in crystalline rock) or as a continuous annular zone (in shale and limestone). The elliptical room design was predicted to perform adequately in crystalline rock when oriented parallel to the maximum horizontal stress direction, but some spalling in crystalline rock and all-around yielding in shale and limestone are anticipated. However, in none of the cases considered was it possible for near-field fracturing to lead to large-scale fracturing or faulting.

The elliptical placement room was in many cases not the optimal shape or aspect ratio for the in situ stress field. Read and Chandler (1997) showed that an oval-like geometry produces lower peak tangential stresses than an elliptical opening if optimized to the expected stresses. In

cases where the in situ stresses are not horizontal and vertical (as for the URL), the geometry of the underground opening may result in higher stress concentrations if not adjusted for the inclined stress field (Read and Chandler 1997). The extent of near-field fracturing and damage development are limited by the stresses and stress gradients around the underground openings. Consequently, propagation of fractures within the damaged zone is considered impossible without an additional driving mechanism (e.g., increase in pore pressure by heating or by gas generation). The occurrence of significant near-field spalling and yielding may compromise the ability to retrieve UFCs from horizontal boreholes, if necessary.

Based on the field observations and experiments at the URL or the Äspö HRL, near-field fracturing in any of the three host rocks will be limited to a few different forms of small-scale cracking resulting from excavation, ventilation, heating and glaciation. These forms of cracking, none of which represent large-scale fracturing, include:

- Spalling and progressive failure in an elliptical or cylindrical room, and in vertical or horizontal placement boreholes;
- Tensile cracking in an elliptical or cylindrical room due to blasting and stress concentrations resulting from high horizontal to vertical stress ratios;
- Near-surface tensile cracking due to ventilation induced drying and shrinkage in clay shales;
- Extensile cracking parallel to the placement room or borehole surfaces, particularly in the crown and invert in high horizontal stress regimes or within 0.3 m when excavation is by blasting; and
- Microcracking in the excavation-damaged zone (EDZ), which may be represented as a plastic deformation zone in sedimentary rock.

Following closure of the repository, the possible sources for fracturing in the far-field rock mass include:

- Uplift at surface and possible subvertical extensile fracturing near surface;
- Possible generation of thermo-poroelastic fractures if pore pressures are high enough;
- Generation of localized shearing along interfaces and extensile fracturing within caprock in layered sedimentary systems; and
- Minor reactivation of thrust faults by heating, glacial loading/unloading, seismic activity or significant erosion.

None of the above potential sources of fracturing is expected to produce either subvertical fractures that extend more than 100 m below surface (i.e., beyond the near-surface zone of extension caused by heave) or more than a few metres from locally activated faults. Any anticipated stress conditions within the rock mass distant from the surface or faults are well below those strength criteria that must be exceeded to induce large-scale fracturing.

6. CONCLUSIONS AND RECOMMENDATIONS

6.1 CONCLUSIONS

The primary conclusion from the RA scoping analyses conducted to date is that the development and propagation of large-scale fracturing either between repository rooms, or between the repository level and other remote natural hydraulic pathways, is implausible. The information reviewed as part of this report supports the RA, examining six specific stress conditions for crystalline and sedimentary rock types, each at two depths. The applicability of the RA to all potential repository environments should be framed within this context. For rock mass stress, rock properties or in situ stress conditions that differ significantly from these specific cases, the RA provides an approach to assess the potential for large-scale fracturing. The essence of this approach is first to define strength criteria that must be exceeded for large-scale fracturing to occur (e.g., intact rock strength and slip along fractures), second to define expected stresses within the rock mass for given scenarios (e.g., excavation, heating and glaciation), and then test the criteria using an accepted approach (e.g., Mohr circles).

The main conclusions are as follows:

- The in situ stresses in the crystalline and sedimentary rock scenarios considered represent thrust fault regimes, with the minimum principal stress vertical. Without a substantial decrease in effective vertical stress or increase in effective horizontal stress, the current deviatoric stresses are insufficient to initiate and propagate new fractures or to remobilize existing fractures in the far-field.
- Heating of the repository level generates an increase in horizontal and (to a lesser extent) vertical stress. The magnitude of the stress change is directly proportional to Young's modulus and thermal expansion coefficient of the rock mass. The calculated stress changes in crystalline rock are significant, whereas those in limestone are less significant, and those in shale are almost negligible. However, when compared with in situ rock strength, the thermal stress increment for all rock types is sufficiently large to be given serious consideration in the analyses. These thermally-induced stresses increase the deviatoric stress in all cases. However, even with the increase in stresses, the calculated stress states are insufficient to initiate and propagate new fractures or remobilize existing fractures in the far-field.
- Glaciation causes a significant increase in the vertical stress component, and a minor increase in the horizontal stress components. For the crystalline rock scenario at 1000 m depth, this increase in the vertical stress reduces the deviatoric stress, but does not alter the thrust fault regime (i.e., the vertical stress remains the minimum principal stress). The effect is to reduce the potential for fracturing. For the sedimentary rock scenarios at 500 and 750 m depth, the increase in the vertical stress component alters the stress regime. In this analysis, glaciation results in the major principal stress switching from horizontal to vertical. In theory, the thrust fault regime is changed to a normal faulting regime, however, anticipated stress conditions either pre-glaciation or during glaciation are insufficient to mobilize thrust faults at any angle. In addition, the stress ratios resulting from glaciation are insufficient to generate new fractures in the far-field.
- The combined thermal and glacial stresses tend to reduce the overall deviatoric stress and increase the mean stress, effectively reducing the likelihood of new fracture initiation and propagation or remobilization of existing fractures or faults. For the

crystalline rock and limestone scenarios, the combined loading represents a thrust fault regime. For the shale scenario at 500 m depth, the combined stresses represent a normal fault regime with the maximum principal stress vertical (as discussed above for glaciation only). This alternation between fault regimes changes the definition of a preferentially oriented fracture or fault over time. Nonetheless, deviatoric and confining stress conditions at depth are insufficient to generate new fractures or fracture slip in the far-field.

- Near-field thermal-mechanical analyses of the various DGR concepts in the different rock types show that some excavation damage is expected near the excavations in all cases owing to the zero confining stress at the periphery of the underground opening. DGR designs with intersecting openings (e.g., the in-floor borehole concept) create higher local stress concentrations than openings of either elliptical or circular cross-sectional geometry. Both the circular and elliptical cross-sectional room designs showed predicted stress-induced yielding (small-scale excavation damage) locally around the openings The in-floor borehole design results in predicted spalling in the borehole and uplift in the invert of the placement room, possibly increasing the permeability of the connected EDZ hydraulic pathway along the room. Excavation damaged rock presents a design issue for sealing of placement boreholes and excavations but does not provide conditions for large-scale fracture propagation. The extent of the near-field effects are limited by the stresses and stress gradients around the underground openings, and so large-scale fracturing resulting from propagation of fractures within the damaged zone is not considered possible. The potential for fracture propagation by additional driving mechanisms, such as thermally-induced hydraulic fracturing, was identified as an important consideration, but was not assessed as part of this report.
- Analyses to date, with the exception of a preliminary simulation of thermo-poroelastic effects around a repository in granite (Chandler 2001), have generally not accounted for the possible generation of significant pore pressures as a result of heating the rock mass. This appears to be the only viable mechanism by which effective stresses can be reduced to the point where hydraulic fracturing is possible. However, unstable propagation of new fractures by this mechanism would require a low permeability rock mass, groundwater flow to the fracture and relatively uniform conditions in the rock mass through which the fracture propagates. Fractures initiated in the near-field by this mechanism are likely to be limited by the near-field stress gradients around underground openings. Therefore, the thermal propagation of natural hydraulic fractures (Detournay and Berchenko, 2001) is an issue only for low permeability, intact rock several metres or more away from the underground openings. This is a research topic that would benefit from additional investigation to help quantify the risk of large-scale fracturing.
- In the absence of large thermally-generated pore pressures, none of the conceived scenarios produce stress conditions that would result in the initiation and propagation of new fractures, or remobilization of existing fractures. Specifically, although glacial events have occurred subsequent to fracturing at the URL, they have had little or no effect on fracture propagation (Everitt and Brown 1994).

It is therefore concluded that the RA is supported by both the analysis results summarized in this document and practical observations from the URL and elsewhere.

6.2 RECOMMENDATIONS

To provide further support for the RA, the following recommendations are made:

- Conduct a detailed thermo-poroelastic analysis of a repository in crystalline rock to assess the likelihood of high induced pore pressures and their effect on fracture initiation and propagation.
- Obtain additional characterization data for the Lindsay Formation limestone and the Queenston Formation shale to confirm the strength and deformation properties of these rock types, and to determine representative thermo-poroelastic properties. Also obtain information about stratigraphy and interfaces between strata.
- Confirm the in situ stresses at depth in the Michigan Basin through a campaign of stress and pore pressure measurements, and compilation of existing in situ measurements.
- Conduct field and laboratory tests to confirm the in situ magnitudes of elastic modulus, Poisson's ratio and thermal expansivity with specific reference to determining the stress increase within the rock mass due to increase in temperature. Assess nonlinearity of material properties and material anisotropy.
- Perform revised thermo-mechanical analyses of thermally-induced stresses using refined rock mass properties and excavation geometries in crystalline rock, accounting for possible changes in near-field rock properties and excavation geometry associated with damage development and progressive failure of the rock mass.
- Conduct additional 2D and 3D thermal-mechanical analyses of the various DGR designs in Lindsay Formation limestone at 750 m depth, and in Queenston Formation shale at 500 m depth, accounting for the anisotropic behaviour of the shale and the layered stratigraphic section in the Michigan Basin to assess the geomechanical response near underground openings and discrete discontinuities (e.g., interfaces between shale and other rock types).
- Conduct numerical sensitivity analyses of the stress conditions in the vicinity of pre-exisiting faults and fractures to assess the range of conditions required to reactivate these features. Such analyses would benefit from field studies designed to assess the in situ thermo-mechanical fracture properties.
- Conduct additional studies on glacial effects including glacial advance/retreat, glacier-generated pore pressure, and temperature profile beneath a glacier.

ACKNOWLEDGEMENTS

The author would like to acknowledge the efforts of Dr. Neil Chandler in reviewing this document. His help in refining the scope and contents of this report is greatly appreciated.

REFERENCES

Adams, J. and J. B. Bell. 1991. Crustal stresses in Canada. In: Slemmons, D. B., E. R. Engdahl, M. D. Zoback and D. D. Blackwell (eds). Neotectonics of North America, Decade map volume to accompany the neotectonic maps, part of the Continent-scale maps of North America, Geological Society of America, 367 – 386

Adams, J. and S. Halchuk. 2003. Fourth generation seismic hazard maps of Canada: Values for over 650 Canadian localities intended for the 2005 National Building Code of Canada. Geological Survey of Canada Open File 4459. Geological Survey of Canada, Ottawa.

Ashby, M.F. and S.D. Hallam. 1986. THe failure of brittle solids containing small cracks under compressive stress states. *Acta Metall. 34*, 497-510.

Ates, Y., D. Bruneau and W.R. Ridgway. 1994. An evaluation of potential effects of seismic events on a used-fuel disposal vault. Atomic Energy of Canada Limited Technical Record, TR-623, COG-94-257.

Atkinson, G.M. and R.K. McGuire. 1993. Probability of damaging earthquakes in northwestern Ontario. Atomic Energy of Canada Limited Contractor's Report, TR-M-0023.

Atomic Energy of Canada Limited (AECL). 1994. Environmental impact statement on the concept for disposal of Canada's nuclear fuel waste. Atomic Energy of Canada Limited Report, AECL-10711, COG-93-1. Chalk River, Canada.

Barton, N.R., R. Lien, and J. Lunde. 1974. Engineering classification of rock masses for design of tunnel support. *Rock. Mech. 6(4),* 189-239.

Baumgartner, P. 2005. Scoping analyses for the design of a deep geologic repository in sedimentary rock. Ontario Power Generation, Nuclear Waste Management Division Supporting Technical Report, 06819-REP-01300-10093-R00.

Baumgartner, P. and Y. Ates. 2002. Packaging plant and repository factors affecting the selection of preferred used-fuel container geometries and capacities. Ontario Power Generation, Nuclear Waste Management Division Report, 06819-REP-01200-10064-R00.

Baumgartner, P., D.M. Bilinsky, C. Onofrei, Y. Ates, F. Bilsky, J.L. Crosthwaite and G.W. Kuzyk. 1995. The in-room emplacement method for a used-fuel disposal facility - preliminary design considerations. Atomic Energy of Canada Limited Technical Record, TR-665, COG-94-533

Baumgartner, P., D.M. Bilinsky, Y. Ates, R.S. Read, J.L. Crosthwaite and D.A. Dixon. 1996. Engineering for a disposal facility using the in-room emplacement method. Atomic Energy of Canada Limited Report, AECL-11595, COG-96-223.

Bieniawski, Z.T. 1976. Rock mass classification in rock engineering. In Proc. Exploration for Rock Engineering Symp., 1, 97-106. Cape Town: Balkema.

Birgersson, L., K. Pers and M. Wilborgh. 2001. Project JADE. Long-term function and safety comparison of repository systems. Swedish Nuclear Fuel and Waste Management Company Technical Report, TR-01-18, Stockholm.

Brady, B.H.G. and E.T. Brown. 1985. *Rock mechanics for underground mining*. George Allen and Unwin: London.

Brown, A., R.A. Everitt, C.D. Martin and C.C. Davidson. 1995. Past and future fracturing in AECL research areas in the Lake Superior Province of the Canadian Pre-Cambrian Shield: with emphasis on the Lac du Bonnet Batholith. Atomic Energy of Canada Limited Report, AECL-11214.

Chandler, N.A., B.H. Kjartanson, E.T. Kozak, C.D. Martin, and P.M. Thompson. 1992. Monitoring the geomechanical and hydrogeological response in granite for AECL Research's Buffer/Container Experiment. In Proc. 33rd U.S. Symp. on Rock Mechanics, Sante Fe, pp. 161-170. Balkema: Rotterdam.

Chandler, N. and C.D. Martin. 1994. The influence of near surface faults on in situ stresses in the Canadian Shield. In Proc. 1st North American Rock Mech. Symp., Austin, pp. 369-376. Balkema: Rotterdam.

Chandler, N.A. 2001. The incorporation of rock pore pressure in repository design and excavation stability analysis. Ontario Power Generation Inc. Report 06819-REP-01200-10068-R00.

Chandler, N., A. Cournut, D. Dixon, C. Fairhurst, F. Hansen, M. Gray, K. Hara, Y. Ishijima, E. Kozak, J. Martino, K. Masumoto, G. McCrank, Y. Sugita, P. Thompson, J. Tillerson, and B. Vignal. 2002. The five year report of the Tunnel Sealing Experiment: An international project of AECL, JNC, ANDRA and WIPP. Atomic Energy of Canada Limited Report, AECL-12727.

Cook, R.F. 1986. Crack propagation thresholds: a measure of surface energy. *J. Materials Research, 1(6)*, 852-860.

Cruden, D.M. 1983. Long-term behaviour in compression of Lac du Bonnet granite. Atomic Energy of Canada Limited Technical Record TR-211.

CTECH. 2002. Conceptual design for a deep geologic repository for used nuclear fuel: Report of a study carried out for Ontario Power Generation, New Brunswick Power, Hydro-Québec and Atomic Energy of Canada Limited. CTECH Report 1106/MD18085/REP/01.

Detournay, E. and I. Berchenko. 2001. Thermoporoelastic response in low porosity rock: characterization of material properties and numerical modeling of near-field rock pore pressures. Ontario Power Generation Nuckear Waste Management Division Report 06819-REP-01200-10067-R00.

Dixon, D.A., N.A. Chandler, S. Stroes-Gascoyne, and J. Graham. 2001. The Isothermal Buffer-Rock-Concrete Plug Interaction Test: Final Report. Ontario Power Generation Nuclear Waste Management Division Report 06819-REP-01200-10056-R00.

Drury, M.J. and T.J. Lewis. 1983. Water movement in Lac du Bonnet batholith as revealed by detailed thermal studies of three closely spaced boreholes. Tectonophysics 95, 337 351.

Eberhardt, E., D. Stead, B. Stimpson, and R.S. Read. 1997. Changes in acoustic event properties with progressive fracture damage. *Int. J. Rock Mech. & Min. Sci.*, 34:3-4, Paper No. 071B.

Engelder, T. 1993. *Stress regimes in the lithosphere.* Princeton University Press, Princeton.

Everitt, R.A. and Brown A. 1986. Subsurface geology of the Underground Research Laboratory. An overview of recent developments. In Proceedings of the 20th Information Meeting of the CNFWMP held in Winnipeg, Canada, October, 1985. AECL Technical Record TR-375. p. 146-181.

Everitt, R.A. and A. Brown. 1994. An approach for investigating fracture propagation history with application to estimating future propagation. Atomic Energy of Canada Limited Technical Record, TR 659, COG-94-513.

Everitt, R.A. and Brown A. 1996. Geological mapping of AECL Research's Underground Research Laboratory. a cross section of thrust faults and associated fractures in the roof zone of an Archean batholith. Proceedings of Fractured and Jointed Rock Masses, a Regional Conference of the International Society for Rock Mechanics. June 1-6th 1992. Granlibakken, California. Volume 1, p. 1-11

Everitt, R, A. Brown, R. Ejeckam, R. Sikorsky, and D. Woodcock. 1998. Litho-structural layering within the Archean Lac du Bonnet Batholith at AECL's Underground Research Laboratory, southeastern Manitoba. *J. Structural Geology*, Vol. 20, No. 9/10, 1291-1304.

Everitt, R.A. and E.Z. Lajtai. 2004. The influence of rock fabric on excavation damage in the Lac du Bonnet granite. *Int. J. Rock Mech. Min. Sci., 41(8)*, 1277-1303.

Fairhurst, C., S.J. Martel and C.H. Scholz. 1996. The possibility of additional mesoscopic fracturing in the vicinity of the Underground Research Laboratory, Pinawa, Canada. Expert panel on fracture propagation Report to Atomic Energy of Canada Limited, TR-M-42.

Golder Associates. 2003. LLW geotechnical feasibility study, western waste management facility, Bruce Site, Tiverton, Ontario. Report to Ontario Power Generation Inc., Golder Associates Ltd. Report 021-1570.

Hoek, E. and E.T. Brown. 1980. Underground Excavations in Rock. The Institution of Mining and Metallurgy, London.

Hoek, E, P.K. Kaiser, and W.F. Bawden. 1995. Support of underground excavations in hard rock. Balkema: Rotterdam.

Horri, H. and S. Nemat-Nasser. 1986. Brittle failure in compression: splitting, faulting and brittle-ductile transition. Phil. Trans. R. Soc. London, A 319, 337-374.

Jaeger, J.C. and N.G.W. Cook. 1979. Fundamentals of rock mechanics. 3rd Edition. Chapman and Hall: London.

Jessop, A.M. and T.J. Lewis. 1978. Heat flow and generation in the Superior Province of the Canadian Shield. Tectonophysics, 50, pp. 55 77.

Johnson, M. D., D. K. Armstrong, B. V. Sanford, P. G. Telford and M. A. Rutka 1992. Paleozoic and Mesozoic geology of Ontario. In: Thurston, P. C., H. R. Williams, R. H. Sutcliffe and G. M. Stott: Geology of Ontario. Ontario Geol. Survey Spec. Vol. 4, part 2, 907 - 1008.

Kelly, D., D.C. Peck, R.S. James. 1993. Petrography of granitic rock samples from the 420 m Level of the Underground Research Laboratory, Pinawa, Manitoba. Contractor's report to AECL Research, Laurentian University.

Kemeny, J.M. and N.G.W. Cook. 1991. Micromechanics of deformation in rocks. In S.P.Shaw, editor, *Toughening Mechanics in Quasi-brittle Materials*, Volume 2, 155-188, Klewer Academic, the Netherlands.

Lajtai, E.Z. and L.P. Bielus. 1986. Stress corrosion cracking of Lac du Bonnet granite in tension and compression. *Rock Mechanics and Rock Engineering*, 19, 71-87.

Lajtai, E.Z. and R.H. Schmidtke. 1986. Delayed failure in rock loaded in uniaxial compression. *Rock Mechanics and Rock Engineering*, 19, 11-25.

Lajtai, E.Z. 1988. The deformation, fracture and strength of Lac du Bonnet granite. Research report 19, University of Manitoba, Geological Engineering Department.

Lau, J.S.O. and N.A. Chandler. 2004. Innovative laboratory testing. *Int. J. Rock Mech. & Min. Sci.* 41 (8): 1427-1445.

Lindgren, E., S. Pettersson and J.-P. Salo. 2003. R&D program for horizontal emplacement KBS-3H. In Proc. 10th International High-Level Radioactive Waste Management Conf., 2003 March 30 – April 02, Las Vegas, Nev., American Nuclear Society.

Maak, P. and G.R. Simmons. 2001. Summary report: A screening study of used-fuel container geometric designs and emplacement methods for a deep geologic repository. Ontario Power Generation Inc. Report 06819-REP-01200-10065-R00. Toronto, Ontario.

Martin C.D. 1990. Characterizing in situ stress domains at the AECL Underground Research Laboratory. *Can. Geotech. J., 27*, pp. 631-646.

Martin, C.D. and N.A. Chandler. 1993. Stress heterogeneity and geological structures. *Int J. Rock mech. Min. Sci. & Geomech. Abstr.,* 30(7), pp. 993-999.

Martin, C.D., N.A. Chandler and A. Brown. 1994. Evaluating the potential for large-scale fracturing at a disposal vault: an example using the Underground Research Laboratory. Atomic Energy of Canada Limited Report AECL-11180, COG-94-465, September 1994.

Martin, C.D. and N.A. Chandler. 1994. The progressive fracture of Lac du Bonnet granite. *Int. J. Rock Mech. Min. Sci. & Geomech. Abstr.,* 31(6), pp. 643-659.

Martin, C.D. and N.A. Chandler. 1996. The potential for vault induced seismicity in nuclear fuel waste disposal: Experience from Canadian Mines. Atomic Energy of Canada Limited Report, AECL-11599.

Martin, C.D., R. Christiansson and J. Söderhäll. 2001. Rock stability considerations for siting and constructing a KBS-3 repository based on experiences from Äspö HRL, AECL's URL, tunnelling and mining. Swedish Nuclear Fuel and Waste Management Co. Technical Report TR-01-38.

Martino, J.B. and N.A. Chandler. 1999. Summary report on thermal hydraulic studies in granite - 1994 to 1999. Ontario Hydro, Nuclear Waste Management Division Report 06819-REP-01200-0092-R00.

Martino, J.B. and N.A. Chandler. 2004. Excavation-induced damage studies at the Underground Research Laboratory. *Int. J. Rock Mech. & Min. Sci., 41*, 1413-1426.

Mazurek, M. 2004. Long-term used nuclear fuel waste management – geoscientific review of the sedimentary sequence in souther Ontario. Institute of Geological Sciences University of Bern, Switzerland Technical Report to Ontario Power Generation Inc. TR 04-01, July 2004.

NAGRA (Nationale Genossenshaft für die Lagerung Radioaktiver Abfälle). 2002. Project Opalinus Clay: Safety Report – Demonstration of disposal feasibility for spent fuel, vitrified high-level waste and long-lived intermediate-level waste (Entsorgungsnachweis). Nationale Genossenshaft für die Lagerung Radioaktiver Abfälle Report, NAGRA Technical Report 02 05.

Novakowski, K. S. and P. A. Lapcevic. 1988. Regional hydrogeology of the Silurian and Ordovician sedimentary rock underlying Niagara Falls, Ontario, Canada. *J. Hydrogeol. 104*, 211 - 236.

Nuclear Waste Management Organization (NWMO). 2005. Choosing a way forward – the future management of Canada's used nuclear fue (final study)l. Nuclear Waste Management Organization Final Report, November 2005.

Olsson, O., S. Emsley, C. Bauer, S. Falls, L. Stenberg. 1996. ZEDEX – A study of the zone of excavation disturbance for blasted and bored tunnels. SKB International Cooperation Report, 96-03.

Ortlepp, W.D. 1992. Assessment of rockburst risk in the Underground Research Laboratory – Pinawa, Manitoba, Canada. Atomic Energy of Canada Limited Technical Record TR-M-00012, Steffen, Robertson & Kirsten Report 195524, August 1992.

Paterson, W.S.B. 1994. The Physics of Glaciers. 3rd Edition. Pergamon.

Peltier, W.R. 2002. A design basis glacier scenario. Ontario Power Generation Inc. Report, 06819-REP-01200-10069-R00.

Read, R.S. and C.D. Martin. 1992. Monitoring the excavation-induced response of granite. In (Tillerson & Wawersik eds.) Proc. 33rd U.S. Symp. on Rock Mechanics, Santa Fe, pp. 201-210. Balkema: Rotterdam.

Read, R.S. 1994. Interpreting excavation-induced displacements around a tunnel in highly stressed granite. Ph.D. Thesis, University of Manitoba, Winnipeg.

Read, R.S. and C.D. Martin. 1996. Technical summary of AECL's Mine-by Experiment. Phase 1 excavation response. Atomic Energy of Canada Limited Report, AECL-11311.

Read, R.S. and J.B. Martino. 1996. Effect of thermal stresses on progressive rock failure at AECL's Underground Research Laboratory. In Proceedings of the International Conference on Deep Geological Disposal of Radioactive Waste, Winnipeg, pp. 7-43:7-53. Canadian Nuclear Society.

Read, R.S. 1997. Effect of rock mass quality on selection of a waste emplacement option. Ontario Hydro, Nuclear Waste Management Division Report, 06819-REP-01240-0003-R00.

Read, R.S., N.A. Chandler, and E.J. Dzik. 1998. In situ strength criteria for tunnel design in highly-stressed rock masses. *Int. J. Rock Mech. & Min. Sci.*, 35(3): 261-278.

Read, R.S., J.B. Martino, N.A. Chandler, E.J. Dzik, S. Oliver, S. Falls and R.P. Young. 1997. Analysis and interpretation of AECL's Heated failure Tests. Ontario Hydro, Nuclear Waste Management Division Report, 06819-REP-01200-0070-R00.

Read, R.S. and N.A. Chandler. 2002. An approach to excavation design for a nuclear fuel waste repository – the Thermal-Mechanical Stability Study final report. Ontario Power Generation Inc. Nuclear Waste Management Division Report 06819-REP-01200-10086-R01.

Read, R.S. and N.A. Chandler. 1997. Minimizing excavation damage through tunnel design in adverse stress conditions. In Proc. 23rd General Assembly - Int. Tunnel. Assoc., World Tunnel Congress `97, Vienna, pp. 23-28. Balkema: Rotterdam.

Read, R.S., J.B. Martino, E.J. Dzik and N.A. Chandler. 1997a. Excavation Stability Study - Analysis and interpretation of results. Ontario Hydro, Nuclear Waste Management Division Report 06819-REP-01200-0028-R00.

Read, R.S. 2003. The role of tunnel design in controlling excavation damage development. In Proc. of European Commission Cluster conference and Workshop "Impact of the excavation disturbed or damaged zone (EDZ) on the performance of radioactive waste geological repositories", Nov 2004, Luxembourg, 239-244.

Read, R.S. 2004. 20 years of excavation response studies at AECL's Underground Research Laboratory. *Int. J. Rock Mech. & Min. Sci.* 41: 1251-1275.

Reinecker, J. O., M. Tingay, P. Connolly and B. Müller. 2004. The 2004 release of the World Stress Map. Available at .world-stress-map.org

Russell, S.B. and G.R. Simmons. 2003. Engineered barrier system for a deep geologic repository. In Proc. 10th Int'l High-Level Radioactive Waste Management Conf., 2003 March 30 – April 02, Las Vegas, Nev., American Nuclear Society.

RWE-NUKEM. 2004. Deep geologic repository in-floor borehole emplacement: Design changes from the in-room emplacement concept. Report to Ontario Power Generation Inc. 89125/REP/06, Issue 1, June 2004.

RWE-NUKEM. 2003. Deep geologic repository in-floor borehole design update finite element analysis. Report to Ontario Power Generation Inc. 80115/REP/01, Issue 1, June 2003.

RWE-NUKEM. 2004a. Deep geologic repository horizontal borehole design update finite element analysis. Report to Ontario Power Generation Inc. 89125/REP/05, Issue 1, May 2004.

RWE-NUKEM. 2004b. Deep geologic repository in sedimentary rock: high-level review. Nuclear Waste Management Organization Report 89148/REP/04, Issue 1, November 2004.

RWE-NUKEM. 2004c. Selection of a single representative sedimentary rock formation for the storage/disposal of used nuclear fuel. Nuclear Waste Management Organization Report 89148/REP/02, Issue 2, November 2004.

Sanford, B. V., F. J. Thompson and G. H. McFall. 1985. Plate tectonics - a possible controlling mechanism in the development of hydrocarbon traps in southwestern Ontario. Bull. Canadian Petrol. Geol. 33, 52-71.

Scholz, C.H. 1990. The mechanics of earthquakes and faulting. Cambridge University Press, Cambridge.

Selvadurai, A.P.S. and T.S. Nguyen. 1995. Scoping analysis of the coupled thermal-hydrological-mechanical behaviour of the rock mass around a nuclear fuel waste repository. In. Proc. Workshop on Hydro-Thermo-Mechanics of Engineered Clay Barriers and Geological Barriers. Montreal. McGill University.

Shen, B. and O. Stephansson. 1996. Site-94, modelling of rock fracture propagation for nuclear waste disposal. Swedish Nuclear Power Inspectorate (SKI) Report 96:18, January 1996.

Simmons, G.R. 2000. Technical specification for a screening-level study to select preferred used fuel disposal container geometries and capacities. Ontario Power Generation Inc. Technical Specification, 06819-TS-01110-10000-R00.

Simmons, G.R. and P. Baumgartner. 1994. The disposal of Canada's nuclear fuel waste: Engineering for a disposal facility. Atomic Energy of Canada Limited Report, AECL-10715, COG-93-5.

Svab, M. and E.Z. Lajtai. 1981. Microstructural control of crack growth in Lac du Bonnet granite. In L. Simpson, editor, Proc. 5th Canadian Fracture Conference, Winnipeg, 219-228. Pergamon Press.

Tait, J.C. and S. Hanna. 2001. Characteristics and radionuclide inventories of used fuel from OPG nuclear generating stations. Ontario Power Generation Inc. Report, 06819-REP-01200-10029-R00, Vol. 3.

Tait, J.C., H. Roman and C.A. Morrison. 2000. Characteristics and radionuclide inventories of used fuel from OPG nuclear generating stations. Ontario Power Generation Inc. Report, 06819-REP-01200-10029-R00, Vol. 1 and 2.

Thompson, P.M., N.A. Chandler, and J.B. Martino. 2002. An assessment of methods for the in situ determination of rock stress during siting and characterization of a geologic repository. Ontario Power Generation Nuclear Waste Management Division Report 06819-REP-01200-10094-R00.

Thorsager, P. and E. Lindgren. 2004. KBS-3H Summary report of work done during basic design. Swedish Nuclear Fuel and Waste Management Company Report, R 04-42, Stockholm.

Wilkins, B.J.S., A.R. Reich, and W.R. Wallace. 1984. Slow cracking in plutonic rocks. Atomic Energy of Canada Limited Technical Record 264.

Wilkins, B.J.S. 1987. The long-term strength of plutonic rocks. Int. J. Rock Mech. Min. Sci. & Geomech. Abstr., 24(6), 379-380.

Yuen, C. 1993. Atomic Energy of Canada Limited used-fuel disposal vault far-field thermal and thermal-mechanical analysis. Contractor's report to Atomic Energy of Canada Limited, Report 931-1721/861-1095, October 1993.

APPENDIX A: BACKGROUND ON THE ORIGINAL AECL REPOSITORY DESIGNS

Table A.1: AECL In-floor Borehole Placement Design

Component	Description
Shafts	Five vertical concrete-lined shafts ranging from 3.95 to 7.9 m excavated diameter, accessing a service shaft complex and an upcast shaft complex at opposite sides of the used fuel placement area.
Access Tunnels	A pair of horizontal central access tunnels connecting the two complexes and providing central access through the repository, with eight pairs of perpendicular horizontal access tunnels to service eight used fuel placement room panels, and a series of perimeter access tunnels connecting the panel access tunnels and the service shaft complex. The central and perimeter access tunnels are rectangular with dimensions 6 m wide by 5 m high. The placement panel access tunnels are 6 m wide and 6.5 m high.
Placement Rooms	Placement rooms are rectangular with an arched roof. Each room is 8.0 m wide with a height ranging from 5.0 m at the sidewall to 5.5 m at the centre of the room, and a length of 230 m. Placement rooms are spaced 30 m apart centreline-to-centreline, with a calculated extraction ratio of 0.267 (slightly higher than the target 0.25). There are 64 rooms per panel for a total of 512 placement rooms.
Placement Boreholes	Vertical boreholes 1.24 m in diameter and 5.0 m deep are drilled in the invert of each placement room at a centre-to-centre grid spacing of 2.1 m. There are 282 placement holes per room in three parallel lines. A total of 144,384 boreholes are required.
Used Fuel	Each fuel bundle consists of 37 used fuel elements and is about 495 mm long and 102 mm in overall diameter. Each bundle has a mass of 23.74 kg and contains 18.93 kg U, with an assumed burnup rate of 685 GJ/kg U (190 MW·h/kg U). For an assumed cooling period of 10 years out-of-reactor, the heat output is about 4.13 W/bundle.
Used Fuel Container	The used fuel container (UFC) is assumed to be a 6.35 mm thick particulate-packed titanium shell with nominal diameter of 645 mm and height of 2246 mm. Each container can accommodate 72 used fuel bundles. For an assumed cooling period of 10 years out-of-reactor, the heat output is about 297.36 W/container. Specified maximum design temperature on outside surface of the placed container is 100°C.
Waste Inventory	191,000 Mg of uranium in the form of 10.1 million used fuel bundles placed in approximately 140,136 UFCs.
Repository Footprint	Single level of placement rooms with overall footprint of approximately 2.0 km by 2.0 km assuming ideal geologic conditions

Table A.2: AECL In-Room Placement Design

Component	Description
Shafts	Five vertical concrete-lined shafts ranging from 3.95 to 7.9 m excavated diameter, accessing a service shaft complex and an upcast shaft complex at opposite sides of the used fuel placement area.
Access Tunnels	A pair of horizontal central access tunnels connecting the two complexes and providing central access through the repository, with perpendicular horizontal access tunnels to service eight used fuel placement room panels, and a series of perimeter access tunnels connecting the panel access tunnels and the service shaft complex. The central and perimeter access tunnels, as well as the placement panel tunnels, are rectangular with dimensions 10 m wide by 4.4 m high.
Placement Rooms	Placement rooms are elliptical in cross-section, nominally 7.3 m wide and 3.0 m high, with a length of 238 m. Placement rooms are spaced 30 m apart centreline-to-centreline, with a calculated extraction ratio of 0.25. There are 64 rooms per panel for a total of 512 placement rooms.
Placement Cavities	Containers are placed horizontally in a mass of precompacted buffer blocks, associated sealing materials and structures. Containers are placed two abreast at 2.21-m centre-to-centre spacing and at a longitudinal spacing of 2.7 m. There are 158 containers per room for a combined total capacity of 80,896 containers.
Used Fuel	Each fuel bundle consists of 37 used fuel elements and is about 495 mm long and 102 mm in overall diameter. Each bundle has a mass of 23.74 kg and contains 18.93 kg U, with an assumed burnup rate of 720 GJ/kg U (200 MW·h/kg U). For an assumed cooling period of 10 years out-of-reactor, the heat output is about 4.58 W/bundle.
Used Fuel Container	The used fuel container (UFC) is assumed to be a 25.4 mm thick particulate-packed copper shell with nominal diameter of 860 mm and length of 1189 mm. Each container can accommodate 72 used fuel bundles. For an assumed cooling period of 10 years out-of-reactor, the heat output is about 330 W/container. Specified maximum design temperature on outside surface of the placed container is 90°C.
Waste Inventory	110,000 Mg of uranium in the form of 5.8 million used fuel bundles placed in 80,707 containers.
Repository Footprint	Single level of placement rooms with overall footprint of approximately 2.0 km by 2.0 km assuming ideal geologic conditions

APPENDIX B: RESULTS FROM NEAR-FIELD ANALYSES OF DGR DESIGNS

Table B.1: Summary of Results for Near-field Analysis of DGR Designs (Room Parallel to Maximum Horizontal Stress)

Case	Rock Type	Depth (m)	DGR Design	Loading Condition	Maximum Distance from Opening to Threshold Intersection (m)						Inputs to Calculations									
					Near-field Hoek Brown Threshold			Mohr-Coulomb Fracture Slip Threshold			σ_H'	σ_h'	σ_v'	a	b	ϕ	σ_3'/σ_1'	m	s	σ_c
					Top	Side	Other	Top	Side	Other										
1	Crystalline	500	NAGRA	Ambient Stress	0.01	0.01	-	0.26	0.09	2.15	60	44	12	1.25	1.25	45	0.17	16.6	1.000	100
2	Crystalline	500	NAGRA	Thermal Stress ($\Delta\sigma_v$=0)	0.11	0.29	1.75	0.28	0.39	>5	108	93	12	1.25	1.25	45	0.17	16.6	1.000	100
3	Crystalline	500	NAGRA	Thermal Stress ($\Delta\sigma_v$=0.3 $\Delta\sigma_h$)	0.10	-	-	0.26	0.18	0.46	114	99	45	1.25	1.25	45	0.17	16.6	1.000	100
4	Crystalline	500	NAGRA	Glacial Stress	0.01	-	-	0.24	0.21	0.25	69	53	39	1.25	1.25	45	0.17	16.6	1.000	100
5	Crystalline	500	NAGRA	Thermal ($\Delta\sigma_v$=0) + Glacial Stress	0.11	-	-	0.26	0.16	0.78	117	102	39	1.25	1.25	45	0.17	16.6	1.000	100
6	Crystalline	500	NAGRA	Thermal ($\Delta\sigma_v$=0.3 $\Delta\sigma_h$) + Glacial Stress	0.11	-	-	0.25	0.19	0.34	123	107	55	1.25	1.25	45	0.17	16.6	1.000	100
7	Crystalline	1000	NAGRA	Ambient Stress	0.01	-	-	0.25	0.19	0.35	63	47	24	1.25	1.25	45	0.17	16.6	1.000	100
8	Crystalline	1000	NAGRA	Thermal Stress ($\Delta\sigma_v$=0)	0.11	0.08	0.11	0.28	0.13	2.73	112	96	24	1.25	1.25	45	0.17	16.6	1.000	100
9	Crystalline	1000	NAGRA	Thermal Stress ($\Delta\sigma_v$=0.3 $\Delta\sigma_h$)	0.11	-	-	0.26	0.16	0.70	117	101	40	1.25	1.25	45	0.17	16.6	1.000	100
10	Crystalline	1000	NAGRA	Glacial Stress	0.01	-	-	0.24	0.23	0.24	72	56	51	1.25	1.25	45	0.17	16.6	1.000	100
11	Crystalline	1000	NAGRA	Thermal ($\Delta\sigma_v$=0) + Glacial Stress	0.11	-	-	0.25	0.19	0.39	121	105	51	1.25	1.25	45	0.17	16.6	1.000	100
12	Crystalline	1000	NAGRA	Thermal ($\Delta\sigma_v$=0.3 $\Delta\sigma_h$) + Glacial Stress	0.11	-	-	0.25	0.20	0.28	126	110	67	1.25	1.25	45	0.17	16.6	1.000	100
13	Crystalline	500	KBS-3H	Ambient Stress	0.01	0.01	-	0.20	0.07	1.65	60	44	12	0.96	0.96	45	0.17	16.6	1.000	100
14	Crystalline	500	KBS-3H	Thermal Stress ($\Delta\sigma_v$=0)	0.09	0.22	1.34	0.21	0.30	>5	108	93	12	0.96	0.96	45	0.17	16.6	1.000	100
15	Crystalline	500	KBS-3H	Thermal Stress ($\Delta\sigma_v$=0.3 $\Delta\sigma_h$)	0.08	-	-	0.20	0.13	0.35	114	99	45	0.96	0.96	45	0.17	16.6	1.000	100
16	Crystalline	500	KBS-3H	Glacial Stress	0.01	-	-	0.18	0.16	0.19	69	53	39	0.96	0.96	45	0.17	16.6	1.000	100
17	Crystalline	500	KBS-3H	Thermal ($\Delta\sigma_v$=0) + Glacial Stress	0.09	-	-	0.20	0.12	0.59	117	102	39	0.96	0.96	45	0.17	16.6	1.000	100
18	Crystalline	500	KBS-3H	Thermal ($\Delta\sigma_v$=0.3 $\Delta\sigma_h$) + Glacial Stress	0.09	-	-	0.19	0.14	0.26	123	107	55	0.96	0.96	45	0.17	16.6	1.000	100
19	Crystalline	1000	KBS-3H	Ambient Stress	0.01	-	-	0.19	0.14	0.27	63	47	24	0.96	0.96	45	0.17	16.6	1.000	100
20	Crystalline	1000	KBS-3H	Thermal Stress ($\Delta\sigma_v$=0)	0.09	0.06	0.09	0.21	0.10	2.09	112	96	24	0.96	0.96	45	0.17	16.6	1.000	100
21	Crystalline	1000	KBS-3H	Thermal Stress ($\Delta\sigma_v$=0.3 $\Delta\sigma_h$)	0.09	-	-	0.20	0.12	0.54	117	101	40	0.96	0.96	45	0.17	16.6	1.000	100
22	Crystalline	1000	KBS-3H	Glacial Stress	0.01	-	-	0.18	0.17	0.18	72	56	51	0.96	0.96	45	0.17	16.6	1.000	100
23	Crystalline	1000	KBS-3H	Thermal ($\Delta\sigma_v$=0) + Glacial Stress	0.09	-	-	0.19	0.14	0.30	121	105	51	0.96	0.96	45	0.17	16.6	1.000	100
24	Crystalline	1000	KBS-3H	Thermal ($\Delta\sigma_v$=0.3 $\Delta\sigma_h$) + Glacial Stress	0.09	-	-	0.19	0.15	0.21	126	110	67	0.96	0.96	45	0.17	16.6	1.000	100
25	Shale	500	NAGRA	Ambient Stress	0.15	0.08	-	0.46	0.36	0.50	20	14	9	1.25	1.25	34	0.28	4.3	0.022	40
26	Shale	500	NAGRA	Thermal Stress ($\Delta\sigma_v$=0)	0.18	0.06	-	0.49	0.34	0.58	22	15	9	1.25	1.25	34	0.28	4.3	0.022	40
27	Shale	500	NAGRA	Thermal Stress ($\Delta\sigma_v$=0.3 $\Delta\sigma_h$)	0.18	0.08	-	0.48	0.35	0.54	22	16	10	1.25	1.25	34	0.28	4.3	0.022	40
28	Shale	500	NAGRA	Glacial Stress	0.19	0.34	-	0.36	0.48	0.50	31	25	37	1.25	1.25	34	0.28	4.3	0.022	40
29	Shale	500	NAGRA	Thermal ($\Delta\sigma_v$=0) + Glacial Stress	0.21	0.33	-	0.38	0.46	0.48	33	27	37	1.25	1.25	34	0.28	4.3	0.022	40
30	Shale	500	NAGRA	Thermal ($\Delta\sigma_v$=0.3 $\Delta\sigma_h$) + Glacial Stress	0.21	0.34	-	0.38	0.46	0.48	33	27	37	1.25	1.25	34	0.28	4.3	0.022	40
31	Limestone	750	NAGRA	Ambient Stress	0.15	0.10	-	0.41	0.38	0.41	26	22	18	1.25	1.25	35	0.27	3.9	0.053	60
32	Limestone	750	NAGRA	Thermal Stress ($\Delta\sigma_v$=0)	0.33	-	0.41	0.51	0.28	1.38	48	43	18	1.25	1.25	35	0.27	3.9	0.053	60
33	Limestone	750	NAGRA	Thermal Stress ($\Delta\sigma_v$=0.3 $\Delta\sigma_h$)	0.33	0.10	-	0.48	0.31	0.65	51	46	26	1.25	1.25	35	0.27	3.9	0.053	60
34	Limestone	750	NAGRA	Glacial Stress	0.19	0.30	-	0.35	0.44	0.45	38	33	45	1.25	1.25	35	0.27	3.9	0.053	60
35	Limestone	750	NAGRA	Thermal ($\Delta\sigma_v$=0) + Glacial Stress	0.33	0.25	-	0.43	0.38	0.43	59	55	45	1.25	1.25	35	0.27	3.9	0.053	60
36	Limestone	750	NAGRA	Thermal ($\Delta\sigma_v$=0.3 $\Delta\sigma_h$) + Glacial Stress	0.34	0.29	-	0.41	0.39	-	63	58	53	1.25	1.25	35	0.27	3.9	0.053	60
37	Shale	500	KBS-3H	Ambient Stress	0.12	0.06	-	0.35	0.28	0.38	20	14	9	0.96	0.96	34	0.28	4.3	0.022	40
38	Shale	500	KBS-3H	Thermal Stress ($\Delta\sigma_v$=0)	0.13	0.05	-	0.37	0.26	0.44	22	15	9	0.96	0.96	34	0.28	4.3	0.022	40
39	Shale	500	KBS-3H	Thermal Stress ($\Delta\sigma_v$=0.3 $\Delta\sigma_h$)	0.13	0.06	-	0.36	0.27	0.41	22	16	10	0.96	0.96	34	0.28	4.3	0.022	40
40	Shale	500	KBS-3H	Glacial Stress	0.14	0.26	-	0.28	0.36	0.38	31	25	37	0.96	0.96	34	0.28	4.3	0.022	40
41	Shale	500	KBS-3H	Thermal ($\Delta\sigma_v$=0) + Glacial Stress	0.16	0.25	-	0.29	0.35	0.36	33	27	37	0.96	0.96	34	0.28	4.3	0.022	40
42	Shale	500	KBS-3H	Thermal ($\Delta\sigma_v$=0.3 $\Delta\sigma_h$) + Glacial Stress	0.16	0.26	-	0.29	0.35	0.36	33	27	37	0.96	0.96	34	0.28	4.3	0.022	40
43	Limestone	750	KBS-3H	Ambient Stress	0.12	0.08	-	0.32	0.29	0.32	26	22	18	0.96	0.96	35	0.27	3.9	0.053	60
44	Limestone	750	KBS-3H	Thermal Stress ($\Delta\sigma_v$=0)	0.25	-	0.32	0.39	0.21	1.05	48	43	18	0.96	0.96	35	0.27	3.9	0.053	60
45	Limestone	750	KBS-3H	Thermal Stress ($\Delta\sigma_v$=0.3 $\Delta\sigma_h$)	0.25	0.08	-	0.36	0.24	0.50	51	46	26	0.96	0.96	35	0.27	3.9	0.053	60
46	Limestone	750	KBS-3H	Glacial Stress	0.14	0.23	-	0.27	0.34	0.35	38	33	45	0.96	0.96	35	0.27	3.9	0.053	60
47	Limestone	750	KBS-3H	Thermal ($\Delta\sigma_v$=0) + Glacial Stress	0.25	0.19	-	0.33	0.29	0.33	59	55	45	0.96	0.96	35	0.27	3.9	0.053	60
48	Limestone	750	KBS-3H	Thermal ($\Delta\sigma_v$=0.3 $\Delta\sigma_h$) + Glacial Stress	0.26	0.22	-	0.32	0.30	-	63	58	53	0.96	0.96	35	0.27	3.9	0.053	60
49	Crystalline	500	KBS-3V(bottom)	Ambient Stress	-	0.02	-	0.16	0.18	0.19	60	44	12	0.93	0.93	45	0.17	16.6	1.000	100
50	Crystalline	500	KBS-3V(bottom)	Thermal Stress ($\Delta\sigma_v$=0)	0.05	0.07	-	0.17	0.18	0.18	108	93	12	0.93	0.93	45	0.17	16.6	1.000	100
51	Crystalline	500	KBS-3V(bottom)	Thermal Stress ($\Delta\sigma_v$=0.3 $\Delta\sigma_h$)	0.06	0.07	-	0.17	0.18	-	114	99	45	0.93	0.93	45	0.17	16.6	1.000	100
52	Crystalline	500	KBS-3V(bottom)	Glacial Stress	-	0.04	-	0.16	0.18	0.18	69	53	39	0.93	0.93	45	0.17	16.6	1.000	100
53	Crystalline	500	KBS-3V(bottom)	Thermal ($\Delta\sigma_v$=0) + Glacial Stress	0.06	0.08	-	0.17	0.18	0.18	117	102	39	0.93	0.93	45	0.17	16.6	1.000	100
54	Crystalline	500	KBS-3V(bottom)	Thermal ($\Delta\sigma_v$=0.3 $\Delta\sigma_h$) + Glacial Stress	0.06	0.08	-	0.17	0.18	0.18	123	107	55	0.93	0.93	45	0.17	16.6	1.000	100
55	Crystalline	1000	KBS-3V(bottom)	Ambient Stress	-	0.03	-	0.16	0.18	0.19	63	47	24	0.93	0.93	45	0.17	16.6	1.000	100
56	Crystalline	1000	KBS-3V(bottom)	Thermal Stress ($\Delta\sigma_v$=0)	0.05	0.07	-	0.17	0.18	0.18	112	96	24	0.93	0.93	45	0.17	16.6	1.000	100
57	Crystalline	1000	KBS-3V(bottom)	Thermal Stress ($\Delta\sigma_v$=0.3 $\Delta\sigma_h$)	0.06	0.08	-	0.17	0.18	0.18	117	101	40	0.93	0.93	45	0.17	16.6	1.000	100
58	Crystalline	1000	KBS-3V(bottom)	Glacial Stress	-	0.04	-	0.16	0.18	0.18	72	56	51	0.93	0.93	45	0.17	16.6	1.000	100
59	Crystalline	1000	KBS-3V(bottom)	Thermal ($\Delta\sigma_v$=0) + Glacial Stress	0.06	0.08	-	0.17	0.18	0.18	121	105	51	0.93	0.93	45	0.17	16.6	1.000	100
60	Crystalline	1000	KBS-3V(bottom)	Thermal ($\Delta\sigma_v$=0.3 $\Delta\sigma_h$) + Glacial Stress	0.07	0.08	-	0.17	0.18	0.18	126	110	67	0.93	0.93	45	0.17	16.6	1.000	100

Table B.1 (concluded)

Case	Rock Type	Depth (m)	DGR Design	Loading Condition	Maximum Distance from Opening to Threshold Intersection (m)						Inputs to Calculations									
					Near-field Hoek Brown Threshold			Mohr-Coulomb Fracture Slip Threshold			σ_H'	σ_h'	σ_v'	a	b	ϕ	σ_3'/σ_1'	m	s	σ_c
					Top	Side	Other	Top	Side	Other										
61	Crystalline	500	KBS-3V(top)	Ambient Stress	0.06	-	-	0.19	0.16	0.19	60	84	0	0.93	0.93	45	0.17	16.6	1.000	100
62	Crystalline	500	KBS-3V(top)	Thermal Stress ($\Delta\sigma_v$=0)	0.15	0.03	-	0.19	0.15	0.22	108	189	1	0.93	0.93	45	0.17	16.6	1.000	100
63	Crystalline	500	KBS-3V(top)	Thermal Stress ($\Delta\sigma_v$=0.3 $\Delta\sigma_h$)	0.13	0.05	-	0.19	0.16	0.20	114	170	1	0.93	0.93	45	0.17	16.6	1.000	100
64	Crystalline	500	KBS-3V(top)	Glacial Stress	0.04	0.02	-	0.18	0.17	0.18	69	76	1	0.93	0.93	45	0.17	16.6	1.000	100
65	Crystalline	500	KBS-3V(top)	Thermal ($\Delta\sigma_v$=0) + Glacial Stress	0.14	0.05	-	0.19	0.16	0.20	117	182	1	0.93	0.93	45	0.17	16.6	1.000	100
66	Crystalline	500	KBS-3V(top)	Thermal ($\Delta\sigma_v$=0.3 $\Delta\sigma_h$) + Glacial Stress	0.14	0.06	-	0.19	0.16	0.19	123	178	1	0.93	0.93	45	0.17	16.6	1.000	100
67	Crystalline	1000	KBS-3V(top)	Ambient Stress	0.05	0.00	-	0.18	0.17	0.18	63	79	0	0.93	0.93	45	0.17	16.6	1.000	100
68	Crystalline	1000	KBS-3V(top)	Thermal Stress ($\Delta\sigma_v$=0)	0.15	0.04	-	0.19	0.15	0.21	112	185	1	0.93	0.93	45	0.17	16.6	1.000	100
69	Crystalline	1000	KBS-3V(top)	Thermal Stress ($\Delta\sigma_v$=0.3 $\Delta\sigma_h$)	0.14	0.05	-	0.19	0.16	0.20	117	180	1	0.93	0.93	45	0.17	16.6	1.000	100
70	Crystalline	1000	KBS-3V(top)	Glacial Stress	0.03	0.03	-	0.17	0.17	-	72	72	1	0.93	0.93	45	0.17	16.6	1.000	100
71	Crystalline	1000	KBS-3V(top)	Thermal ($\Delta\sigma_v$=0) + Glacial Stress	0.14	0.06	-	0.19	0.16	0.20	121	177	1	0.93	0.93	45	0.17	16.6	1.000	100
72	Crystalline	1000	KBS-3V(top)	Thermal ($\Delta\sigma_v$=0.3 $\Delta\sigma_h$) + Glacial Stress	0.13	0.07	-	0.18	0.16	0.19	126	173	1	0.93	0.93	45	0.17	16.6	1.000	100
73	Shale	500	KBS-3V(bottom)	Ambient Stress	0.08	0.16	-	0.27	0.35	0.37	20	14	9	0.93	0.93	34	0.28	4.3	0.022	40
74	Shale	500	KBS-3V(bottom)	Thermal Stress ($\Delta\sigma_v$=0)	0.09	0.17	-	0.27	0.35	0.36	22	15	9	0.93	0.93	34	0.28	4.3	0.022	40
75	Shale	500	KBS-3V(bottom)	Thermal Stress ($\Delta\sigma_v$=0.3 $\Delta\sigma_h$)	0.09	0.17	-	0.27	0.35	0.35	22	16	10	0.93	0.93	34	0.28	4.3	0.022	40
76	Shale	500	KBS-3V(bottom)	Glacial Stress	0.16	0.21	-	0.29	0.34	0.34	31	25	37	0.93	0.93	34	0.28	4.3	0.022	40
77	Shale	500	KBS-3V(bottom)	Thermal ($\Delta\sigma_v$=0) + Glacial Stress	0.17	0.22	-	0.29	0.34	0.34	33	27	37	0.93	0.93	34	0.28	4.3	0.022	40
78	Shale	500	KBS-3V(bottom)	Thermal ($\Delta\sigma_v$=0.3 $\Delta\sigma_h$) + Glacial Stress	0.17	0.22	-	0.29	0.34	0.34	33	27	37	0.93	0.93	34	0.28	4.3	0.022	40
79	Limestone	750	KBS-3V(bottom)	Ambient Stress	0.09	0.14	-	0.27	0.32	0.32	26	22	18	0.93	0.93	35	0.27	3.9	0.053	60
80	Limestone	750	KBS-3V(bottom)	Thermal Stress ($\Delta\sigma_v$=0)	0.19	0.21	-	0.28	0.31	0.31	48	43	18	0.93	0.93	35	0.27	3.9	0.053	60
81	Limestone	750	KBS-3V(bottom)	Thermal Stress ($\Delta\sigma_v$=0.3 $\Delta\sigma_h$)	0.20	0.23	-	0.29	0.31	-	51	46	26	0.93	0.93	35	0.27	3.9	0.053	60
82	Limestone	750	KBS-3V(bottom)	Glacial Stress	0.15	0.19	-	0.28	0.31	0.31	38	33	45	0.93	0.93	35	0.27	3.9	0.053	60
83	Limestone	750	KBS-3V(bottom)	Thermal ($\Delta\sigma_v$=0) + Glacial Stress	0.22	0.25	-	0.29	0.30	0.30	59	55	45	0.93	0.93	35	0.27	3.9	0.053	60
84	Limestone	750	KBS-3V(bottom)	Thermal ($\Delta\sigma_v$=0.3 $\Delta\sigma_h$) + Glacial Stress	0.23	0.26	-	0.29	0.30	-	63	58	53	0.93	0.93	35	0.27	3.9	0.053	60
85	Shale	500	KBS-3V(top)	Ambient Stress	0.14	0.14	-	0.31	0.31	-	20	20	0	0.93	0.93	34	0.28	4.3	0.022	40
86	Shale	500	KBS-3V(top)	Thermal Stress ($\Delta\sigma_v$=0)	0.17	0.14	-	0.33	0.30	-	22	24	1	0.93	0.93	34	0.28	4.3	0.022	40
87	Shale	500	KBS-3V(top)	Thermal Stress ($\Delta\sigma_v$=0.3 $\Delta\sigma_h$)	0.17	0.15	-	0.32	0.30	-	22	24	1	0.93	0.93	34	0.28	4.3	0.022	40
88	Shale	500	KBS-3V(top)	Glacial Stress	0.09	0.23	-	0.25	0.37	0.47	31	18	1	0.93	0.93	34	0.28	4.3	0.022	40
89	Shale	500	KBS-3V(top)	Thermal ($\Delta\sigma_v$=0) + Glacial Stress	0.13	0.23	-	0.27	0.35	0.38	33	22	1	0.93	0.93	34	0.28	4.3	0.022	40
90	Shale	500	KBS-3V(top)	Thermal ($\Delta\sigma_v$=0.3 $\Delta\sigma_h$) + Glacial Stress	0.13	0.23	-	0.26	0.35	0.38	33	22	1	0.93	0.93	34	0.28	4.3	0.022	40
91	Limestone	750	KBS-3V(top)	Ambient Stress	0.15	0.12	-	0.30	0.29	-	26	29	0	0.93	0.93	35	0.27	3.9	0.053	60
92	Limestone	750	KBS-3V(top)	Thermal Stress ($\Delta\sigma_v$=0)	0.34	0.17	0.35	0.34	0.25	0.38	48	76	1	0.93	0.93	35	0.27	3.9	0.053	60
93	Limestone	750	KBS-3V(top)	Thermal Stress ($\Delta\sigma_v$=0.3 $\Delta\sigma_h$)	0.33	0.19	-	0.34	0.25	0.35	51	75	1	0.93	0.93	35	0.27	3.9	0.053	60
94	Limestone	750	KBS-3V(top)	Glacial Stress	0.11	0.20	-	0.26	0.33	0.35	38	27	1	0.93	0.93	35	0.27	3.9	0.053	60
95	Limestone	750	KBS-3V(top)	Thermal ($\Delta\sigma_v$=0) + Glacial Stress	0.31	0.22	-	0.32	0.27	0.32	59	74	1	0.93	0.93	35	0.27	3.9	0.053	60
96	Limestone	750	KBS-3V(top)	Thermal ($\Delta\sigma_v$=0.3 $\Delta\sigma_h$) + Glacial Stress	0.30	0.24	-	0.31	0.28	0.31	63	73	1	0.93	0.93	35	0.27	3.9	0.053	60
97	Crystalline	500	AECL	Ambient Stress	0.42	0.00	0.42	1.74	0.40	3.26	60	44	12	3.57	2.1	45	0.17	16.6	1.000	100
98	Crystalline	500	AECL	Thermal Stress ($\Delta\sigma_v$=0)	0.98	0.22	2.49	17.19	29.21	35.00	108	93	12	3.57	2.1	45	0.17	16.6	1.000	100
99	Crystalline	500	AECL	Thermal Stress ($\Delta\sigma_v$=0.3 $\Delta\sigma_h$)	0.89	0.00	0.90	1.58	0.36	1.60	114	99	45	3.57	2.1	45	0.17	16.6	1.000	100
100	Crystalline	500	AECL	Glacial Stress	0.55	0.06	0.56	1.44	0.33	1.44	69	53	39	3.57	2.1	45	0.17	16.6	1.000	100
101	Crystalline	500	AECL	Thermal ($\Delta\sigma_v$=0) + Glacial Stress	0.89	0.09	0.82	1.58	0.40	1.60	117	102	39	3.57	2.1	45	0.17	16.6	1.000	100
102	Crystalline	500	AECL	Thermal ($\Delta\sigma_v$=0.3 $\Delta\sigma_h$) + Glacial Stress	0.89	0.00	0.90	1.58	0.36	1.59	123	107	55	3.57	2.1	45	0.17	16.6	1.000	100
103	Crystalline	1000	AECL	Ambient Stress	0.55	0.00	0.56	1.58	0.36	1.59	63	47	24	3.57	2.1	45	0.17	16.6	1.000	100
104	Crystalline	1000	AECL	Thermal Stress ($\Delta\sigma_v$=0)	0.89	0.17	0.90	1.92	0.40	4.48	112	96	24	3.57	2.1	45	0.17	16.6	1.000	100
105	Crystalline	1000	AECL	Thermal Stress ($\Delta\sigma_v$=0.3 $\Delta\sigma_h$)	0.89	0.00	0.90	1.58	0.36	1.60	117	101	40	3.57	2.1	45	0.17	16.6	1.000	100
106	Crystalline	1000	AECL	Glacial Stress	0.42	0.11	0.42	1.19	0.33	1.21	72	56	51	3.57	2.1	45	0.17	16.6	1.000	100
107	Crystalline	1000	AECL	Thermal ($\Delta\sigma_v$=0) + Glacial Stress	0.89	0.04	0.90	1.58	0.36	1.59	121	105	51	3.57	2.1	45	0.17	16.6	1.000	100
108	Crystalline	1000	AECL	Thermal ($\Delta\sigma_v$=0.3 $\Delta\sigma_h$) + Glacial Stress	0.89	0.14	0.90	1.44	0.36	1.46	126	110	67	3.57	2.1	45	0.17	16.6	1.000	100
109	Shale	500	AECL	Ambient Stress	1.08	0.20	1.09	2.11	0.53	2.14	20	14	9	3.57	2.1	34	0.28	4.3	0.022	40
110	Shale	500	AECL	Thermal Stress ($\Delta\sigma_v$=0)	1.08	0.20	1.09	2.11	0.53	2.15	22	15	9	3.57	2.1	34	0.28	4.3	0.022	40
111	Shale	500	AECL	Thermal Stress ($\Delta\sigma_v$=0.3 $\Delta\sigma_h$)	1.08	0.20	1.09	2.11	0.53	2.14	22	16	10	3.57	2.1	34	0.28	4.3	0.022	40
112	Shale	500	AECL	Glacial Stress	0.00	0.53	0.96	0.89	0.64	1.72	31	25	37	3.57	2.1	34	0.28	4.3	0.022	40
113	Shale	500	AECL	Thermal ($\Delta\sigma_v$=0) + Glacial Stress	0.42	0.53	0.91	1.08	0.64	1.55	33	27	37	3.57	2.1	34	0.28	4.3	0.022	40
114	Shale	500	AECL	Thermal ($\Delta\sigma_v$=0.3 $\Delta\sigma_h$) + Glacial Stress	0.42	0.53	0.91	1.08	0.64	1.55	33	27	37	3.57	2.1	34	0.28	4.3	0.022	40
115	Limestone	750	AECL	Ambient Stress	0.89	0.25	0.91	1.74	0.53	1.78	26	22	18	3.57	2.1	35	0.27	3.9	0.053	60
116	Limestone	750	AECL	Thermal Stress ($\Delta\sigma_v$=0)	1.58	0.22	1.46	2.55	0.48	2.56	48	43	18	3.57	2.1	35	0.27	3.9	0.053	60
117	Limestone	750	AECL	Thermal Stress ($\Delta\sigma_v$=0.3 $\Delta\sigma_h$)	1.44	0.27	1.46	2.11	0.53	2.14	51	46	26	3.57	2.1	35	0.27	3.9	0.053	60
118	Limestone	750	AECL	Glacial Stress	0.00	0.48	0.79	1.08	0.58	1.46	38	33	45	3.57	2.1	35	0.27	3.9	0.053	60
119	Limestone	750	AECL	Thermal ($\Delta\sigma_v$=0) + Glacial Stress	1.44	0.40	1.45	1.74	0.53	1.78	59	55	45	3.57	2.1	35	0.27	3.9	0.053	60
120	Limestone	750	AECL	Thermal ($\Delta\sigma_v$=0.3 $\Delta\sigma_h$) + Glacial Stress	1.31	0.48	1.33	1.74	0.53	1.75	63	58	53	3.57	2.1	35	0.27	3.9	0.053	60

Maximum principal stress

Stress concentration at base of ellipse (a=3.655 m, b=2.15 m)

Table B.2: Summary of Results for Near-field Analysis of DGR Designs (Room Parallel to Minimum Horizontal Stress)

Case	Rock Type	Depth (m)	DGR Design	Loading Condition	Maximum Distance from Opening to Threshold Intersection (m)						Inputs to Calculations									
					Near-field Hoek Brown Threshold			Mohr-Coulomb Fracture Slip Threshold			σ_H'	σ_h'	σ_v'	a	b	ϕ	σ_3'/σ_1'	m	s	σ_c
					Top	Side	Other	Top	Side	Other										
1	Crystalline	500	NAGRA	Ambient Stress	0.06	0.13	-	0.28	0.21	5.00	60	44	12	1.25	1.25	45	0.17	16.6	1.000	100
2	Crystalline	500	NAGRA	Thermal Stress ($\Delta\sigma_v$=0)	0.14	0.34	2.4	0.28	0.45	>5	108	93	12	1.25	1.25	45	0.17	16.6	1.000	100
3	Crystalline	500	NAGRA	Thermal Stress ($\Delta\sigma_v$=0.3 $\Delta\sigma_h$)	0.13	-	-	0.26	0.16	0.70	114	99	45	1.25	1.25	45	0.17	16.6	1.000	100
4	Crystalline	500	NAGRA	Glacial Stress	0.05	-	-	0.25	0.20	0.30	69	53	39	1.25	1.25	45	0.17	16.6	1.000	100
5	Crystalline	500	NAGRA	Thermal ($\Delta\sigma_v$=0) + Glacial Stress	0.14	-	-	0.26	0.14	1.23	117	102	39	1.25	1.25	45	0.17	16.6	1.000	100
6	Crystalline	500	NAGRA	Thermal ($\Delta\sigma_v$=0.3 $\Delta\sigma_h$) + Glacial Stress	0.14	-	-	0.26	0.18	0.46	123	107	55	1.25	1.25	45	0.17	16.6	1.000	100
7	Crystalline	1000	NAGRA	Ambient Stress	0.05	-	-	0.26	0.16	0.80	63	47	24	1.25	1.25	45	0.17	16.6	1.000	100
8	Crystalline	1000	NAGRA	Thermal Stress ($\Delta\sigma_v$=0)	0.14	0.14	0.93	0.28	0.19	4.32	112	96	24	1.25	1.25	45	0.17	16.6	1.000	100
9	Crystalline	1000	NAGRA	Thermal Stress ($\Delta\sigma_v$=0.3 $\Delta\sigma_h$)	0.14	-	-	0.26	0.14	1.11	117	101	40	1.25	1.25	45	0.17	16.6	1.000	100
10	Crystalline	1000	NAGRA	Glacial Stress	0.05	-	-	0.25	0.21	0.25	72	56	51	1.25	1.25	45	0.17	16.6	1.000	100
11	Crystalline	1000	NAGRA	Thermal ($\Delta\sigma_v$=0) + Glacial Stress	0.14	-	-	0.26	0.18	0.56	121	105	51	1.25	1.25	45	0.17	16.6	1.000	100
12	Crystalline	1000	NAGRA	Thermal ($\Delta\sigma_v$=0.3 $\Delta\sigma_h$) + Glacial Stress	0.14	-	-	0.25	0.19	0.33	126	110	67	1.25	1.25	45	0.17	16.6	1.000	100
13	Crystalline	500	KBS-3H	Ambient Stress	0.05	0.10	-	0.21	0.16	3.84	60	44	12	0.96	0.96	45	0.17	16.6	1.000	100
14	Crystalline	500	KBS-3H	Thermal Stress ($\Delta\sigma_v$=0)	0.11	0.26	1.84	0.21	0.35	>5	108	93	12	0.96	0.96	45	0.17	16.6	1.000	100
15	Crystalline	500	KBS-3H	Thermal Stress ($\Delta\sigma_v$=0.3 $\Delta\sigma_h$)	0.10	-	-	0.20	0.12	0.54	114	99	45	0.96	0.96	45	0.17	16.6	1.000	100
16	Crystalline	500	KBS-3H	Glacial Stress	0.04	-	-	0.19	0.15	0.23	69	53	39	0.96	0.96	45	0.17	16.6	1.000	100
17	Crystalline	500	KBS-3H	Thermal ($\Delta\sigma_v$=0) + Glacial Stress	0.11	-	-	0.20	0.11	0.94	117	102	39	0.96	0.96	45	0.17	16.6	1.000	100
18	Crystalline	500	KBS-3H	Thermal ($\Delta\sigma_v$=0.3 $\Delta\sigma_h$) + Glacial Stress	0.11	-	-	0.20	0.13	0.35	123	107	55	0.96	0.96	45	0.17	16.6	1.000	100
19	Crystalline	1000	KBS-3H	Ambient Stress	0.04	-	-	0.20	0.12	0.61	63	47	24	0.96	0.96	45	0.17	16.6	1.000	100
20	Crystalline	1000	KBS-3H	Thermal Stress ($\Delta\sigma_v$=0)	0.11	0.11	0.71	0.21	0.14	3.32	112	96	24	0.96	0.96	45	0.17	16.6	1.000	100
21	Crystalline	1000	KBS-3H	Thermal Stress ($\Delta\sigma_v$=0.3 $\Delta\sigma_h$)	0.11	-	-	0.20	0.11	0.85	117	101	40	0.96	0.96	45	0.17	16.6	1.000	100
22	Crystalline	1000	KBS-3H	Glacial Stress	0.04	-	-	0.19	0.16	0.19	72	56	51	0.96	0.96	45	0.17	16.6	1.000	100
23	Crystalline	1000	KBS-3H	Thermal ($\Delta\sigma_v$=0) + Glacial Stress	0.11	-	-	0.20	0.13	0.43	121	105	51	0.96	0.96	45	0.17	16.6	1.000	100
24	Crystalline	1000	KBS-3H	Thermal ($\Delta\sigma_v$=0.3 $\Delta\sigma_h$) + Glacial Stress	0.11	-	-	0.19	0.14	0.25	126	110	67	0.96	0.96	45	0.17	16.6	1.000	100
25	Shale	500	NAGRA	Ambient Stress	0.23	0.03	-	0.53	0.30	1.00	20	14	9	1.25	1.25	34	0.28	4.3	0.022	40
26	Shale	500	NAGRA	Thermal Stress ($\Delta\sigma_v$=0)	0.24	0.01	-	0.54	0.29	1.35	22	15	9	1.25	1.25	34	0.28	4.3	0.022	40
27	Shale	500	NAGRA	Thermal Stress ($\Delta\sigma_v$=0.3 $\Delta\sigma_h$)	0.24	0.03	-	0.54	0.30	1.13	22	16	10	1.25	1.25	34	0.28	4.3	0.022	40
28	Shale	500	NAGRA	Glacial Stress	0.25	0.31	-	0.39	0.44	-	31	25	37	1.25	1.25	34	0.28	4.3	0.022	40
29	Shale	500	NAGRA	Thermal ($\Delta\sigma_v$=0) + Glacial Stress	0.26	0.31	-	0.40	0.43	-	33	27	37	1.25	1.25	34	0.28	4.3	0.022	40
30	Shale	500	NAGRA	Thermal ($\Delta\sigma_v$=0.3 $\Delta\sigma_h$) + Glacial Stress	0.28	0.31	-	0.40	0.43	-	33	27	37	1.25	1.25	34	0.28	4.3	0.022	40
31	Limestone	750	NAGRA	Ambient Stress	0.20	0.09	-	0.44	0.35	0.48	26	22	18	1.25	1.25	35	0.27	3.9	0.053	60
32	Limestone	750	NAGRA	Thermal Stress ($\Delta\sigma_v$=0)	0.35	-	0.68	0.53	0.25	2.00	48	43	18	1.25	1.25	35	0.27	3.9	0.053	60
33	Limestone	750	NAGRA	Thermal Stress ($\Delta\sigma_v$=0.3 $\Delta\sigma_h$)	0.35	0.09	0.39	0.49	0.30	0.81	51	46	26	1.25	1.25	35	0.27	3.9	0.053	60
34	Limestone	750	NAGRA	Glacial Stress	0.23	0.29	-	0.38	0.41	0.41	38	33	45	1.25	1.25	35	0.27	3.9	0.053	60
35	Limestone	750	NAGRA	Thermal ($\Delta\sigma_v$=0) + Glacial Stress	0.36	0.24	-	0.43	0.36	0.44	59	55	45	1.25	1.25	35	0.27	3.9	0.053	60
36	Limestone	750	NAGRA	Thermal ($\Delta\sigma_v$=0.3 $\Delta\sigma_h$) + Glacial Stress	0.36	0.29	-	0.41	0.38	0.41	63	58	53	1.25	1.25	35	0.27	3.9	0.053	60
37	Shale	500	KBS-3H	Ambient Stress	0.17	0.02	-	0.40	0.23	0.77	20	14	9	0.96	0.96	34	0.28	4.3	0.022	40
38	Shale	500	KBS-3H	Thermal Stress ($\Delta\sigma_v$=0)	0.18	0.01	-	0.41	0.22	1.04	22	15	9	0.96	0.96	34	0.28	4.3	0.022	40
39	Shale	500	KBS-3H	Thermal Stress ($\Delta\sigma_v$=0.3 $\Delta\sigma_h$)	0.18	0.02	-	0.41	0.23	0.86	22	16	10	0.96	0.96	34	0.28	4.3	0.022	40
40	Shale	500	KBS-3H	Glacial Stress	0.19	0.24	-	0.30	0.34	-	31	25	37	0.96	0.96	34	0.28	4.3	0.022	40
41	Shale	500	KBS-3H	Thermal ($\Delta\sigma_v$=0) + Glacial Stress	0.20	0.24	-	0.31	0.33	-	33	27	37	0.96	0.96	34	0.28	4.3	0.022	40
42	Shale	500	KBS-3H	Thermal ($\Delta\sigma_v$=0.3 $\Delta\sigma_h$) + Glacial Stress	0.21	0.24	-	0.31	0.33	-	33	27	37	0.96	0.96	34	0.28	4.3	0.022	40
43	Limestone	750	KBS-3H	Ambient Stress	0.15	0.07	-	0.34	0.27	0.36	26	22	18	0.96	0.96	35	0.27	3.9	0.053	60
44	Limestone	750	KBS-3H	Thermal Stress ($\Delta\sigma_v$=0)	0.27	-	0.52	0.40	0.19	1.53	48	43	18	0.96	0.96	35	0.27	3.9	0.053	60
45	Limestone	750	KBS-3H	Thermal Stress ($\Delta\sigma_v$=0.3 $\Delta\sigma_h$)	0.27	0.07	0.30	0.37	0.23	0.62	51	46	26	0.96	0.96	35	0.27	3.9	0.053	60
46	Limestone	750	KBS-3H	Glacial Stress	0.17	0.22	-	0.29	0.32	0.32	38	33	45	0.96	0.96	35	0.27	3.9	0.053	60
47	Limestone	750	KBS-3H	Thermal ($\Delta\sigma_v$=0) + Glacial Stress	0.28	0.18	-	0.33	0.28	0.34	59	55	45	0.96	0.96	35	0.27	3.9	0.053	60
48	Limestone	750	KBS-3H	Thermal ($\Delta\sigma_v$=0.3 $\Delta\sigma_h$) + Glacial Stress	0.28	0.22	-	0.32	0.29	0.32	63	58	53	0.96	0.96	35	0.27	3.9	0.053	60
49	Crystalline	500	KBS-3V(bottom)	Ambient Stress	0.02	-	-	0.18	0.16	0.19	60	44	12	0.93	0.93	45	0.17	16.6	1.000	100
50	Crystalline	500	KBS-3V(bottom)	Thermal Stress ($\Delta\sigma_v$=0)	0.07	0.05	-	0.18	0.17	0.18	108	93	12	0.93	0.93	45	0.17	16.6	1.000	100
51	Crystalline	500	KBS-3V(bottom)	Thermal Stress ($\Delta\sigma_v$=0.3 $\Delta\sigma_h$)	0.07	0.06	-	0.18	0.17	-	114	99	45	0.93	0.93	45	0.17	16.6	1.000	100
52	Crystalline	500	KBS-3V(bottom)	Glacial Stress	0.04	-	-	0.18	0.16	0.18	69	53	39	0.93	0.93	45	0.17	16.6	1.000	100
53	Crystalline	500	KBS-3V(bottom)	Thermal ($\Delta\sigma_v$=0) + Glacial Stress	0.08	0.06	-	0.18	0.17	0.18	117	102	39	0.93	0.93	45	0.17	16.6	1.000	100
54	Crystalline	500	KBS-3V(bottom)	Thermal ($\Delta\sigma_v$=0.3 $\Delta\sigma_h$) + Glacial Stress	0.08	0.06	-	0.18	0.17	0.18	123	107	55	0.93	0.93	45	0.17	16.6	1.000	100
55	Crystalline	1000	KBS-3V(bottom)	Ambient Stress	0.03	-	-	0.18	0.16	0.19	63	47	24	0.93	0.93	45	0.17	16.6	1.000	100
56	Crystalline	1000	KBS-3V(bottom)	Thermal Stress ($\Delta\sigma_v$=0)	0.07	0.05	-	0.18	0.17	0.18	112	96	24	0.93	0.93	45	0.17	16.6	1.000	100
57	Crystalline	1000	KBS-3V(bottom)	Thermal Stress ($\Delta\sigma_v$=0.3 $\Delta\sigma_h$)	0.08	0.06	-	0.18	0.17	0.18	117	101	40	0.93	0.93	45	0.17	16.6	1.000	100
58	Crystalline	1000	KBS-3V(bottom)	Glacial Stress	0.04	-	-	0.18	0.16	0.18	72	56	51	0.93	0.93	45	0.17	16.6	1.000	100
59	Crystalline	1000	KBS-3V(bottom)	Thermal ($\Delta\sigma_v$=0) + Glacial Stress	0.08	0.06	-	0.18	0.17	0.18	121	105	51	0.93	0.93	45	0.17	16.6	1.000	100
60	Crystalline	1000	KBS-3V(bottom)	Thermal ($\Delta\sigma_v$=0.3 $\Delta\sigma_h$) + Glacial Stress	0.08	0.07	-	0.18	0.17	0.18	126	110	67	0.93	0.93	45	0.17	16.6	1.000	100

Table B.2 (concluded)

Case	Rock Type	Depth (m)	DGR Design	Loading Condition	Maximum Distance from Opening to Threshold Intersection (m)						Inputs to Calculations									
					Near-field Hoek Brown Threshold			Mohr-Coulomb Fracture Slip Threshold			σ_H'	σ_h'	σ_v'	a	b	ϕ	σ_3'/σ_1'	m	s	σ_c
					Top	Side	Other	Top	Side	Other										
61	Crystalline	500	KBS-3V(top)	Ambient Stress	0.10	-	-	0.20	0.12	0.64	118	44	0	0.93	0.93	45	0.17	16.6	1.000	100
62	Crystalline	500	KBS-3V(top)	Thermal Stress ($\Delta\sigma_v$=0)	0.19	-	-	0.20	0.13	0.46	223	93	1	0.93	0.93	45	0.17	16.6	1.000	100
63	Crystalline	500	KBS-3V(top)	Thermal Stress ($\Delta\sigma_v$=0.3 $\Delta\sigma_h$)	0.17	-	-	0.19	0.14	0.28	202	99	1	0.93	0.93	45	0.17	16.6	1.000	100
64	Crystalline	500	KBS-3V(top)	Glacial Stress	0.09	-	-	0.19	0.14	0.30	110	53	1	0.93	0.93	45	0.17	16.6	1.000	100
65	Crystalline	500	KBS-3V(top)	Thermal ($\Delta\sigma_v$=0) + Glacial Stress	0.18	-	-	0.20	0.14	0.31	216	102	1	0.93	0.93	45	0.17	16.6	1.000	100
66	Crystalline	500	KBS-3V(top)	Thermal ($\Delta\sigma_v$=0.3 $\Delta\sigma_h$) + Glacial Stress	0.17	0.01	-	0.19	0.14	0.27	211	107	1	0.93	0.93	45	0.17	16.6	1.000	100
67	Crystalline	1000	KBS-3V(top)	Ambient Stress	0.09	-	-	0.20	0.13	0.44	113	47	0	0.93	0.93	45	0.17	16.6	1.000	100
68	Crystalline	1000	KBS-3V(top)	Thermal Stress ($\Delta\sigma_v$=0)	0.18	-	-	0.20	0.13	0.38	219	96	1	0.93	0.93	45	0.17	16.6	1.000	100
69	Crystalline	1000	KBS-3V(top)	Thermal Stress ($\Delta\sigma_v$=0.3 $\Delta\sigma_h$)	0.18	-	-	0.20	0.14	0.31	214	101	1	0.93	0.93	45	0.17	16.6	1.000	100
70	Crystalline	1000	KBS-3V(top)	Glacial Stress	0.08	-	-	0.19	0.14	0.24	106	56	1	0.93	0.93	45	0.17	16.6	1.000	100
71	Crystalline	1000	KBS-3V(top)	Thermal ($\Delta\sigma_v$=0) + Glacial Stress	0.17	0.00	-	0.19	0.14	0.28	211	105	1	0.93	0.93	45	0.17	16.6	1.000	100
72	Crystalline	1000	KBS-3V(top)	Thermal ($\Delta\sigma_v$=0.3 $\Delta\sigma_h$) + Glacial Stress	0.17	0.02	-	0.19	0.14	0.24	207	110	1	0.93	0.93	45	0.17	16.6	1.000	100
73	Shale	500	KBS-3V(bottom)	Ambient Stress	0.16	0.08	-	0.35	0.27	0.37	20	14	9	0.93	0.93	34	0.28	4.3	0.022	40
74	Shale	500	KBS-3V(bottom)	Thermal Stress ($\Delta\sigma_v$=0)	0.17	0.09	-	0.35	0.27	0.36	22	15	9	0.93	0.93	34	0.28	4.3	0.022	40
75	Shale	500	KBS-3V(bottom)	Thermal Stress ($\Delta\sigma_v$=0.3 $\Delta\sigma_h$)	0.17	0.09	-	0.35	0.27	0.35	22	16	10	0.93	0.93	34	0.28	4.3	0.022	40
76	Shale	500	KBS-3V(bottom)	Glacial Stress	0.21	0.16	-	0.34	0.29	0.34	31	25	37	0.93	0.93	34	0.28	4.3	0.022	40
77	Shale	500	KBS-3V(bottom)	Thermal ($\Delta\sigma_v$=0) + Glacial Stress	0.22	0.17	-	0.34	0.29	0.34	33	27	37	0.93	0.93	34	0.28	4.3	0.022	40
78	Shale	500	KBS-3V(bottom)	Thermal ($\Delta\sigma_v$=0.3 $\Delta\sigma_h$) + Glacial Stress	0.22	0.17	-	0.34	0.29	0.34	33	27	37	0.93	0.93	34	0.28	4.3	0.022	40
79	Limestone	750	KBS-3V(bottom)	Ambient Stress	0.14	0.09	-	0.32	0.27	0.32	26	22	18	0.93	0.93	35	0.27	3.9	0.053	60
80	Limestone	750	KBS-3V(bottom)	Thermal Stress ($\Delta\sigma_v$=0)	0.21	0.19	-	0.31	0.28	0.31	48	43	18	0.93	0.93	35	0.27	3.9	0.053	60
81	Limestone	750	KBS-3V(bottom)	Thermal Stress ($\Delta\sigma_v$=0.3 $\Delta\sigma_h$)	0.23	0.20	-	0.23	0.20	-	51	46	26	0.93	0.93	35	0.27	3.9	0.053	60
82	Limestone	750	KBS-3V(bottom)	Glacial Stress	0.19	0.15	-	0.31	0.28	0.31	38	33	45	0.93	0.93	35	0.27	3.9	0.053	60
83	Limestone	750	KBS-3V(bottom)	Thermal ($\Delta\sigma_v$=0) + Glacial Stress	0.25	0.22	-	0.30	0.29	0.30	59	55	45	0.93	0.93	35	0.27	3.9	0.053	60
84	Limestone	750	KBS-3V(bottom)	Thermal ($\Delta\sigma_v$=0.3 $\Delta\sigma_h$) + Glacial Stress	0.26	0.23	-	0.30	0.29	0.30	63	58	53	0.93	0.93	35	0.27	3.9	0.053	60
85	Shale	500	KBS-3V(top)	Ambient Stress	0.26	0.02	0.40	0.41	0.21	1.29	33	14	0	0.93	0.93	34	0.28	4.3	0.022	40
86	Shale	500	KBS-3V(top)	Thermal Stress ($\Delta\sigma_v$=0)	0.28	0.03	0.45	0.41	0.21	1.23	37	15	1	0.93	0.93	34	0.28	4.3	0.022	40
87	Shale	500	KBS-3V(top)	Thermal Stress ($\Delta\sigma_v$=0.3 $\Delta\sigma_h$)	0.28	0.04	0.43	0.41	0.21	1.16	37	16	1	0.93	0.93	34	0.28	4.3	0.022	40
88	Shale	500	KBS-3V(top)	Glacial Stress	0.21	0.16	-	0.34	0.29	0.34	31	25	1	0.93	0.93	34	0.28	4.3	0.022	40
89	Shale	500	KBS-3V(top)	Thermal ($\Delta\sigma_v$=0) + Glacial Stress	0.23	0.16	-	0.34	0.28	0.35	36	27	1	0.93	0.93	34	0.28	4.3	0.022	40
90	Shale	500	KBS-3V(top)	Thermal ($\Delta\sigma_v$=0.3 $\Delta\sigma_h$) + Glacial Stress	0.23	0.16	-	0.34	0.28	0.35	36	27	1	0.93	0.93	34	0.28	4.3	0.022	40
91	Limestone	750	KBS-3V(top)	Ambient Stress	0.21	0.07	-	0.35	0.23	0.49	39	22	0	0.93	0.93	35	0.27	3.9	0.053	60
92	Limestone	750	KBS-3V(top)	Thermal Stress ($\Delta\sigma_v$=0)	0.39	0.12	0.51	0.36	0.22	0.61	86	43	1	0.93	0.93	35	0.27	3.9	0.053	60
93	Limestone	750	KBS-3V(top)	Thermal Stress ($\Delta\sigma_v$=0.3 $\Delta\sigma_h$)	0.38	0.15	0.45	0.35	0.23	0.50	86	46	1	0.93	0.93	35	0.27	3.9	0.053	60
94	Limestone	750	KBS-3V(top)	Glacial Stress	0.19	0.15	-	0.31	0.28	-	38	33	1	0.93	0.93	35	0.27	3.9	0.053	60
95	Limestone	750	KBS-3V(top)	Thermal ($\Delta\sigma_v$=0) + Glacial Stress	0.36	0.19	-	0.34	0.25	0.37	84	55	1	0.93	0.93	35	0.27	3.9	0.053	60
96	Limestone	750	KBS-3V(top)	Thermal ($\Delta\sigma_v$=0.3 $\Delta\sigma_h$) + Glacial Stress	0.35	0.21	-	0.33	0.26	0.35	84	58	1	0.93	0.93	35	0.27	3.9	0.053	60
97	Crystalline	500	AECL	Ambient Stress	0.61	0.04	0.61	2.11	0.40	10.50	60	44	12	3.57	2.1	45	0.17	16.6	1.000	100
98	Crystalline	500	AECL	Thermal Stress ($\Delta\sigma_v$=0)	1.08	0.25	3.74	17.19	29.21	35.00	108	93	12	3.57	2.1	45	0.17	16.6	1.000	100
99	Crystalline	500	AECL	Thermal Stress ($\Delta\sigma_v$=0.3 $\Delta\sigma_h$)	0.89	0.10	0.90	1.58	0.36	1.60	114	99	45	3.57	2.1	45	0.17	16.6	1.000	100
100	Crystalline	500	AECL	Glacial Stress	0.74	0.00	0.74	1.58	0.36	1.46	69	53	39	3.57	2.1	45	0.17	16.6	1.000	100
101	Crystalline	500	AECL	Thermal ($\Delta\sigma_v$=0) + Glacial Stress	0.98	0.15	0.90	1.74	0.40	1.61	117	102	39	3.57	2.1	45	0.17	16.6	1.000	100
102	Crystalline	500	AECL	Thermal ($\Delta\sigma_v$=0.3 $\Delta\sigma_h$) + Glacial Stress	0.98	0.10	0.99	1.58	0.36	1.60	123	107	55	3.57	2.1	45	0.17	16.6	1.000	100
103	Crystalline	1000	AECL	Ambient Stress	0.61	0.00	0.61	1.58	0.36	1.60	63	47	24	3.57	2.1	45	0.17	16.6	1.000	100
104	Crystalline	1000	AECL	Thermal Stress ($\Delta\sigma_v$=0)	0.98	0.22	0.99	2.11	0.40	7.89	112	96	24	3.57	2.1	45	0.17	16.6	1.000	100
105	Crystalline	1000	AECL	Thermal Stress ($\Delta\sigma_v$=0.3 $\Delta\sigma_h$)	0.98	0.15	0.90	1.74	0.40	1.61	117	101	40	3.57	2.1	45	0.17	16.6	1.000	100
106	Crystalline	1000	AECL	Glacial Stress	0.74	0.09	0.68	1.44	0.33	1.45	72	56	51	3.57	2.1	45	0.17	16.6	1.000	100
107	Crystalline	1000	AECL	Thermal ($\Delta\sigma_v$=0) + Glacial Stress	0.89	0.10	0.90	1.58	0.36	1.60	121	105	51	3.57	2.1	45	0.17	16.6	1.000	100
108	Crystalline	1000	AECL	Thermal ($\Delta\sigma_v$=0.3 $\Delta\sigma_h$) + Glacial Stress	0.98	0.14	0.99	1.58	0.36	1.59	126	110	67	3.57	2.1	45	0.17	16.6	1.000	100
109	Shale	500	AECL	Ambient Stress	1.31	0.22	1.31	2.55	0.53	2.57	20	14	9	3.57	2.1	34	0.28	4.3	0.022	40
110	Shale	500	AECL	Thermal Stress ($\Delta\sigma_v$=0)	1.31	0.25	1.32	2.55	0.48	2.60	22	15	9	3.57	2.1	34	0.28	4.3	0.022	40
111	Shale	500	AECL	Thermal Stress ($\Delta\sigma_v$=0.3 $\Delta\sigma_h$)	1.31	0.22	1.32	2.55	0.53	2.56	22	16	10	3.57	2.1	34	0.28	4.3	0.022	40
112	Shale	500	AECL	Glacial Stress	0.81	0.48	0.92	1.31	0.58	1.44	31	25	37	3.57	2.1	34	0.28	4.3	0.022	40
113	Shale	500	AECL	Thermal ($\Delta\sigma_v$=0) + Glacial Stress	0.89	0.48	0.97	1.44	0.58	1.50	33	27	37	3.57	2.1	34	0.28	4.3	0.022	40
114	Shale	500	AECL	Thermal ($\Delta\sigma_v$=0.3 $\Delta\sigma_h$) + Glacial Stress	0.89	0.48	0.97	1.44	0.58	1.50	33	27	37	3.57	2.1	34	0.28	4.3	0.022	40
115	Limestone	750	AECL	Ambient Stress	1.08	0.22	1.09	1.92	0.48	1.96	26	22	18	3.57	2.1	35	0.27	3.9	0.053	60
116	Limestone	750	AECL	Thermal Stress ($\Delta\sigma_v$=0)	1.08	2.69	2.70	1.31	0.44	3.48	48	43	18	3.57	2.1	35	0.27	3.9	0.053	60
117	Limestone	750	AECL	Thermal Stress ($\Delta\sigma_v$=0.3 $\Delta\sigma_h$)	1.58	0.27	1.60	2.32	0.48	2.34	51	46	26	3.57	2.1	35	0.27	3.9	0.053	60
118	Limestone	750	AECL	Glacial Stress	0.74	0.48	0.78	1.31	0.53	1.36	38	33	45	3.57	2.1	35	0.27	3.9	0.053	60
119	Limestone	750	AECL	Thermal ($\Delta\sigma_v$=0) + Glacial Stress	1.44	0.40	1.47	1.92	0.53	1.93	59	55	45	3.57	2.1	35	0.27	3.9	0.053	60
120	Limestone	750	AECL	Thermal ($\Delta\sigma_v$=0.3 $\Delta\sigma_h$) + Glacial Stress	1.44	0.44	1.46	1.74	0.53	1.78	63	58	53	3.57	2.1	35	0.27	3.9	0.053	60

Maximum principal stress
Stress concentration at base of ellipse (a=3.655 m, b=2.15 m)